



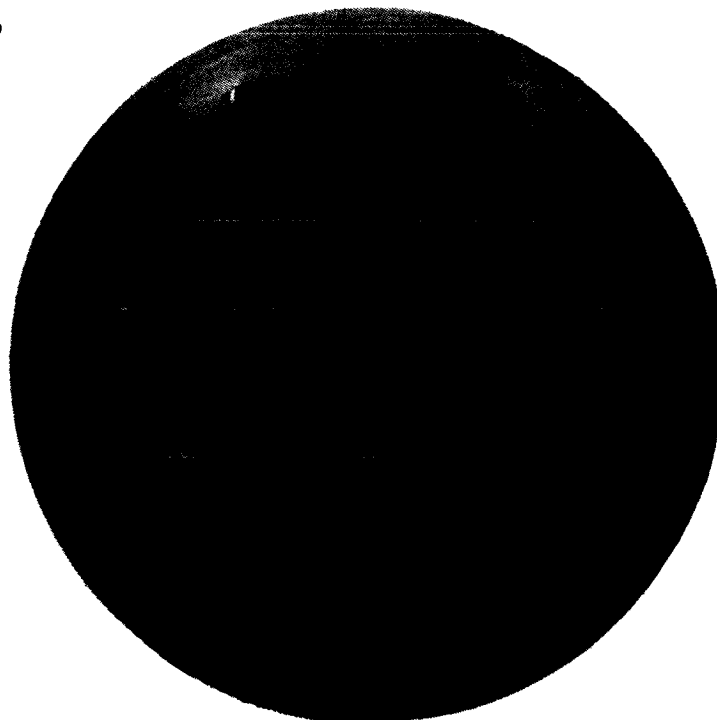
# Carbon Deposition Model For Oxygen-Hydrocarbon Combustion

Contract NAS 8-34715  
Interim Final Report 2427-IFR  
September 1987

Prepared For:  
National Aeronautics And Space Administration  
George C. Marshall Space Flight Center

By:  
R. Hernandez,  
J.I. Ito,  
K.Y. Niiya

Volume I



N88-27254

Unclas  
G3/25 0104580

(NASA-CR-179375) CARBON DEPOSITION MODEL  
FOR OXYGEN-HYDROCARBON COMBUSTION, VOLUME I  
Interim Final Report (Aerojet TechSystems  
Co.) 252 p CSCL 21B

Aerojet  
TechSystems  
Company

INTERIM FINAL REPORT

VOLUME I

CARBON DEPOSITION MODEL FOR OXYGEN-  
HYDROCARBON COMBUSTION

Contract NAS 8-34715

Prepared For:

National Aeronautics and Space Administration  
George C. Marshall Space Flight Center  
Huntsville, Alabama 35812

Prepared By:

  
R. Hernandez  
Project Engineer

Approved By:

  
S.D. Mercer  
Program Manager

Aerojet TechSystems Company  
P.O. Box 13222  
Sacramento, CA 95813

September 1987

RPT/AA0631-a/087



## ABSTRACT

This report presents the design, fabrication, and testing of subscale hardware used in the evaluation of carbon deposition characteristics of liquid oxygen and three hydrocarbon fuels for both main chamber and preburner/gas generator operating conditions. In main chamber conditions, the deposition of carbon on the combustion chamber wall was investigated at mixture ratios of 2.0 to 4.0 and at chamber pressures of 1000 to 1500 psia. No carbon deposition on the chamber walls was detected at these main chamber mixture ratios.

In preburner/gas generator operating conditions, the deposition of carbon on the turbine simulator tubes was evaluated at mixture ratios of 0.20 to 0.60 and at chamber pressures of 720 to 1650 psia. The results of the tests showed carbon deposition rate to be a strong function of mixture ratio and a weak function of chamber pressure. Further analyses evaluated the operational consequences of carbon deposition on preburner/gas generator performance.

PRECEDING PAGE BLANK NOT FILMED

## FOREWORD

The Carbon Deposition Model for Oxygen-Hydrocarbon Combustion Program (Contract NAS 8-34715) was conducted by Aerojet TechSystems Company (ATC) for the NASA-Marshall Space Flight Center. Fred Braam was the NASA-Marshall Program Manager. At ATC, the Program Manager was Roy W. Michel from June 1982 to December 1984 and Steve D. Mercer was the Program Manager from June 1985 to the present. The Project engineer was Merlyn F. Lausten from June 1982 to December 1984. Under his direction the program was initiated, the literature review was conducted, the water-cooled hardware was designed and fabricated, and the 1984 main chamber and preburner/gas generator test programs with  $\text{LO}_2/\text{RP-1}$  were conducted. Rosemary Hernandez was the Project Engineer from June 1985 to the present. Under her direction, the uncooled hardware was designed and fabricated, and the 1985 and 1986 preburner/gas generator test programs with  $\text{LO}_2/\text{RP-1}$ ,  $\text{LO}_2/\text{propane}$  and  $\text{LO}_2/\text{methane}$  were conducted. The initial Program Analysts were Salvatore Buccella and James J. Fang (June 1982 to December 1984) followed by Karen Y. Niiya; the Program Designers were Kin Y. Wong, and Sarah E. Tobin; and the Test Engineers were Blake W. Cathroe, Wally N. Jukes, and Arnold R. Keller. Significant contributions in this program were also made by the following ATC personnel:

William E. Anderson  
Edward L. Carey  
Richard L. Ewen  
William G. Hooper  
Jackson I. Ito  
James K. Kehoe  
Sharon L. Munger  
Yolanda Palmer  
Donald C. Rousar  
Winston Y. Shui  
William A. Thompson  
William R. Thompson  
Richard E. Walker

This interim report covers the period of performance from 1 June 1982 to 30 September 1987. This report covers the carbon deposition literature review, the hardware design and fabrication, the the 1984 main chamber and preburner/gas generator test programs with  $\text{LO}_2/\text{RP-1}$ , and the 1985 to 1986 preburner/gas generator test programs with  $\text{LO}_2/\text{RP-1}$ ,  $\text{LO}_2/\text{propane}$ , and  $\text{LO}_2/\text{methane}$ .

This report has been published in two volumes. Volume I covers the main body of the report plus Appendixes A through D. Volume II covers the data plots of all the test programs. An additional report will be published covering the design and test activities of the follow-on program. Tentatively, the follow-on program is to include  $\text{LO}_2/\text{LNG}$  gas generator testing and higher injection density testing with either  $\text{LO}_2/\text{LNG}$  or  $\text{LO}_2/\text{methane}$  to verify the lack of carbon buildup without the use of a high purity fuel, and to verify the lack of carbon at higher injection densities respectively. Also, lack of correlation between predicted and measured gas temperatures, and between predicted and measured specie and quantity generation at low mixture ratios for  $\text{LO}_2/\text{propane}$  and  $\text{LO}_2/\text{methane}$  is to be rectified by incorporating the fuel chemistry for both propane and methane into the existing Fuel Rich Combustion Model (FRCM).

## TABLE OF CONTENTS

	<u>Page</u>
1.0 Introduction	1
1.1 Background	1
1.2 Objectives	3
2.0 Summary	4
3.0 Conclusions and Recommendations	6
3.1 Impact of Fuel Type on C*, Temperature, and Carbon Deposition	6
3.2 Operational Consequences on Gas Generator Performance	6
3.3 Future Activities	8
4.0 Technical Discussion	9
4.1 Hardware Descriptions	9
4.1.1 Main Chamber Assembly	9
4.1.1.1 Igniter	14
4.1.1.2 Injector	14
4.1.1.3 Acoustic Resonator and Film Coolant Manifold	17
4.1.1.4 Turbulence Ring and Film Coolant Injection Manifold	17
4.1.1.5 Calorimetric Barrel Section	20
4.1.1.6 Calorimetric Throat Section	23
4.1.2 Preburner/Gas Generator Assembly	24
4.1.2.1 1984 Preburner/Gas Generator Configuration	26
4.1.2.1.1 Preburner/Gas Generator Injector	26
4.1.2.1.2 Water-Cooled Turbulence Ring and Film Coolant Injection Manifold	30
4.1.2.1.3 Turbine Simulator	30
4.1.2.2 1985-1986 Preburner/Gas Generator Modified Configuration	33
4.1.2.2.1 Uncooled Turbulence Ring Assembly	35
4.1.2.2.2 Uncooled Upstream L' Section with Temperature Rake and Pressure Taps	35
4.1.2.2.3 Uncooled Downstream L' Section with Pressure Tap	38
4.1.2.2.4 Uncooled Exit Nozzles	38
4.1.2.2.5 Uncooled Turbine Simulator Assembly	41
4.1.2.3 Alternate Throat Configurations	41

## TABLE OF CONTENTS (cont.)

	<u>Page</u>
4.2 Test Facility	46
4.2.1 Propellant Feedsystem	46
4.2.2 Instrumentation	49
4.2.3 Data Measurement Consistency	54
4.2.3.1 Pressure Measurements	54
4.2.3.2 Combustion Gas Temperature Uniformity	55
4.3 Main Chamber Test Results	60
4.3.1 C* Performance	60
4.3.2 Carbon Deposition	63
4.3.3 Main Chamber Thermal Analysis	68
4.3.3.1 Calorimetric Chamber Design	68
4.3.3.2 Thermal Design Parameters	69
4.3.3.3 Nozzle Test Data and Analysis	76
4.3.3.4 Calorimetric Barrel Section Test Data and Analysis	82
4.3.3.5 Experimental Cg Profile	91
4.4 Gas Generator Test Results	99
4.4.1 Test Summary	99
4.4.2 Gas Temperature	99
4.4.3 C* Performance	105
4.4.4 Carbon Deposition	114
4.4.4.1 Turbine Simulator Flow Blockage Analysis	118
4.4.4.2 Effect of Fuel Selection and Mixture Ratio upon Exhaust Plume Appearance	120
4.4.4.3 Effect of Mixture Ratio upon Deposition Rate	120
4.4.4.4 Effect of Chamber Pressure on Deposition Rate	127
4.4.4.5 Effect of Mass Flux on Deposition Rate (1985 RP-1 Tests, Only)	127
4.4.4.6 Effect of Velocity on Deposition Rate (1985 RP-1 Tests, Only)	129
4.4.4.7 Effect of Turbine Simulator Geometry on Deposition Rate	129
4.4.4.8 Effect of Shutdown Transients on Residual Carbon Deposits	129

## TABLE OF CONTENTS (cont.)

	<u>Page</u>
4.5 Fuel-Rich Hydrocarbon Combustion Data Analysis	134
4.5.1 Related Experience	134
4.5.2 Fuel Property Comparisons	137
4.5.3 Fuel-Rich Combustion Model	140
4.5.3.1 Hydrocarbon Decomposition Kinetics	146
4.5.3.1.1 Gas Temperature (MRGG) Effects	146
4.5.3.1.2 Pressure Effects	146
4.5.3.1.3 Gas Residence Time Effects	146
4.5.3.2 Injector Design Effects	148
4.5.3.2.1 Droplet Atomization Distribution	150
4.5.3.2.2 Fuel Volatility Influences	151
4.5.3.2.3 Mixing Uniformity Effect on Carbon Deposition	152
4.5.3.2.4 Mixer Design Benefits	153
References	157
Distribution List	158
Appendix A: Nomenclature and Unit Conversion Factors	A-1
Appendix B: Literature Review of Carbon Deposition Model	B-1
Appendix C: Hardware Drawings	C-1
Appendix D-1: LO <sub>2</sub> /RP-1 Main Chamber and Water-Cooled Gas Generator Data Reduction Equations	D-1
Appendix D-2: LO <sub>2</sub> /RP-1 Gas Generator Data Reduction Equations	D-4
Appendix D-3: LO <sub>2</sub> /Propane and LO <sub>2</sub> /Methane Gas Generator Data Reduction Equations	D-7

## LIST OF TABLES

<u>Table No.</u>		<u>Page</u>
I	Main Combustor Design Conditions	13
II	Preburner Design Conditions	25
III	1984 RP-1 Carbon Deposition Main Chamber Test Summary	61
IV	Initial Chamber Thermal Design Parameters	71
V	Main Chamber Circuit Hydraulic Parameters	73
VI	Baseline Main Chamber Gas-Side Thermal Parameters	74
VII	Predicted Main Chamber Cooling Circuit Thermal Parameters	75
VIII	Clean-Wall Predictions for the Nozzle	77
IX	Nozzle Test Data	78
X	Channel Model 2-D Predictions for Maximum Flux Nozzle Location	83
XI	Barrel Sections Test Data	84
XII	Channel Model 2-D Predictions for the 8-in. Barrel Section (System as Orificed)	89
XIII	Channel Model 2-D Predictions for the 8-in. Barrel Section (Up-rated Orificing)	92
XIV	Summary of Test-Derived Gas-Side Heat Flux Data	94
XV	1984-1986 Gas Generator Test Program	100
XVI	1984 RP-1 Carbon Deposition Preburner Data Test Summary	101
XVII	1985 RP-1 Carbon Deposition Preburner Test History	102
XVIII	1986 LOX/Propane Test History	103
XIX	1986 LOX/Methane Test History	104
XX	Comparison of Hydrocarbon Fuel Properties	138
XXI	Fuel-Rich Combustion Model Chemical Reactions	145

## LIST OF FIGURES

<u>Figure No.</u>		<u>Page</u>
1	Gas Generator Operating Limits	7
2	Main Chamber Assembly	10
3	Main Chamber Assembly Schematic	11
4	Main Combustion Chamber Design Heat Flux	12
5	Main Chamber OFO Triplet Element Injector Pattern	15
6	Injector Body	16
7	Resonator/Fuel Film Cooling Manifold	18
8	Main Combustor Turbulence Ring/FFC Manifold	19
9	Calorimetric Barrel (L')	21
10	Calorimetric Nozzle	22
11	Water-Cooled Preburner/Gas Generator Configuration	27
12	1984 Gas Generator/Preburner Assembly	28
13	Preburner/Gas Generator FOF Triplet Element Injector Pattern	29
14	Water-Cooled Turbulence Ring and Film Coolant Injection Manifold	31
15	Cooled Preburner Turbine Simulator	32
16	Preburner/Gas Generator Assembly	34
17	Preburner Uncooled Turbulence Ring	36
18	Uncooled Upstream L' Section with Thermocouple Rake and Pressure Taps	37
19	Uncooled Downstream L' Section with Pressure Tap	39
20	Uncooled Exit Nozzles	40
21	Turbine Simulator Orifice Plate and Nozzles	42
22	Test Series with Subsonic 3D Turbine Simulator	43
23	Test Series with Sonic Conditions at the Turbine Simulator Configuration	45
24	Bay 6 LOX/Hydrocarbon Test Facility	47
25	Propellant Feed System Schematic	48
26	Typical Main Chamber Instrumentation	50
27	Water Cooled Configuration Instrumentation	51
28	Preburner/Gas Generator Modified Hardware Configuration Instrumentation	52



LIST OF FIGURES (cont.)

<u>Figure No.</u>		<u>Page</u>
29	Upstream Pressure Measurement Comparison at $P_c = 1000$ psi (6.89 MPa)	56
30	Upstream Pressure Measurement Comparison at $P_c = 1500$ psi (10.34 MPa)	57
31	Upstream Pressure Measurement Comparison at $P_c = 750$ psi (5.17 MPa)	58
32	Preburner/Gas Generator Gas Temperature Thermocouple Locations	59
33	Main Chamber Combustion Efficiency	62
34	Mid $P_c$ (Ref. 3) $LO_2$ /Propane Nozzle Heat Flux	64
35	Main Chamber $LO_2$ /RP-1 Nozzle Heat Flux	65
36	Main Chamber Heat Flux Results Show no Carbon Build-up	66
37	Main Combustion Chamber Exhaust Plume	67
38	Design $C_g$ Profile for Carbon Deposition Nozzle	70
39	Gas-Side Heat Fluxes as a Function of Chamber Pressure (Inlet Section of Nozzle)	79
40	Gas-Side Heat Fluxes as a Function of Chamber Pressure - Convergent Section of Nozzle	80
41	Gas-Side Heat Fluxes as a Function of Chamber Pressure (Nozzle Section Downstream of Throat)	81
42	Gas-Side Heat Fluxes as a Function of Chamber Pressure - 12 in. (30.48 cm) Barrel Section	85
43	Gas-Side Heat Fluxes as a Function of Chamber Pressure - 8 in. (20.32 cm) Barrel Section	86
44	Axial Variation in Gas-Side Heat Flux - 8 in. (20.32 cm) Barrel Section	88
45	Predicted Burnout Safety Factor and Maximum Gas-Side Wall Temperature as a Function of Chamber Pressure - Coolant Flow Rates for Test Orificing	90
46	Predicted Burnout Safety Factor and Maximum Gas-Side Wall Temperature as a Function of Coolant Flow Rate - Barrel at Chamber Pressure of 1750 psia (12.06 MPa)	93
47	Nozzle Gas-Side Heat Flux as a Function of Mixture Ratio and Nozzle Area Ratio	95
48	Comparison of Test Derived and Design $C_g$ Values in the Nozzle	97
49	Experimental $C_g$ Profile for Carbon Deposition Main Chamber	98

## LIST OF FIGURES (cont.)

<u>Figure No.</u>		<u>Page</u>
50	Gas Temperatures for LO <sub>2</sub> /RP-1	106
51	Gas Temperatures for LO <sub>2</sub> /Propane	107
52	Gas Temperatures for LO <sub>2</sub> /Methane	108
53	C* Performance for LO <sub>2</sub> /RP-1	110
54	C* Performance for LO <sub>2</sub> /Propane	111
55	C* Performance for LO <sub>2</sub> /Methane	112
56	Carbon Buildup with LO <sub>2</sub> /RP-1	115
57	Carbon Buildup with LO <sub>2</sub> /Propane	116
58	Condition of the Turbine Simulator after Testing with LO <sub>2</sub> /Methane	117
59	Exhaust Plumes for LO <sub>2</sub> /RP-1	121
60	Exhaust Plumes for LO <sub>2</sub> /Propane	122
61	Exhaust Plumes for LO <sub>2</sub> /Methane	123
62	Carbon Deposition for LO <sub>2</sub> /RP-1	124
63	Carbon Deposition for LO <sub>2</sub> /Propane	125
64	Carbon Deposition for LO <sub>2</sub> /Methane	126
65	Effect of Mass Flux on Deposition Rate	128
66	Effect of Gas Velocity on Deposition Rate	130
67	Comparison of Thermocouple Response	132
68	Comparison of Back-to-Back Tests	133
69	Long Duration Carbon Deposition Effects in Titan I Gas Generators	135
70	Fuel-Rich LO <sub>2</sub> /RP-1 Combustion Model	141
71	Fuel Vaporization Model	142
72	Fuel-Rich Combustion Model Reaction Schematic	144
73	Gas Residence Time vs Temperature for Methane Decomposition	149
74	Packed Column Technology is Mature in Chemical Process Industry	156

## LIST OF APPENDICES

<u>Appendix.</u>		<u>Page</u>
A	Nomenclature and Unit Conversion Factors	A-1
B	Literature Review of Carbon Deposition Model	B-1
C	Hardware Drawings	C-1
D-1	LO <sub>2</sub> /RP-1 Main Chamber and Water-Cooled Gas Generator Data Reduction Equations	D-1
D-2	LO <sub>2</sub> /RP-1 Gas Generator Data Reduction Equations	D-4
D-3	LO <sub>2</sub> /Propane and LO <sub>2</sub> /Methane Gas Generator Data Reduction Equations	D-7
E-1	1984 LO <sub>2</sub> /RP-1 Main Chamber Data Plots	E-1
E-2	1984 LO <sub>2</sub> /RP-1 Gas Generator Data Plots	E-2
E-3	1985 LO <sub>2</sub> /RP-1 Gas Generator Data Plots	E-3
E-4	1986 LO <sub>2</sub> /Propane Gas Generator Data Plots	E-4
E-5	1986 LO <sub>2</sub> /Methane Gas Generator Data Plots	E-5

## 1.0 INTRODUCTION

### 1.1 BACKGROUND

Advanced engine studies have indicated significant mission performance and life cycle cost benefits are associated with  $\text{LO}_2$ /hydrocarbon propellant engine systems. Potential long range applications include a high pressure liquid rocket booster for space shuttle, a block II propellant system for OMS and RCS engines on space shuttle orbiter, an advanced single stage-to-orbit shuttle replacement vehicle, ALS and a heavy lift launch vehicle. Studies supported by both NASA-MSFC and the Air Force have indicated that there may well be near-term (~ 1995 ) applications.

The development of the combustion devices for this next generation booster engine is hampered because of the lack of critical data or contradictory existing data. Combustion devices can be broken down into two general categories: main chamber combustion devices and preburner or gas generator devices. In main chamber devices, compatibility characteristics of  $\text{LO}_2$ /HC injectors are ambiguous, at best, because of differing injector designs, hardware configurations and test conditions. Consequently, the gas-side heat flux, the controlling parameter in the thrust chamber design, is unknown. The cooling limits of these main chambers will restrict their operating chamber pressure; thus, stringent cooling requirements will be required for the development of these high pressure reusable engines. Low pressure hydrocarbon engine data has shown that carbon deposition on the chamber wall forms an insulating layer and can be beneficial from a cooling standpoint. The extent of carbon deposition on the main combustor chamber walls may determine the engine's operating pressure capability by minimizing the effect of the combustion heat flux at the chamber wall.

In preburner/gas generators, carbon buildup on the turbine blades may render hydrocarbon gas generators or preburners unsuitable for reusable applications. The design of these engines will require an understanding of the factors controlling carbon deposition and how it is impacted by fuel composition. Unknown reaction kinetics at low mixture ratios typical of preburners/gas generators and an incomplete database; i.e., limited low mixture ratio gas temperature data and carbon deposition characteristics for  $\text{LO}_2$ /RP-1

and  $\text{LO}_2$ /methane, and no data for  $\text{LO}_2$ /propane; make it difficult to characterize  $\text{LO}_2$ /HC combustion for the rational selection of the most promising propellant combination and combustor design parameters for future technology efforts and engine development programs.

In the past, soot accumulation in the turbine drive system was low enough that it did not severely penalize the design of expendable engines due to their short operating life. Future high-pressure reusable long-operating life hydrocarbon engine requirements will not be so tolerant. Accumulated soot buildup in the turbine nozzles of a gas generator cycle engine will not be tolerated in future reusable booster engines. While several  $\text{LO}_2$ /RP-1 fueled engines have been developed in the past, a consistent set of data spanning the hydrocarbon fuels of interest to the next generation booster engines has not been generated over the relevant range of operating conditions.

## 1.0, Introduction (cont.)

### 1.2 OBJECTIVES

The overall objective of this program was to develop an empirical model describing the deposition of carbon (soot) on the walls of oxygen/hydrocarbon combustors and turbine drive systems. The program was conducted in several phases. The initial phase evaluated,  $\text{LO}_2/\text{RP-1}$  combustion at main chamber and gas generator mixture ratios. The second phase verified the gas generator mixture ratio data from the initial phase through use of additional instrumentation and an expanded test condition matrix. The third phase evaluated  $\text{LO}_2/\text{propane}$  and  $\text{LO}_2/\text{methane}$  propellants at gas generator mixture ratios.

## 2.0 SUMMARY

The generation and deposition of carbon have been studied using subscale hardware with  $\text{LO}_2/\text{RP-1}$ ,  $\text{LO}_2/\text{propane}$ , and  $\text{LO}_2/\text{methane}$  at low mixture ratio conditions and with  $\text{LO}_2/\text{RP-1}$  at main chamber mixture ratios. One universal test set-up and the same triplet injector was used throughout the testing. Carbon deposition during main chamber operation with  $\text{LO}_2/\text{RP-1}$  was studied for mixture ratios of 2.0 to 4.0 and chamber pressures of 1000 to 1500 psia (6.89 to 10.34 MPa). Seven data tests were conducted at main chamber conditions. Ignition on all tests was reliable and smooth. Very high combustion efficiency, >99%, was achieved at the nominal design mixture ratio of 3.0. Efficiency dropped slightly at both higher and lower mixture ratios but still remained relatively high compared to the 90-93% range of the operational  $\text{LO}_2/\text{RP-1}$  engines developed during the 1955 - 1965 era. Test data for chamber pressures of 980 and 1510 psia (6.76 to 10.41 MPa) and a mixture ratio of 3 were analyzed in depth. But all the test data plots are available in Appendix E. Nozzle heat flux data when extrapolated to a  $P_c$  of 2000 psia (13.78 MPa) gave results suggesting an overstatement of the  $C_g$  at the nozzle inlet and a slight understatement at the throat. Barrel section heat flux data showed an axial flux dependency. Thermal data together with visual post-test inspection show no evidence of carbon deposition on the chamber walls.

The deposition of carbon on the turbine simulator tubes during preburner/gas generator testing was evaluated at mixture ratios of 0.20 to 0.60 and at chamber pressures from 720 to 1650 psia (4.96 to 11.38). A total of 55 tests were conducted at preburner/gas generator conditions. Nearly 2000 seconds of test data were collected for each fuel for a total of 6832 seconds in the same test setup. Test durations ranged from 100 to 200 seconds. The mixture ratios tested covered the range of interest for state-of-the-art turbopump machinery; i.e., 1300 to 1600°F gas. Ignition was reliable and smooth once the start sequence was tailored for each fuel. Both  $\text{LO}_2/\text{RP-1}$  and  $\text{LO}_2/\text{propane}$  had a fuel lead as indicated by the pressure rise in the inlet manifold whereas the  $\text{LO}_2/\text{methane}$  required a slight oxidizer lead. The reduced data plots are bound separately in Appendix E. The results show that the carbon deposition rate is a strong function of mixture ratio and a weak function of chamber pressure. The results also indicate that there is a mixture

ratio that will minimize deposition for  $\text{LO}_2/\text{RP-1}$ . Gas generator testing with  $\text{LO}_2/\text{propane}$  revealed a threshold mixture ratio for which carbon deposition begins and becomes very heavy. Carbon deposition was not detected for  $\text{LO}_2/\text{methane}$  at any mixture ratio tested. From the carbon deposition analyses, the turbine drive operating limits were defined for each fuel tested. Data from this program indicated that methane is the only hydrocarbon fuel tested that can be run without carbon deposition over the desired gas generator operating temperature range.

It must be remembered that the test hardware designed to promote uniform combustion upstream of the turbine simulator; and that carbon deposition can occur due to either poor injector performance or fuel chemistry. This program has shown that carbon deposition can occur due to fuel chemical kinetics. An increase in gas generator size will require a coarser injection pattern which may also contribute to carbon deposition.



### 3.0 CONCLUSIONS AND RECOMMENDATIONS

#### 3.1 IMPACT OF FUEL TYPE ON C\*, TEMPERATURE AND CARBON DEPOSITION

The preburner test data from this program have shown that methane gives a C\* performance within 10% of the One Dimensional Equilibrium (ODE) predicted value, while propane and RP-1 test data are within 14% and 40%, respectively, of their ODE predicted C\* performances. Both propane and methane exhibited C\* performances between 3000 to 4000 fps (914 to 1219-m/s), while RP-1 showed C\* performances between 1600 to 3000 fps (488 to 914 m/s). Gas temperatures were highest for propane (1100 to 1900°F) (866 to 1311K) with both methane and RP-1 between 800 to 1300°F (700 to 977K). Methane produced no carbon while both RP-1 and propane deposited carbon above a certain threshold mixture ratio.

#### 3.2 OPERATIONAL CONSEQUENCES ON GAS GENERATOR PERFORMANCE

The results of the carbon deposition and gas temperatures as a function of mixture ratio for all three propellant combinations tested are summarized in Figure 1. The curves on each plot indicate the measured gas temperature as a function of mixture ratio tested for each fuel. Superimposed on each plot is the desired temperature range for the operation of state-of-the-art turbine drives. The highlighted area indicates the region where operation for each fuel will not incur or at least minimally incur carbon buildup. The intersection of the highlighted area with the area delineating the desired temperature range indicates the region of acceptable performance for a gas generator for each fuel.

Figure 1 indicates LO<sub>2</sub>/RP-1 cannot be operated in the desirable temperature range for gas generators without incurring undesirable carbon buildup. LO<sub>2</sub>/propane can be operated in the desired temperature range up to a maximum of 1500°F (1088K). Operation with LO<sub>2</sub>/methane is unrestricted over the desired gas generator operating temperature range. Therefore to minimize carbon deposition, methane is the hydrocarbon fuel to choose for operation in a bipropellant hydrocarbon engine.

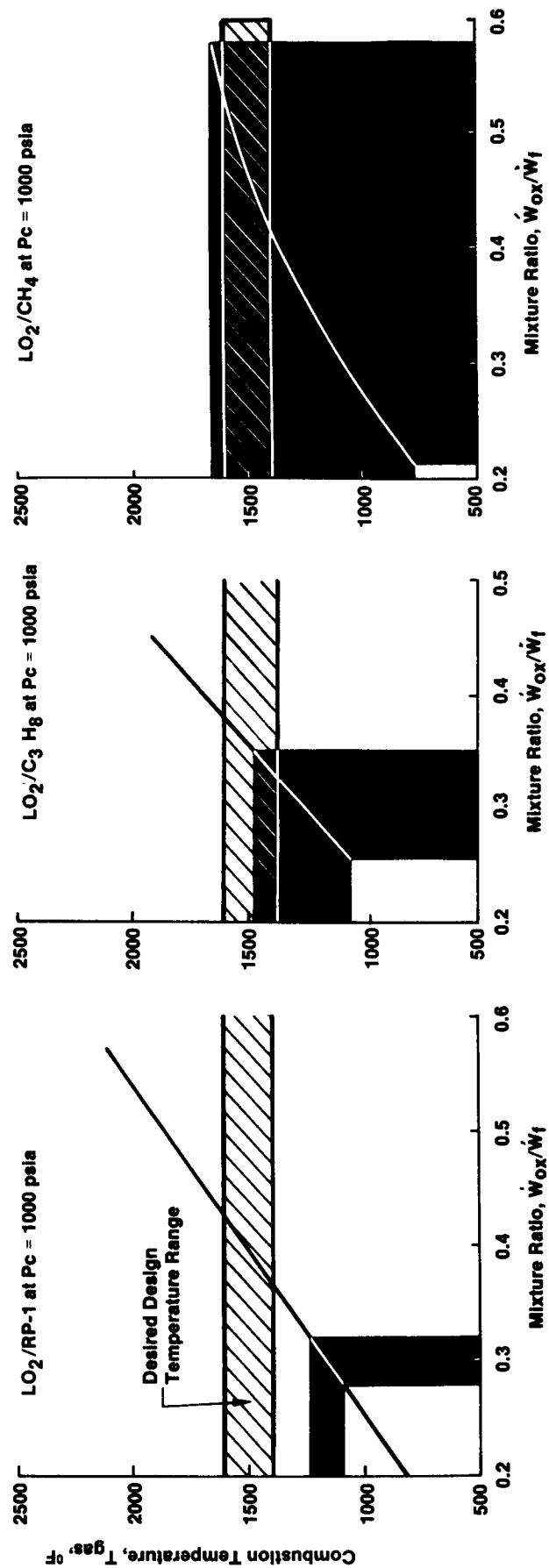


Figure 1. Gas Generator Operating Limits

### 3.0 Conclusions and Recommendations (cont.)

#### 3.3 FUTURE ACTIVITIES

It is recommended that additional testing be conducted to better understand and characterize the carbon deposition under gas generator operation; specifically, further fuel-rich tests with liquefied natural gas (LNG) to verify the lack of carbon buildup without the use of a high purity fuel, and fuel-rich gas generator tests with propane to further define the sharp transition from no carbon buildup to excessive buildup. Also, lack of correlation between predicted  $C^*$  performance and gas temperatures at low mixture ratios and measured gas temperature for  $LO_2$ /propane and  $LO_2$ /methane should be corrected by incorporating the fuel chemistry for both propane and methane into the existing Fuel Rich Combustion Model (FRCM) (Ref. 1).

## 4.0 TECHNICAL DISCUSSION

### 4.1 HARDWARE DESCRIPTIONS

Two basic test assemblies were built; one to simulate main chamber conditions, and one to simulate gas generator or preburner conditions. To obtain the maximum experimental test data at minimum cost, the test hardware was built in a modular design. This bolted modular concept provided test hardware flexibility by allowing the interchange of many of the chamber components from the main chamber assembly to the gas generator assembly. The details of the main chamber assembly and the gas generator/preburner assembly are discussed below. A drawing package of the hardware used in this program is provided in Appendix C.

#### 4.1.1 Main Chamber Assembly

Testing at main chamber operating conditions took place in 1984 in the hardware shown in Figure 2; and the main chamber configuration is schematically depicted in Figure 3. The main chamber assembly consisted of a gaseous  $H_2/O_2$  igniter assembly, an EDM OFO triplet injector including a separate film cooling circuit, a water-cooled copper acoustic cavity, two water-cooled cylindrical nickel liner barrel or L' sections and a water-cooled copper-lined nozzle throat section. The long L' sections, turbulence ring, and 22:1 contraction ratio were incorporated into the system in order to promote uniform combustion. This was done to assure that main chamber deposition could be evaluated for propellant chemistry effects rather than TCA design sensitivities. The water-cooled chamber and throat sections were circumferential coolant flow calorimeters. The projected high throat heat fluxes for the high pressure main chamber operating conditions, see Figure 4, required high pressure water in conjunction with thin chamber gas-side walls for the cooled nozzle. The component gas-side wall materials and thicknesses were selected to provide a range of conditions for soot buildup. The components were designed to be interchangeable and utilize standard pipe flanges to keep the cost of fabrication to a minimum. Individual components were mechanically joined using self-energizing Teflon-coated Raco seals for effective sealing. The main combustor design parameters are summarized in Table I. A detailed discussion of the main combustor components follows below:

ORIGINAL PAGE IS  
OF POOR QUALITY

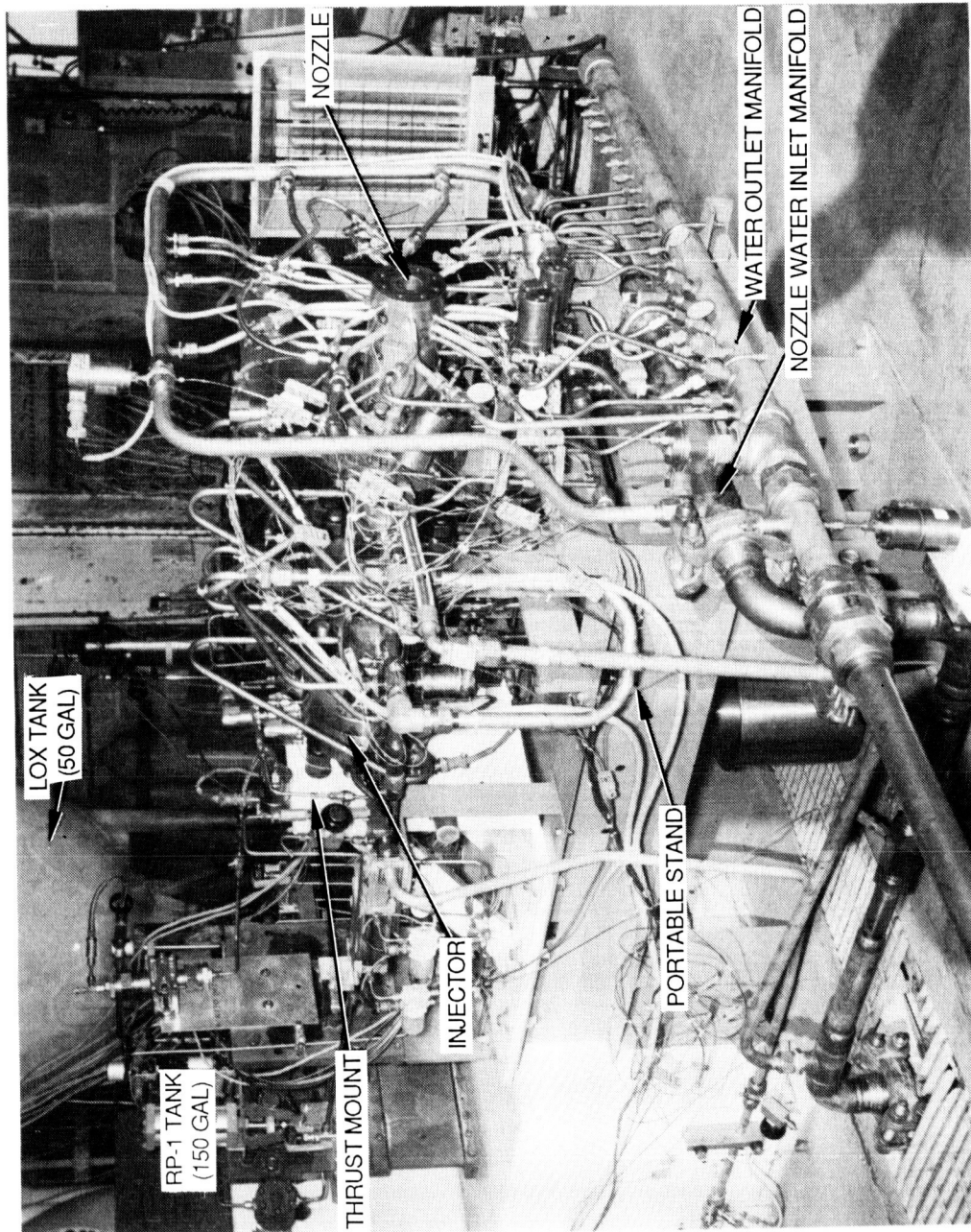
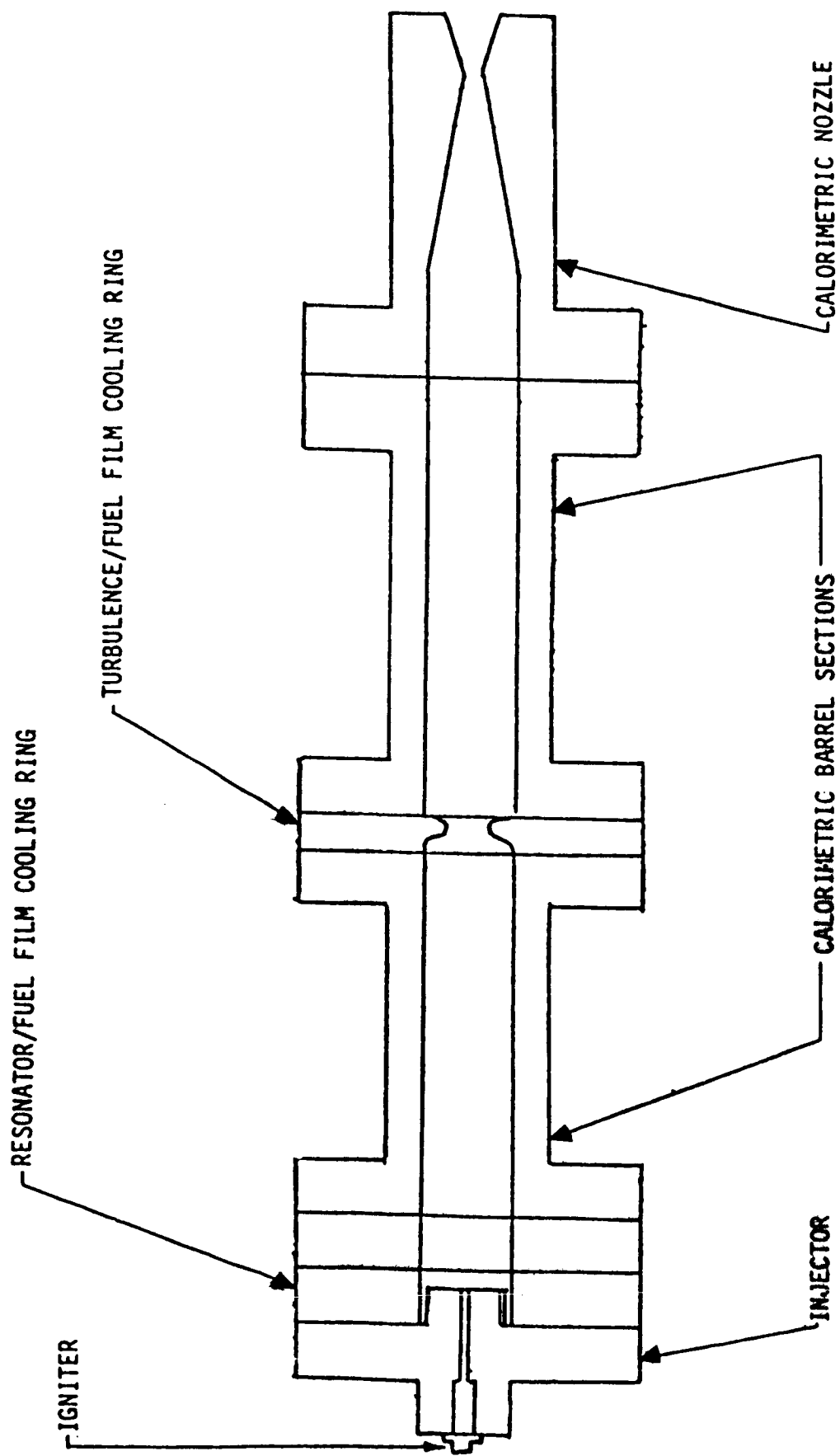


Figure 2. Main Chamber Assembly



NOTE: SKETCH NOT TO SCALE

**Figure 3. Main Chamber Assembly Schematic**

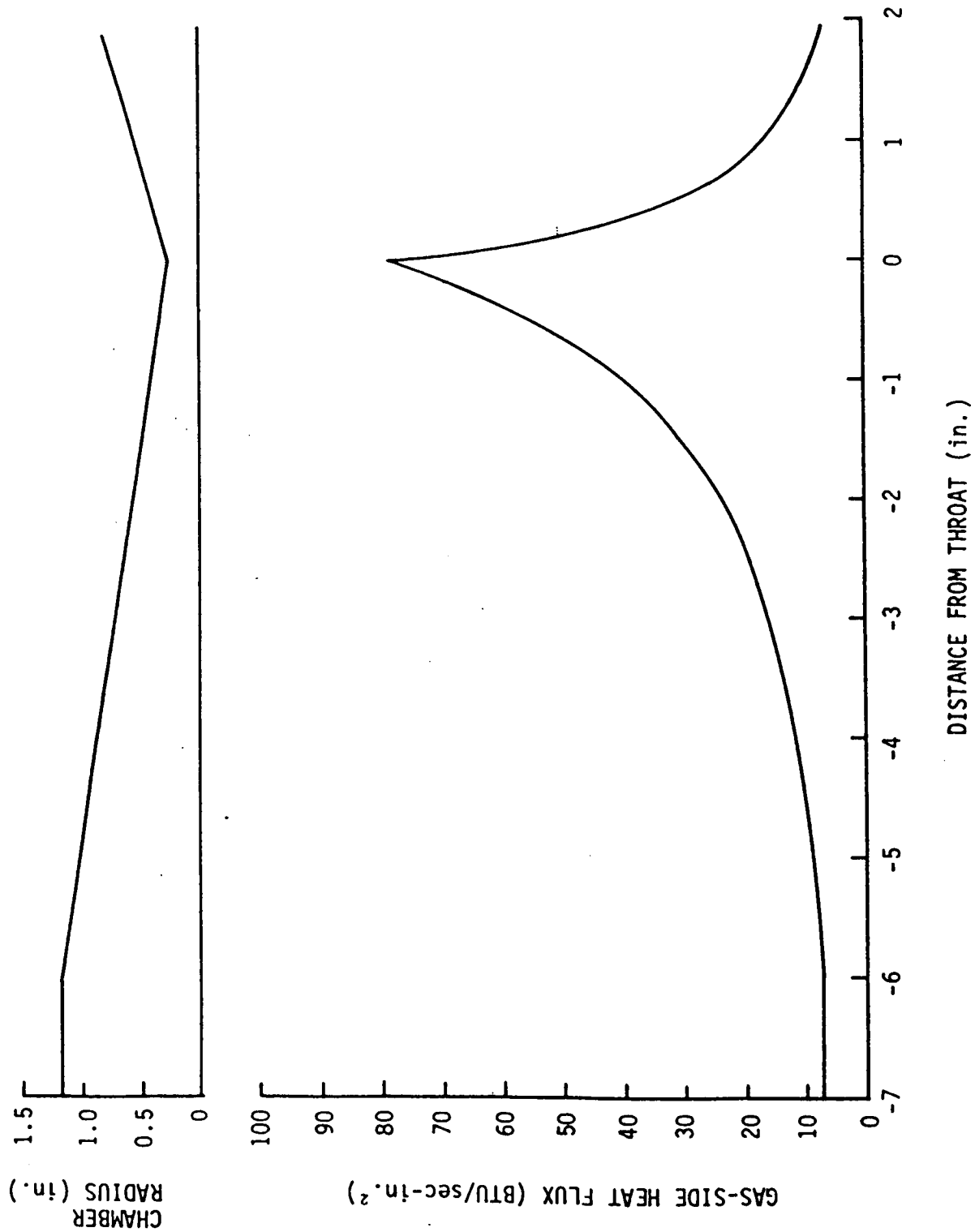


Figure 4. Main Combustion Chamber Design Heat Flux

TABLE I

MAIN COMBUSTOR DESIGN CONDITIONS

Design Parameters

$$P_c = 2000 \text{ psia (1500 - 2000 psia) [13.78 MPa (10.34-13.78 MPa)]}$$

$$MR = 3.0 (2.0 - 4.0)$$

$$W_f = 0.555 \text{ lb/sec (0.25 kg/sec)}$$

$$W_o = 1.665 \text{ lb/sec (0.76 kg/sec)}$$

$$A_t = 0.196 \text{ in}^2 (12.65 \text{ cm}^2)$$

$$D_t = 0.50 \text{ in (1.27 cm)}$$

$$D_c = 2.38 \text{ in. (6.05 cm)}$$



## 4.1, Hardware Descriptions (cont.)

### 4.1.1.1 Igniter

An existing gaseous hydrogen/gaseous oxygen spark igniter was used for both the main combustor assembly and the gas generator/preburner assembly with only minor modifications. This igniter was used on a NASA-funded preburner program (NAS 3-22647) (Ref. 2) and a NASA-funded hydrocarbon combustion program (NAS 9-15958) (Ref. 3), in addition to the present contract. The igniter assembly was bolted to the backside of the injector body such that the igniter fires through the center of injector face. This igniter configuration has been in use at ATC for over a decade and has been employed in more than 100,000 engine firings. Its use is considered to be routine.

### 4.1.1.2 Injector

The injector design was based on the EDM (electro discharge machined) triplet injector used on NASA Contract 9-15958 (Ref. 3). The injector was stable under all operating conditions, was in good condition at the end of testing, and provided 97-99% efficiency.

The injector had a 2.18-inch (5.54 cm) face diameter and contained 18 elements arranged in a single row. The oxidizer-rich OFO triplet had 0.024-inch (0.061 cm) oxidizer orifices and 0.021-inch (0.053 cm) fuel orifices. The element configuration is illustrated in Figure 5. The injector body is shown in Figure 6. The concentric ring manifold injector was a weldment consisting of a nickel core body, a solid nickel face plate, and a stainless steel fuel inlet cover. Nickel was used as the face material for cooling purposes. All subcomponents were joined by electron beam welding. The oxidizer manifold was located in the injector flange, outboard of the injector channels. An oxidizer inlet line welded to the flange fed the manifold via a drilled passage. The oxidizer manifold was machined eccentric to the injector axis to provide a constant velocity flow configuration. This manifold fed three radial oxidizer manifolds which in turn fed the face ring through the

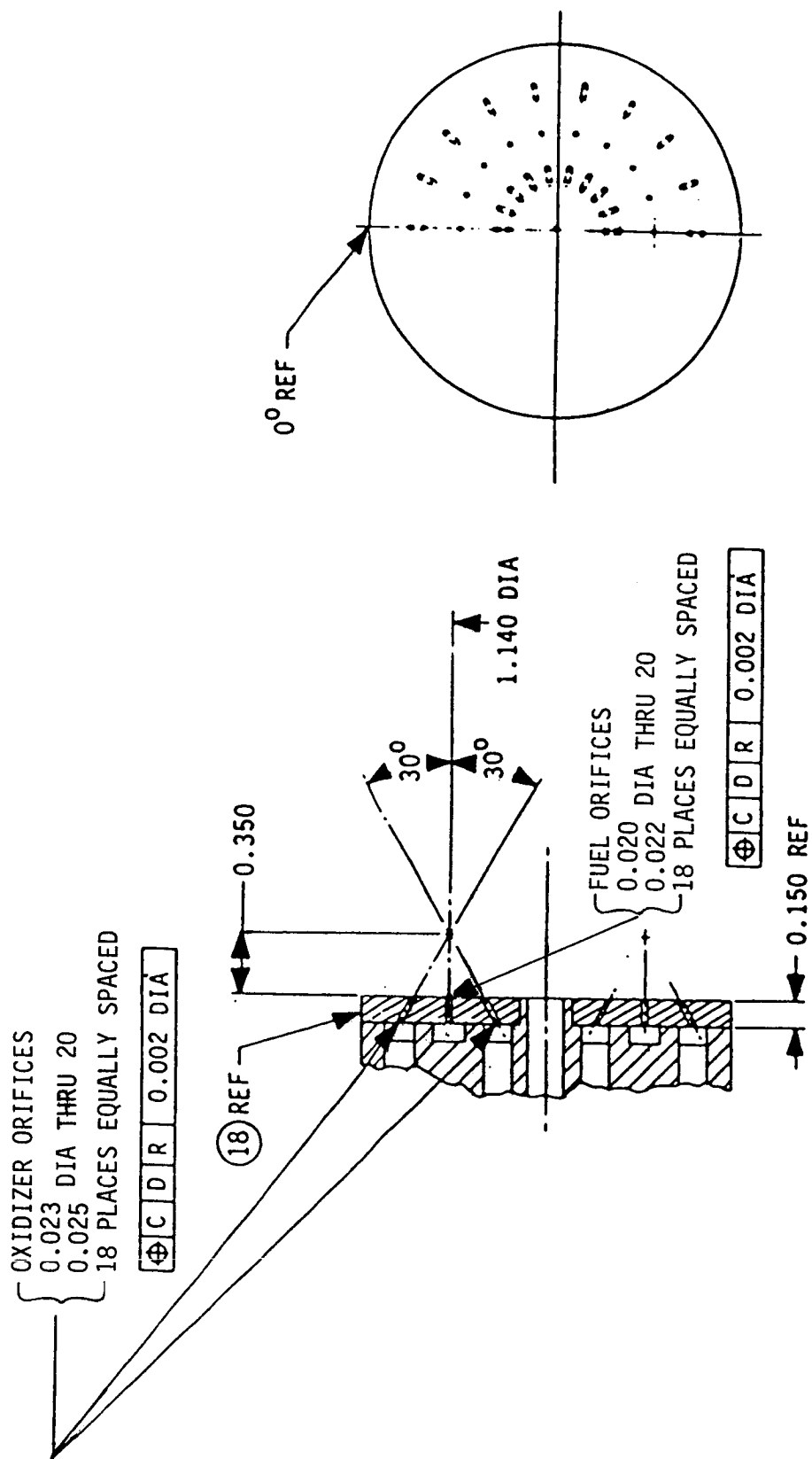


Figure 5. Main Chamber OFO Triplet Element Injector Pattern

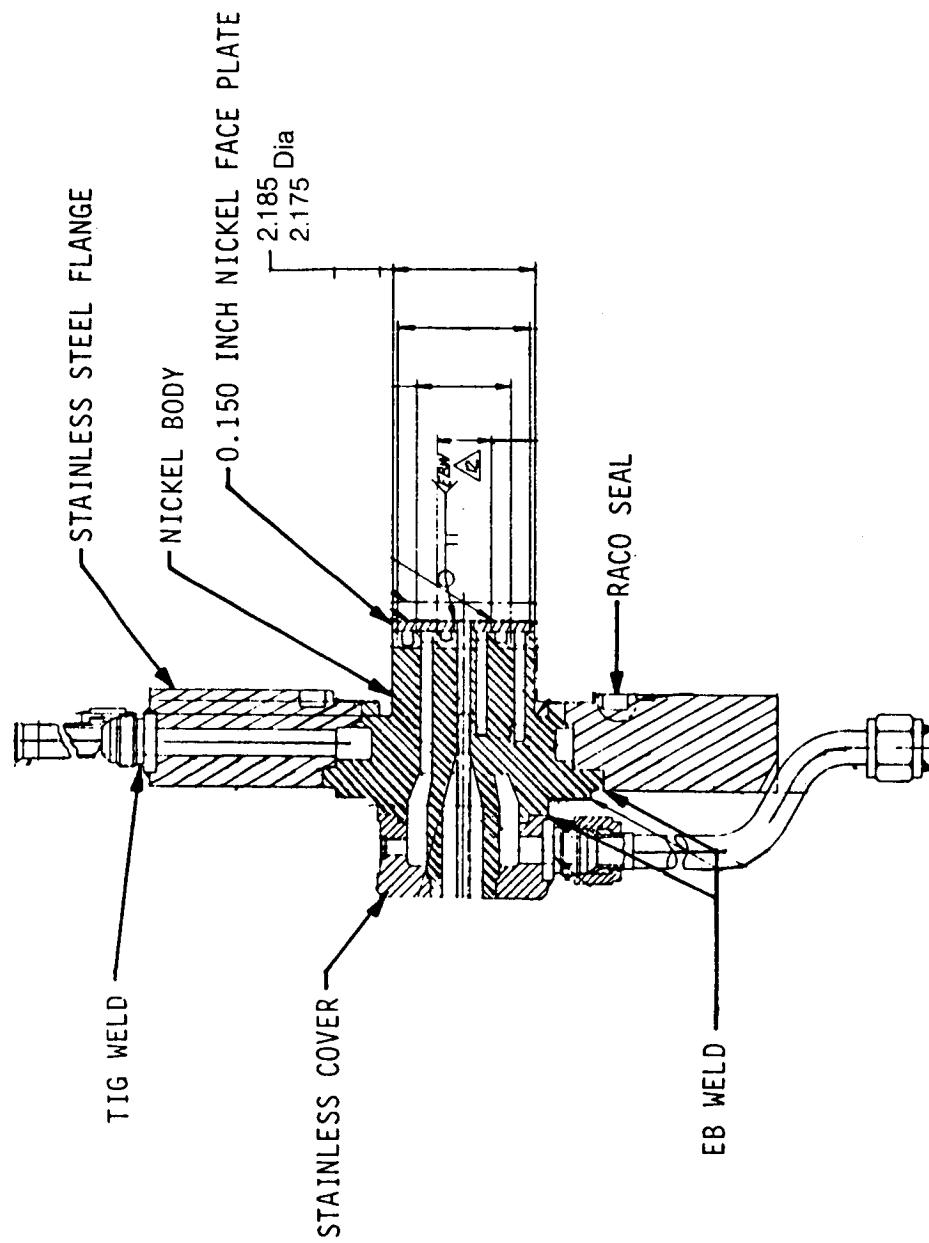


Figure 6. Injector Body

#### 4.1, Hardware Descriptions (cont.)

axially-directed downcomers. The fuel manifold was located on the injector's back surface and had a single inlet which was offset to clear the central igniter. The fuel downcomers were fitted between the three radial oxidizer manifolds and connected the fuel manifold to the individual face rings.

The injector body also incorporated instrumentation for measuring propellant inlet pressures and temperatures. High frequency pressure transducers (Kistlers) were also located in each of the propellant inlet manifolds.

##### 4.1.1.3 Acoustic Resonator and Film Coolant Manifold

A water-cooled quarter-wave acoustic resonator with an integral fuel-film coolant manifold was used to provide combustion stability (see Figure 7). Interchangeable cavity tuning rings were provided to allow operation with both the main chamber injector and the preburner injector. The unit was made out of copper to provide maximum cooling margin when the fuel-film cooling circuit was not flowing. Eighteen 0.015-inch diameter (0.038 cm) holes directed the film coolant flow against the edge of the injector. These 18 atomized jets performed as splash plate elements to uniformly distribute the flow around the periphery of the chamber.

##### 4.1.1.4 Turbulence Ring and Film Coolant Injection Manifold

A water-cooled turbulence ring with an integral film coolant manifold was used to promote mixing. The copper liner was brazed into a stainless steel flange as shown in Figure 8. To promote mixing, the turbulence ring protruded approximately 0.44 inches (1.12 cm) from the chamber wall into the flow field. The leading square-edge on the turbulence ring had been machined to a smooth, tapered edge for use in the higher temperature main chamber combustion gases. The ratio of turbulence ring area to chamber area (i.e., 0.57) was the same as was found most effective on the ATC preburner

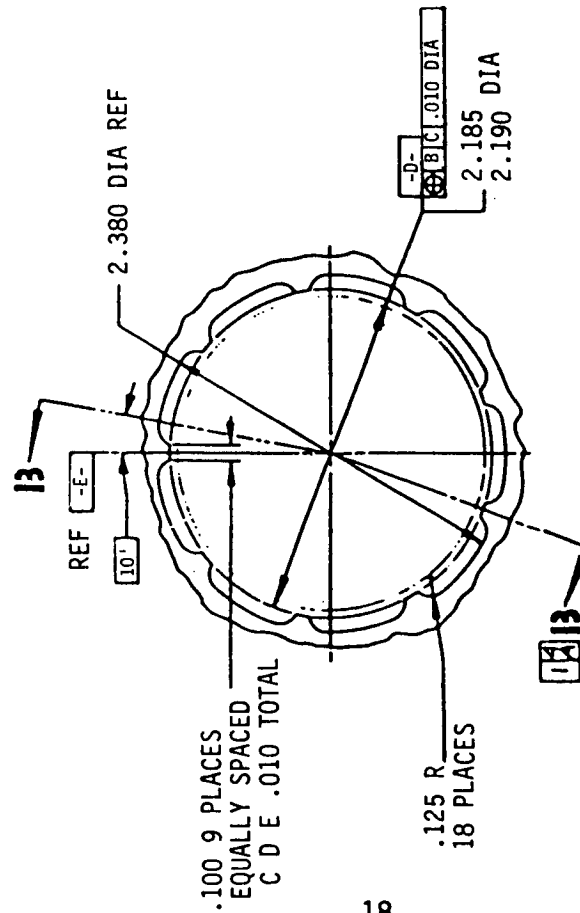
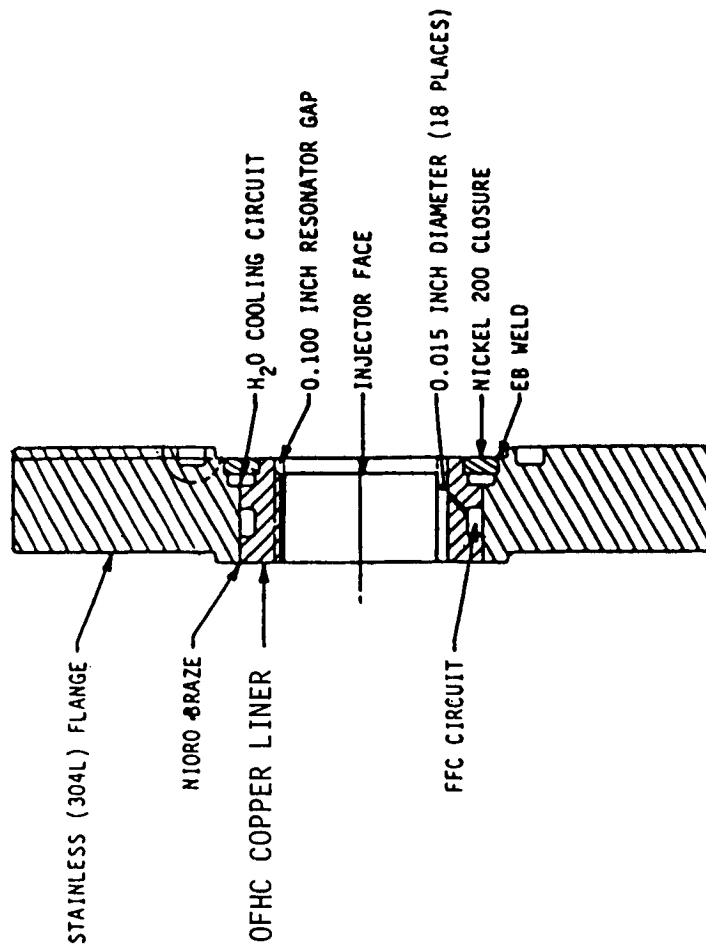
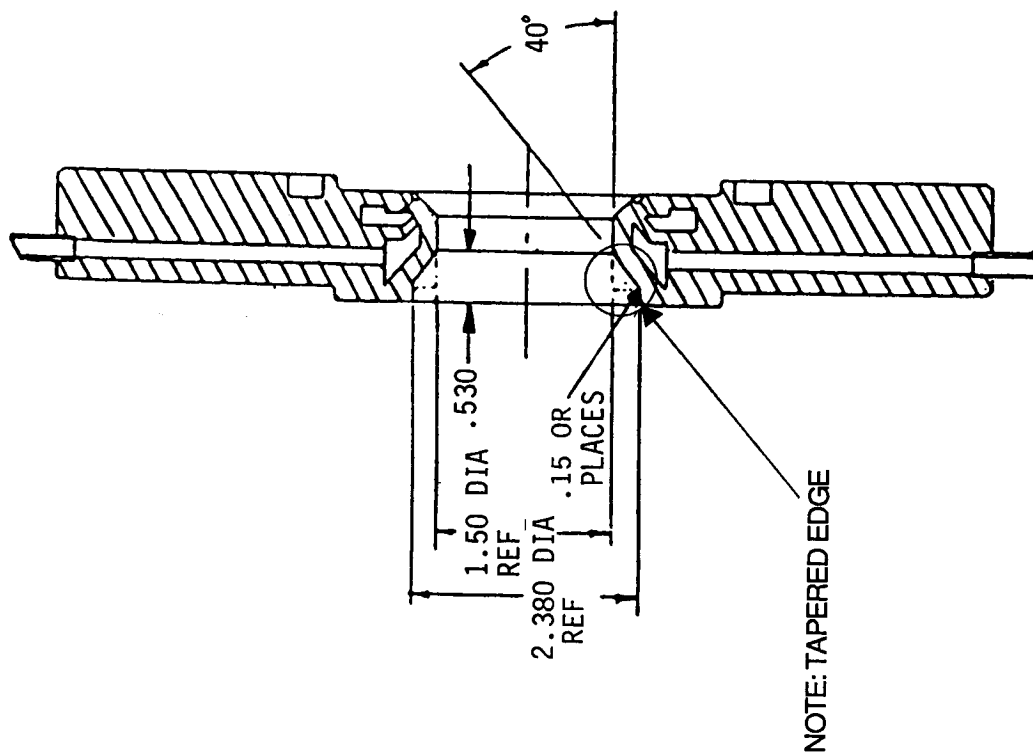


Figure 7. Resonator/Fuel Film Cooling Manifold



**Figure 8. Main Combustor Turbulence Ring/FFC Manifold**

#### 4.1, Hardware Descriptions (cont.)

contract (Ref. 1). The integral film coolant manifold allowed water or any other fluid to be injected at the start and/or end of the firing to clean the carbon off of the turbine simulator and chamber walls.

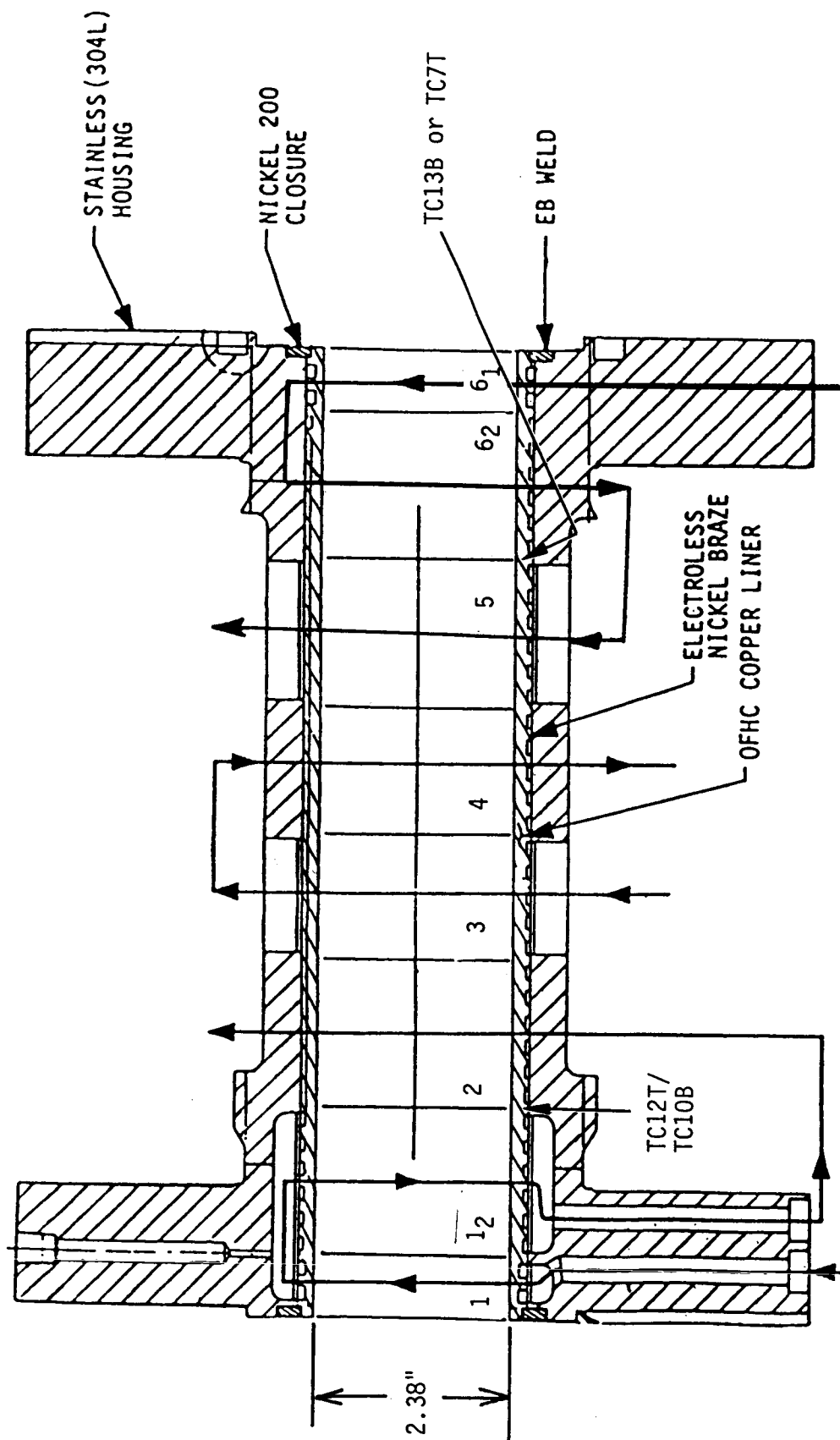
##### 4.1.1.5 Calorimetric Barrel Section

The combustion chamber consisted of two subcomponents; two water-cooled cylindrical barrel or L' (Figure 9) sections, and a water-cooled throat section (Figure 10) which were bolted together. Each of the cylindrical chamber sections had a nickel liner designed to operate from 1500 to 1800°F (1090 to 1256K) while the throat section had a copper liner and operated from 800 to 1200°F (700 to 922K) surface temperature. This difference in surface temperature was designed to aid in evaluating the effect of surface temperature on deposition and spalling.

Both the cylindrical and throat sections used a circumferential coolant flow scheme similar to that used in References 3 and 4. The circumferential coolant flow allowed the heat input to be measured at different axial locations.

The cylindrical chamber sections were designed as series flow calorimeter devices. With a series flow calorimeter, the discharge flow from one calorimeter section became the inlet flow for the next calorimeter section. The coolant temperature was measured between the adjoining flow sections. This approach minimized the number of coolant supply circuits and flow measurements required on the test stand.

The two cylindrical chamber sections fabricated were 8 inches (20.32 cm) long and 12 inches (30.48 cm) long. The sections were essentially identical except for length and could be used together or separately. The two different lengths provided flexibility in the selection of chamber L' section and in the location of the turbulence ring. Because they are so similar, only the 8-inch (20.32 cm) long section is described.



NOTE: TC12T AND TC13B ARE WALL T/C FOR THE 12-INCH BARREL SECTION  
TC10B AND TC7T ARE WALL T/C FOR THE 8-INCH BARREL SECTION

Figure 9. Calorimetric Barrel (L')



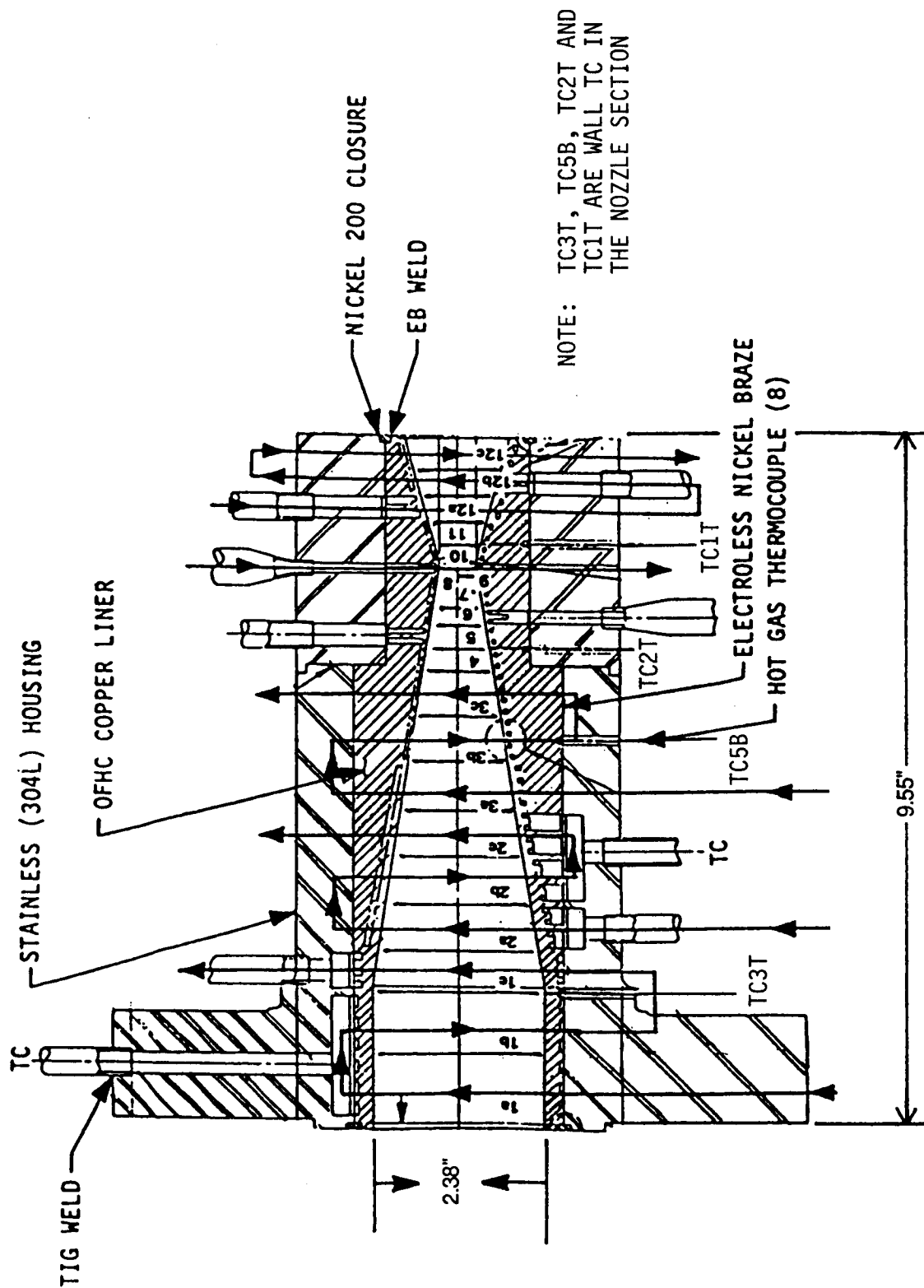


Figure 10. Calorimetric Nozzle

#### 4.1, Hardware Descriptions (cont.)

The slots forming the coolant passages in the liners were machined perpendicular to the thrust axis. The cylindrical section contained 28 circumferential channels in the liner which were split into four coolant circuits in the 8-inch (20.32 cm) barrel section. The 12-inch barrel (30.48 cm) section contained 38 circumferential channels which were split into six coolant circuits. The calorimeter sections at the ends of the chamber were plumbed separately to provide added cooling capability. The middle of the chamber consisted of one circuit which had three calorimeter sections in series and one circuit with two in series. Each inlet manifold, turn-around, and outlet was instrumented for temperature measurements and each outlet was instrumented for pressure measurement. The cylindrical section was a three-piece brazed assembly. The inner liner was made out of nickel while the structural housing was made out of stainless steel. The circumferential cooling slots were lathe-turned into the nickel liner. Backside manifolding for the coolant channels was accomplished by machining axial passages 180° apart in the sleeve. The flame side of the cylindrical section was copper-plated to the thickness of 0.001 to 0.003 inches (0.0025 to 0.0076 cm) two inches (5.08 cm) on the downstream end of the 8-inch (20.32 cm) calorimeter section.

##### 4.1.1.6 Calorimetric Throat Section

The high heat flux experienced in the throat area required that copper be used as the throat section liner. The nozzle section also included a short cylindrical length, thus in conjunction with the barrel section, provided soot buildup sites on high temperature nickel, high temperature copper, and low temperature copper in the same cylindrical length for any given test. The throat section contained 56 channels and was separated into fourteen coolant circuits. The barrel portion of the nozzle consisted of three calorimeter sections flowing in series, each with two channels flowing in parallel. The calorimeter sections in the convergent portion of the nozzle consisted of three channels flowing in parallel. There were three circuits in this part of the nozzle, each with three calorimeter sections flowing in

#### 4.1, Hardware Descriptions (cont.)

series. The heat flux in the throat portion of the nozzle required separately plumbed calorimeter sections, each with two channels flowing in parallel. The one circuit for the nozzle portion consisted of two calorimeter sections plumbed in series, one with three channels flowing in parallel and one with two channels flowing in parallel. Each inlet and outlet was instrumented for pressure and temperature measurements. The eight-inch (20.32 cm) long throat section was designed to have a contraction ratio of 22.66 in a length of 6.0 inches (15.24 cm) and an expansion area ratio of 9.0 at the  $P_c = 2000$  psia (13.78 MPa) design condition (0.50 inch (1.27 cm) diameter throat). The channels in the throat section were slotted to depth, and the gas-side wall thicknesses verified. Split-ring copper inserts were brazed into the annular slots creating the proper cross-section coolant flow channel as well as the inlet and outlet passages. The nickel distribution sleeve and stainless steel outer structural housing were fabricated similar to the cylindrical section. The aft flange of the throat section was required to accommodate the proof and leak check test fixture. The holes for the surface thermocouples were drilled from the backside through the lands and the thermocouples were brazed in place.

##### 4.1.2 Preburner/Gas Generator Assembly

The fuel-rich preburner/gas generator, like the main chamber assembly, was modular in design to maximize experimental test data at minimal cost. This permitted the selection of various components to form numerous test configurations. Two basic configurations were tested: one using water-cooled hardware, and one using a combination of water-cooled and uncooled hardware. Only  $LO_2$ /RP-1 was tested using both test configurations.  $LO_2$ /propane and  $LO_2$ /methane used the combination hardware setup (see Section 4.1.2.2). The design requirements for the preburner/gas generator test conditions for both configurations are given in Table II. The components used in each configuration are listed below along with a description of each component if not previously given.

TABLE II

PREBURNER DESIGN CONDITIONS

Design Parameters

$$P_c = 2000 \text{ psia (1500 - 2000 psia) [13.78 MPa (10.34-13.78 MPa)]}$$

$$MR = 0.5 \text{ (.25 - .40)}$$

$$W_f = 2.39 \text{ lb/sec (1.08 kg/sec)}$$

$$W_o = 1.19 \text{ lb/sec (0.54 kg/sec)}$$

$$A_t = 0.196 \text{ in}^2 \text{ (12.65 cm}^2\text{)}$$

$$D_t = .50 \text{ in (1.27 cm)}$$

$$D_c = 2.38 \text{ in (6.05 cm)}$$

## 4.1, Hardware Descriptions (cont.)

### 4.1.2.1 1984 Preburner/Gas Generator Configuration

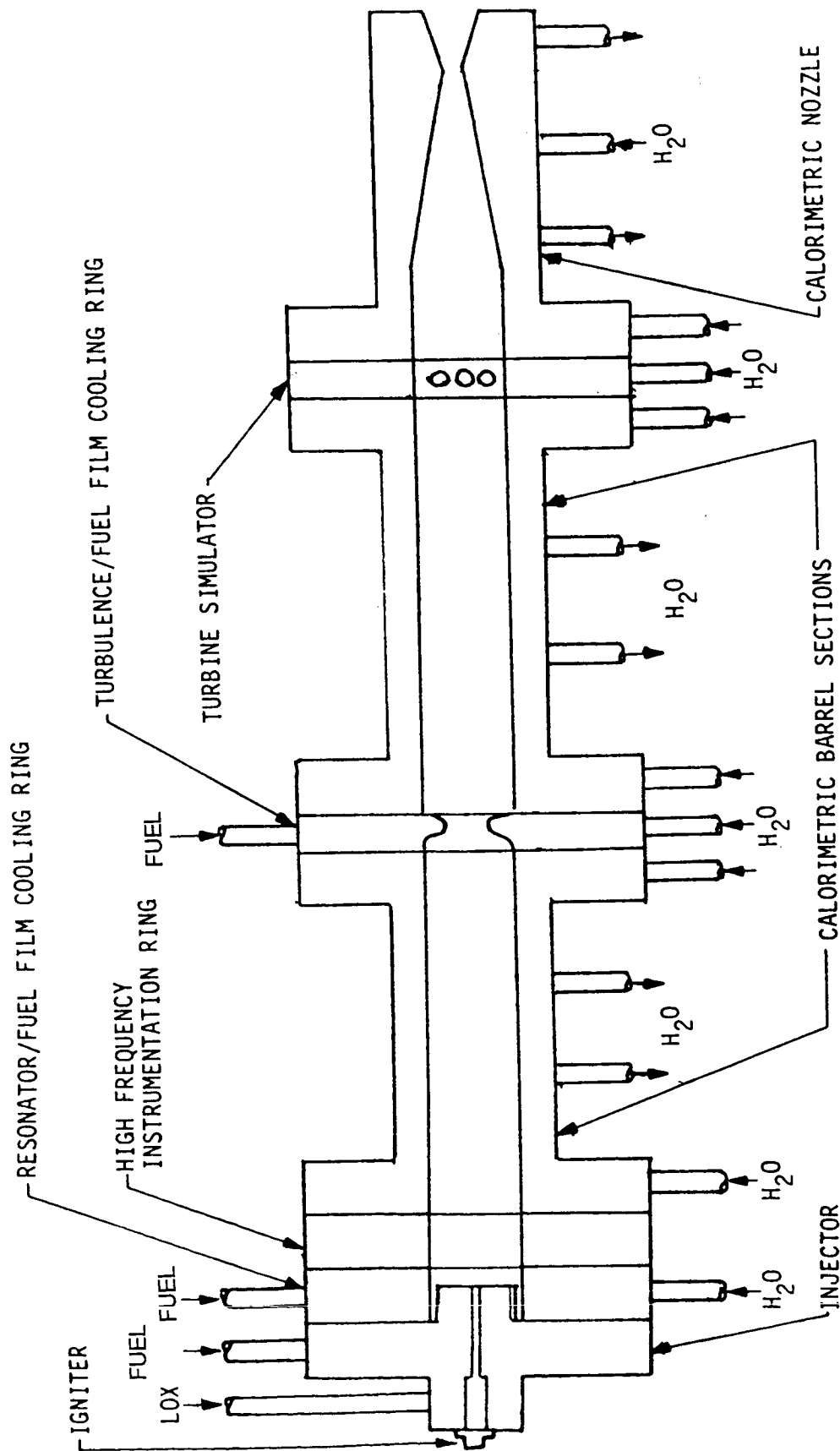
The preburner/gas generator assembly utilized many of the same components as the main combustor assembly including the gaseous hydrogen/gaseous oxygen igniter, the cylindrical water-cooled chamber sections, and the water-cooled copper lined throat sections. Additional components required for the preburner/gas generator assembly included the preburner/gas generator injector, a water-cooled turbulence ring, and a water-cooled turbine simulator. This water-cooled configuration is shown schematically in Figure 11 and in the photograph in Figure 12. These components are described in the following three subsections.

#### 4.1.2.1.1 Preburner/Gas Generator Injector

The injector for the fuel-rich preburner/gas generator was the same one used in the main chamber configuration. The preburner/gas generator injector was rotated 180° on the test stand in order to reverse the location of the oxidizer and fuel circuit inlets so the injector could operate as a fuel-rich FOF triplet instead of an oxidizer-rich OFO triplet.

The injector, shown in Figure 13, utilized a conventional uniform mixture ratio F-O-F triplet pattern similar to the ones used for other LO<sub>2</sub>/hydrocarbon gas generators (Jupiter, Atlas, and H-1). While gas generators typically operate at temperatures that do not require actively cooled chambers, this hardware was water cooled to allow operation at higher than nominal gas generation mixture ratios and hotter resulting gas temperatures to evaluate carbon deposition thresholds without incurring thermal damage.

This 18-element injector pattern was stable under all preburner/gas generator operating conditions of the present contract, and provided an extremely uniform gas mixture when operated with a turbulence ring.



NOTE: SKETCH NOT TO SCALE

Figure 11. Water-Cooled Preburner/Gas Generator Configuration

ORIGINAL PAGE IS  
OF POOR QUALITY

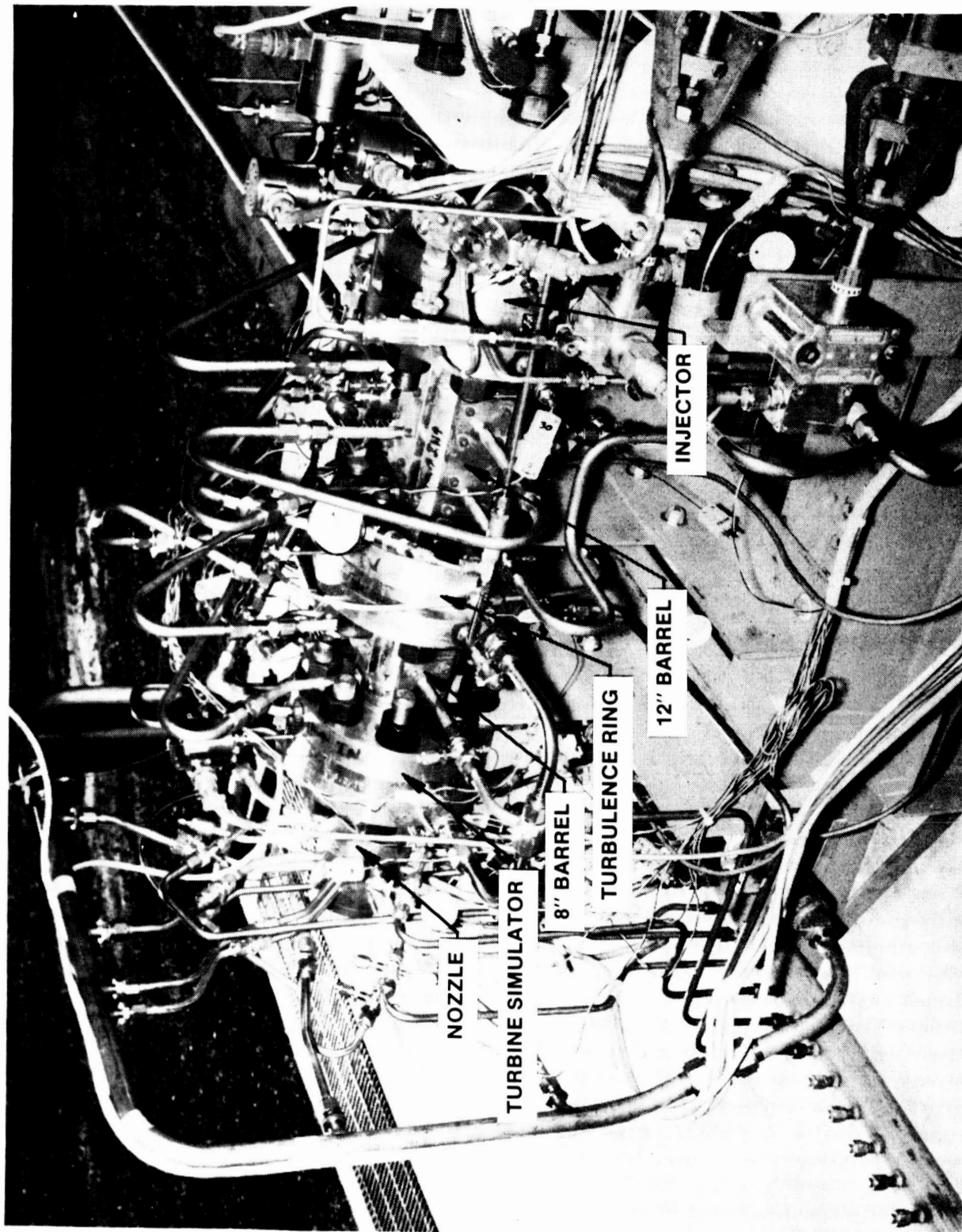


Figure 12. 1984 Gas Generator/Preburner Assembly

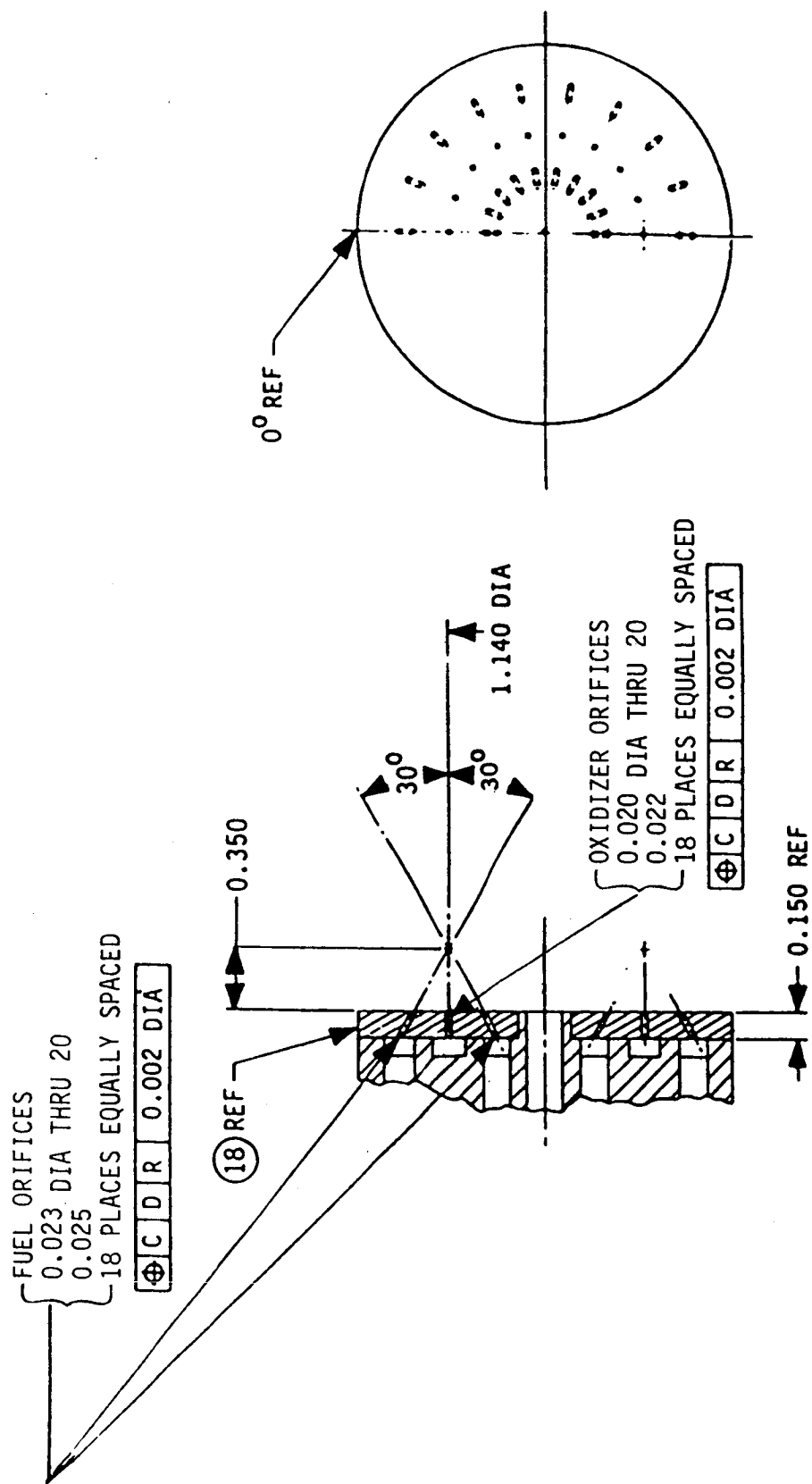


Figure 13. Preburner/Gas Generator FOF Triplet Element Injector Pattern



#### 4.1, Hardware Descriptions (cont.)

##### 4.1.2.1.2 Water-Cooled Turbulence Ring and Film Coolant Injection Manifold

A water-cooled turbulence ring used in preburner/gas generator testing was essentially the same one described in Section 4.1.1.4. The difference is that the leading edge of the turbulence ring is a square edge as opposed to the tapered edge used in main chamber testing. This difference is pointed out in Figure 14.

##### 4.1.2.1.3 Turbine Simulator

The function of the turbine simulator was to provide a surface which would exhibit the same carbon deposition characteristics as the nozzles and blades of a gas turbine or the injection orifices or passages in a secondary injector for a staged combustion engine. In addition, the turbine simulator was to provide some type of continuous reading on the carbon deposition during a firing.

The design configuration selected was water-cooled to allow some mixture ratio margin in testing (see Figure 15). It consisted of six 3/8-inch (0.95 cm) diameter tubes which were brazed into a copper liner which, in turn, was brazed into the steel structural flange during the same furnace run. The total flow area between the vanes was selected to simulate the engine turbine inlet velocity to accurately characterize soot deposition. The long narrow slot flow passage geometry was selected to maximize its wetted perimeter so that the cross sectional area for a given amount of soot buildup could be readily measured experimentally. The turbine simulator contained two pressure taps, one immediately upstream of the tubes and one immediately downstream. They were used to monitor the pressure drop of the gas stream as it flowed across the tubes of the simulator, and to infer carbon buildup in the flow passages.

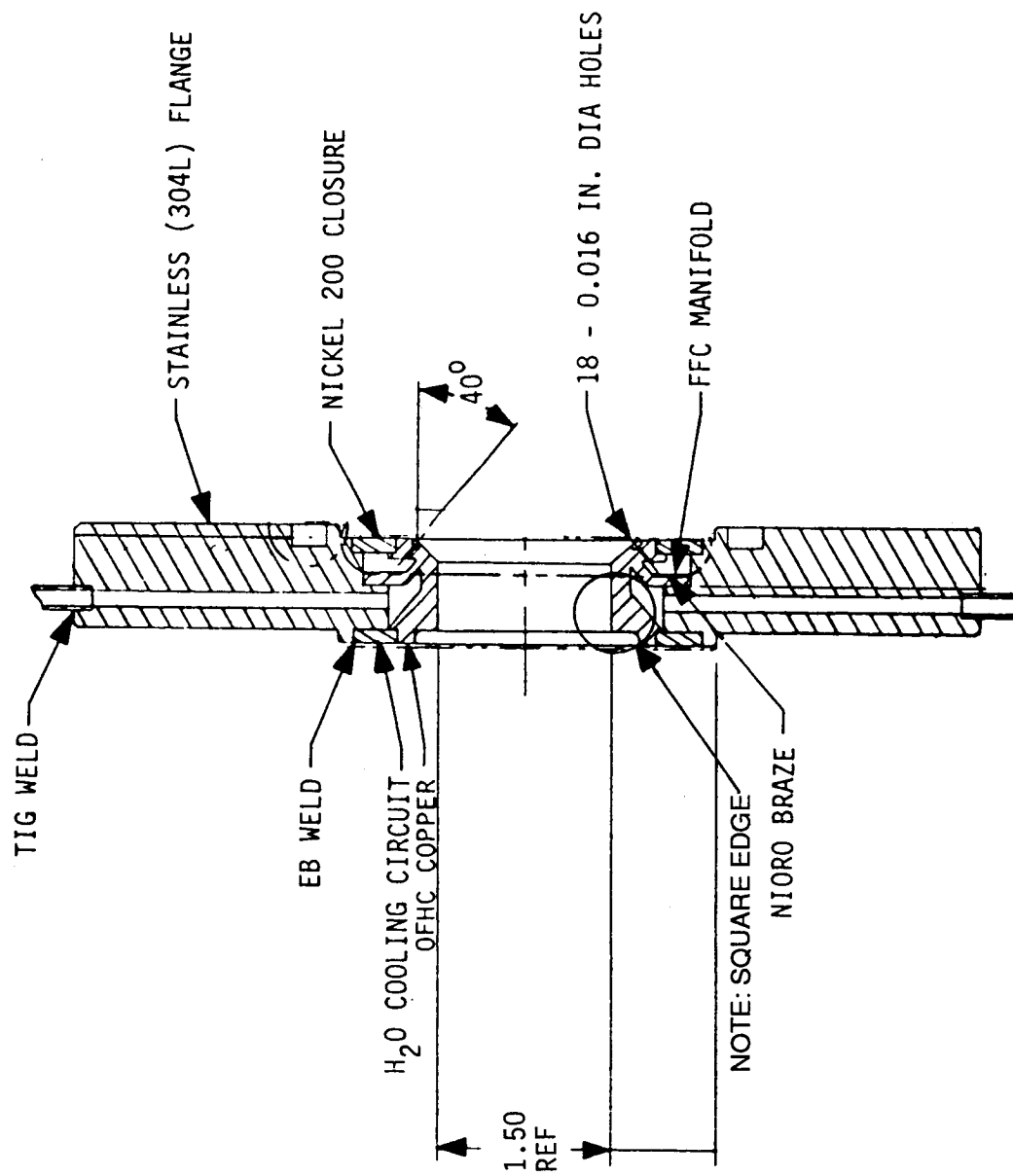


Figure 14. Water-Cooled Turbulence Ring and Film Coolant Injection Manifold

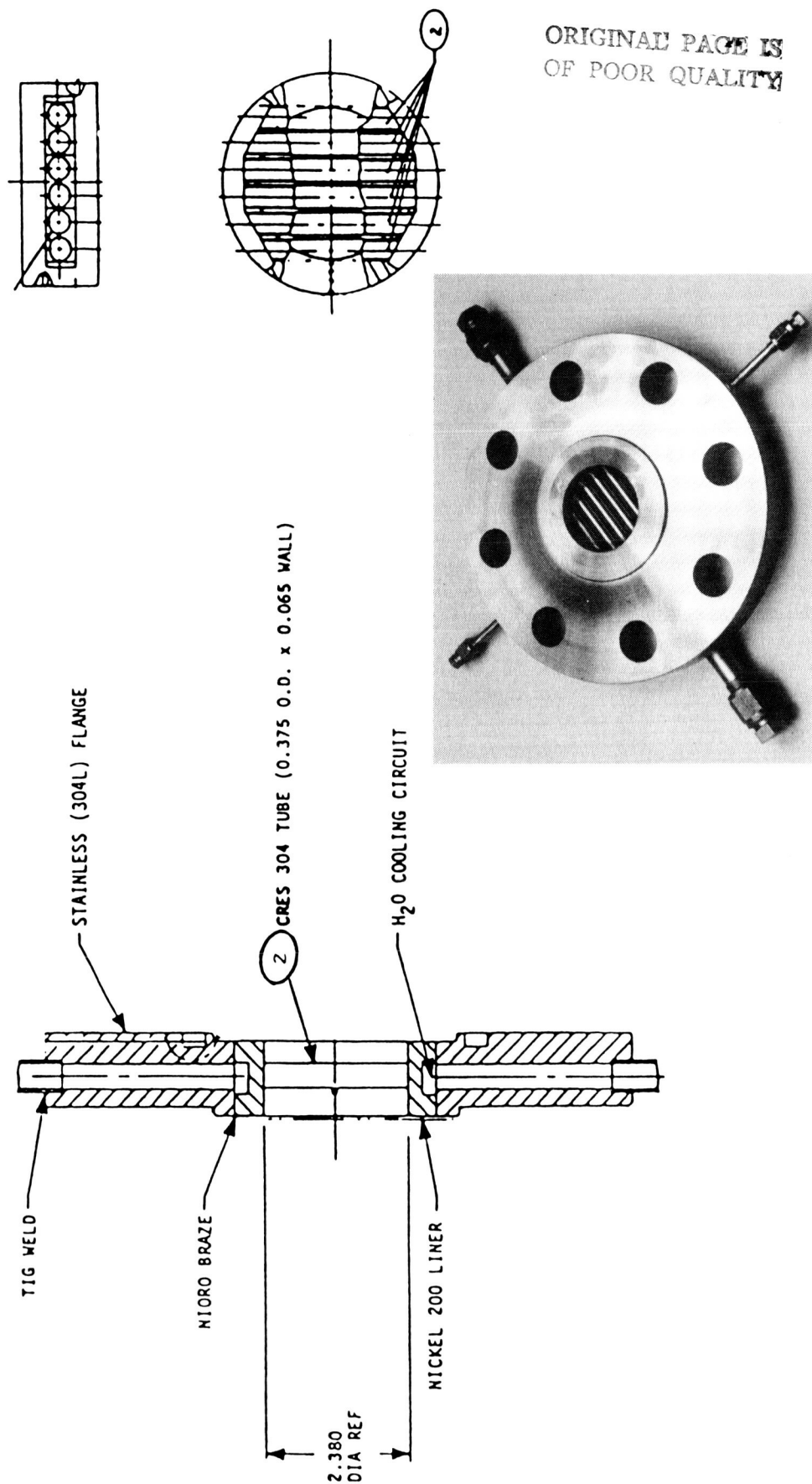


Figure 15. Cooled Preburner Turbine Simulator

#### 4.1, Hardware Descriptions (cont.)

##### 4.1.2.2 1985-1986 Preburner/Gas Generator Modified Configuration

A modified preburner/gas generator configuration was used in the 1985 and 1986 preburner/gas generator test series. Many of the same components used in the water-cooled configuration were used along with some uncooled hardware components. The hardware modifications were as follows:

(1) The new hardware configuration added pressure taps both farther upstream and farther downstream of the turbine simulator. This was done because there was some question whether the close position of both the upstream and downstream pressure taps to the turbine simulator tubes were being affected by acceleration and/or static pressure recovery effects which could have affected accuracy of the pressure measures in the 1984 tests.

(2) An uncooled exit nozzle was used to increase data acquisition capability and to reduce testing costs.

(3) A thermocouple rake was added downstream of the turbulence ring and immediately anterior to the turbine simulator so that turbine inlet gas temperature uniformity could be measured.

This modified configuration is shown schematically and in the photograph in Figure 16. The assembly used the existing gaseous hydrogen/gaseous oxygen igniter, the cylindrical water-cooled chamber sections, the FOF triplet injector used in the cooled configuration, and the water-cooled turbine simulator. The additional components required for the assembly were an uncooled, upstream L' section with thermocouple rake and pressure taps, an uncooled downstream L' section with a pressure tap, an uncooled turbulence ring, an uncooled turbine simulator with a nozzle insert, and two converging, uncooled exit nozzles.

NOTE: SKETCH NOT TO SCALE

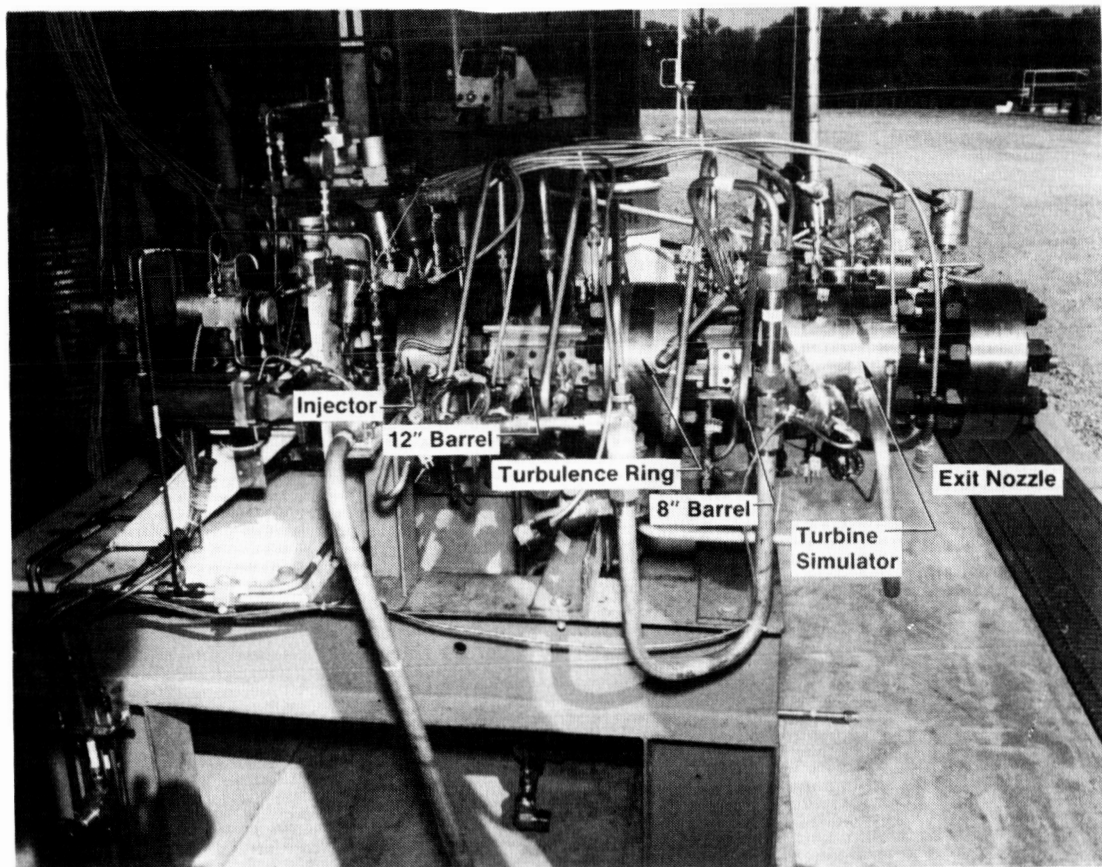
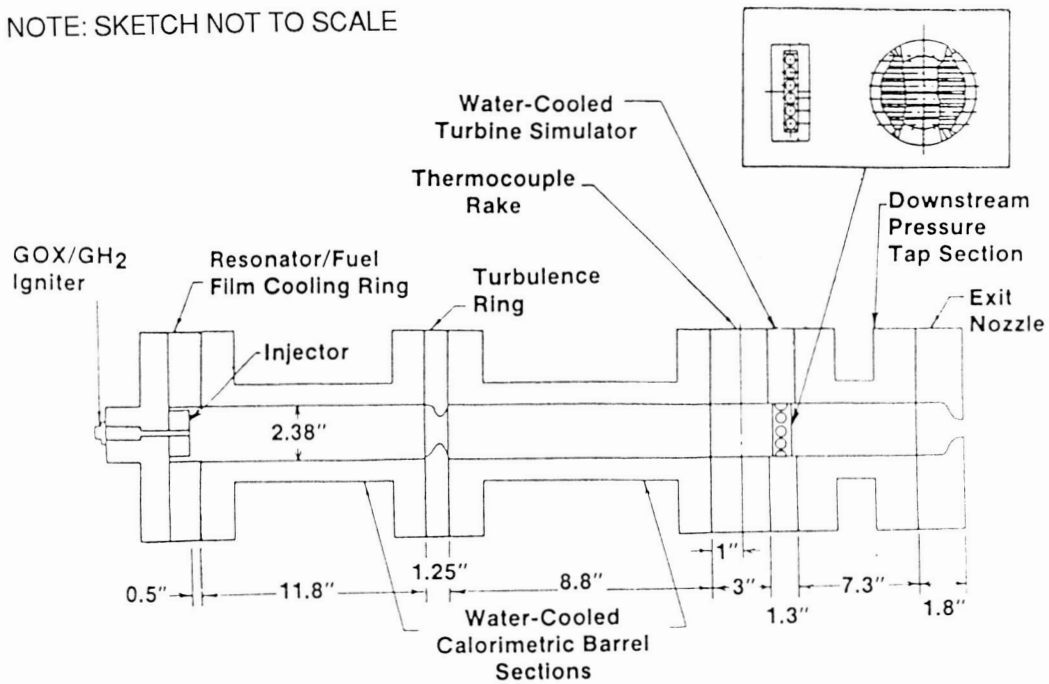


Figure 16. Preburner/Gas Generator Assembly

#### 4.1, Hardware Descriptions (cont.)

##### 4.1.2.2.1 Uncooled Turbulence Ring Assembly

The uncooled turbulence ring assembly was a mixing device used to provide uniform gas temperatures to the turbine simulator. Experience with high pressure preburners (Ref. 1) has shown that a well-designed turbulence ring can easily provide gas temperature uniformity of  $\pm 50^{\circ}\text{F}$  (27.8K). The leading square edge of the water-cooled turbulence ring was machined to a smooth, tapered-edge for use in the higher temperature main chamber combustion gases. To maintain the same geometry as was used in the previous preburner/gas generator testing, a leading square-edge turbulence ring was deemed necessary. Due to the lower combustion temperatures encountered in preburner/gas generator testing, an uncooled turbulence ring was built to reduce program costs and facilitate the test setup. Turbulence ring dimensions were obtained from the former water-cooled unit.

The uncooled turbulence ring assembly was comprised of turbulence ring holder with a turbulence ring insert as shown in Figure 17. The assembly was fabricated from a stainless steel flange. To promote mixing the turbulence ring protruded 0.44 inches (1.12 cm) from the chamber wall into the combustion zone. The turbulence ring was fabricated as an insert and insert holder to facilitate insert replacement should excessive erosion occur during preburner testing. Two inserts were fabricated to ensure completion of the gas generator/preburner test series.

##### 4.1.2.2.2 Uncooled Upstream L' Section with Temperature Rake and Pressure Taps

The upstream L' section was made from a 3-inch (7.62 cm) stainless steel flange (see Figure 18abc). Six thermocouples are located around the chamber periphery: starting at  $45^{\circ}$  from the top in  $45^{\circ}$  increments in a counter-clockwise direction. These thermocouples were placed in the gas stream at varying emersion depths (see Figure 18d). The two pressure taps were located at the top and at  $90^{\circ}$  from the top in a clockwise direction. All the instrumentation was attached to the flange by either an AN (pressure tap)

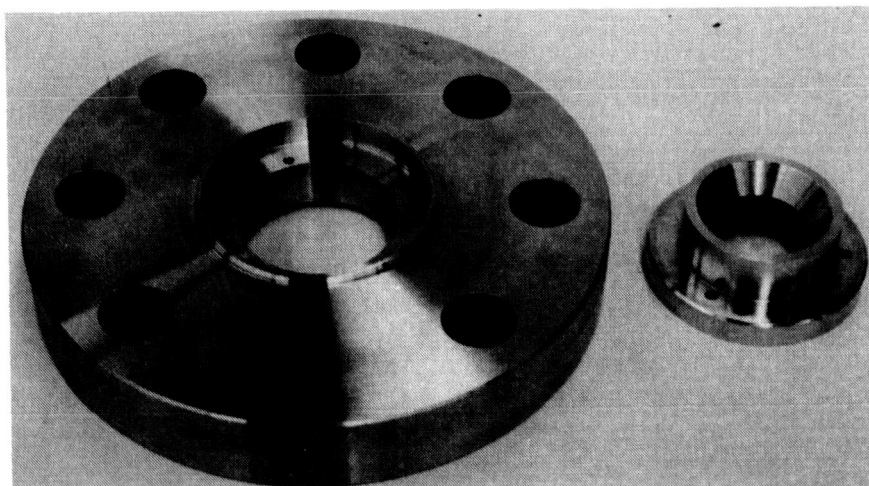
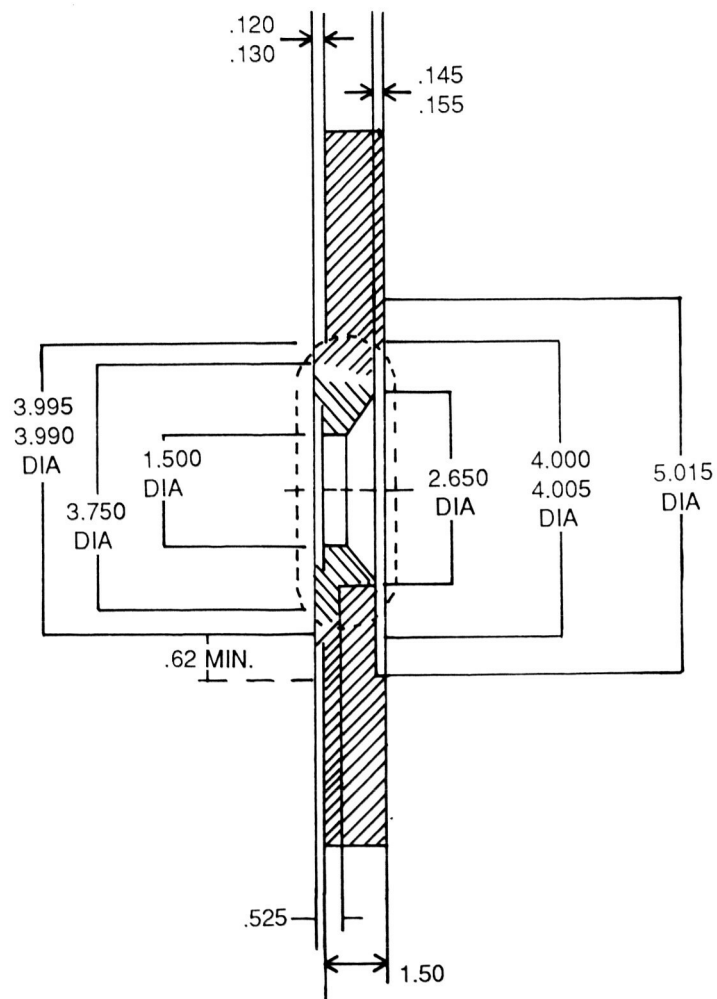


**Figure 17. Preburner Uncooled Turbulence Ring**

Technical drawing of a mechanical part, likely a shaft or rod, showing dimensions and surface finish specifications.

**Dimensions:**

- Overall length: 100
- Top section diameter: 3.995 DIA (tolerance .0005)
- Second section diameter: 2.380 DIA (tolerance .0005)
- Third section diameter: 4.000 DIA (tolerance .0005)
- Bottom section diameter: 1.00 DIA
- Bottom section length: 100
- Bottom section depth: 3.00
- Bottom section width: 1.00
- Bottom section thickness: .10
- Bottom section surface finish: 100

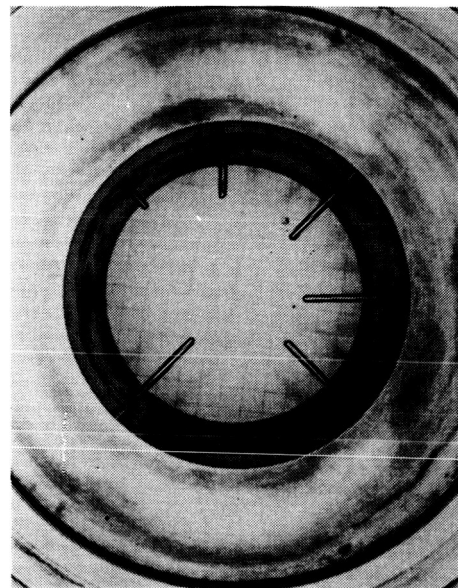
**Surface Finish Specifications:**

- Top section: 0.001 (tolerance .0005)
- Second section: 0.001 (tolerance .0005)
- Third section: 0.001 (tolerance .0005)
- Bottom section: 100

**Other Features:**

- Top section: 145, 155
- Second section: 62 MIN
- Third section: 4.000 DIA
- Bottom section: 1.00 DIA x 3.00 DEEP
- Bottom section: .002 DIA THRU SF .100 DIA 6 PLACES
- Bottom section: 100
- Bottom section: 6 PLACES

b.



d.

37



#### 4.1, Hardware Descriptions (cont.)

fitting or Swagelok (thermocouple) fitting which was then welded to the flange to ensure leak-proof operation. The purpose of this L' section was to locate the instrumentation upstream of the point of rapid gas acceleration to ensure true measurement of static gas pressure and temperature. This section was designed to be interchangeable with existing hardware.

##### 4.1.2.2.3 Uncooled Downstream L' Section with Pressure Tap

The uncooled downstream L' section was constructed from two standard flanges and a three-inch (7.62 cm) nominal diameter double extra strength pipe as shown in Figure 19. The three pieces were welded together to withstand near 3000 psia (20.68 MPa) pressure. The pressure tap was attached to the flange by a union which was welded to the flange. The function of this piece of hardware was to measure the downstream pressure at a distance far enough from the turbine simulator to reflect accurate static pressures.

##### 4.1.2.2.4 Uncooled Exit Nozzles

Two uncooled converging exit nozzles were used in the preburner/gas generator testing. The diameters of the throats were 0.5-inch (1.27 cm) and 0.354-inch (0.90 cm). The smaller (.354-inch (0.90 cm)) diameter throat was used in the higher chamber pressure tests (~ 1500 psia (10.34 MPa)). The 0.5-inch (1.27 cm) diameter throat was used during the lower chamber pressure tests. These uncooled nozzles functioned as a flow control device during subsonic testing. The use of these uncooled nozzles simplified the testing operation by eliminating the need for the fourteen water circuits in the calorimetric nozzle section during the low (<1500°F (<1090K)) combustion temperature gas generator/preburner testing. One uncooled converging exit nozzle is shown in Figure 20.

ORIGINAL PAGE IS  
OF POOR QUALITY

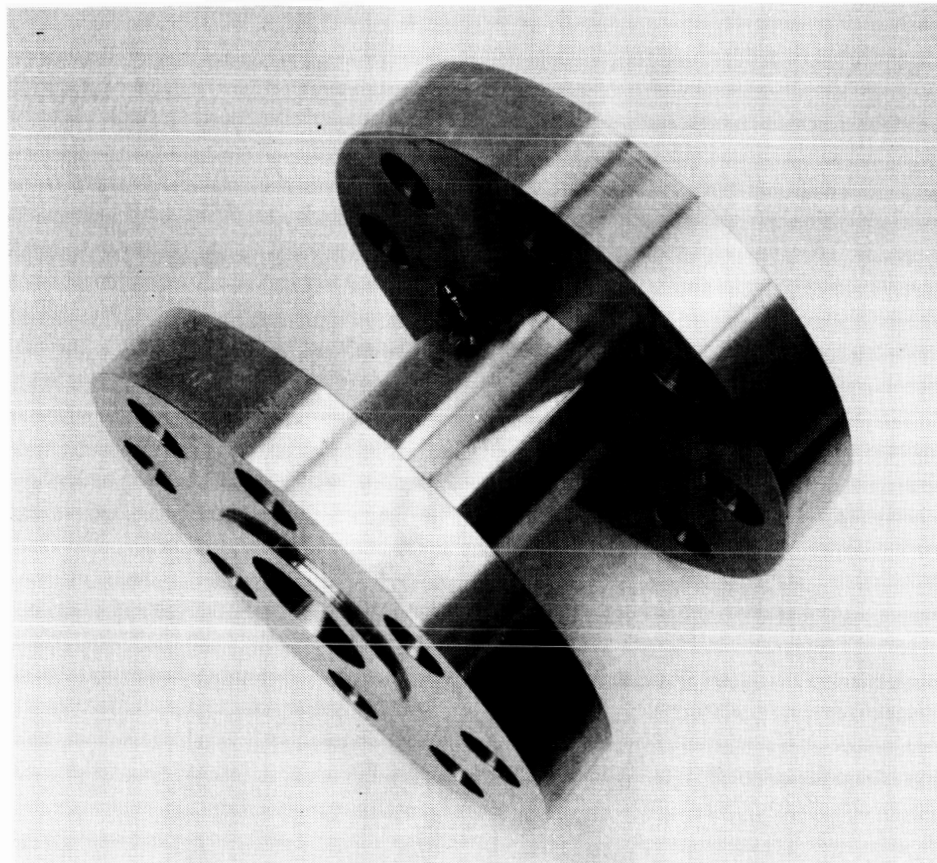
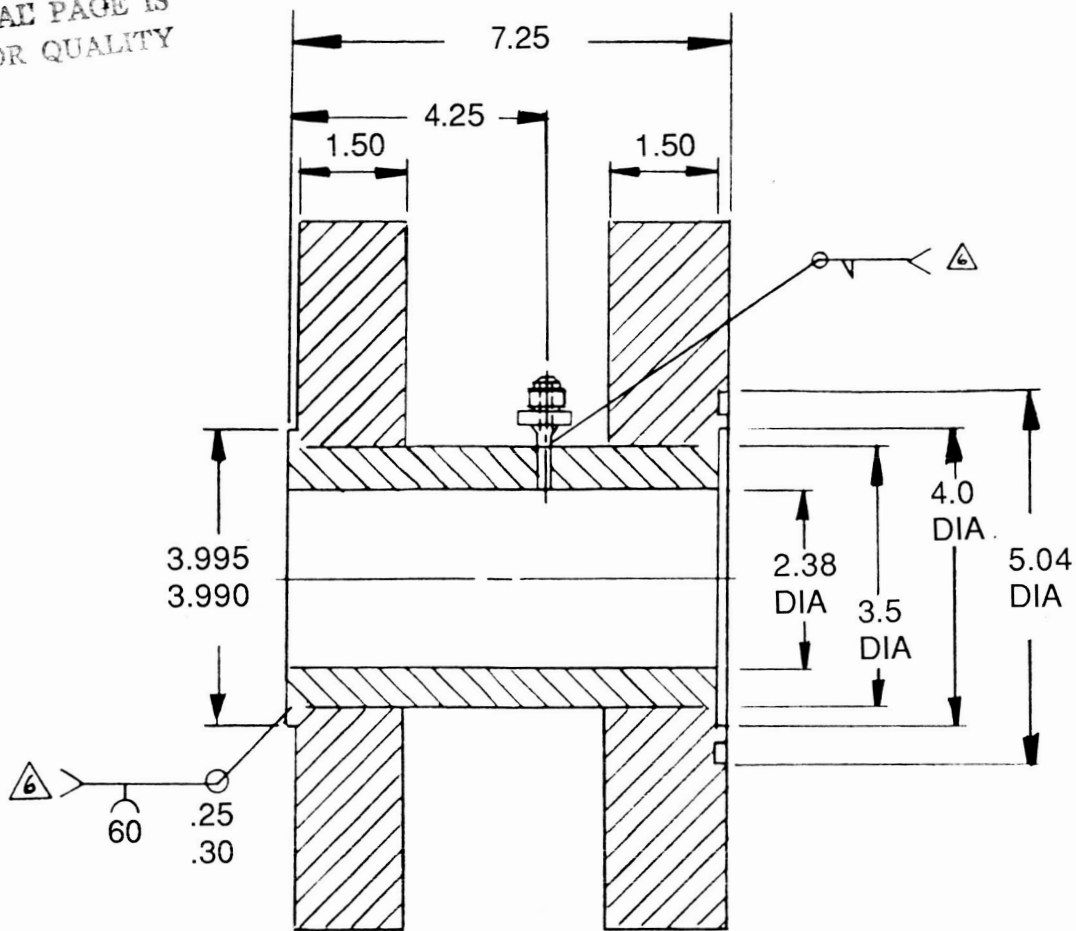
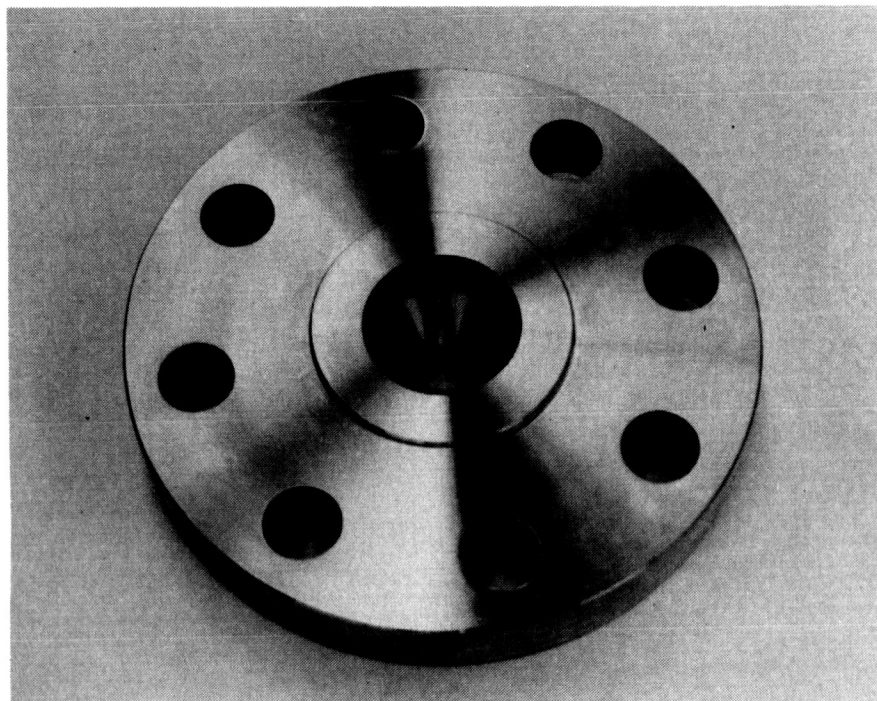
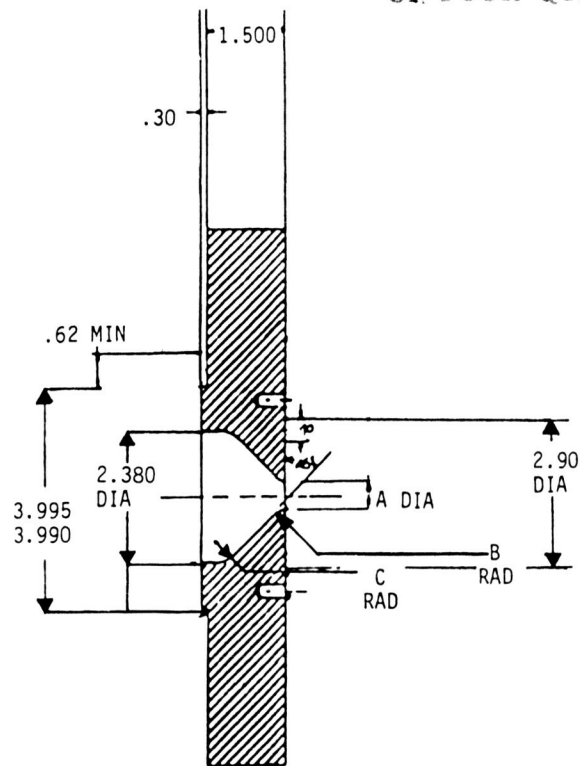


Figure 19. Uncooled Downstream L' Section with Pressure Tap

ORIGINAL PAGE IS  
OF POOR QUALITY



**Figure 20. Uncooled Exit Nozzles**

#### 4.1, Hardware Descriptions (cont.)

##### 4.1.2.2.5 Uncooled Turbine Simulator Assembly

The design configuration selected for the uncooled turbine simulator assembly was the conventional converging-diverging De Laval type since the nozzles of most rocket engine turbines are basically similar to those of rocket thrust chambers.

The turbine simulator used was composed of a stainless steel orifice plate holder/flange and an uncooled nozzle insert (Figure 21, View C, -4 Nozzle Drawing No. 1198640). This uncooled nozzle had the same throat area as the water-cooled turbine simulator flow area, and was used to compare the configurational change of the two turbine simulators. All inserts were uncooled. The holder was designed to interface with the other hardware equipment. The assembly arrangement was used to facilitate changes in turbine simulator configuration at minimal costs.

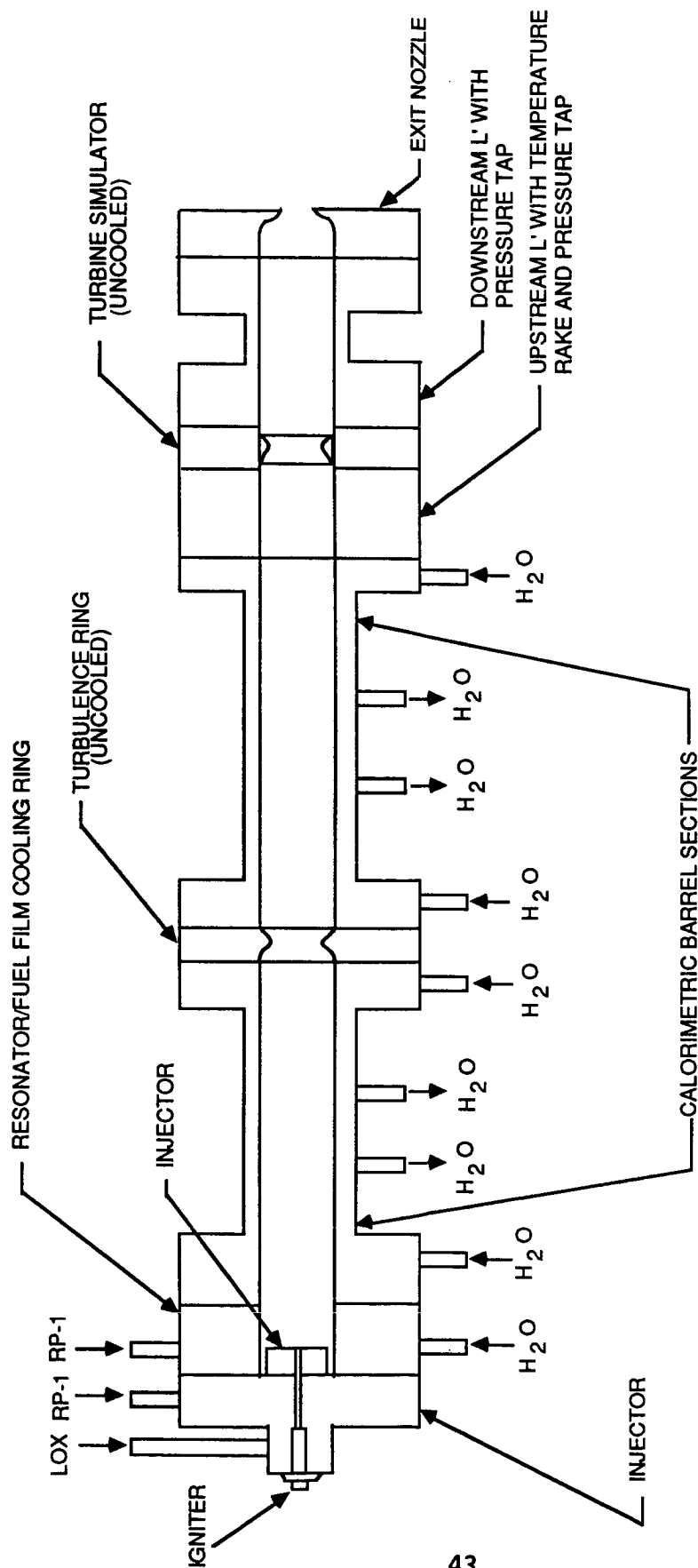
##### 4.1.2.3 Alternate Throat Configurations

Slight modifications from the set-up shown in Figure 16 were made for a few RP-1 and propane tests. In RP-1 tests 2427-936-A6-139 through 141 and 1986 propane tests 2427-229-A6-131 through 133, a smaller diameter (0.354 in. [0.90 cm] vs 0.5 in. [1.27 cm]) exit nozzle was used. This hardware change was necessitated because the facility tanks could not be pressurized high enough to provide the required fuel flowrates at 1500 psia (10.34 MPa) and lower mixture ratios with the larger existing exit nozzle.

In RP-1 tests 2427-936-A6-156 through 160, a conventional, uncooled, 3-D converging turbine simulator throat was installed, replacing the cooled tubular slot turbine simulator, to see if any carbon deposition would occur (see Figure 22). These tests used a fuel-rich shutdown procedure. Unfortunately, since the new piece was uncooled, it thermally expanded inward under transient radial constraint reducing the throat area. The pressure differential measurement correspondingly increased, which gave an initially erroneous belief that carbon had deposited in the throat. Upon physical



# HARDWARE SET UP 2



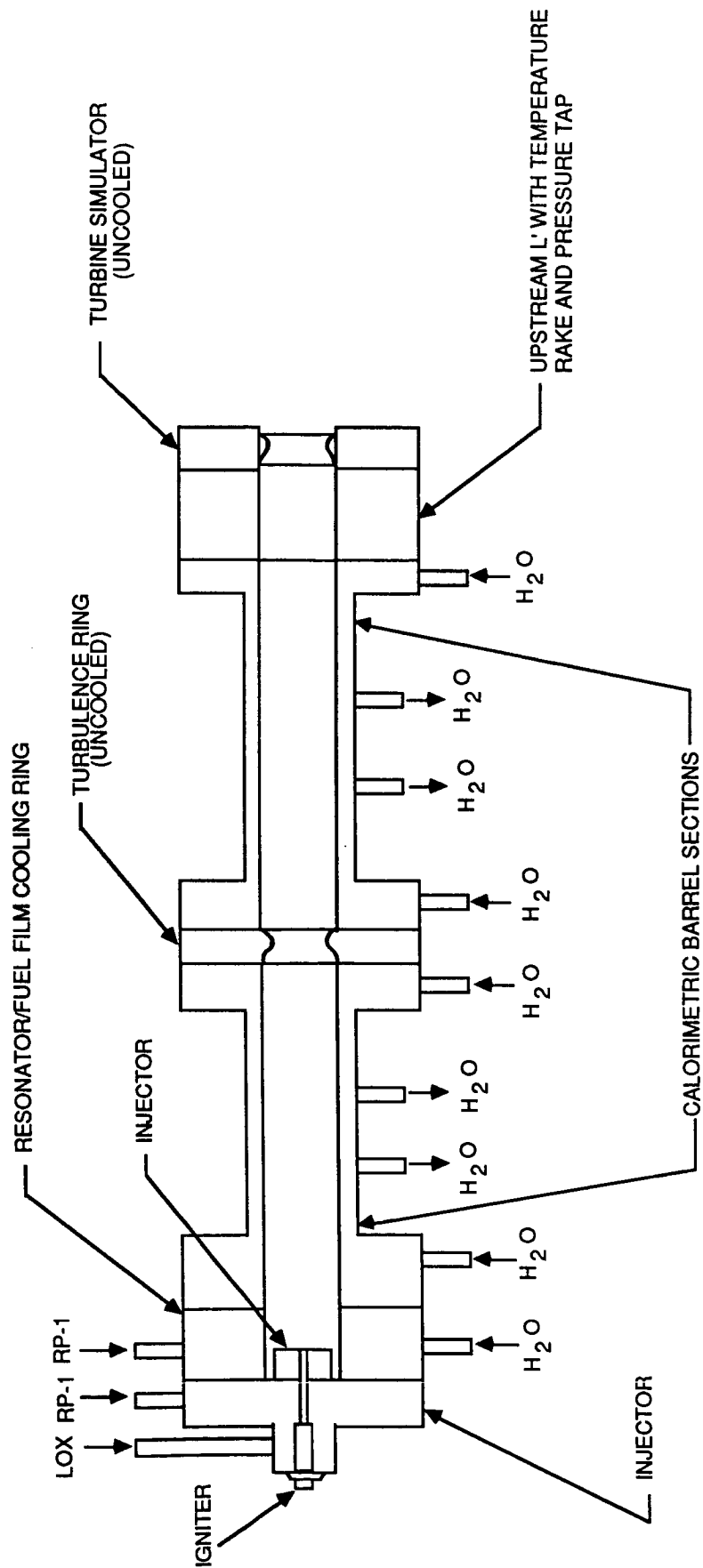
NOTE: SKETCH NOT TO SCALE

Figure 22. Test Series with a Subsonic 3D Turbine Simulator

#### 4.1, Hardware Descriptions (cont.)

inspection, no carbon was present. In test 160, the exit nozzle was removed as shown in Figure 23 to yield sonic conditions at the turbine simulator throat to see whether the abrupt static pressure reduction across the sonic line would cause decomposition into  $C(s) + GH_2$  leaving a solid carbon residue but no carbon deposition occurred.

# HARDWARE SET UP 3



NOTE: SKETCH NOT TO SCALE

Figure 23. Test Series with Sonic Conditions at the Turbine Simulator Configuration



## 4.0, Technical Discussion (cont.)

### 4.2 TEST FACILITY

The subscale hot-fire testing was conducted in Bay 6 of the ATC Test Zone "A". The setup consists of the fuel and oxidizer feedsystems, a water coolant feedsystem, a thrust stand, the test hardware, the igniter feed systems, and the instrumentation. The Bay 6 facility and the supporting equipment is shown in Figure 24.

#### 4.2.1 Propellant Feedsystem

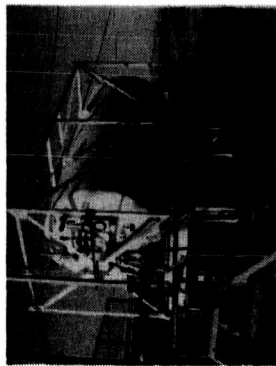
A schematic of the propellant feedsystem is shown in Figure 25. The propellants were supplied to the engine from pressurized tankage. The oxidizer and fuel tanks were pressurized with helium. Both the fuel and oxidizer tanks and lines were jacketed to provide temperature control with liquid nitrogen, as required to condition the propellants. The RP-1 fuel run tank capacity was 200 gal (757 l), the propane/methane run tank capacity was 150 gal (567.8 l), and the oxidizer tank was 50 gal (189.2 l) capacity. All tanks could be operated to 5500 psia (37.91 MPa).

Both dry GN<sub>2</sub> and solvent purges were provided for flushing the fuel and oxidizer manifolds following each test. Extreme care was taken to avoid contaminating the fuel and oxidizer manifolds to prevent damaging explosions. Established solvent flush and purge sequences were used to avoid such problems.

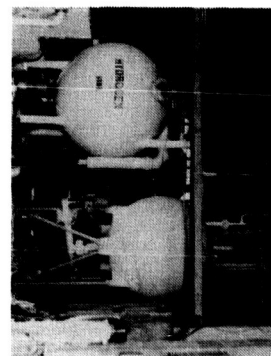
The GO<sub>2</sub>/GH<sub>2</sub> igniter was fed propellant from high pressure 'K' bottles. Sonic venturis were used to control the flowrates. An existing GLA power supply provided the required spark energy for ignition.

Deionized water for cooling of the thrust chamber components (calorimeter chambers, resonators, etc.) was supplied from a 3000 psi (20.68 MPa), 175 gallon (662.4 l) tank situated adjacent to the test bay during the main chamber test program and the 1984 water-cooled preburner/gas generator program.

ORIGINAL PAGE IS  
OF POOR QUALITY

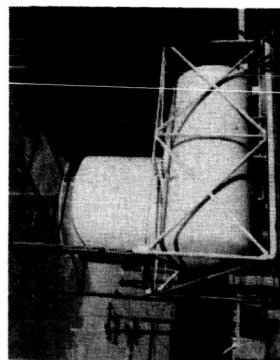


LIQUID OXYGEN  
1800 gal.  
50 psig



# EQUIPMENT PLACEMENT

REVEMENT



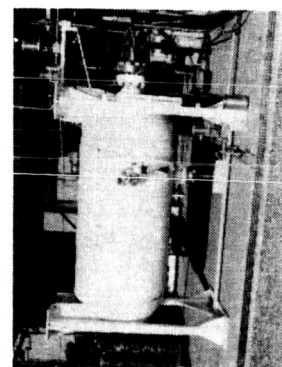
GN2 (OXID)  
35 FT<sup>3</sup>  
3600 psig

GN2 (FUEL)  
35 FT<sup>3</sup>  
3600 psig

LIQUID METHANE -  
LIQUID HYDROGEN  
3000 gal 200 psig

LIQUID NITROGEN  
1800 GAL 50 psig

LIQUID PROPANE  
1000 gal - 250 psig



GO2/GN2  
50 FT<sup>3</sup>  
8000 psig

HYDRAULIC  
SYSTEM

FROM GOX CONVERTER

GH2 68 FT<sup>3</sup> 8000 psig

GHe 18 FT<sup>3</sup> 8000 psig

LIQUID

160 GAL 5500 psig

LIQUID  
OXYGEN  
60 GAL 5500 psig

BAY  
A-6

BAY  
A-7

TPA TEST STANDS  
(FUTURE)

RP-1 RUN  
TANK 400 GAL

TEST STAND



Figure 24. Bay 6 LOX/Hydrocarbon Test Facility

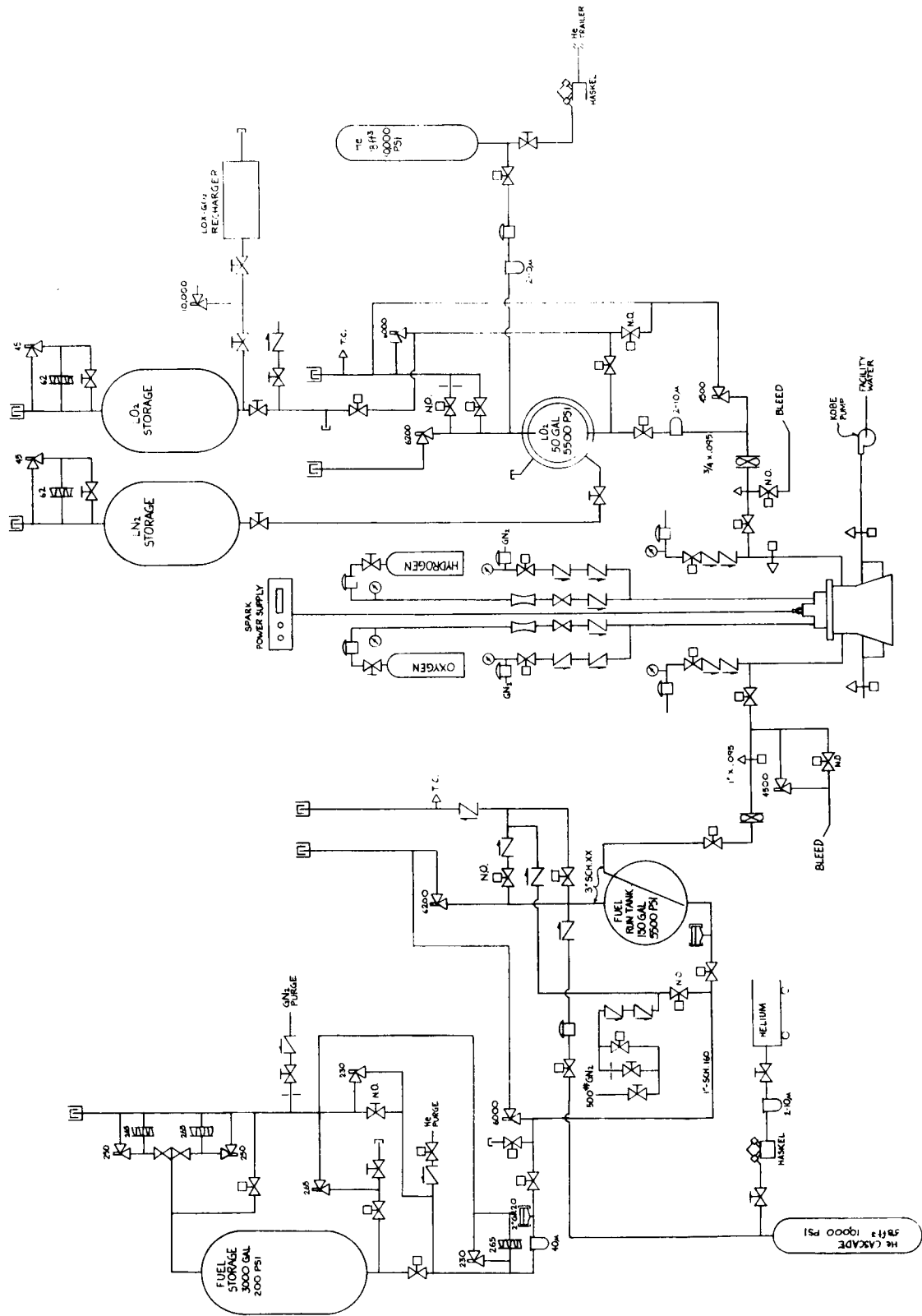


Figure 25. Propellant Feed System Schematic

ORIGINAL PAGE IS  
OF POOR QUALITY

## 4.2, Test Facility (cont.)

This tank fed an inlet manifold located next to the test stand. This manifold constituted a common coolant supply plenum for all circuits in the cooled hardware. Each cooling circuit was supplied through its own individual high pressure (4000 psi (27.57 MPa)) flex line leading from the manifold to the test hardware. The flow in each circuit was controlled by an orifice in the discharge side of the circuit. This location for the flow control orifices maintained high pressure in the cooling circuit and maximized the burnout safety factor. The individual cooling circuits discharged through flex lines to a common discharge manifold and then to a drain.

In subsequent preburner/gas generator testing, an eight gpm (0.5 l/sec), 1000 psi (6.89 MPa) Kobe water pump was used to provide water for cooling. The addition of this pump increased the run duration of the test program. Again, the pressure flex lines were used.

The use of the flex lines was a significant cost savings feature. It permitted partial disassembly of the test hardware without breaking all the high pressure cooling connections. It also allowed the cooled hardware assembly to be modified (to add an L' section, to insert a turbulence ring, etc.) without altering any hard plumbing.

### 4.2.2. Instrumentation

Circuits from Bay 6 and Bay 7 were used to instrument the feedsystem and test hardware. The feedsystem was instrumented as shown in Figure 26. The water-cooled configuration was instrumented as shown in Figure 27. The figure specifically shows the preburner/gas generator hardware instrumentation. For the main chamber configuration, the main water line inlet would bypass the turbine simulator and would flow directly into the turbulence ring. The modified preburner/gas generator hardware was instrumented as shown in Figure 28.

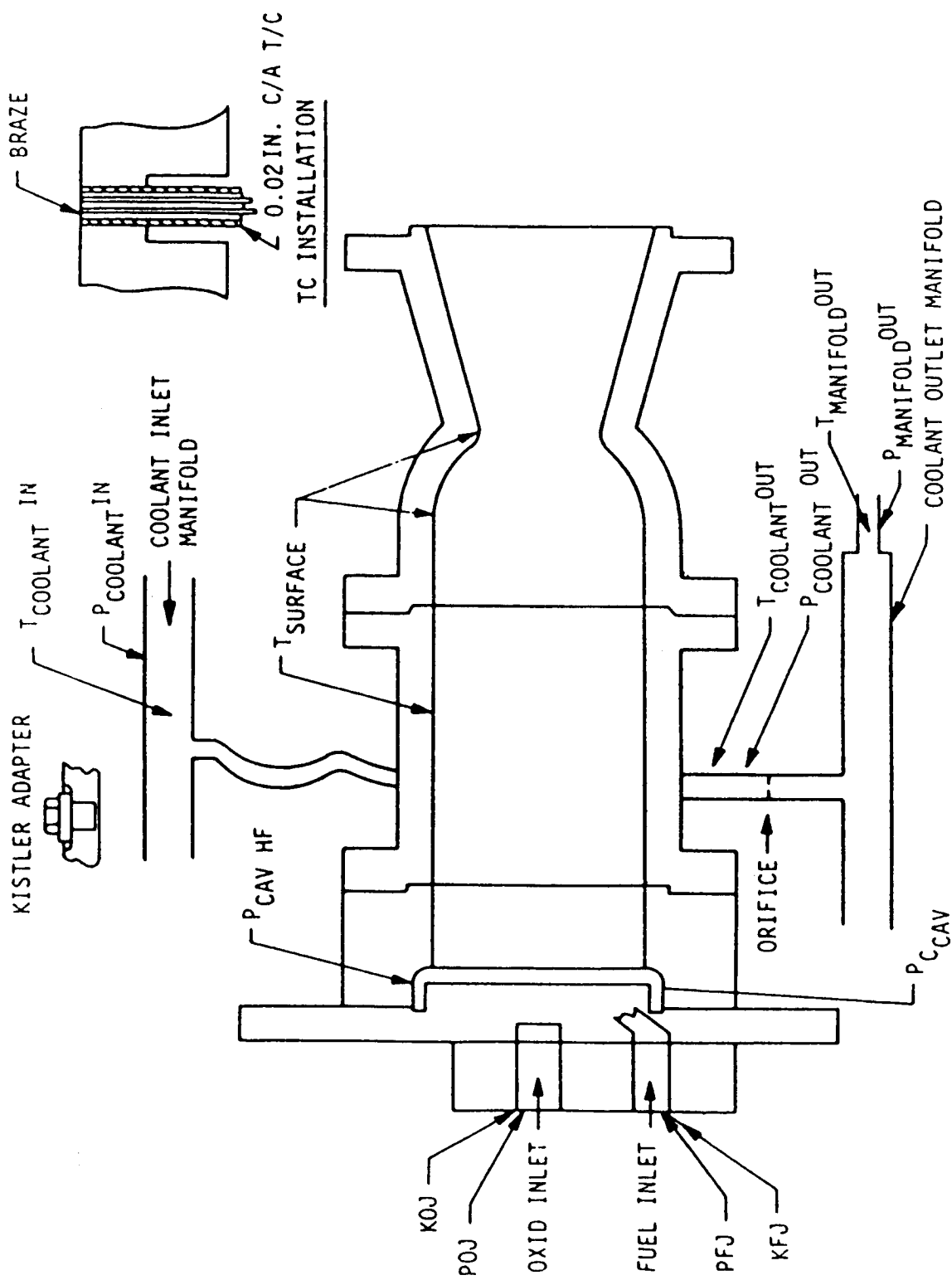


Figure 26. Typical Main Chamber Instrumentation

ORIGINAL PAGE IS  
OF POOR QUALITY

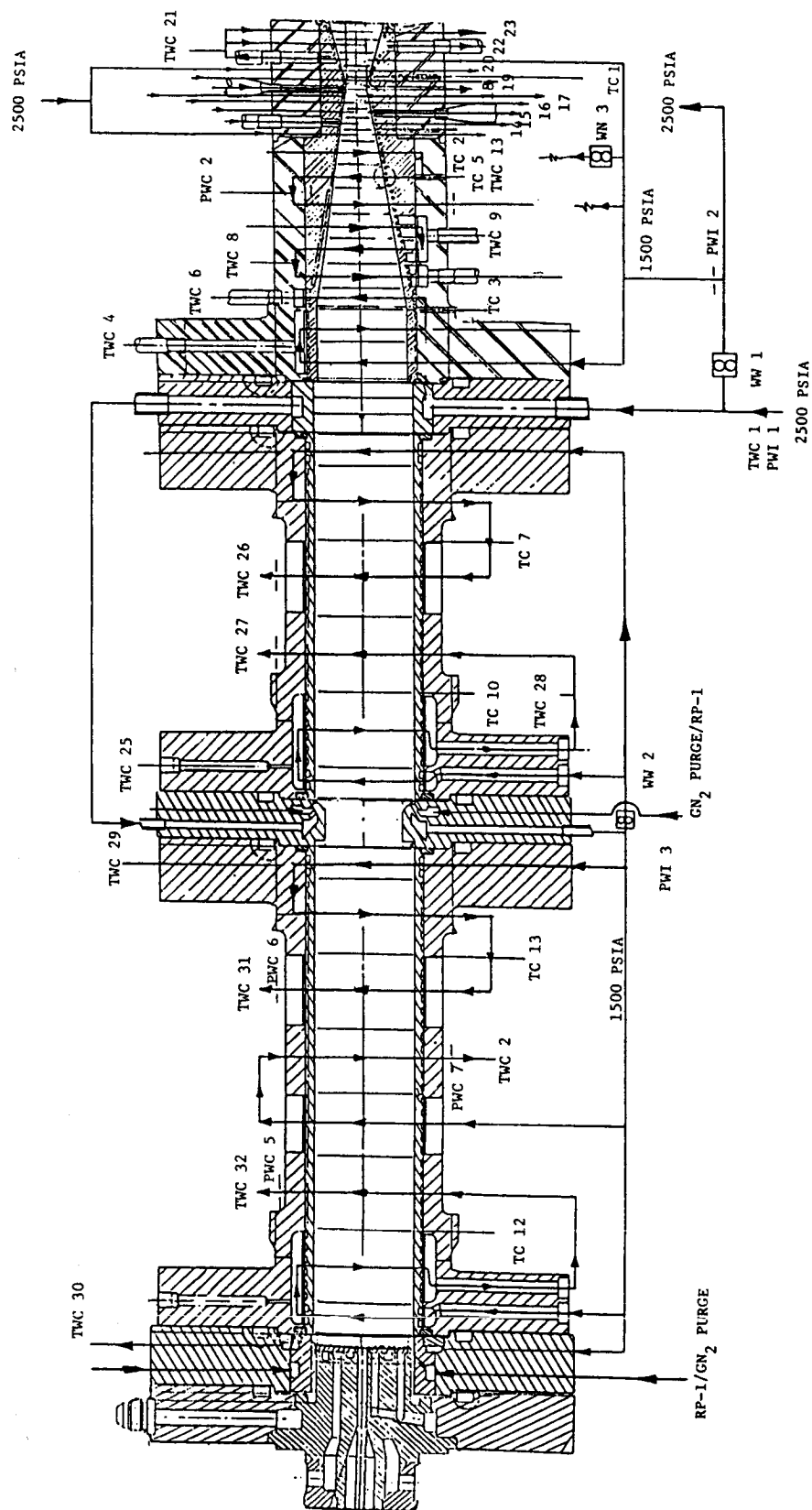


Figure 27. Water-Cooled Configuration Instrumentation

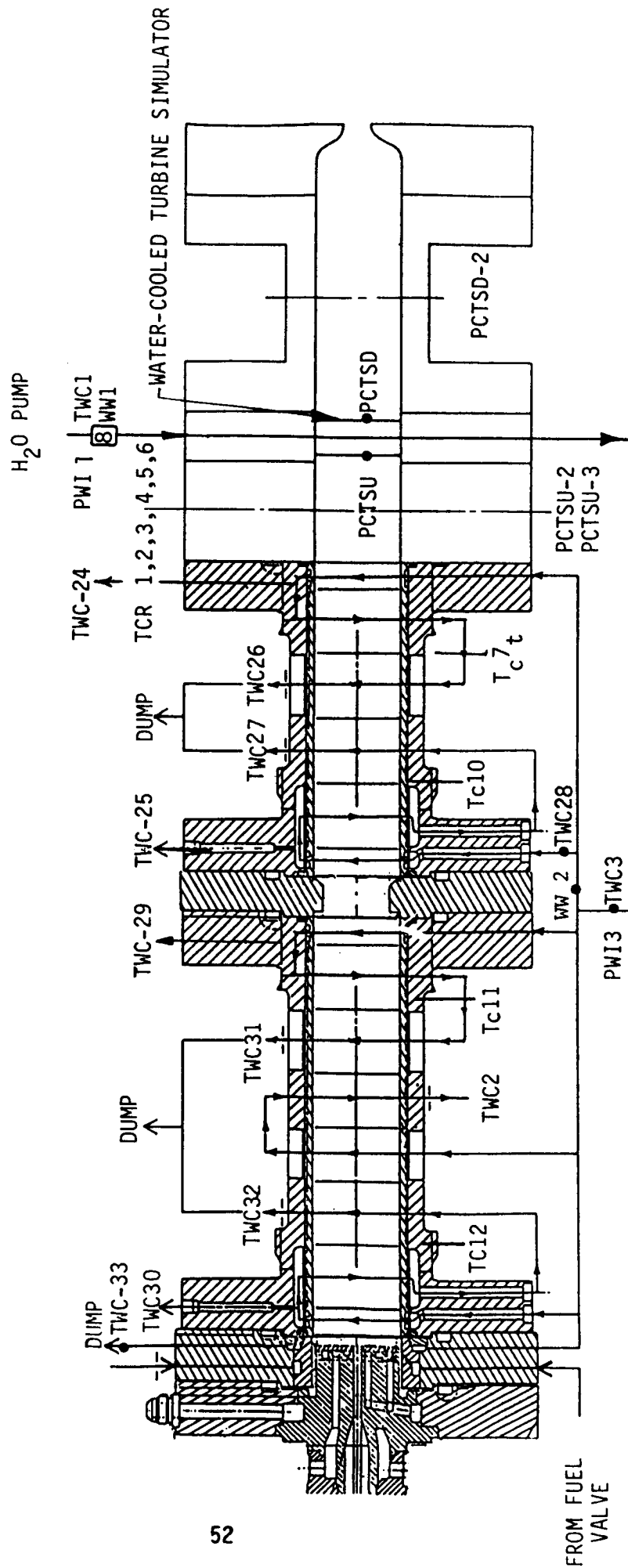


Figure 28. Preburner/Gas Generator Modified Hardware Configuration Instrumentation

## 4.2, Test Facility (cont.)

The pressure and thermal data were measured using the frequency response pressure transducers and thermocouples. These measured parameters were recorded on both a digital data acquisition system and an analog oscillograph. The measured data were reduced and printed out on an on-line computer.

Thrust was not measured due to the errors which would result from the large number of flexible high pressure lines attached to the test hardware. Injector performance was determined on the basis of chamber pressure ( $C^*$ ) measurements.

The feedsystem was instrumented to measure tank pressures and temperatures and flowrates. Each of the propellant flows was measured with a turbine flow meter. The propellant density was determined from temperature and pressure measurements made at the flowmeter. The igniter flowrates were determined by measuring the pressures and temperatures at the inlet to calibrated sonic venturis.

The instrumentation used for determining the heat input to the calorimeter circuits is illustrated in the cooling circuit shown in Figure 26. The total water flow, water pressure, and water temperature in the inlet manifold was measured. The discharge line from each cooling circuit contains a custom made flow control orifice. This orifice was sized to give the desired flow considering the measured Kw of the cooling circuit and the pressure in the coolant supply manifold. (The discharge manifold runs at nearly atmospheric pressure). Immediately upstream of each flow control orifice the coolant pressure and temperature was measured. The coolant temperature was also measured in the cross-overs connecting the series calorimeter circuits and in the discharge coolant manifold. This measurement system had several redundancies in it which allowed the data to be checked for consistency. These redundancies applied to both the flow and the heat input.



## 4.2, Test Facility (cont.)

The test hardware was instrumented to measure the injector manifold pressures, the injector face pressure, and the chamber wall temperatures. The steady-state pressures were measured with Taber transducers.

The chamber wall and nozzle throat temperatures were measured using 0.020 (0.05 cm) inch diameter Chromel/Alumel thermocouples brazed to the inside wall surface as shown in Figure 26.

High frequency response chamber pressure oscillations were measured using Kistler pressure transducers. The Kistlers were mounted in adapters as shown in Figure 26 to provide thermal protection from the hot combustion gases. The Kistler output was recorded on magnetic tape and played back on an oscillograph at reduced speed for data analysis.

### 4.2.3 Data Measurement Consistency

#### 4.2.3.1 Pressure Measurements

The questions regarding the validity of the pressure measurements immediately upstream and downstream of the turbine simulator in the 1984 RP-1 tests were answered in the 1985 RP-1 tests when additional pressure taps were placed upstream and downstream of the turbine simulator. The upstream pressure taps were placed 2.41 inches (6.12 cm) from the turbine simulator tubes ( $L/D = 1.01$ ); and the downstream pressure tap was placed 5.64 inches (12.46 cm)  $L/D = 2.37$ ) from the tubes.

## 4.2, Test Facility (cont.)

The pressure taps were labeled as follows:

<u>Tap</u>	<u>Distance from Turbine Simulator (in.)</u>	<u>(cm)</u>
PCTSU	0.032	(0.081)
PCTSU-2	2.41	(6.12)
PCTSU-3	2.41	(6.12)
PCTSD	0.072	(0.183)
PCTSD-2	5.64	(14.32)

Figures 29, 30 and 31 show minimal differences in pressure measurement due to differences in pressure tap location. This means the pressure measurement for the 1984 RP-1 tests were satisfactory.

### 4.2.3.2 Combustion Gas Temperature Uniformity

Combustion gas temperatures for each fuel were obtained for most of these tests. A temperature rake with six thermocouples at varying immersion depths was used to measure gas temperatures for the 1985 to 1986 test series. No gas temperatures were measured during the 1984 test series. Figure 32 shows the temperature rake gas thermocouple immersion depths and circumferential locations. The gas temperature range for each fuel is shown in Figures 50, 51, and 52. Only thermocouples at comparable immersion depths were used to determine the average gas temperature. Figure 51 shows that the temperature spread for propane increased at mixture ratios over 0.35, which was probably due to streaks in the chamber where the exothermic reactions from the breakup of the C = C bonds during carbon deposition occurred. Both Figures 50 and 52 show that RP-1 and methane experienced very little temperature spread.

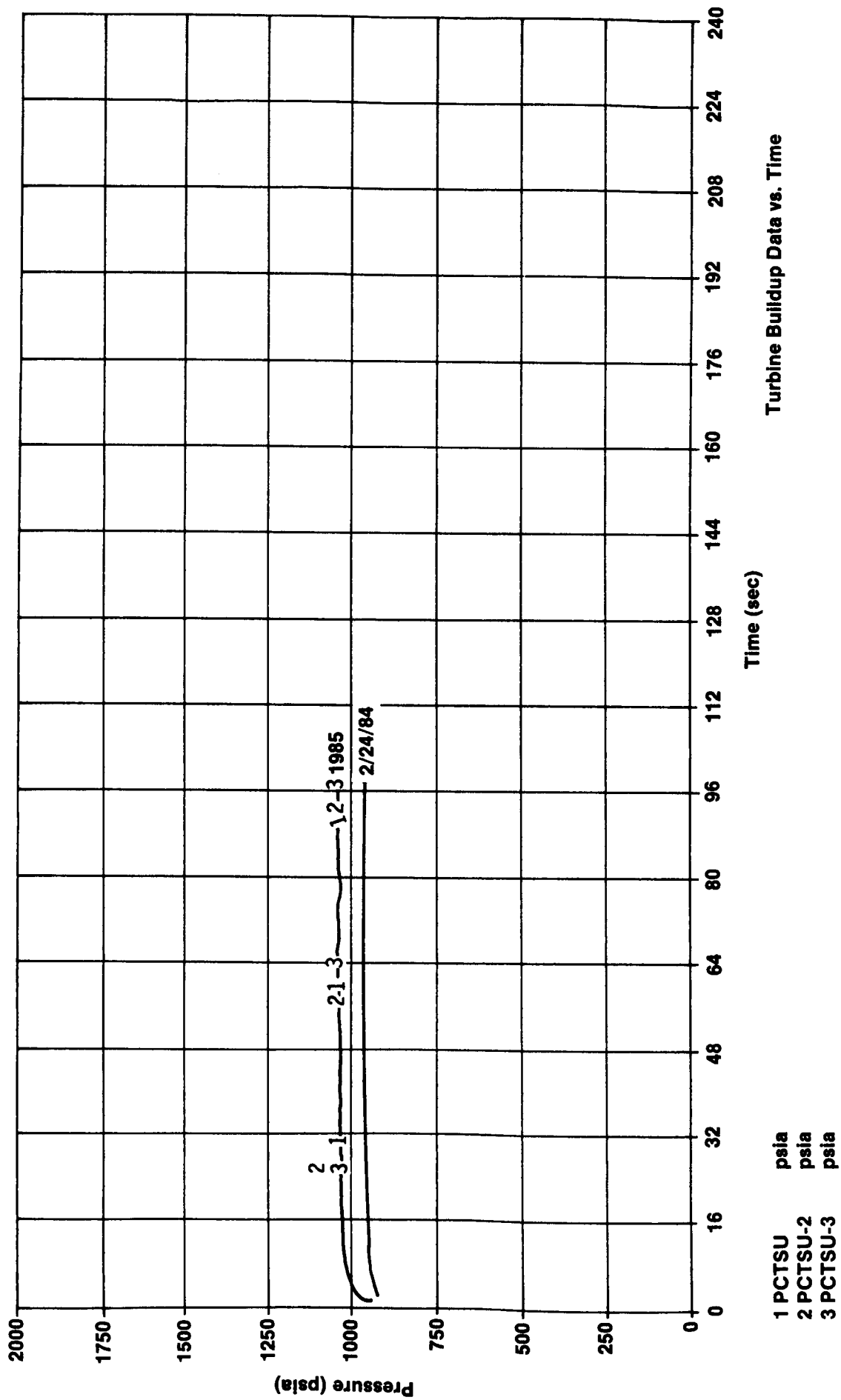


Figure 29. Upstream Pressure Measurement Comparison at  $P_c = 1000$  psi

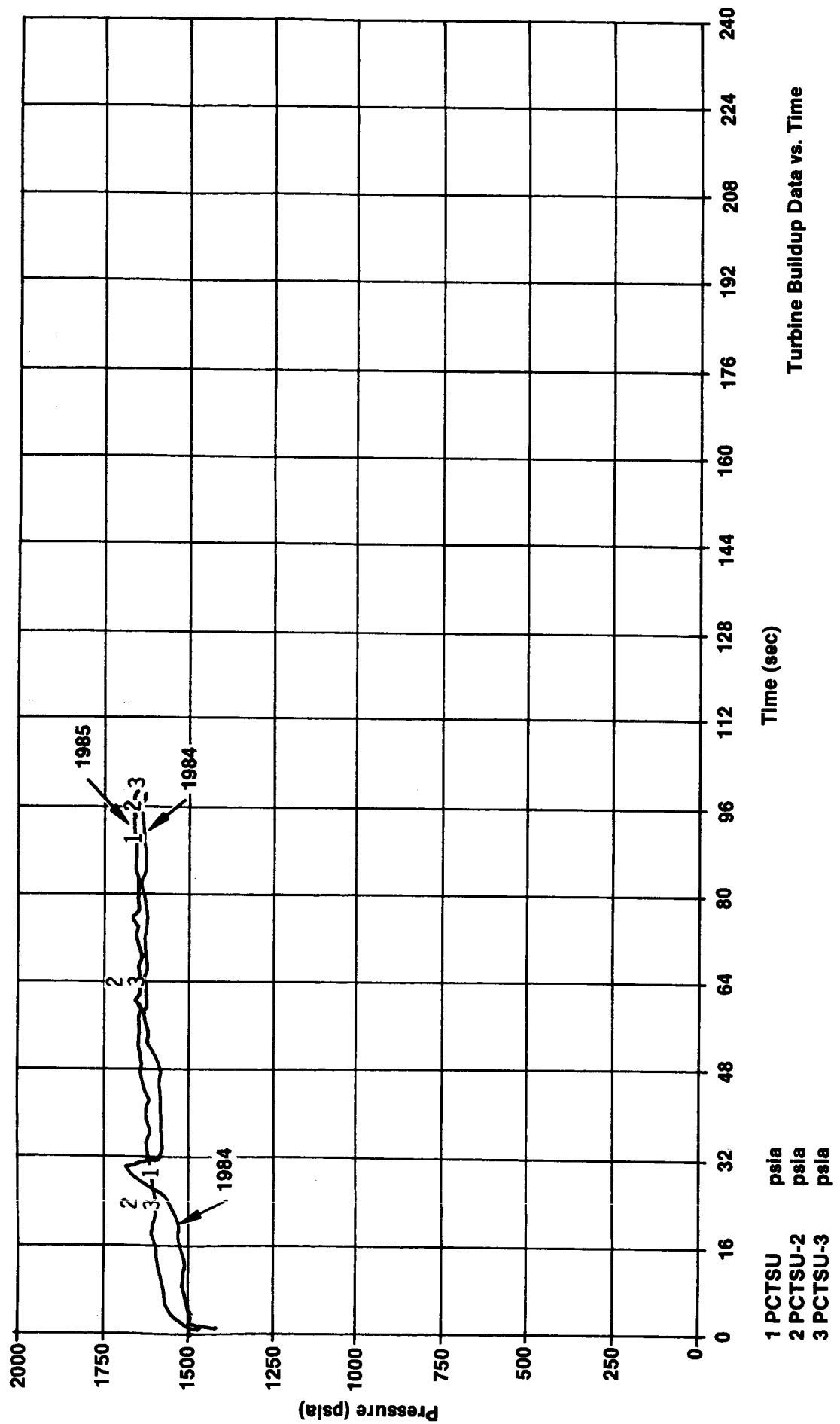


Figure 30. Upstream Pressure Measurement Comparison at  $P_c = 1500$  psi

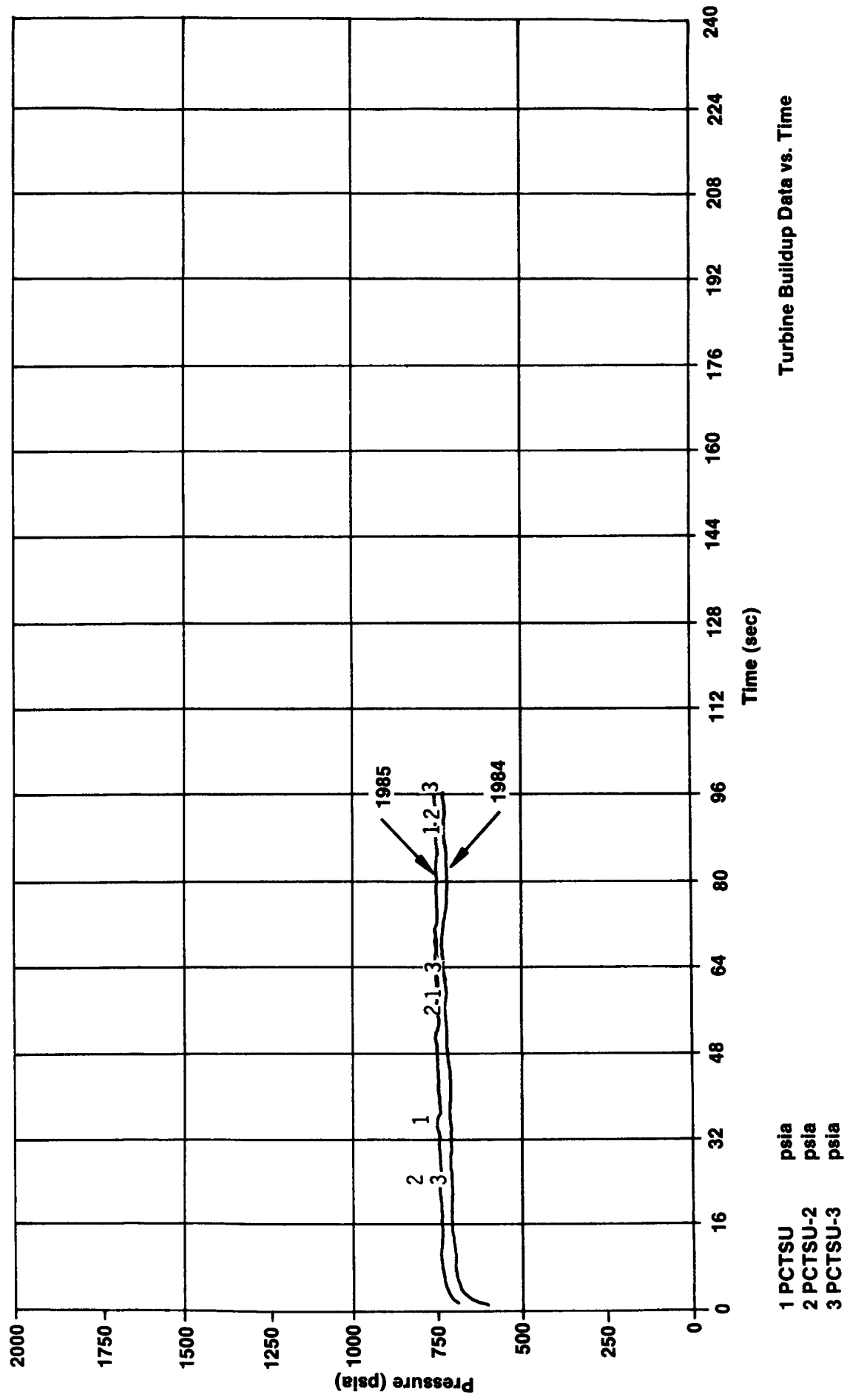
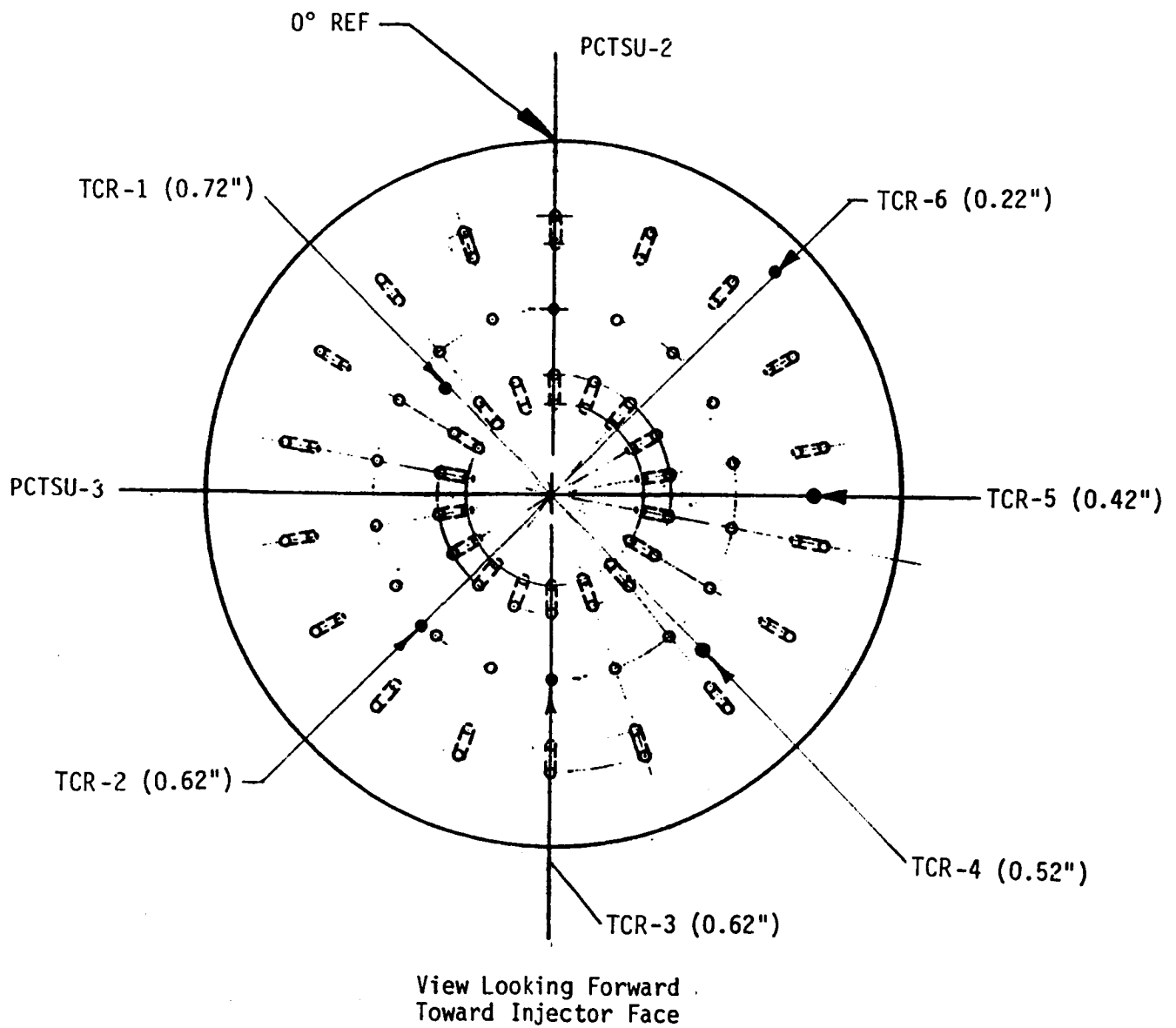


Figure 31. Upstream Pressure Measurement Comparison at  $P_c = 750$  psi



**Figure 32. Preburner/Gas Generator Gas Temperature Thermocouple Locations**

## 4.0, Technical Discussion (cont.)

### 4.3 MAIN CHAMBER TEST RESULTS

Nine checkout tests with durations less than 1.0 second and sixteen data tests with durations between 3 to 40 seconds were conducted at main chamber operating conditions using LO<sub>2</sub>/RP-1 as shown in Table III. Ignition on all tests was reliable and smooth.

#### 4.3.1 C\* Performance

The combustion efficiency, % C\*, for the main chamber tests was calculated using the equation:

$$C^*_{\text{Test}} = \frac{(P_c - 1) A_t g_c}{\dot{w}_t}, \text{ where } P_c - 1 \text{ is the Taber transducer}$$

pressure measurement in the chamber, and the equation:

$$\%C^* = C^*_{\text{Test}} / C^*_{\text{ODE}}$$

Very high C\* combustion efficiency, >99%, was achieved at the nominal design mixture ratio of 3.0. As noted in Figure 33, the C\* efficiency dropped slightly at both higher and lower mixture ratios but still remained relatively high compared to the 90-95% range of the operational LO<sub>2</sub>/RP-1 engines developed during the 1955-1963 era.

Past analyses of 1960 technology main chamber performance had revealed two primary reasons for low performance efficiency. The first was due to inadequate atomization of the RP-1 streams and its resultant incomplete fuel vaporization. This was often compounded by having to utilize coarse injector patterns to achieve stable combustion. The second reason for low performance was due to incomplete LO<sub>2</sub>/RP-1 mixing. The poor mixing results in scarcity of oxygen vapors between adjacent fuel droplets within the fuel-rich zones which further reduces fuel droplet burning rate (lower performance) and often contributes to residual unburned carbon particles (deposition).

TABLE III

## 1984 RP-1 CARBON DEPOSITION MAIN CHAMBER TEST SUMMARY

TEST NO.	DATE	DURATION (SEC)	P <sub>C</sub> (PSIA)	MR	W <sub>t</sub> (lbm/sec)	C* (fps)	COMMENTS
RLB-936-201	3/19/84	0.2	920	3.0*			Checkout.
202	3/19/84	3.2	980	2.7*	1.12	5540	Checkout.
203	3/19/84	3.2	1510	3.0*	1.68	5525	Checkout.
204	3/19/84	3.2	1480	2.1*	1.68	5450	Checkout.
205	3/19/84	-	-	-	-	-	Test aborted due to H2O pressure "kill" error.
206	3/19/84	3.2	1525	4.2*	1.791	5267	Checkout.
207	3/19/84	0.2	2003	3.0*	-	-	Duration limited due to high heat fluxes
208	3/19/84	0.2	1890	2.0*	-	-	Duration limited due to high heat fluxes.
209	3/19/84	0.2	1940	4.0*	-	-	Duration limited due to high heat fluxes.
210	3/19/84	0.2	2002	3.0*	-	-	Duration limited due to high heat fluxes.
211	5/3/84	0.7	1498	2.81*	-	-	Aborted due to bad coolant outlet temperature measurement (Twc 27). Good checkout test.
212	5/3/84	3.6	1502	2.91*			
213	5/3/84	17.3	1527	3.16*	1.69	5593	Aborted after 17.3 seconds due to excessive coolant outlet temperature (Twc 26 = 200 F) in 8" barrel section. No apparent carbon build-up.
214	5/3/84	35	1492	3.04	1.64	5640	No apparent carbon build-up
215	5/3/84	40	1475	2.05	1.65	5576	No apparent carbon build-up. Nozzle water leak noted.
216	5/3/84	40	1000	3.0	-	-	Computer problem prevented acquiring digital data. Nozzle removed and inspected. No significant carbon build-up noted. Leak at convergent nozzle repair area.
217	6/6/84	3.6	1000	1.9*	-	-	1L instability (~900 Hz) encountered (~800 psi peak to peak). Injector P increased for next test.
218	6/6/84	0.3	1000	2.0*	-	-	1L instability (~900 Hz) encountered (~300 psi peak to peak). Aborted due to low P <sub>c</sub> kill parameter (825 psia). Injector ΔP increased for next test.
219	6/6/84	0.1	1000	2.1*	-	-	1L instability (~900 Hz) encountered (~300 psi peak to peak). Aborted due to bad coolant outlet temperature (Twc 27).
220	6/6/84	0.1	1000	2.2*	-	-	1L instability (~900 Hz) encountered (~300 psi peak to peak). Aborted due to bad coolant outlet temperature (Twc 2).
221	6/7/84	3.6	980	2.0*	1.10	5490	Good checkout test. 1L apparently caused by warm LOX for tests 217 thru 220.
222	6/7/84	25	1025	2.3	1.13	5660	No apparent carbon build-up.
223	6/7/84	3.6	1508	2.2*	1.66	5590	Fuel film cooling injected downstream of turbulence ring.
224	6/7/84	25	1530	2.4	1.66	5740	Good fuel film cooling data test. No apparent carbon build-up.
225	6/7/84	3.6	1506	2.6*	1.64	5670	Fuel film cooling injected at injector.
226	6/7/84	10.3	1506	2.6	1.65	5656	Good fuel film cooling data test. No apparent carbon build-up. Aborted due to bad coolant outlet temperature (Twc 6).

\* Mixture ratio doesn't reach steady-state until approximately 1.0 seconds.



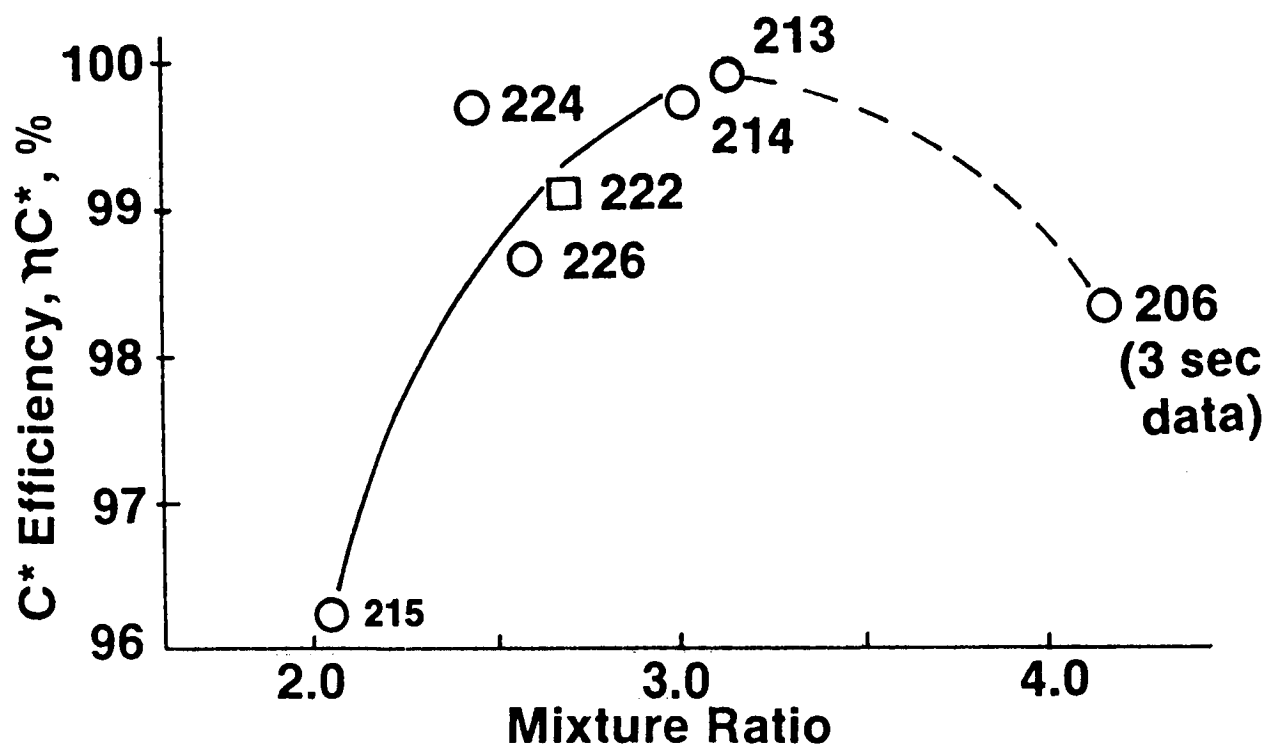


Figure 33. Main Chamber Combustion Efficiency

### 4.3, Main Chamber Test Results (cont.)

Due to the fine ( $D_o = 0.024$  in. (0.061 cm) and  $D_f = 0.021$  in. (0.053 cm) O-F-O triplet injector pattern and long ( $L' = 20$  in. (50.8 cm) chamber length, the main chamber was capable of achieving complete RP-1 vaporization performance. All triplet elements, however, are extremely injection momentum ratio sensitive in terms of intra-element mixing. At low mixture ratios, the axial fuel jet cores through. At high mixture ratios, the  $LO_2$  jets over-penetrate the fuel stream. The optimum mixing operating mixture ratio can be adjusted either higher or lower by modifying the fuel to oxidizer injection orifice area ratio. It was fortuitous that the F-O-F gas generator injector element, when reversed to an O-F-O, optimized very near the  $LO_2$ /RP-1 main chamber design mixture ratio.

#### 4.3.2 Carbon Deposition

The primary approach used to determine carbon deposition for main chamber operating conditions was to measure heat flux versus time. The rate of reduction in heat flux is proportional to the carbon deposition rate, and the final carbon layer thickness is proportional to the ratio of the final steady state reduced heat flux divided by the initial heat flux before carbon build-up. This approach was successfully used previously (Ref. 3) for  $LO_2$ /propane testing at 300 psi (2.07 MPa) chamber pressure. Figure 34 shows the reduction in heat flux as carbon build-up occurred.

In the main chamber tests, the measured heat flux did not decrease with firing time as expected (Figure 35), and no significant carbon build-up was noted on the chamber walls during post test inspection. Figure 36 shows that for the range of mixture ratios tested, the measured heat fluxes for the main chamber tests indicated that no carbon deposition had occurred.

No carbon content was ever visible in the exhaust plume during steady state operation (see Figure 37). This lack of carbon deposition is not consistent with the experience of the industry during previous  $LO_2$ /RP-1 development programs such as Titan I and F-1, for example, and is due to the higher combustion efficiency range which was achieved.

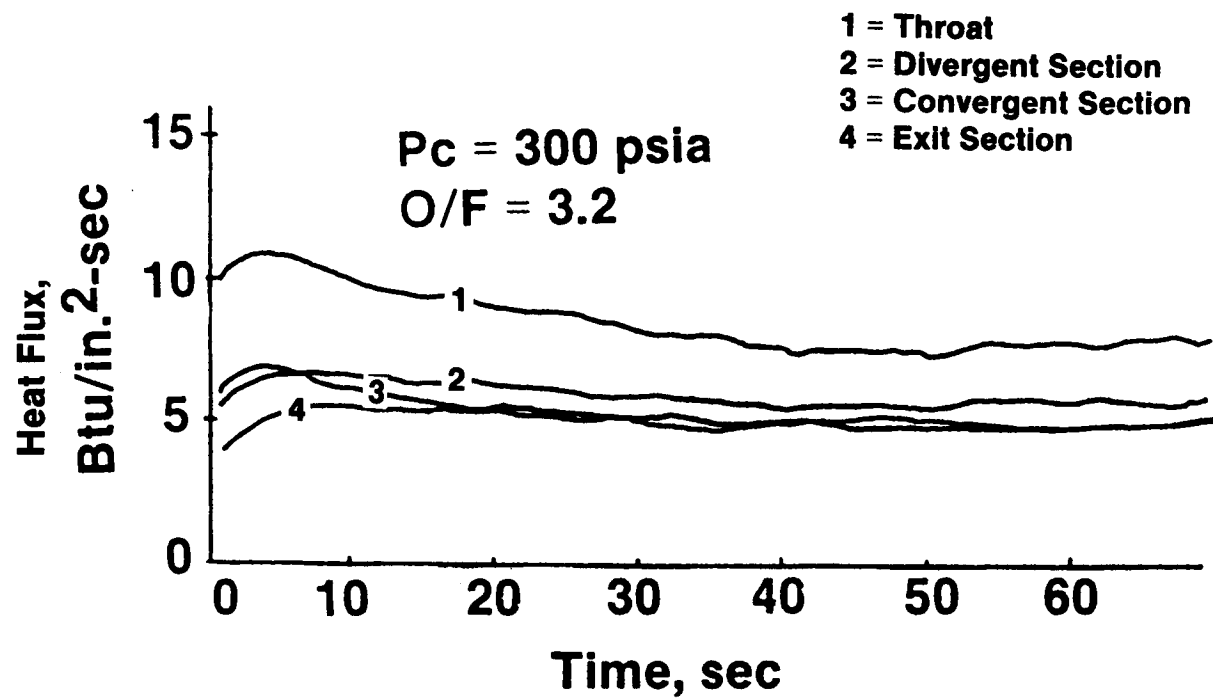


Figure 34. Mid  $P_c$  (Ref. 3)  $LO_2$ /Propane Nozzle Heat Flux

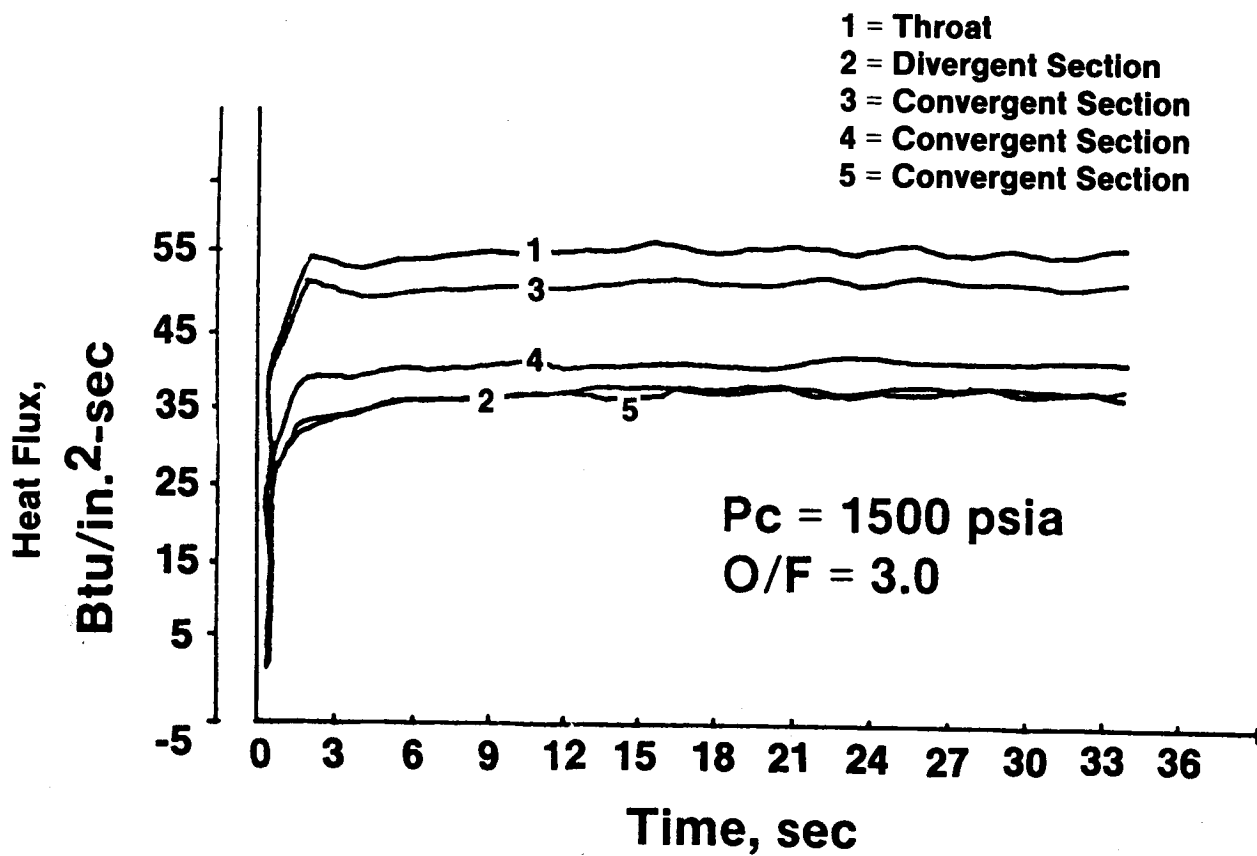
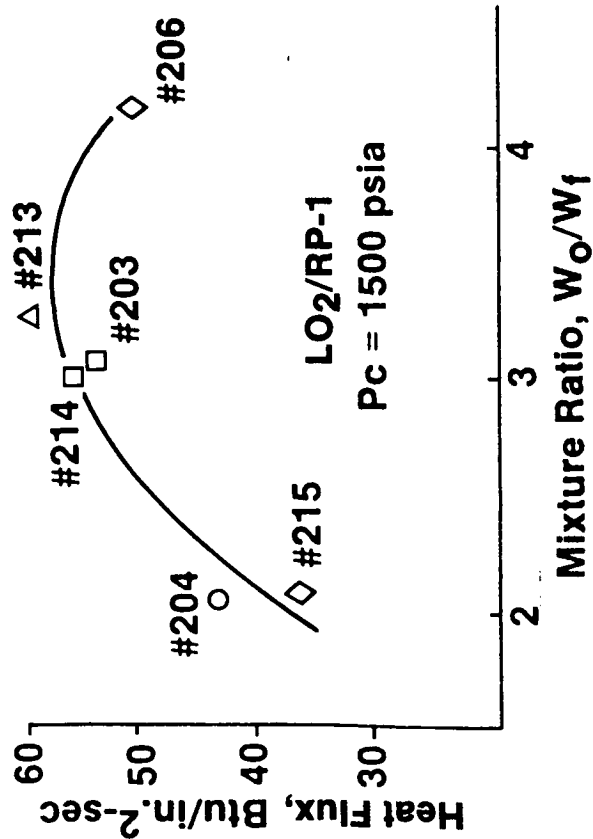
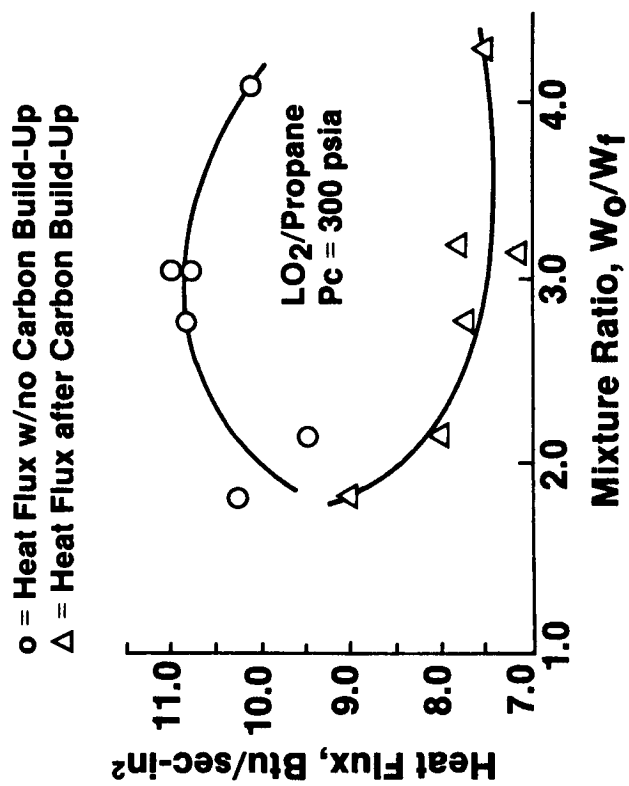


Figure 35. Main Chamber LO<sub>2</sub>/RP-1 Nozzle Heat Flux



36a. Main Chamber Heat Flux Data



36b. Test Data from Ref 3 Shows Effect of Carbon Deposition on Heat Flux

Figure 36. Main Chamber Heat Flux Results Show No Carbon Build-Up

ORIGINAL PAGE IS  
OF POOR QUALITY

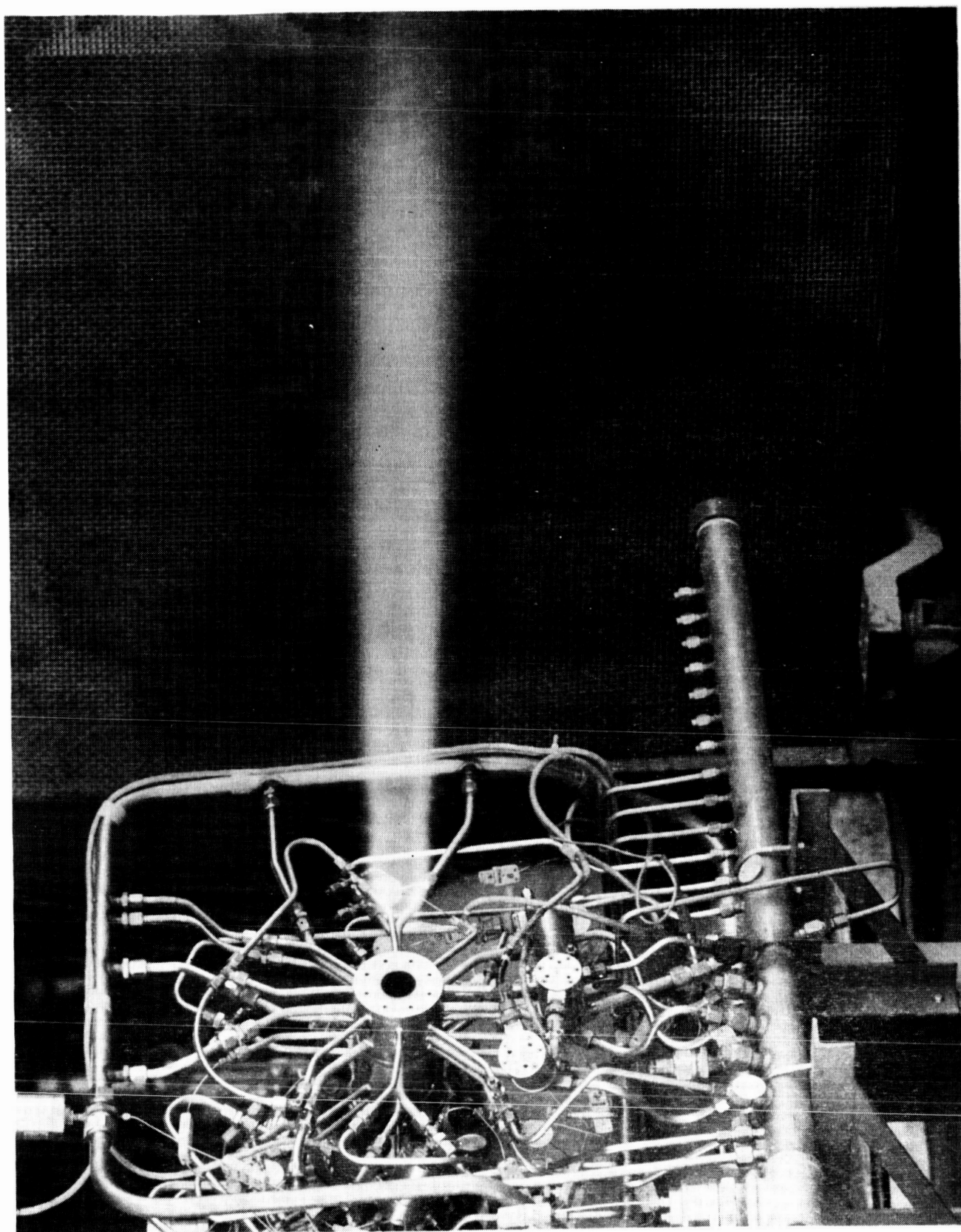


Figure 37. Main Combustion Chamber Exhaust Plume

#### 4.3, Main Chamber Test Results (cont.)

A similar lack of significant carbon deposition on the chamber walls with  $\text{LO}_2/\text{RP-1}$  propellants was also noted during a recent technology test program at 1200 and 2000 psia (8.27 and 13.78 MPa) chamber pressure and with combustion efficiencies generally in the 94-98% range (Reference 5).

The theoretical One Dimensional Equilibrium (ODE) gas composition does not predict carbon deposition at main chamber operating mixture ratios above 2.0. On the other hand, it does predict solid carbon at mixture ratios around 1.0. The past development engines which experienced carbon deposition had such poor mixing efficiencies that it had local mixture ratios in the deposition range even though the overall main chamber operating mixture ratios should have been carbon deposition free. This test program proved that carbon deposition at main chamber test conditions is attributable to injector design limitations only. It is not a hydrocarbon chemistry problem. Thermochemical carbon deposition limits at main chamber conditions are adequately predicted by equilibrium chemistry.

##### 4.3.3 Main Chamber Thermal Analysis

This section presents the thermal characteristics, channel geometry, flow circuitry, and water flow rates for two calorimetric barrel sections and one calorimetric nozzle. The design objective for this hardware was to determine reductions in heat load, if any, resulting from the deposition of carbon on the gas-side chamber wall.

##### 4.3.3.1 Calorimetric Chamber Design

Two barrel sections of Nickel-200 were designed for use with the nozzle. The longer barrel section (12 in.) (30.48 cm) consisted of 38 circumferential channels forming four separate and independent cooling water circuits, each with three heat load measurement segments in series. The shorter barrel section (8 in.) (20.32 cm) consisted of 26 channels forming three circuits in a similar fashion. Coolant water flow rates of 3.22 and

#### 4.3, Main Chamber Test Results (cont.)

2.30 lbm/sec (1.46 and 1.04 kg/s) (1.46 and 1.04 kg/s) were calculated for the long and short barrels respectively. The maximum predicted gas-side wall temperature was 1780°F (1244K). The bulk temperature rise for each heat load measurement segment was calculated to be at least 60°F (288K) for measurement accuracy; the minimum burnout safety factor (BOSF) was 2.14.

The 2000 psia (13.78 MPa) Pc nozzle of zirconium-copper consisted of 57 channels forming 13 circuits to give 23 heat load measurement segments. Three segments were connected in series wherever possible. The maximum gas-side wall temperature of 1410°F (1038K) and minimum BOSF of 1.43 were predicted for the throat. For the required coolant water flow rate of 8.32 lbm/sec (3.77 kg/s), bulk temperature rises were predicted to vary from 28 to 73°F (271 to 296K). All tests were performed using this nozzle.

The original three-channel cooling section design for the 2000 Pc (13.78 MPa) nozzle resulted in a channel located at the section mid-point with a potential high stress concentration. The nozzle was modified to a four channel module with the same total water flow area and thus the same coolant velocity. Heat transfer characteristics were considered sufficiently similar that re-analysis of the nozzle was not required.

SINDA (Systems Improved Numerical Differencing Analyzer) single channel analyses of oversize channels with land widths and gas-side wall thicknesses at the maximum tolerance limit were used to define the chamber design at each heat load measurement segment based on the worst channel. A Cg profile developed from test data obtained in the High Density Fuel and Mid-Pc programs was used to predict clean-wall gas-side heat fluxes for a mixture ratio of 3.0. This profile is shown in Figure 38.

##### 4.3.3.2 Thermal Design Parameters

The initial thermal design parameters for the main chamber are listed in Table IV. The design was constrained by these guidelines except where an internal inconsistency became apparent. For example, maintaining a



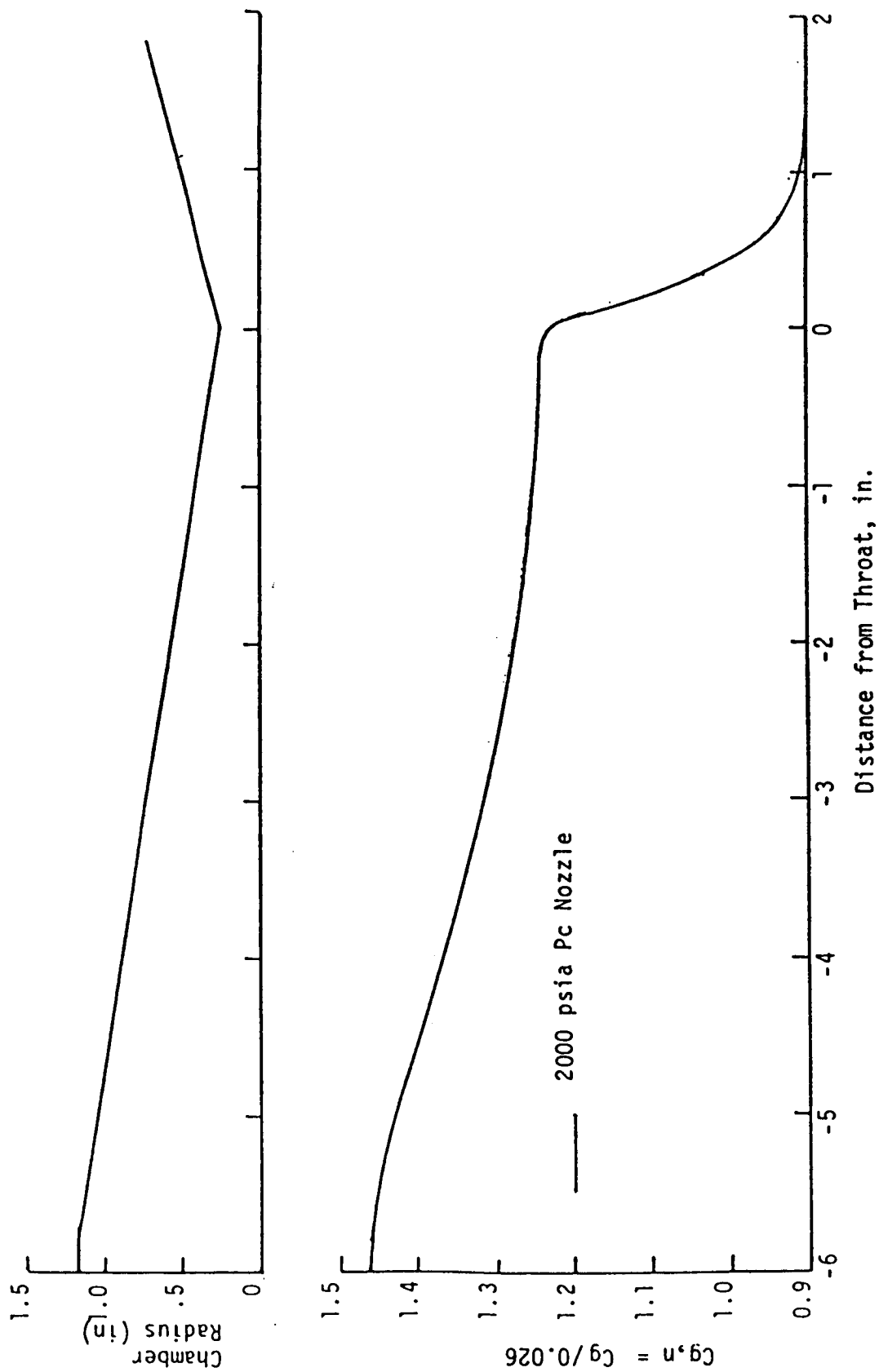


Figure 38. Design  $C_g$  Profile for Carbon Deposition Nozzle

TABLE IV  
INITIAL CHAMBER THERMAL DESIGN PARAMETERS

1.	Gas-Side Wall Temperature, °F	
	Barrel (Ni 200)	750
	Nozzle (Zr-Cu)	900
2.	Maximum Inlet Pressure, psia	3000 (nom) 3300 (max)
3.	Cooling Channel Tolerances, in.	
	Width	+ 0.003
	Depth, Wall Thickness	± 0.005
4.	Channel Width, in.	
	$W_{\max} = 1.414 t_{\min} (F_{TY}/P_{in})^{0.5}$	
	Where:	
	$W_{\max}$	= Maximum channel width, in.
	$t_{\min}$	= Minimum gas-side wall thickness, in.
	$F_{TY}$	= Yield strength, psi
	$P_{in}$	= Inlet pressure, psia
5.	Coolant Bulk Temperature Rise (Design Point), °F	60
6.	Burnout Safety Factor BOSF (Based on experimental Cg profile from the high density fuel study)	≥ 1.5
7.	Coolant-Side Heat Transfer Coefficient (Based on maximum channel width and depth)	
8.	Coolant Pressure	$P_{cool} > P_{gas}$

#### 4.3, Main Chamber Test Results (cont.)

throat gas-side wall temperature of 900°F (755K) resulted in a gas-side wall thickness considerably less than practically achievable. In this case, higher gas-side wall temperatures up to 1410°F (1038K) were allowed.

The design water inlet pressure and flow rate for each individual circuit are given in Table V together with cold flow measurements of circuit KW factors. Circuit pressure drops and outlet pressures based on these data are tabulated. Preliminary test setup data indicated the need for higher inlet pressures for all circuits with an inlet pressure below 2500 psia (17.24 MPa). The resulting circuit flow rates and pressure drops are given as final design parameters. The total coolant flow rate to the nozzle was increased by 13.4%; water flow to the 8 in. (20.32 cm) barrel was decreased by 0.3% while that to the 12 in. (30.48 cm) barrel was increased 1.2%.

The clean-wall gas-side parameters were generated using the non-design option of the ATC SCALED computer program. The baseline system was selected as LOX/RP-1 at a chamber pressure of 2000 psia (13.78 MPa) and a mixture ratio of 3.0. The TRAN72 and Rao Nozzle programs provided the recovery temperatures for the design geometry; limiting values of 760, 1410, and 760°F (677, 1038, and 677K) were input respectively for the barrel, throat, and nozzle gas-side wall temperatures. Using the  $C_g$  profile of Figure 38, the SCALED program computes the gas-side coefficient  $h_g$  and the gas-side flux,  $\dot{q}_g$ . These parameters are given in Table VI as a function of area ratio.

The interpolated mean gas-side heat fluxes together with circuit gas-side areas established the circuit heat load which in turn gave the predicted circuit coolant bulk temperature rises for the appropriate circuit flow rates. The results of these calculations are presented in Table VII. Predicted bulk temperature increases ranged from 13.9 to 55.2°F (263 to 286K) for the nozzle and from 21.8 to 58.1°F (267 to 287K) for the barrel sections.

TABLE V

## MAIN CHAMBER CIRCUIT HYDRAULIC PARAMETERS

Circuit	INITIAL DESIGN				FINAL DESIGN			
	P (in) <sup>*</sup> psia	$\dot{W}$ <sup>**</sup> lbm/sec	KW <sup>**</sup>	$\Delta P$ <sup>***</sup> psi	P (out) psia	P (in) psia	$\Delta P$ psi	$\dot{W}$ lbm/sec
<u>NOZZLE</u>								
1	1500	1.05	0.0800	172	1328	1720	190	1.10
2	1500	0.77	0.0468	271	1229	1720	290	0.79
3	1500	1.43	0.0474	910	590	1720	1100	1.57
4	2500	0.59	0.0278	450	2050	2500	440	0.58
5	2500	0.60	0.0287	437	2063	2500	450	0.61
6	2500	0.55	0.0284	375	2125	2500	450	0.60
7	2500	0.60	0.0238	635	1865	2500	640	0.60
8	2500	1.17	0.0302	1501	999	2500	1450	1.15
9	2500	0.72	0.0195	1363	1137	2500	1600	0.78
10	2500	0.93	0.0558	278	2222	2500	1210	1.94
11	2500	0.60	0.0312	370	2130	2500	460	0.67
12-1	1500	1.00	0.0852	138	1762	1720	150	1.05
12-2	1370	0.55	0.0613	80	290	1570	90	0.58
12-3	1370	0.45	0.0600	56	1314	1570	60	0.47
		<u>11.01</u>						<u>12.49</u>
<u>TURBULENCE</u>								
<u>RING</u>	2500	11.31	0.437	670	1830			
<u>8" BARREL</u>								
1	1500	1.46	0.182	64	1436	1540	70	1.47
2	1400	1.46	0.340	18	1382	1470	20	1.47
4	1500	1.46	0.182	64	1436	1540	60	1.46
3	1400	1.46	0.342	17	1383	1480	20	1.46
		<u>5.84</u>						<u>5.82</u>
<u>12" BARREL</u>								
1	1500	1.46	0.190	59	1441	1540	60	1.52
2	1400	1.46	0.366	16	1384	1480	20	1.52
3	1500	1.22	0.300	16	1484	1540	20	1.18
4	1475	1.22	0.300	15	1459	1520	20	1.18
5	1500	1.46	0.185	62	1438	1480	20	1.49
6	1400	1.46	0.340	18	1382	1540	60	1.49
		<u>8.28</u>						<u>8.38</u>
<u>RESONATOR</u>	1500	3.69	0.170	471	1029			

\* Design values

\*\* Cold flow measurements for individual circuits

\*\*\* Based on cold flow measurements

TABLE VI

LO<sub>2</sub>/RP-1

## BASELINE MAIN CHAMBER GAS-SIDE THERMAL PARAMETERS

(Pc = 2000 psia, MR = 3)

Area Ratio	Recovery Temp., °F	Wall Temp., °F	Coefficient Btu/in <sup>2</sup> -sec-°F	Flux <sub>2</sub> Btu/in <sup>2</sup> -sec	Barrel
22.66	6420	760	0.00134	7.58	
21.19	6420	760	0.00141	7.96	
19.77	6420	760	0.00148	8.37	
18.41	6420	760	0.00156	8.85	
17.09	6420	760	0.00166	9.37	
15.82	6420	760	0.00176	9.96	
14.59	6420	768	0.00187	10.59	
13.42	6420	792	0.00200	11.26	
12.30	6420	814	0.00214	12.01	
11.22	6420	836	0.00230	12.87	
10.20	6420	856	0.00249	13.85	
9.22	6420	879	0.00270	14.95	
8.30	6420	901	0.00294	16.22	
7.42	6420	922	0.00322	17.69	
6.59	6419	942	0.00355	19.44	
5.81	6419	961	0.00394	21.51	
5.08	6419	978	0.00441	24.00	
4.40	6419	1013	0.00498	26.93	
3.76	6419	1048	0.00569	30.55	
3.18	6418	1080	0.00657	35.09	
2.65	6418	1182	0.00767	40.15	
2.16	6416	1308	0.00909	46.41	
1.72	6413	1361	0.0111	55.84	
1.34	6405	1378	0.0137	69.11	
1.00	6377	1410	0.0173	85.98	Throat
1.78	6285	1370	0.00804	39.52	
2.78	6244	1080	0.00475	24.53	
4.00	6215	950	0.00328	17.25	
5.44	6193	850	0.00241	12.88	
7.11	6174	760	0.00184	9.98	Exit
9.00	6158	660	0.00147	8.09	

TABLE VII

PREDICTED MAIN CHAMBER COOLING CIRCUIT  
THERMAL PARAMETERS

(LOX/RP-1,  $P_c = 2000$ ,  $MR = 3.0$ )

<u>Circuit</u>	<u>Surface Area</u> <u>in<sup>2</sup></u>	<u>Flow Rate</u> <u>lbm/sec</u>	<u>Temp. Rise</u> <u>°F</u>	<u>Heat Input</u> <u>Btu/sec</u>	<u>Gas Side</u> <u>Heat Flux*</u> <u>Btu/in<sup>2</sup>-sec</u>
<u>NOZZLE</u>					
1-1	7.69	1.10	53.0	58.3	7.58
1-2	6.56	1.10	45.2	49.7	7.58
1-3	4.19	1.10	30.1	33.1	7.90
2-1	4.32	0.79	49.4	39.0	9.03
2-2	3.89	0.79	52.2	41.2	10.6
2-3	3.46	0.79	55.2	43.6	12.6
3-1	3.03	1.57	29.9	47.0	15.5
3-2	2.60	1.57	32.6	51.2	19.7
3-3	2.17	1.57	26.3	57.1	26.3
4	0.924	0.58	54.5	31.6	34.2
5	0.710	0.61	47.2	28.8	40.6
6	0.554	0.60	43.8	26.3	47.5
7	0.485	0.60	46.2	27.7	57.1
8	0.393	1.15	23.9	27.5	70.0
9	0.308	0.78	32.4	25.3	82.1
10	0.469	1.94	13.9	26.9	57.4
11	0.782	0.67	37.2	24.9	31.8
12-1	1.09	1.05	20.9	21.9	20.1
12-2	1.32	.58	31.6	18.3	13.9
12-3	1.97	.47	41.3	19.4	9.85
<u>8" BARREL</u>					
1-1	5.44	1.47	22.6	33.2	6.10
1-2	13.46	1.47	55.9	82.2	6.10
2	13.46	1.47	55.9	82.2	6.10
3	13.46	1.46	56.3	82.2	6.10
4-2	13.46	1.46	56.3	82.2	6.10
4-1	5.44	1.46	22.7	33.2	6.10
<u>12" BARREL</u>					
1-1	5.44	1.52	21.8	33.2	6.10
1-2	13.46	1.52	54.1	82.2	6.10
2	13.46	1.52	54.1	82.2	6.10
3	11.22	1.18	58.1	68.6	6.10
4	11.22	1.18	58.1	68.6	6.10
5	13.46	1.49	55.2	82.2	6.10
6-2	13.46	1.49	55.2	82.2	6.10
6-1	5.44	1.49	22.3	33.2	6.10

Mean value

#### 4.3, Main Chamber Test Results (cont.)

The final predictive step was to utilize the ATC SINDA channel model to predict the two-dimensional temperature and local flux fields for each circuit with local geometry, and with design gas-side and coolant-side parameters. The results of these individual calculations are given in Table VIII. These predictions showed the BOSF criterion was not met at the throat (Circuits 8 and 9) and that the throat gas-side wall temperature was above the initial criterion of 900°F (755K) but below the revised limit of 1410°F (1038K).

##### 4.3.3.3 Nozzle Test Data and Analyses

Two tests of Test Series RLB6-936 were evaluated in depth for their thermal characteristics: Test 202 was conducted at a  $P_c$  of 980 psia (6.76 MPa) and an MR of 2.72 while Test 203 was conducted at a  $P_c$  of 1510 psia (10.41 MPa) and an MR of 3.04. Calorimetrically-determined nozzle gas-side heat fluxes and measured gas-side wall temperatures are given in Table IX for each nozzle coolant circuit. The flux data are plotted in Figures 39 through 41 and extrapolated to a  $P_c$  of 2000 psia (13.78 MPa) for comparison with the predicted fluxes.

Shown on each plot is a reference line with a slope of 0.8 since the flux was nominally proportional to the 0.8 power of the chamber pressure. The data for the inlet section of the nozzle, Figure 39, was characterized by slopes ranging from 0.89 to 1.13. The single predicted point shown (Circuit N1-1) agreed well with the extrapolation from the lower test pressures.

The high flux convergent section of the nozzle, Figure 40, exhibited interesting data trends. The extrapolation of the Circuit N3-3 data to 2000 psia (13.78 MPa) gave a flux value 30.6 Btu/in.<sup>2</sup>-sec (5.00 kW/cm<sup>2</sup>) of 21 Btu/in.<sup>2</sup>-sec (3.43 kW/cm<sup>2</sup>), considerably less than the predicted flux of 30.6 (5.00) kW/cm<sup>2</sup>. The data for successfully lower area ratio circuits showed a decreasing 2000 psia (13.78 MPa) flux differential until, at an area

TABLE VIII

## CLEAN-WALL PREDICTIONS FOR THE NOZZLE

(Pc = 2000 psia)

Circuit	Gas-Side Wall Temp. °F	Gas-Side Flux (max) Btu/in <sup>2</sup> -sec	Coolant-Side Flux (max) Btu/in <sup>2</sup> -sec	Burnout Flux Btu/in <sup>2</sup> -sec	BOSF	Coolant Velocity ft/sec
N1-1	748	7.66	13.0	25.0	1.92	47.8
N2-3	737	13.9	10.1	26.3	2.60	50.1
N3-1	698	17.5	15.4	33.7	2.19	101
N3-3	914	30.6	27.9	60.4	2.16	132
N4	1043	36.2	38.3	74.4	1.94	153
N5	1092	43.6	38.3	78.2	2.04	160
N6	1193	51.2	46.5	95.1	2.05	195
N7	1371	60.6	58.8	89.2	1.52	188
N8	1337	75.0	65.8	95.7	1.45	226
N9	1353	84.2	90.1	122	1.35	310
N10	1066	71.5	67.1	111	1.65	246
N11	1017	37.9	40.1	87.3	2.18	176
N12-1	594	19.4	15.5	46.6	3.01	92.6
N12-3	612	9.92	16.8	29.6	1.76	60.6



TABLE IX  
NOZZLE TEST DATA

<u>PARAMETER</u>		
TEST <sup>*</sup>	202	203
Time, sec	3	3
Chamber Pressure, psia	980	1510
MR	2.72	3.04
<u>CIRCUIT</u>	<u>GAS-SIDE HEAT FLUX, Btu/in<sup>2</sup>-sec</u>	
N1-1	4.1	6.1
N1-2	3.0	4.7
N1-3	3.6 (292,325) <sup>**</sup>	5.3 (428,472)
N2-1	5.9	9.6
N2-2	1.5	2.4
N2-3	3.5	4.6
N3-1	5.2	8.5
N3-2	7.4 (540)	11.8 (851)
N3-3	12.6	17.2
N4	13.8 (777)	20.5 (1168)
N5	15.6	26.9
N6	16.5	31.2
N7	22.1	40.3
N8	36.0	58.1
N9	41.3	68.3
N10	33.3 (633)	47.3 (922)
N11	11.5	17.1
N12-1	9.3	12.5
N12-2	3.2	5.0
N12-3	2.0	3.2

\* Test Series RLB6-936

\*\* Measured gas-side wall temperatures, °F

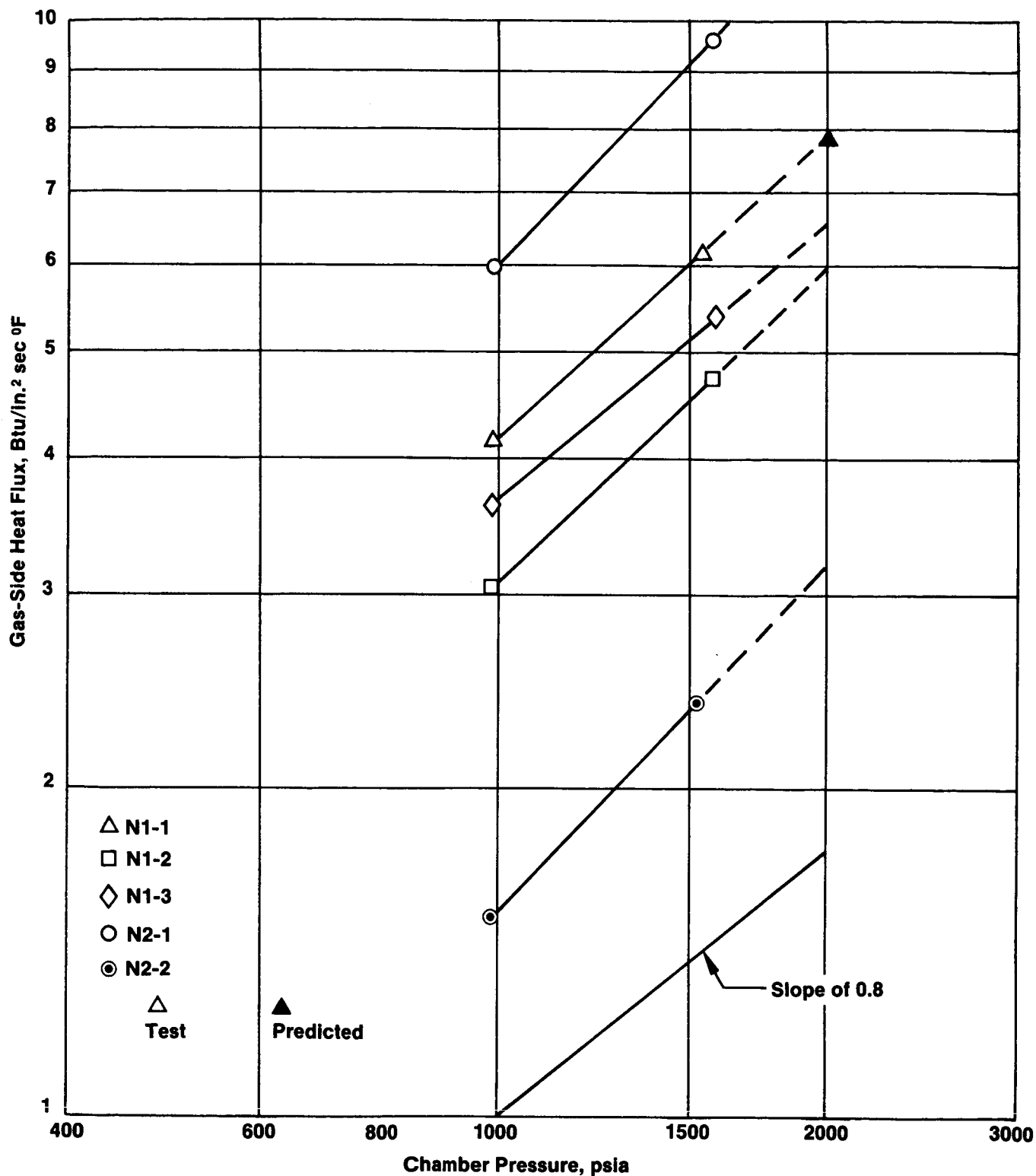


Figure 39. Gas-Side Heat Fluxes as a Function of Chamber Pressure - Inlet Section of Nozzle for LO<sub>2</sub>/RP-1, MR = 3.0

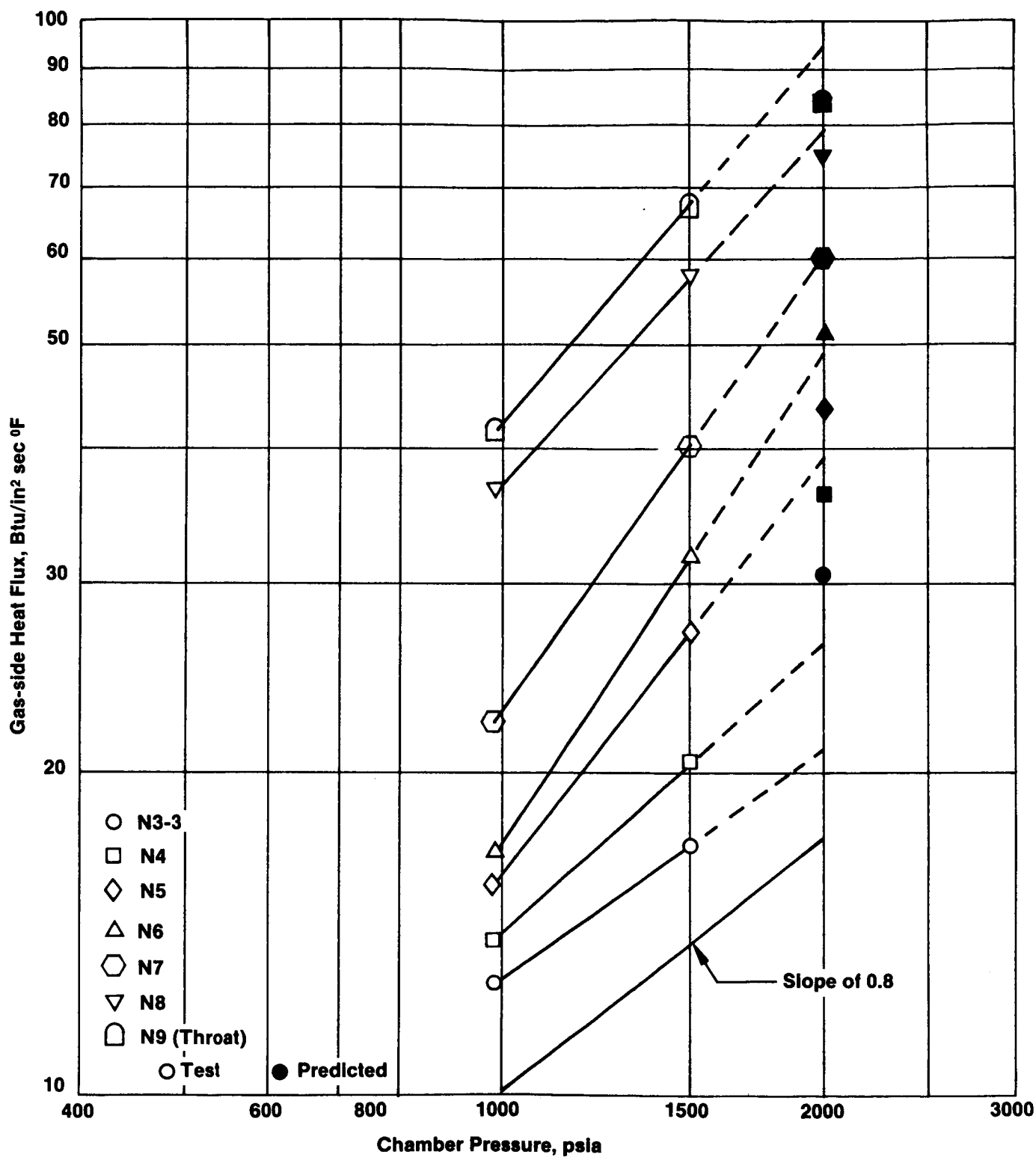


Figure 40. Gas-side Heat Fluxes as a Function of Chamber Pressure - Convergent Section of Nozzle for LO<sub>2</sub>/RP-1, MR = 3.0

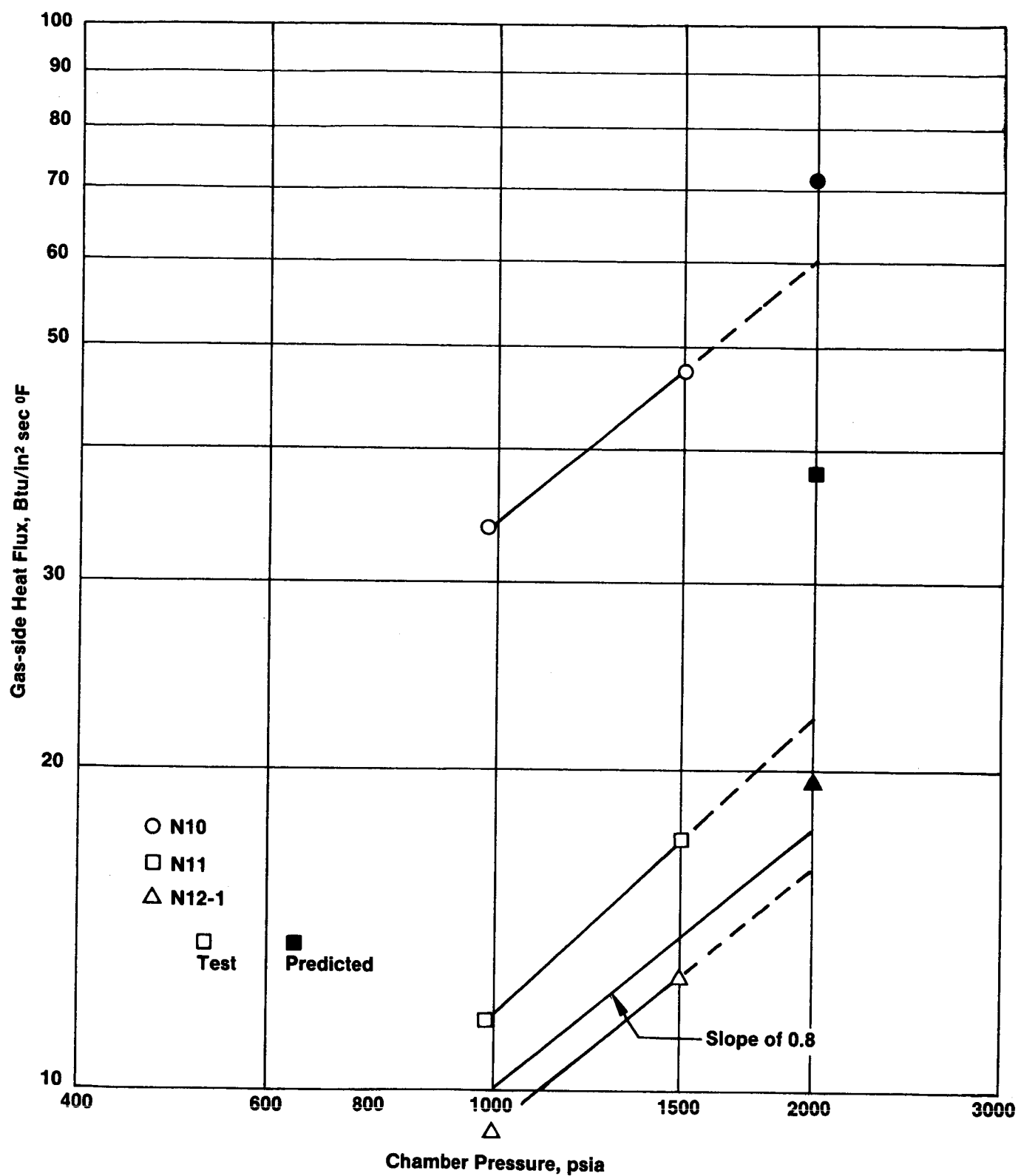


Figure 41. Gas-side Heat Fluxes as a Function of Chamber Pressure - Nozzle Section Downstream of Throat for LO<sub>2</sub>/RP-1, MR = 3.0

#### 4.3, Main Chamber Test Results (cont.)

ratio of 2.64 (Circuit N7), the extrapolated and predicted fluxes are the same. Then, as the throat is approached, the extrapolated 2000 psia (13.78 MPa) fluxes were somewhat greater than the predicted values. This suggests that the  $C_g$  profile of Figure 38 overstates the gas-side coefficient in the nozzle convergent mid-section, resulting in a flux high prediction. (Note: A low value for the experimental gas-side flux due to carbon deposition is discounted based on the clean wall appearance after testing.) Experimental correlation slopes vary from 0.72 (Circuit N3-3) to 1.47 (Circuit N6).

Fluxes for the section downstream of the throat showed similar trends. Predicted fluxes at a  $P_c$  of 2000 psia (13.78 MPa) were greater than those extrapolated; correlation slopes ranged from 0.81 to 0.892, close to the nominal value of 0.8.

Throat (Circuit N9) data from the extrapolation of Figure 40 were input to the SINDA channel model with the appropriate channel geometry and coolant parameters for the prediction of coolant-side fluxes and the burnout safety factor. The results of these analyses are given in Table X. These calculations showed no BOSF margin at a chamber pressure of 2000 psia (13.78 MPa) and a gas-side wall temperature exceeding the relaxed limit of 1410°F (1038K) for zirconium-copper.

##### 4.3.3.4 Calorimetric Barrel Section Test Data and Analysis

Barrel-section calorimetric data for the same tests discussed above were evaluated. The clean-wall gas-side flux was predicted as 6.10 Btu/in.<sup>2</sup>-sec (0.997 kW/cm<sup>2</sup>) for a chamber pressure of 2000 psia (13.78 MPa). Calorimetric test data are presented in Table XI, and are plotted in Figures 42 and 43 for the 8 in. (20.32 cm) and 12 in. (30.48 cm) barrel sections, respectively.

TABLE X

LO<sub>2</sub>/RP-1

CHANNEL MODEL 2-D PREDICTIONS FOR MAXIMUM FLUX NOZZLE LOCATION, MR = 3

Chamber Pressure psia	Coolant		Velocity ft/sec	Heat Fluxes			Max. Gas-Side Wall Temp. °F
	Pressure psia	Temp. °F		Gas-Side Btu/in <sup>2</sup> -sec	Coolant Btu/in <sup>2</sup> -sec	Burnout Btu/in <sup>2</sup> -sec	
1500	900	87	310	67.8	60.8	123.3	1145
1600	900	89	310	73.1	65.7	122.8	1227
1700	900	91	310	78.4	75.2	122.3	1292
1800	900	93	310	83.8	89.0	121.8	1350
1900	900	95	310	89.2	104.4	121.3	1407
2000	900	97	310	94.7	121.0	120.8	1463

CHANNEL	Wall Thickness	=	0.045 in.
	Width	=	0.040 in.
	Depth	=	0.0365 in.
	Land Width	=	0.060 in.
	Closeout Thickness	=	0.050 in.

TABLE XI

LO<sub>2</sub>/RP-1

## BARREL SECTIONS TEST DATA

PARAMETER

Test <sup>*</sup>	202	203
Time, sec.	3.51	3.51
Chamber Pressure, psia	980	1510
MR	2.72	3.04

CIRCUITGAS-SIDE HEAT FLUX, Btu/in<sup>2</sup>-sec

8B1 & 2	4.3 (690) <sup>**</sup>	7.1 (1098)
8B3	3.3 (844)	5.5 (1298)
8B4-2	3.1	4.8
8B4-1	3.7	6.1
12B1-1	4.4	6.2
12B1-2 & 12B2	3.6 (1080)	5.8 (1524)
12B3 & 12B4	2.8	4.7
12B5	2.9 (709)	4.7
12B6-1 & 2	2.8	4.3

\* Test Series RLB6-936

\*\* Measured gas-side wall temperatures, °F

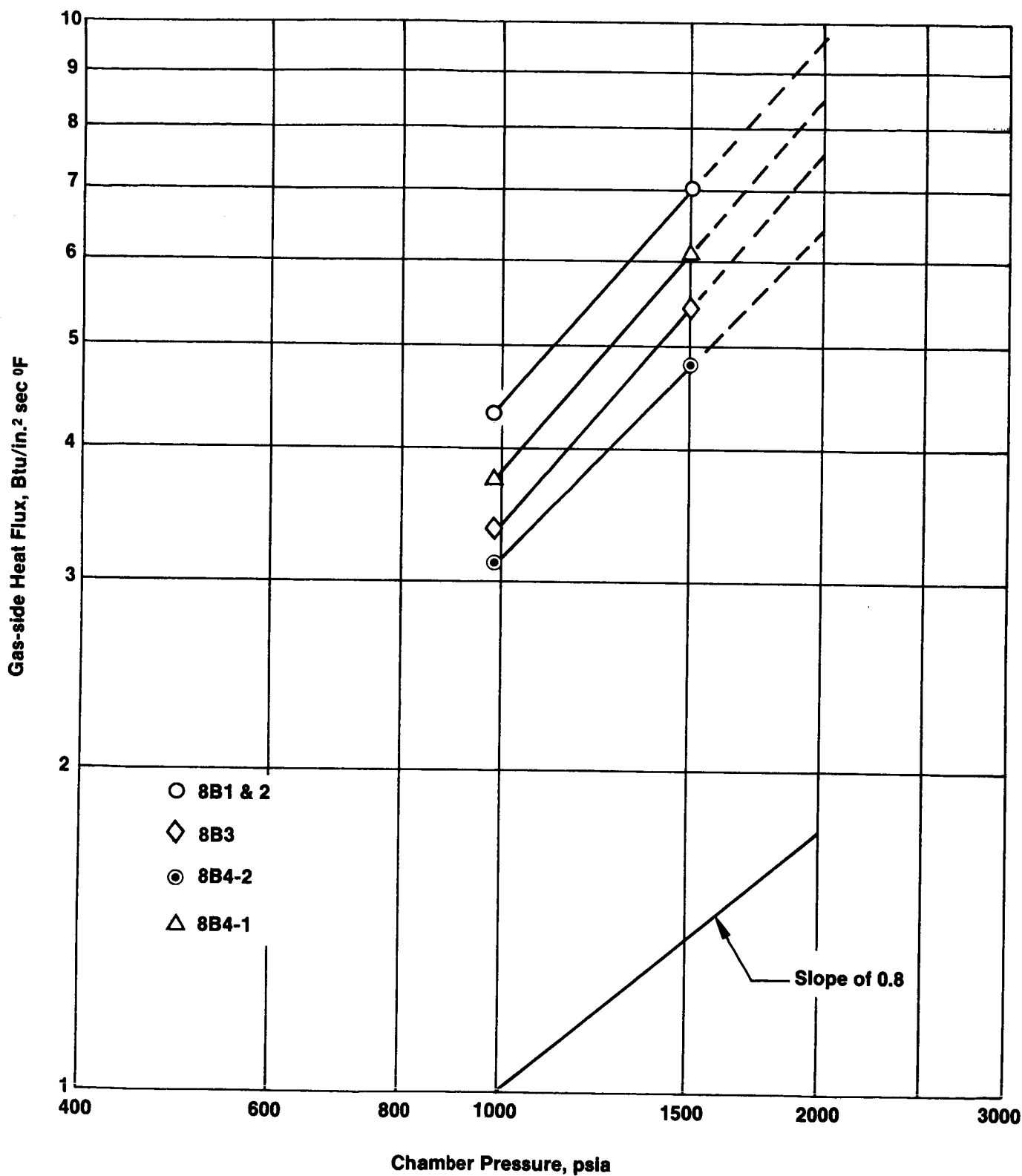


Figure 42. Gas-side Heat Fluxes as a Function of Chamber Pressure - 8 in. Barrel Section for LO<sub>2</sub>/RP-1



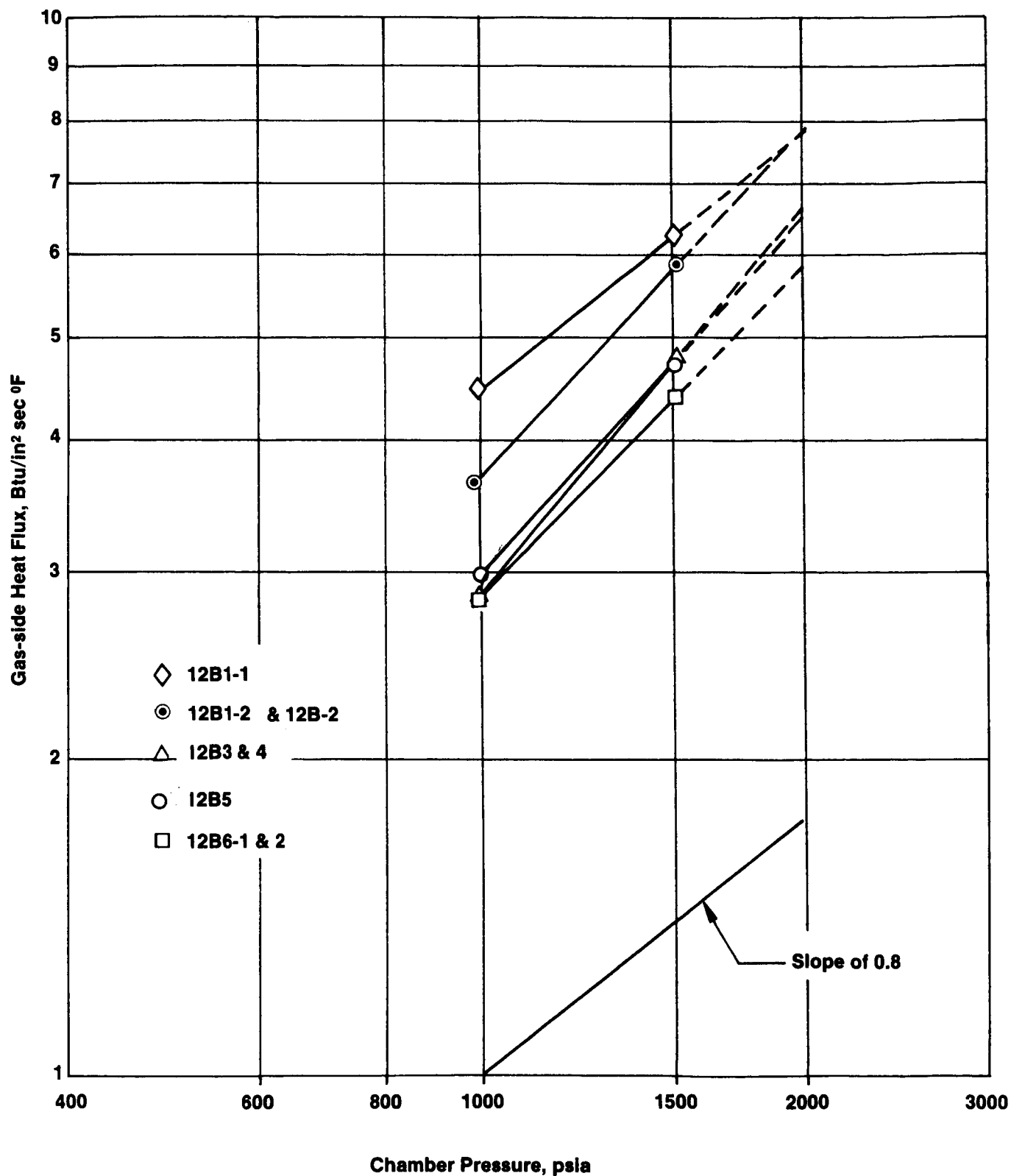


Figure 43. Gas-side Heat Fluxes as a Function of Chamber Pressure - 12 in. Barrel Section for LO<sub>2</sub>/RP-1

#### 4.3, Main Chamber Test Results (cont.)

The data for the upstream 12 in. (30.48 cm) barrel section exhibits slopes greater than 0.8; all data extrapolations to a chamber pressure of 2000 psia (13.78 MPa) except for the 12B6 circuits gave gas-side fluxes ranging from 6.4 to 7.9 Btu/in.<sup>2</sup>-sec (1.05 to 1.29 kW/cm<sup>2</sup>), which are greater than the predicted value of 6.10 Btu/in.<sup>2</sup>-sec (0.997 kW/cm<sup>2</sup>). Slopes for the correlation curves ranged from 0.8 to 1.2. In this case, the C<sub>g</sub> profile appeared to understate the gas-side heat transfer coefficient.

The data for the downstream 8 in. (20.32 cm) barrel section downstream of the turbulence ring showed a greater regularity with correlation slopes ranging from 1.0 to 1.2. Each circuit extrapolation to a P<sub>c</sub> of 2000 psia (13.78 MPa) resulted in a gas-side flux greater than that predicted; extrapolated fluxes ranged from 6.4 to 7.9 Btu/in.<sup>2</sup>-sec (1.05 to 1.58 kW/cm<sup>2</sup>). The comment above relative to the C<sub>g</sub> profile applied here also.

Inspection of the data shown in Figure 43 for the 8 in. (20.32 cm) barrel section suggested a correlation of gas-side flux with axial distance. Flux as a function of location and chamber pressure is shown in Figure 44, indicating boundary layer development following the trip at the turbulence ring between the two barrel sections. Also shown is the axial flux profile as extrapolated to a chamber pressure of 2000 psia (13.78 MPa) in Figure 43.

The SINDA channel model was utilized to predict thermal parameters for the pressure region between the maximum test pressure (1510 psia) (10.41 MPa) and the design pressure of 2000 psia (13.78 MPa). The results of these calculations are given in Table XII, the burnout safety factor and maximum gas-side wall temperature are shown as a function of P<sub>c</sub> in Figure 45. The BOSF for the barrel was less than 1.0 at chamber pressures above 1785 psia (12.31 MPa) while the throat value for this parameter equaled 1.0 at a P<sub>c</sub> of 2000 psia (13.78 MPa).

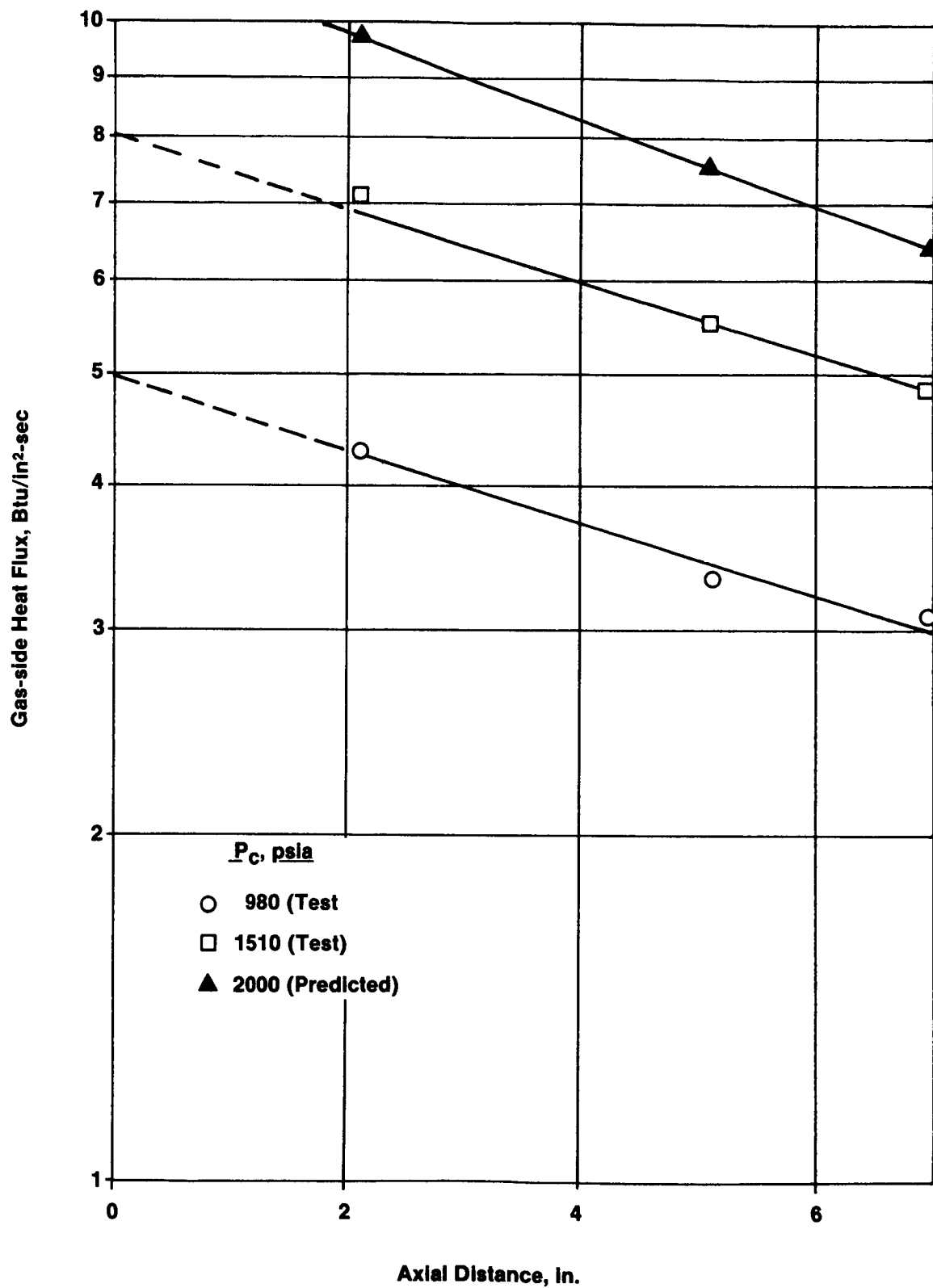
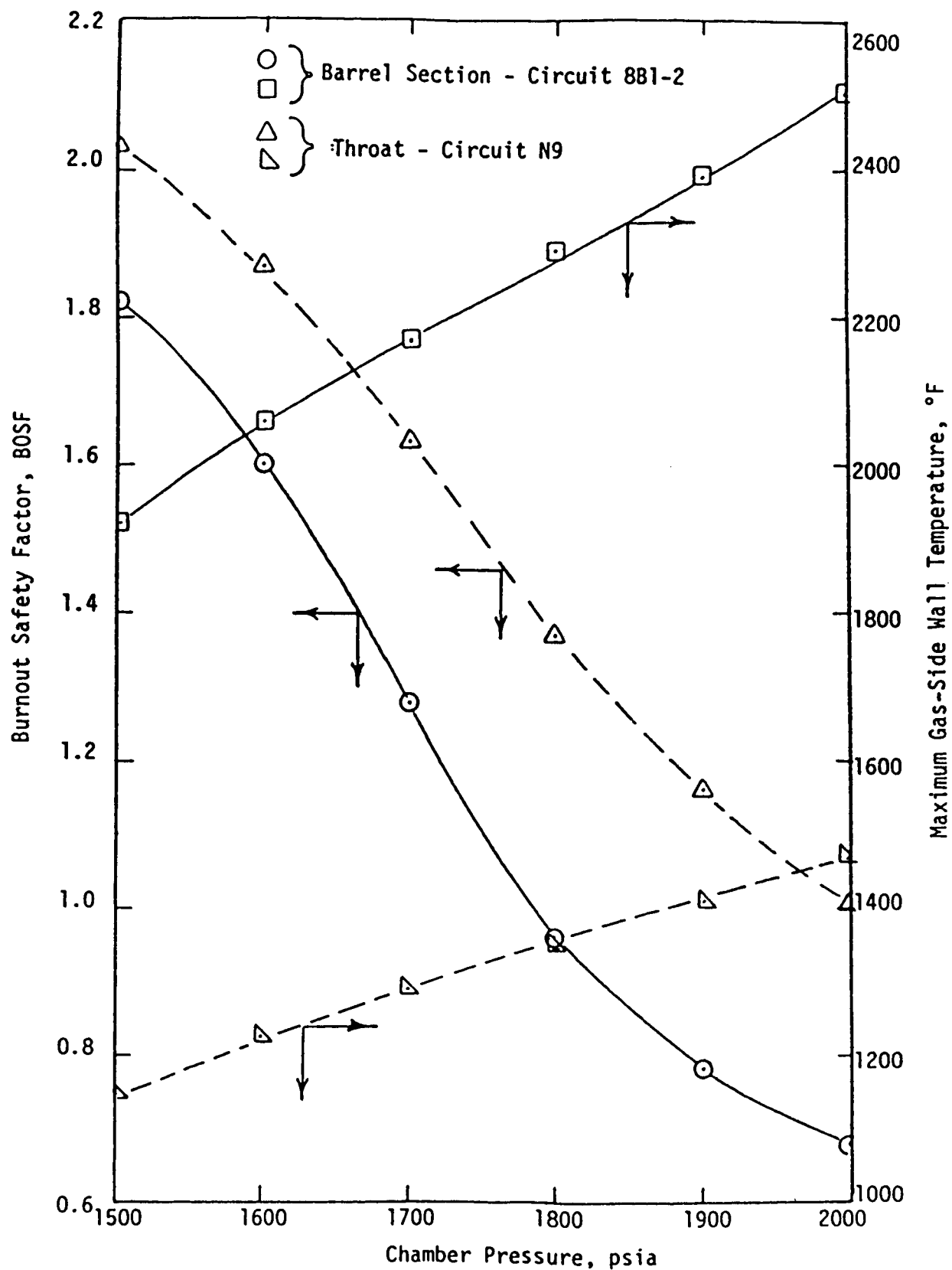


Figure 44. Axial Variation in Gas-side Heat Flux - 8 in. Barrel Section for LO<sub>2</sub>/RP-1

TABLE XII

LO<sub>2</sub>/RP-1CHANNEL MODEL 2-D PREDICTIONS FOR THE 8-IN BARREL SECTION  
(SYSTEM AS ORIFICED)

Circuit	Chamber Pressure psia	Pressure psia	Temp. °F	Velocity ft/sec	Gas-Side Btu/in <sup>2</sup> -sec	Coolant Btu/in <sup>2</sup> -sec	Burnout Btu/in <sup>2</sup> -sec	BOSF	Max. Gas-Side Wall Temp. °F
881	1500	1470	162	30.9	7.8	9.1	16.6	1.82	1916
	1600	1470	170	31.0	8.5	10.2	16.4	1.60	2059
	1700	1470	178	31.1	9.1	13.1	16.2	1.24	2166
	1800	1470	187	31.2	9.8	16.7	16.0	0.96	2289
	1900	1470	195	31.3	10.4	19.9	15.8	0.79	2392
	2000	1470	204	31.4	11.1	23.1	15.6	0.68	2511
882	1500	1450	219	31.6	6.8	8.3	15.2	1.83	1708
	1600	1450	232	31.8	7.3	9.0	14.9	1.66	1813
	1700	1450	244	32.0	7.8	9.7	14.6	1.50	1918
	1800	1450	258	32.2	8.4	10.8	14.3	1.32	2044
	1900	1450	271	32.4	8.9	13.9	14.0	1.01	2136
	2000	1450	284	32.6	9.5	18.0	13.7	0.76	2244



**Figure 45. Predicted Burnout Safety Factor and Maximum Gas-side Wall Temperature as a Function of Chamber Pressure - Coolant Flow Rates for Test Orificing**

#### 4.3, Main Chamber Test Results (cont.)

The as-tested throat channel geometry and coolant flow rates resulted in a maximum gas-side temperature greater than 1410°F (1038K) at a chamber pressure of 1900 psia (13.10 MPa), while for the nickel barrel, wall temperatures ranged from 1916 to 1511°F (1320 to 1650K).

SINDA channel analyses were then performed in which circuit flow control orificing was changed to increase the coolant flow rates. A chamber pressure of 1750 psia (12.06 MPa) was selected and the thermal parameters for barrel circuits 8B1-2 and 8B4-1 were calculated for increased circuit flow rates of 110, 120 and 130%. The results of these calculations are given in Table XIII, and the parameters of Figure 45 are replotted in Figure 46. The increased coolant flow resulted in significantly higher BOSF values and was somewhat less effective in reducing wall temperatures.

##### 4.3.3.5 Experimental Cg Profile

The test data obtained in thirteen tests for chamber pressures ranging from 981 psia (6.76 MPa) to 1540 psia (10.62 MPa) and for mixture ratios varying from 2.05 to 4.16 were analyzed to develop an experimental Cg profile. The pertinent data for these tests are given in Table XIV. Note that four tests with fuel film cooling were included to ascertain the possible effect of a fuel-rich boundary layer.

The maximum throat gas-side heat flux measured was 59.3 Btu/in.<sup>2</sup>-sec (9.69 kW/cm<sup>2</sup>) at a chamber pressure of 1530 psia (10.55 MPa) and a mixture ratio of 3.20 (Test 213). The effect of mixture ratio on the gas-side flux is shown in Figure 47 for tests at chamber pressures from 1470 to 1540 psia (10.13 to 10.62 MPa). These data were for tests both with and without fuel film cooling.

TABLE XIII

CHANNEL MODEL 2-D PREDICTIONS FOR THE 8-IN BARREL SECTION  
(UPRATED ORIFICING)

Circuit	Chamber Pressure psia	Orifice Factor	Pressure psia	Temp. °F	Velocity ft/sec	Gas-Side Btu/in <sup>2</sup> -sec	Coolant Btu/in <sup>2</sup> -sec	Burnout Btu/in <sup>2</sup> -sec	BOSF	Max. Gas-Side Wall Temp. °F
881-2	1750	1.0	1540	183	31.1	9.4	14.6	16.1	1.10	2219
		1.1	1540	172	34.2	9.4	12.5	17.5	1.40	2209
		1.2	1540	163	37.0	9.4	11.4	18.7	1.64	2196
		1.3	1540	155	40.1	9.4	11.5	20.1	1.75	2177
884-1	1750	1.0	1540	92	49.3	7.2	19.6	26.4	1.35	2062
		1.1	1540	89	54.4	7.2	17.5	28.7	1.64	2053
		1.2	1540	87	59.1	7.2	15.7	30.8	1.96	2046
		1.3	1540	85	64.1	7.2	14.6	33.1	2.27	2035

NOTE: Coolant Inlet Temperature = 60°F

Gas-Side Heat Flux Extrapolated From Test Data

CHANNEL	Circuit 881-2	Circuit 884-1
Wall Thickness, in.	0.150	0.100
Width, in.	0.156	0.156
Depth, in.	0.060	0.110
Land Width, in.	0.144	0.400
Closeout Thickness, in.	0.050	0.050

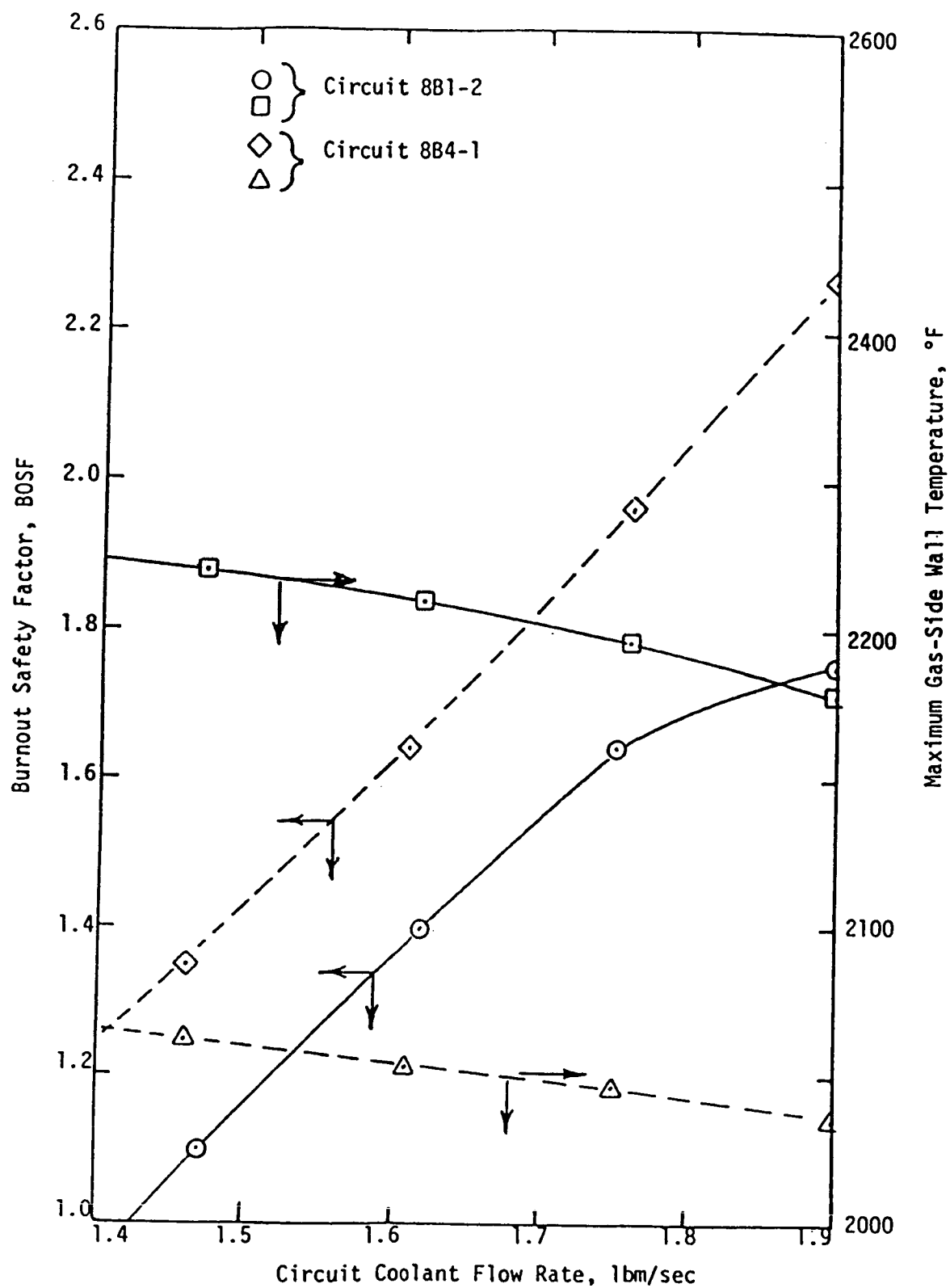


**Figure 46. Predicted Burnout Safety Factor and Maximum Gas-side Wall Temperature as a Function of Coolant Flow Rate - Barrel at Chamber Pressure of 1750 psia**



TABLE XIV

## SUMMARY OF TEST-DERIVED GAS-SIDE HEAT FLUX DATA

Test No.	Pc psia	MR	Duration	Gas-Side Heat Flux, Btu/in <sup>2</sup> -sec					
				12B3,4 Z=5.8	8B4-1 Z=8.3	N3 $\epsilon_c=6.5$	N4 $\epsilon_c=3.3$	N9 tht	N11 $\epsilon_c=2.3$
202	981	2.68	3.1	2.7	4.1	6.6	11.2	28.1	9.9
203	1510	3.05	3.1	4.5	6.4	10.6	18.2	56.0	16.1
204	1480	2.08	3.1	3.2	4.7	8.0	15.1	43.3	12.3
206	1530	4.16	3.1	4.8	6.6	10.7	19.2	52.0	18.7
213	1530	3.20	16.2	5.1	7.8	12.5	18.9	59.3	18.2
214	1490	3.05	34.2	4.9	7.5	12.0	22.5	56.5	17.3
215	1470	2.05	39.6	3.2	5.1	9.0	14.4	39.6	11.0
221	980	2.15	3.6	2.4	3.0	5.6	8.5	21.6	7.6
222	1030	2.35	24.2	2.9	4.1	7.3	11.4	32.9	9.3
223	1500	2.19	3.1	4.3	3.7	8.1	13.3	42.8	11.9
224	1540	2.50	24.2	4.2	4.9	11.2	17.8	51.3	14.7
225	1500	2.80	3.6	3.2	5.2	10.3	14.2	51.4	14.3
226	1510	2.62	10.2	3.2	5.5	10.6	14.9	49.5	13.6

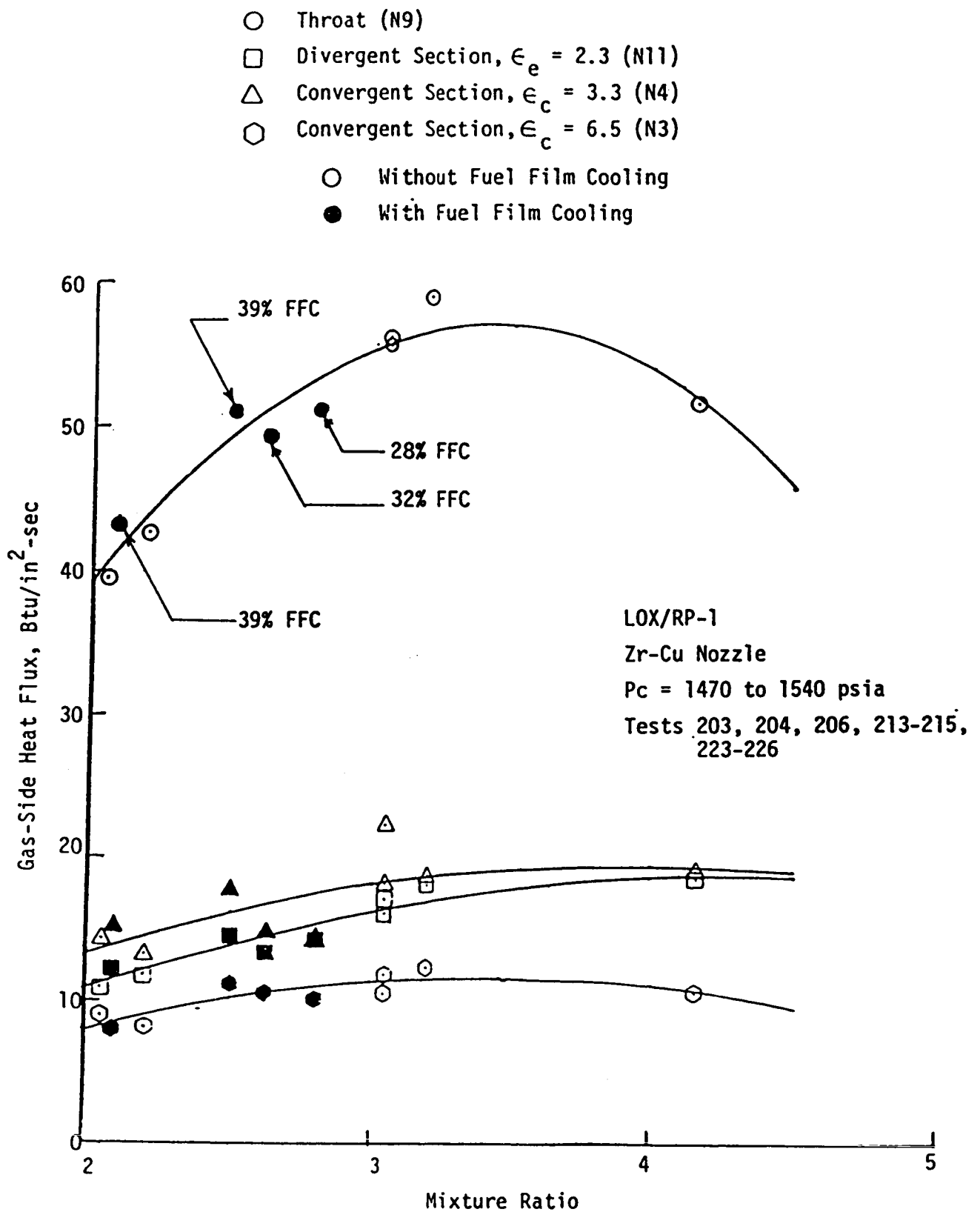


Figure 47. Nozzle Gas-side Heat Flux as a Function of Mixture Ratio and Nozzle Area Ratio

#### 4.3, Main Chamber Test Results (cont.)

It is immediately apparent that, for the test hardware employed, there was no effect of fuel film cooling on nozzle gas-side heat fluxes. This was attributed to the large L/D characterizing the main chamber and to a high level of turbulent mixing.

Only the throat station showed an appreciable effect of mixture ratio upon the gas-side flux. The curve given resulted from a polynomial regression fit to the data; the maximum flux of 57.3 Btu/in.<sup>2</sup>-sec (9.37 kW/cm<sup>2</sup>) occurred at mixture ratios of 3.4 to 3.5. Data from both the convergent and divergent sections showed a much flatter variation with mixture ratio.

The effect of both chamber pressure and mixture ratio upon experimentally-derived C<sub>g</sub> profiles is shown in Figure 48. At a high chamber pressure (~ 1500 psia) (~ 10.34 MPa) an increase in mixture ratio from 2 to 3 resulted in a large increase in C<sub>g</sub> for the barrel sections (~50%) and a slightly smaller increase (~44%) at the nozzle throat. For MR values of about 2.1, an increase in P<sub>c</sub> from 980 to 1420 psia (6.76 to 9.79 MPa) was not significant in enhancing the C<sub>g</sub> profile in the first barrel section but has an effect downstream of the turbulence ring. Nozzle data showed a P<sub>c</sub> effect upstream of the throat which disappeared in the divergent section.

The design C<sub>g</sub> profile (Figure 49) gave a normalized C<sub>g</sub> value of 1.47 for the cylindrical barrel sections. The test data for the aft end of the 12 in. (30.48 cm) section at a P<sub>c</sub> of 1490 psia (10.27 MPa) and an MR of 3.05 gave a C<sub>g,n</sub> of 1.40. The C<sub>g</sub> at the aft end of the 8 in. (20.32 cm) barrel section was 1.0. Since an increase in chamber pressure has been shown to result in a higher C<sub>g</sub> profile, it is apparent that the profile for a P<sub>c</sub> of 2000 psia (13.78 MPa) would show C<sub>g</sub> values significantly greater than the design value. This is in agreement with the conclusion made in Section 4.3.3.4.

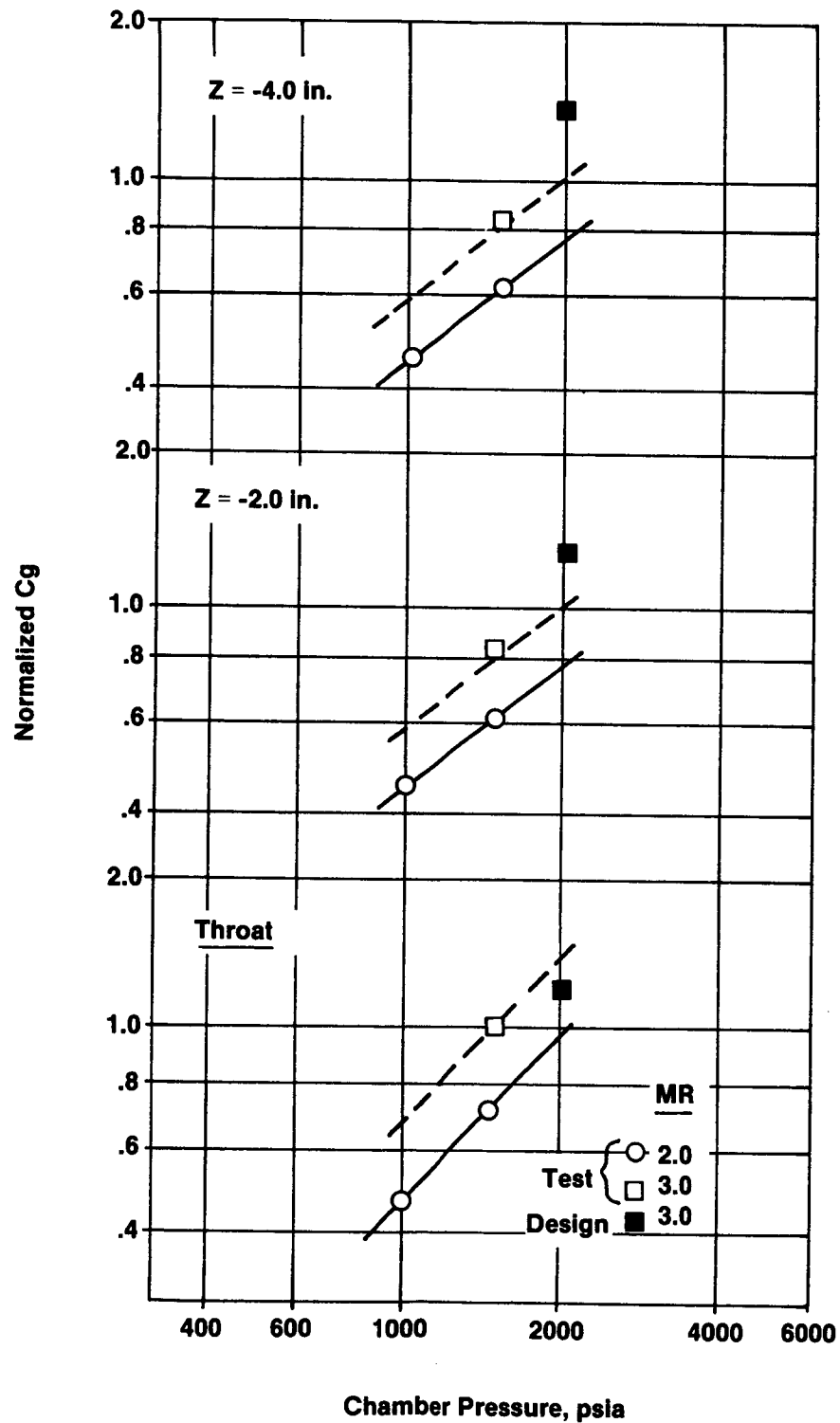


Figure 48. Comparison of Test-derived and Design  $C_g$  Values in the Nozzle

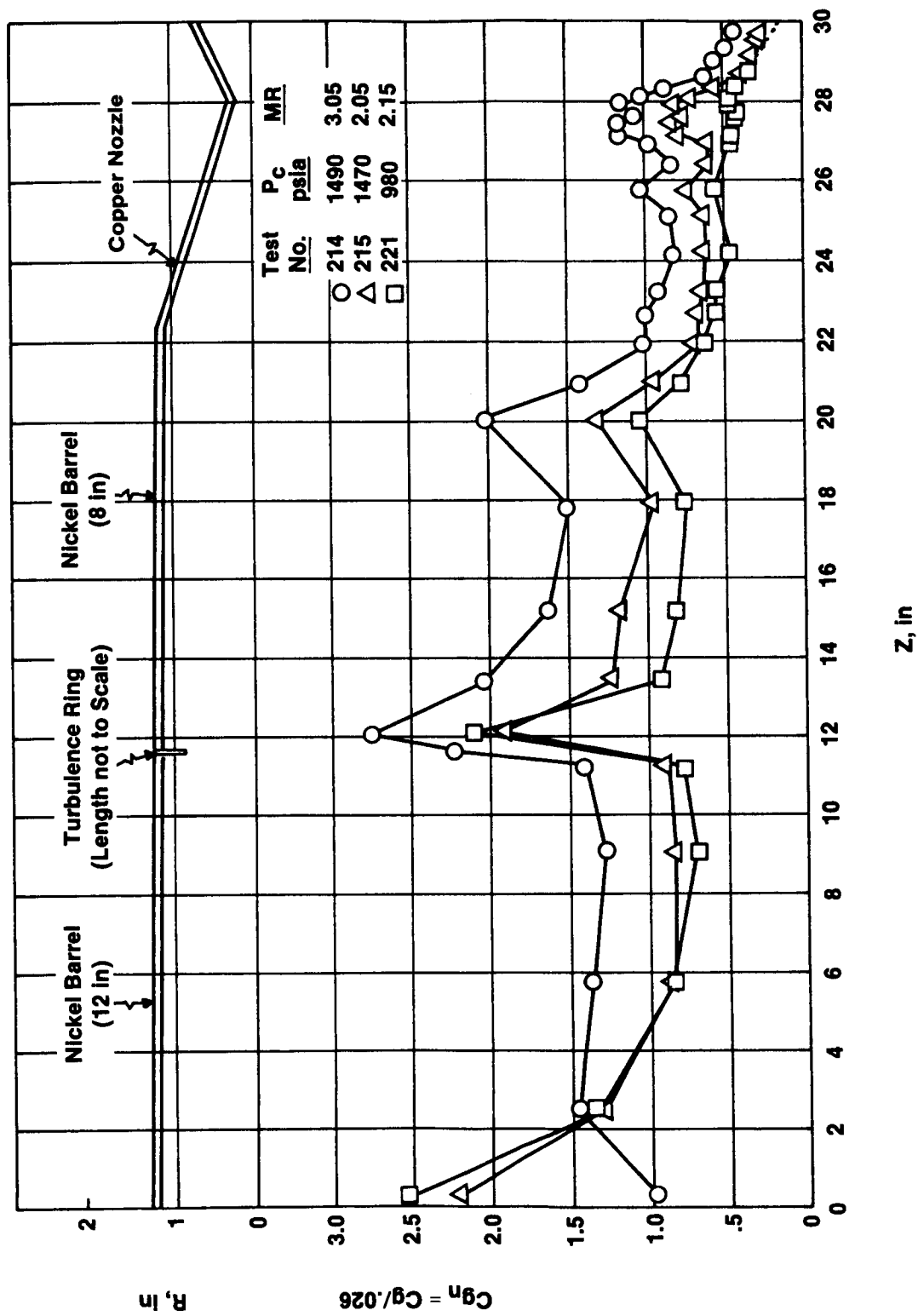


Figure 49. Experimental  $C_g$  Profile for the Carbon Deposition Main Chamber

## 4.0, Technical Discussion (cont.)

### 4.4 GAS GENERATOR TEST RESULTS

#### 4.4.1 Test Summary

A summary of the entire gas generator test program is shown in Table XV. The number of tests, operating ranges and cumulative test durations with RP-1, propane and  $\text{CH}_4$  fuels are listed therein. Detailed summaries of the RP-1, propane and methane test series are given in Tables XVI, XVII, XVIII, and XIX. The test durations (100 to 200 sec) covered the nominal mission duty cycle requirements for booster engines (160 sec). The chamber pressure range tested was 720 to 1650 psia (4.96 to 11.38 MPa), and the mixture ratios tested covered the range of interest for state-of-the-art high pressure turbine technology; i.e., 1300 to 1600°F (977 to 1144K) gas. A total of 55 tests were performed. Data scatter due to variability in test conditions was reduced by accumulating approximately 2000 seconds of test time for each propellant combination using a single hardware configuration, giving a total of 6832 seconds of burn time.

Ignition was reliable and smooth once the start sequence was tailored for each fuel. The ignition startup sequence, as indicated by the pressure rise in the inlet manifold, for each propellant combination was as follows:

- 25 msec fuel lead for  $\text{LO}_2$ /RP-1
- 15 msec fuel lead for  $\text{LO}_2$ /propane
- 15 msec ox lead for  $\text{LO}_2$ /methane

#### 4.4.2 Gas Temperature

All three hydrocarbon fuels (RP-1, propane, and methane) tested with  $\text{LO}_2$  at fuel-rich gas generator mixture ratios exhibited increasing gas temperature with increasing gas generator mixture ratios as shown in

TABLE XV  
1984-1986 GAS GENERATOR TEST PROGRAM

<u>Fuel</u>	<u>No. Tests</u>	<u>Pc Range (psia)</u>	<u>MR Range</u>	<u>Temperature Range (°F)</u>	<u>Total Duration (sec)</u>
LO <sub>2</sub> /RP-1	33	720-1650	0.20-0.58	820-1525	2542
LO <sub>2</sub> /Propane	12	820-1560	0.26-0.44	1175-1860	2310
LO <sub>2</sub> /Methane	<u>10</u>	750-1580	0.21-0.60	580-1640	<u>1980</u>
	55				6832

TABLE XVI

## 1984 RP-1 CARBON DEPOSITION PREBURNER DATA TEST SUMMARY

TEST NO.	DATE	DURATION (SEC)	P <sub>C</sub> (PSIA)	MR	W <sub>t</sub> (lbm/sec)	C* (fps)	COMMENTS
RLB-936-113	2/24/84	-	-	-	-	-	Test aborted. Sequence error.
114	2/24/84	100.0	950	0.35	2.2	2500	Very little build-up on turbine simulator.
115	2/24/84	100.0	1040	0.55	1.4	3900	Significant build-up on turbine simulator. Photos taken and turbine simulator cleaned.
116	2/29/84	-	-	-	-	-	Test aborted. LOX TCV (thrust chamber valve) did not open.
117	2/29/84	100.0	990	0.26	2.75	2100	Very little build-up on turbine simulator.
118	2/29/84	5.0	1000	0.26	-	-	No test to test build-up. Photos taken and turbine simulator and nozzle cleaned.
119	2/29/84	100.0	1500	0.38	3.2	2900	Some build-up on turbine simulator.
120	2/29/84	15.0	1490	0.85	4.34	1990	No test to test build-up. LOX bleed valve left open. Cleaned nozzle but not turbine simulator.
121	2/29/84	100.0	1590	0.57	2.3	3800	Rapid turbine simulator build-up.
122	2/29/84	24.0	1530	0.93	1.88	4380	Some turbine simulator build-up. Photos taken and turbine simulator and nozzle cleaned. Slight melting/erosion of downstream side of turbine simulator noted.
123	3/01/84	-	-	-	-	-	Test aborted. Sequence error.
124	3/01/84	18.0	745	0.35	1.71	2650	Test aborted. False indication of high coolant outlet temperature.
125	31/01/84	100.0	745	0.33	1.63	2600	Very little build-up on turbine simulator. Cleaned nozzle but not turbine simulator.
126	3/01/84	100.0	710	0.23	2.1	1950	No turbine simulator build-up.
127	3/01/84	8.0	1020	0.73	1.37	3900	Some turbine simulator build-up.
128	3/01/84	8.0	1060	1.20	1.28	4500	Some turbine simulator build-up. Photos taken and turbine simulator and nozzle cleaned. Significant melting/erosion of downstream side of turbine simulator.
129	3/2/84	100.0	1515	0.37	3.25	2800	Very little build-up on turbine simulator.
130	3/2/84	100.0	1490	0.38	3.25	2750	Very little build-up on turbine simulator. No test to test build-up
131	3/2/84	100.0	1480	0.39	3.25	2750	Very little build-up on turbine simulator. Photos taken. No test to test build-up



TABLE XVII

## 1985 RP-1 CARBON DEPOSITION PREBURNER TEST HISTORY

TEST NO.	DATE	DURATION (SEC)	P <sub>C</sub> (PSIA)	MR	W <sub>t</sub> (lbm/sec)	C* (fps)	Hardware setup	Exit Nozzle	Turbine Simulator	COMMENTS
2427-936-A6-105	10/22/85	1.0	1000	0.35	-	-	1	-1	Cooled	Checkout.
106	10/22/85	3.0	1000	0.35	-	-	1	-1	Cooled	Checkout.
107	10/22/85	10.0	1000	0.35	-	-	1	-1	Cooled	Checkout.
Test series I										
113	10/23/85	100.0	1000	0.35	2.20	2850	1	-1	Cooled	Photo taken of downstream L' and Exit Nozzle.
115	10/23/85	100.0	1000	0.30	2.55	2350	1	-1	Cooled	
116	10/23/85	100.0	1000	0.25	2.90	2100	1	-1	Cooled	D <sub>t</sub> = .4975 in after test
118	10/23/85	100.0	1000	0.20	3.22	1900	1	-1	Cooled	
119	10/23/85	100.0	1000	0.40	1.88	3150	1	-1	Cooled	
120	10/23/85	100.0	750	0.24	2.20	1900	1	-1	Cooled	Before test D <sub>t</sub> = .4912 in.
121	10/23/85	100.0	750	0.28	1.95	2150	1	-1	Cooled	
122	10/23/85	100.0	750	0.32	1.80	2250	1	-1	Cooled	
139	11/07/85	100.0	1500	0.35	1.56	3100	1	-3	Cooled	Nozzle change. Photo taken of Turbine sim.
140	11/07/85	100.0	1500	0.29	1.88	2550	1	-3	Cooled	
141	11/07/85	100.0	1500	0.24	1.92	2500	1	-3	Cooled	
144	11/18/85	100.0	1500	0.37	3.20	3050	1	-1	Cooled	Pop on Start-up
Test series II										
145-148	11/18/85	10.0	-	-	-	-	1	-1	Cooled	Checkout tests.
149	11/18/85	100.0	1500	0.34	3.00	2900	1	-1	Cooled	Fuel rich Shutdown.
150	11/18/85	100.0	1500	0.35	2.95	2475	1	-1	Cooled	Fuel rich Shutdown.
151	11/18/85	100.0	1500	0.35	2.95	3000	1	-1	Cooled	Fuel rich Shutdown.
152	11/19/85	100.0	1500	0.35	2.80	2900	1	-1	Cooled	Water flow to Turbine simulator turned off.
153	11/19/85	73.1	1500	0.34	2.80	3000	1	-1	Cooled	High Pc kill. Water to Turbine simulator turned off.
154	11/19/85	74.8	1500	0.34	2.80	2900	1	-1	Cooled	High Pc kill. Water to Turbine simulator turned off.
155	11/19/85	95.0	1000	0.36	1.80	3100	1	-1	Cooled	High Pc kill. Water to Turbine simulator turned off. Photo taken of hardware.
Test series III										
156	11/19/85	200.0	1500	0.35	1.55	2900	2	-1	-4	New hardware configuration. Subsonic testing with 3D turbine simulator.
157	11/19/85	200.0	1500	0.31	1.80	2575	2	-1	-4	Subsonic testing with 3D Turbine simulator.
158	11/19/85	200.0	1500	0.25	2.10	2150	2	-1	-4	Subsonic testing with 3D Turbine simulator.
160	11/19/85	119.0	1500	0.34	3.30	-	3	None	-4	Sonic testing with 3D Turbine simulator. High Pc kill. Photo taken of hardware.

TABLE XVIII

## 1986 LOX/PROPANE TEST HISTORY

TEST NO.	DATE	DURATION (SEC)	P <sub>C</sub> (PSIA)	MR	$\dot{W}_t$ (lbm/sec)	C* (fps)	COMMENTS
2427-229-A6-101-107	5/21/86	-	-	-	-	-	Checkout tests. First hot fire attempt did not achieve ignition. Checkout, $A_E = .1832 \text{ in}^2$
109*	5/23/86	-	960	0.30	-	-	
113	5/29/86	200.0	1036	0.26	2.04	2950	
114	5/29/86	200.0	1085	0.35	1.90	3360	
120	5/29/86	200.0	1219	0.44	1.59	4000	After test $A_E = .1833 \text{ in}^2$
125	6/9/86	200.0	1020	0.29	1.95	3130	Dark plume observed.
126	6/10/86	200.0	1081	0.41	1.50	4050	
128	6/10/86	200.0	873	0.39	1.17	3690	
129	6/10/86	200.0	868	0.33	1.43	3130	
130	6/10/86	200.0	820	0.34	1.30	3320	Turbine simulator leaked at end of test.
131**	6/19/86	200.0	1473	0.29	1.55	3060	
132**	6/19/86	200.0	1484	0.33	1.40	3360	
133**	6/19/86	200.0	1497	0.38	1.17	3850	Dark plume observed.
134	6/19/86	200.0	1561	0.39	2.05	3850	Turbine simulator leaked at 110 seconds into the run. Dark plume observed.

NOTES : \* Duration on the checkout test was 1 second. All other tests were 200 seconds.  
 \*\* - 3 exit nozzle was used on these three tests. All other tests used the -1 exit nozzle.  
 A five percent area reduction at the throat was experienced after test 120.  
 $A_E$  = area of the exit nozzle.

TABLE XIX

## 1986 LOX/METHANE TEST HISTORY

TEST NO.	DATE	DURATION (SEC)	P <sub>C</sub> (PSIA)	MR	$\dot{W}_t$ (lbm/sec)	C* (ps)	COMMENTS
2427-229-A6-135-136	7/24/86	-	-	-	-	-	Checkout tests, Ignition not achieved.
137	7/24/86	2.5	1018	0.358	-	-	Ignition achieved with a 15 msec or lead.
138	7/30/86	200.0	1110	0.39	1.59	3900	Turbine simulator leaked at end of test.
139	7/30/86	180.0	1073	0.23	1.82	3310	Duration = 180 sec. High temp shut-down.
140	7/30/86	200.0	1077	0.265	1.77	3280	At t = 40 sec fuel pressure increased.
141	7/30/86	200.0	935	0.31	1.44	3650	Injector plugged.
142	8/18/86	-	1046	0.59	-	-	Checkout.
143	8/18/86	200.0	1098	0.54	1.51	3830	Calibration error during run. Previous Kwox used.
144	8/18/86	200.0	1080	0.55	1.47	3840	Fuel tank pressure increased at t = 20 sec.
149	8/18/86	200.0	775	0.22	1.49	2790	
151	8/18/86	200.0	788	0.50	1.12	3580	
152	8/18/86	200.0	773	0.33	1.27	3180	Minor turbine simulator leak detected.
153	8/19/86	200.0	1500	0.58	2.15	3790	Turbine simulator leaked.

NOTES: Duration on the checkout test was 2.5 second. All other tests were 200 seconds in duration except where noted.

-1 exit nozzle was used on all LOX/Methane tests.

#### 4.4, Gas Generator Test Results (cont.)

Figures 50, 51, and 52, respectively. The higher mixture ratio increased the available bipropellant combustion enthalpy, which in turn increased the resultant fuel-rich combustion product gas temperature.

The  $\text{LO}_2/\text{RP-1}$  gas temperatures shown in Figure 50 are substantially (as much as  $700^\circ\text{F}$  ( $644\text{K}$ ) lower than the standardized JANNAF ODE combustion model prediction. However, it is closely predicted (within  $\pm 100^\circ\text{F}$  ( $311\text{K}$ ) by the Fuel Rich Combustion Model (FRCM) which will be described in greater detail in subsection 4.5.3. The FRCM was developed by Aerojet for NASA/LeRC Contract NAS 3-21753, Reference 1. The FRCM was developed specifically for RP-1 rich gas generator/preburner operation but was not developed to account for either propane or methane combustion performance. A secondary chamber pressure effect upon gas temperature is also evident at low mixture ratios.

The  $\text{LO}_2/\text{propane}$  temperature data shown in Figure 51 start out 21% lower than ODE predictions in a trend similar to the  $\text{LO}_2/\text{RP-1}$  data but exhibit a discontinuous step increase from lower than ODE prediction to higher than ODE prediction above 0.38 mixture ratio. The chamber pressure effect is almost negligible except for the two data points at 0.40 mixture ratio which appear to be affected by kinetics differences.

The  $\text{LO}_2/\text{methane}$  gas generator combustion temperatures range from 62% to 100% of the ODE performance model prediction as shown in Figure 52.

##### 4.4.3 C\* Performance

The C\* performance for the gas generator test series was calculated using the equation:

$$C^* = \frac{(\text{PCTSD}) A_t g_c}{\dot{w}_t},$$

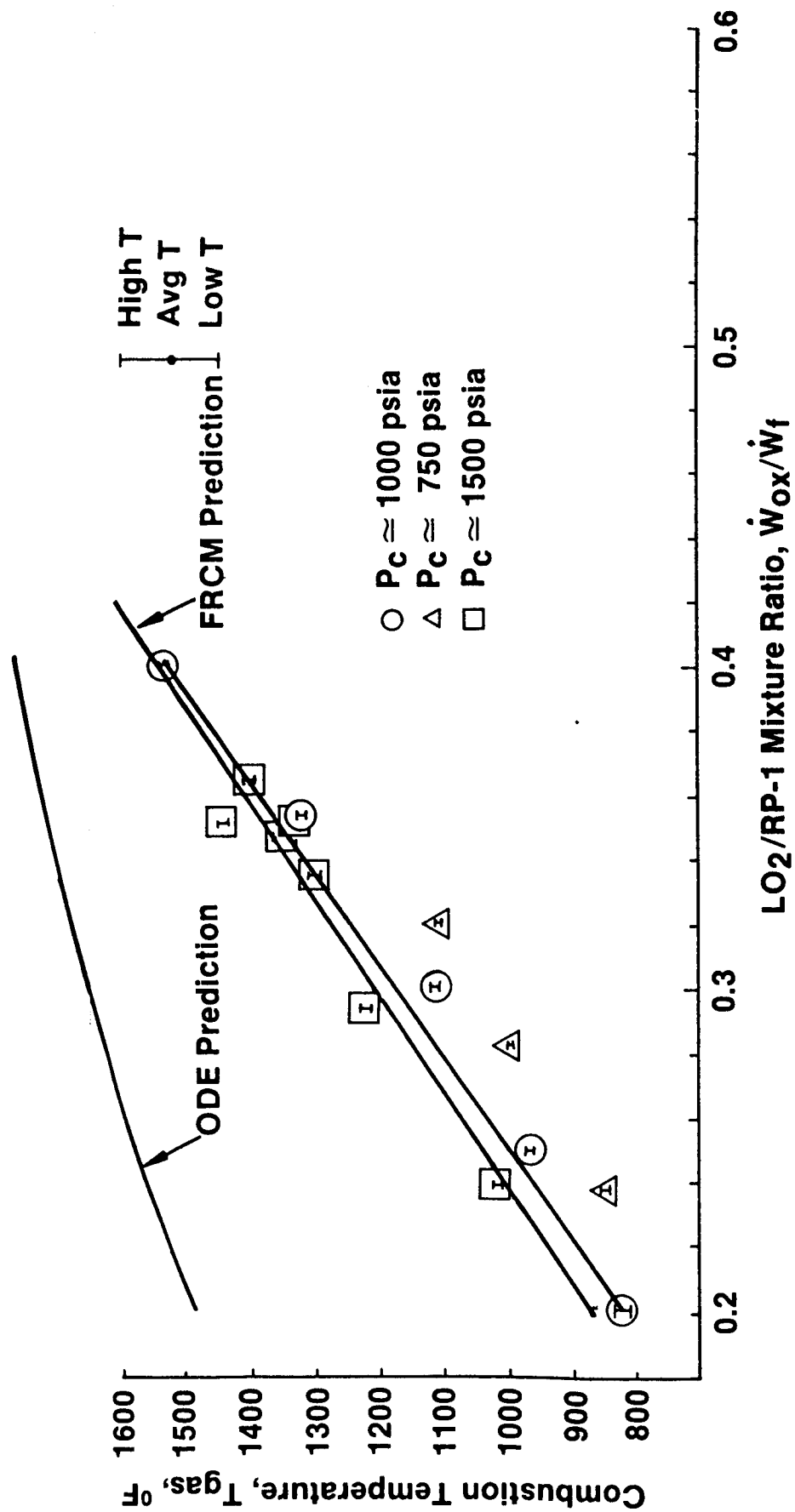


Figure 50. Gas Temperature for LO<sub>2</sub>/RP-1

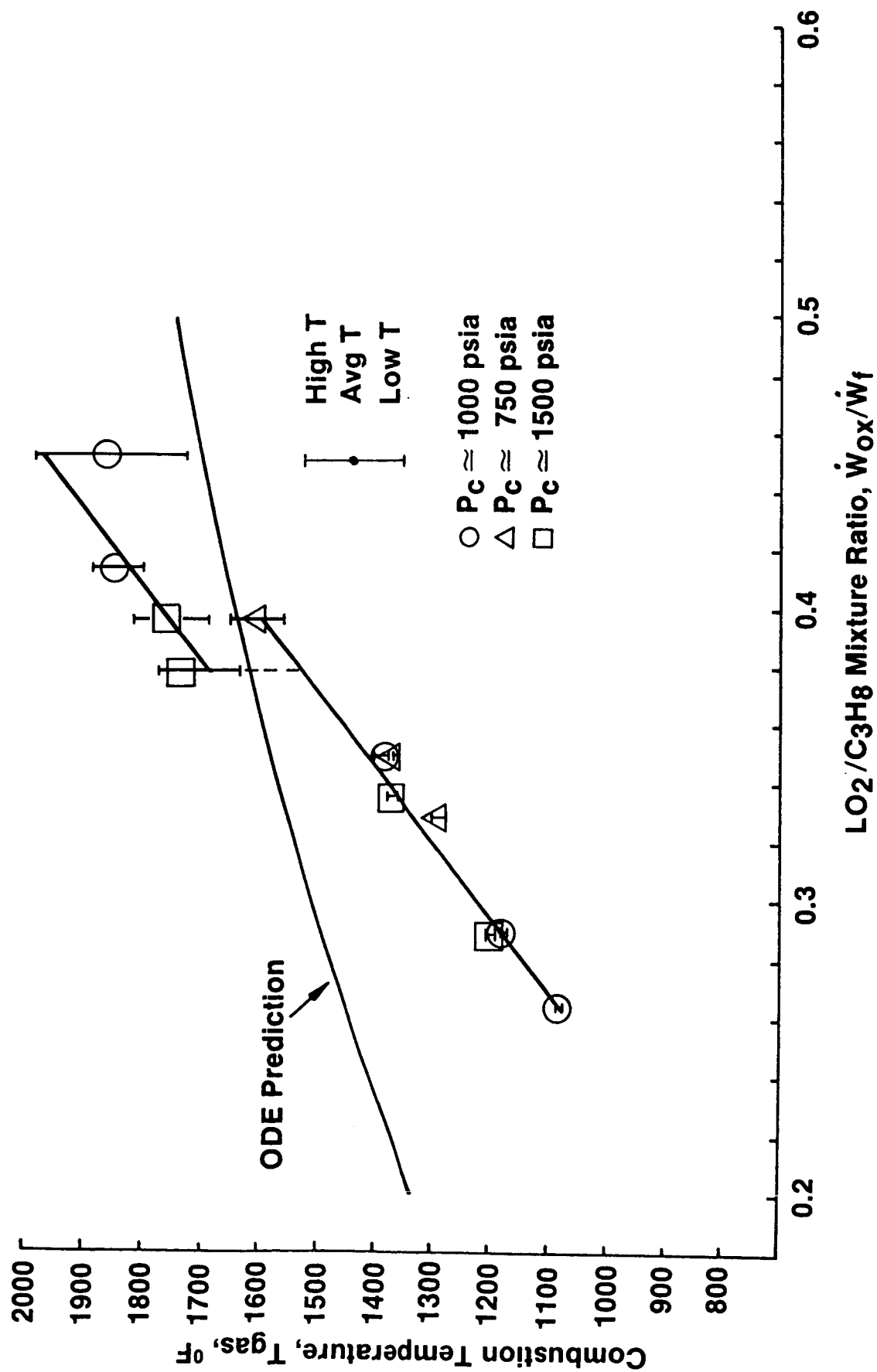


Figure 51. Gas Temperatures for  $\text{LO}_2/\text{Propane}$

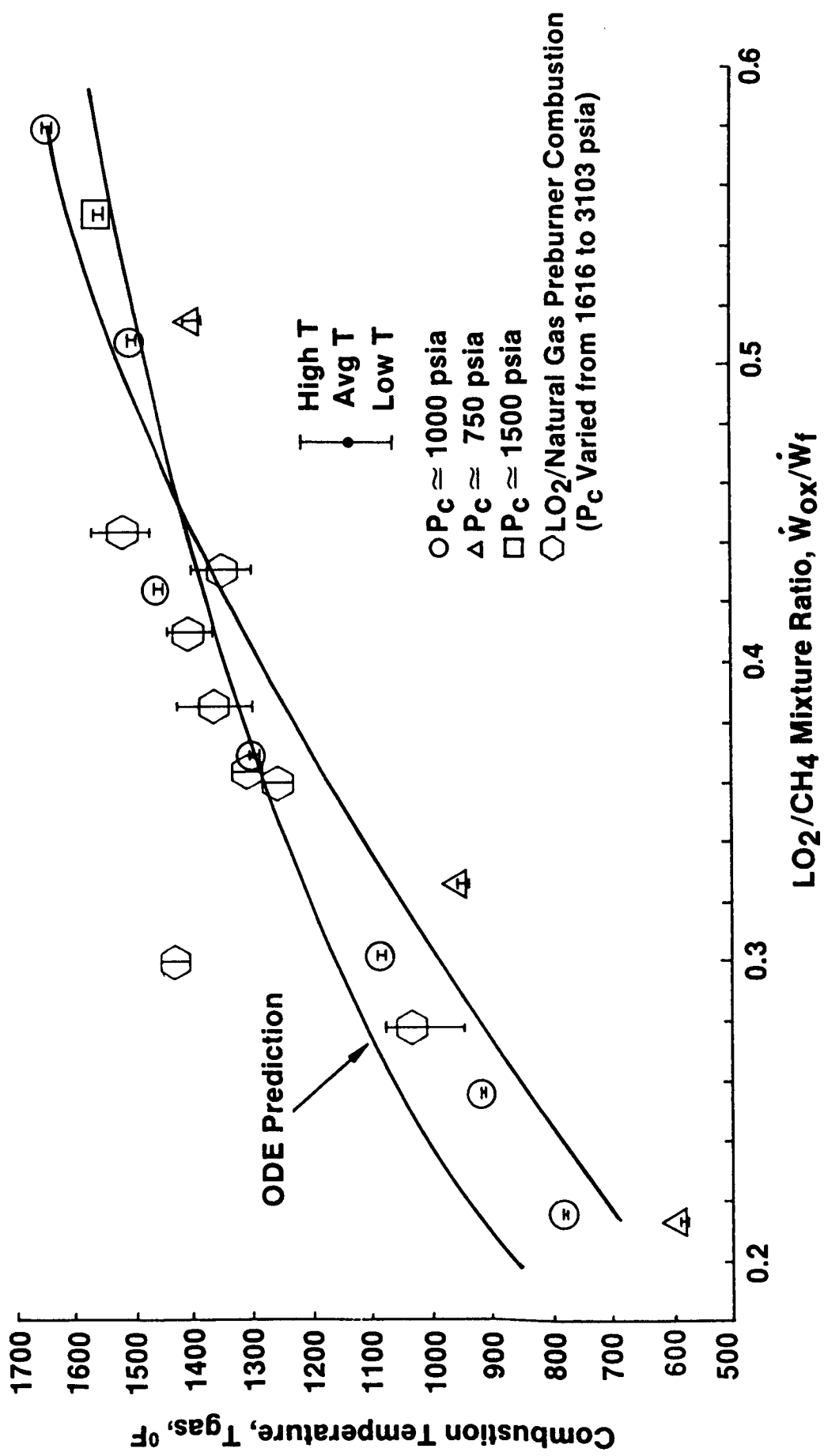


Figure 52. Gas Temperatures for LO<sub>2</sub>/Methane

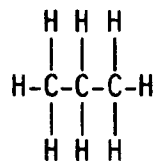
#### 4.4, Gas Generator Test Results (cont.)

where PCTSD is the stagnation chamber pressure downstream of the turbine simulator. The theoretical  $C^*$  predictions were made using the ODE computer program.  $C^*$  predictions, for RP-1 only, were also made using the FRCM.

The measure  $C^*$  data for the gas generator tests are summarized in Tables XVI, XVII, XVIII, and XIX. These  $C^*$  data are compared to the ODE and FRCM (RP-1 only) theoretical predictions in Figures 53, 54 and 55. These figures show that the  $C^*$  performance has little pressure dependence over the  $P_c$  range of 750 to 1500 psia (5.17 to 10.34 MPa). The mixture ratio appears to have the largest effect on  $C^*$  performance, increasing  $C^*$  by 1000 fps (30480 cm/sec) with an increase of only 0.2 to 0.3 in mixture ratio.

As shown in Figure 53, the FRCM predicts  $C^*$  efficiency of  $LO_2$ /RP-1 at low mixture ratios within 10%. The FRCM predicts the effect of kinetically limited fuel decomposition reactions on the  $C^*$  performance of RP-1 rich gas generators. The  $C^*$  performance is much lower than the predicted ODE  $C^*$  performance because the oxidizer is the limiting reagent which means that most of the fuel is going through the chamber unoxidized.

Propane, on the other hand, shows a distinct step in the  $C^*$  curve which is not predicted by ODE (Figure 54). This step is also seen in the gas temperature versus mixture ratio plot for propane in Figure 51. A possible mechanism for this is as follows. The propane molecule has the form





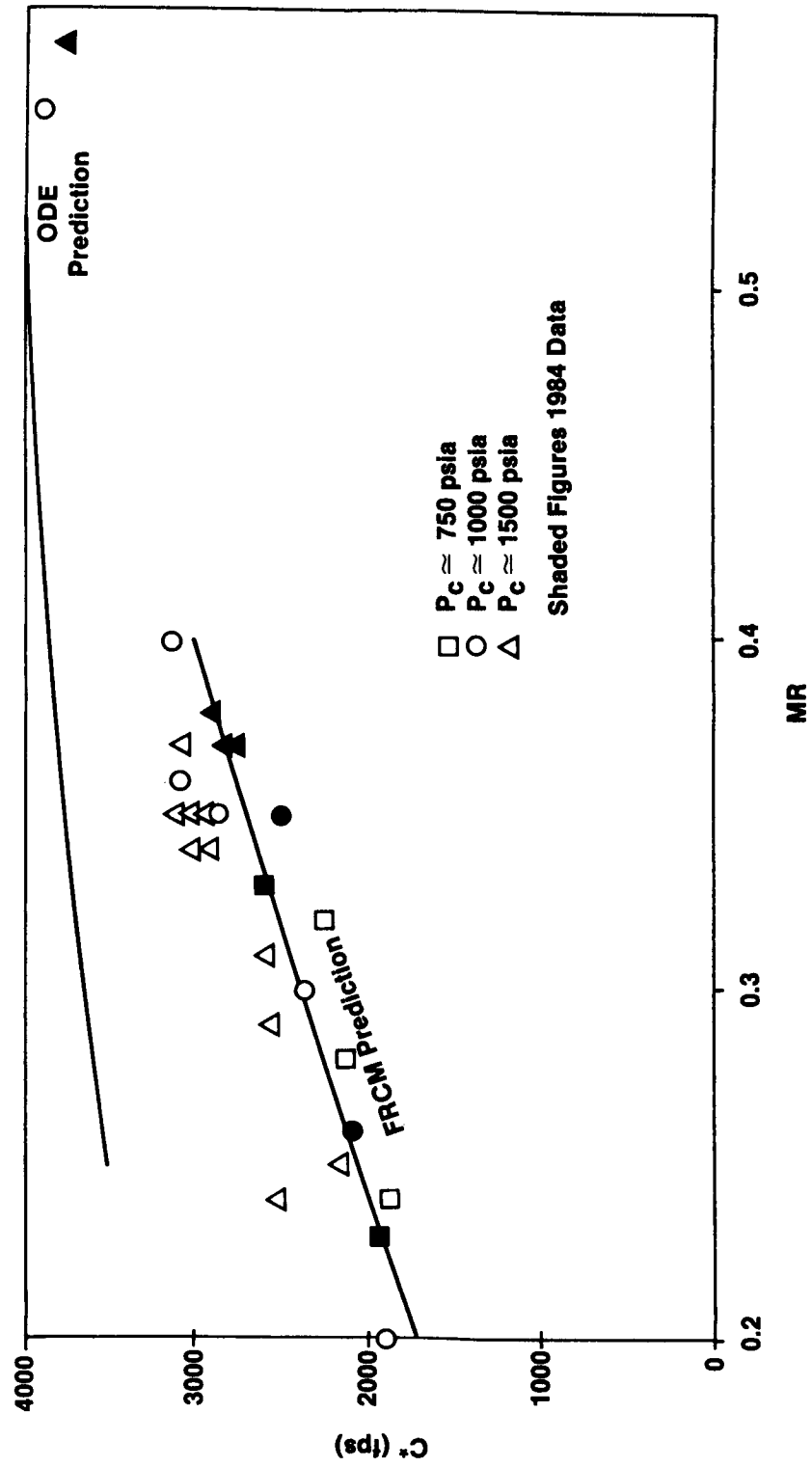


Figure 53.  $C^*$  Performance for  $LO_2/RP-1$

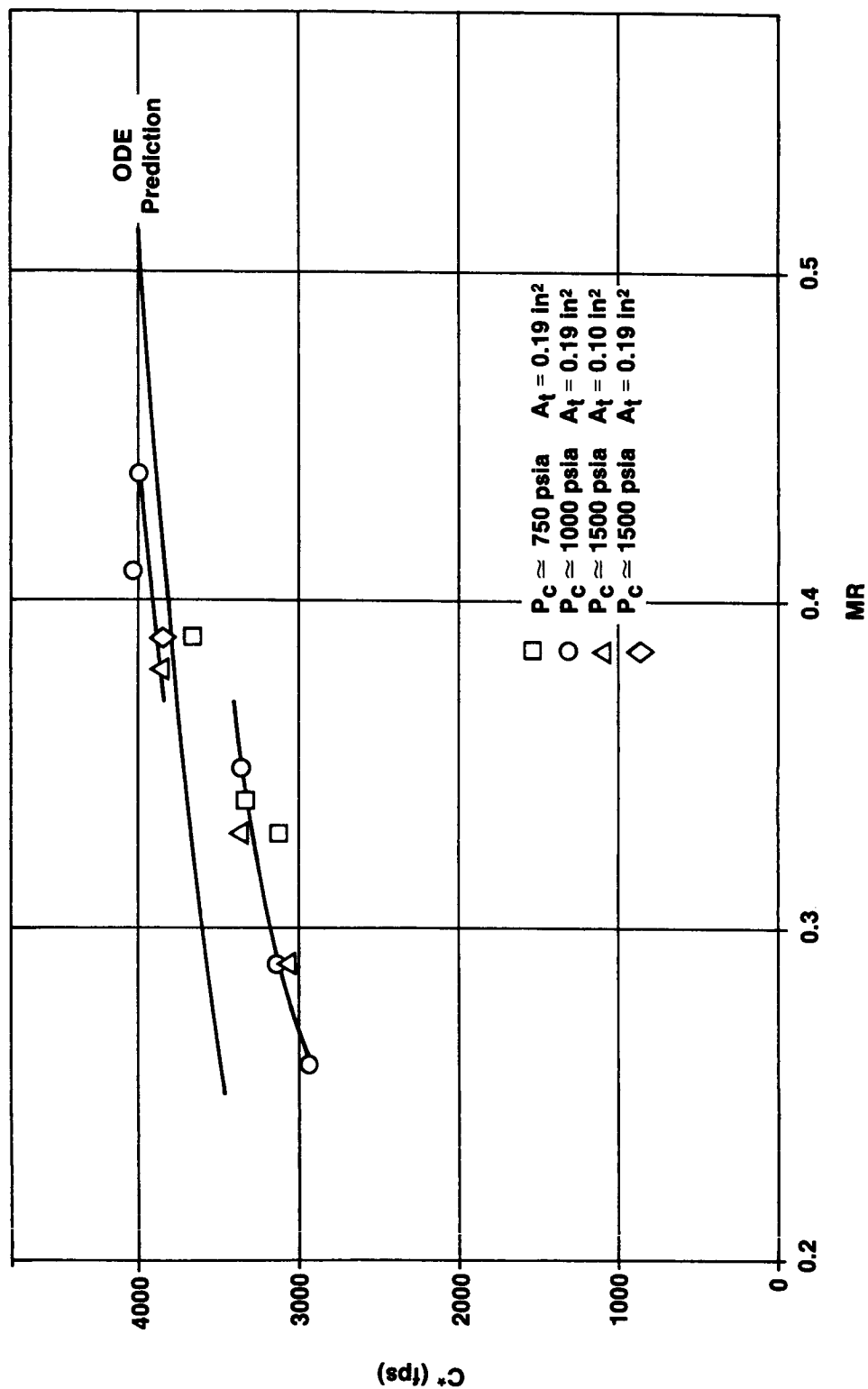


Figure 54.  $C^*$  Performance for LO<sub>2</sub>/Propane

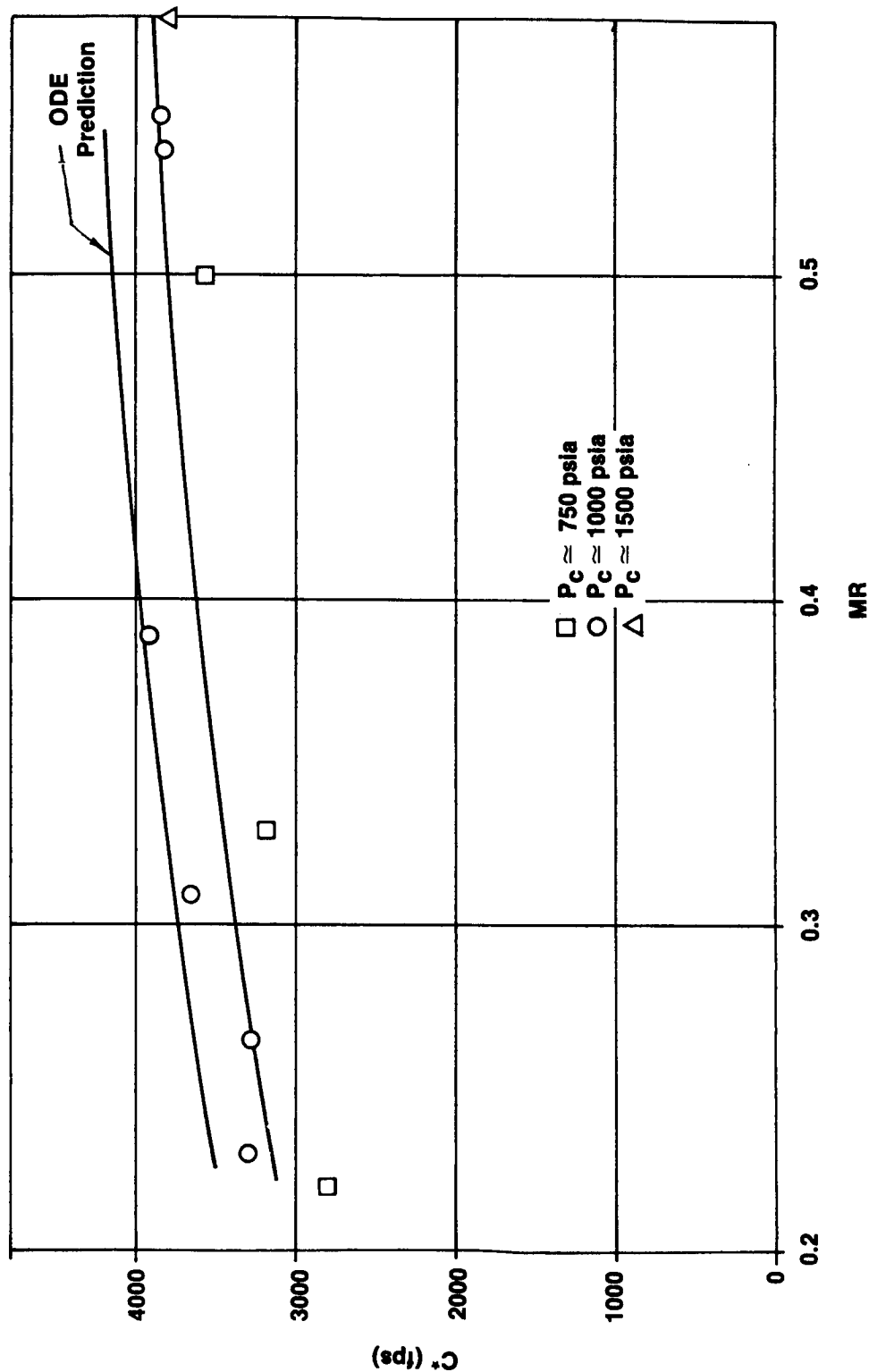
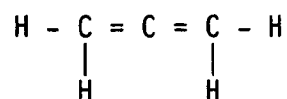


Figure 55.  $C^*$  Performance for  $\text{LO}_2/\text{Methane}$

#### 4.4, Gas Generator Test Results (cont.)

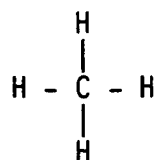
The secondary hydrogens, which are connected to the center carbon, are much more easily removed from the carbon chain. Once they are removed, a double bond would form between the carbon atoms which releases two more hydrogen atoms as H<sub>2</sub> gas. The molecule would now have the following configuration.



The next bonds to break would either be the C-H bonds or the C=C double bonds. If the temperature were high enough, the C=C bonds would break, which would give a large step increase in the energy of the system. This step increase could manifest itself as a C\* step or a gas temperature step. Further research into the mechanism of propane decomposition should be made to verify this hypothesized mechanism.

The reason why RP-1 did not exhibit as abrupt a step increase in C\* or temperature may be because RP-1 has a longer carbon chain, and many other single bonds would break before any double bonds. It is theorized that if the gas temperature were raised high enough, the C\* step for RP-1 would also occur. Historical F-1 gas generator data shows that just such a step occurs around 1550 to 1600°F (1116 to 1144K).

The C\* plot in Figure 55 for methane shows that this hydrocarbon gives C\* performances within 10% of the ODE predictions. This is probably due to the simple nature of the this molecule:



The only bond energy required is the energy to break C-H bonds, which is relatively low compared to double bond dissociation energies. Furthermore, methane might also undergo a C\* step if it were tested at gas temperatures above 1600°F (1144K) (see Figure 52).

## 4.4, Gas Generator Test Results (cont.)

### 4.4.4 Carbon Deposition

Four mutually complementary methods were used to detect carbon deposition at gas generator conditions:

- Visible (black) particulate laden exhaust plume
- Gas temperature and C\* operation on the high performance step
- Unusually rapid increase in turbine simulator pressure drop
- Post test hardware disassembly and physical observation of carbon deposition

The most graphic way to characterize carbon deposition was by observation of the turbine simulator tubes during hardware teardown. The hardware was routinely disassembled after an indication of a large increase in pressure drop across the turbine simulator during a single test. Figures 56, 57 and 58 show actual carbon buildup on the tubes for each fuel. Figure 56 shows the buildup of carbon for LO<sub>2</sub>/RP-1. The carbon was soft and easily removed. The center of the turbine simulator trapped small cylindrical carbon particles. These particles were assumed to have been built up around the fuel injection streams during the test and subsequently dislodged upon shutdown by the postfire gaseous purge. Figure 57 shows the carbon buildup for LO<sub>2</sub>/propane. The deposits formed hard lumps, and would shatter when cut. The deposits became progressively harder and buildup rate increased with increasing chamber pressure and mixture ratios. Figure 58 shows the condition of the turbine simulator after six 200-second tests with LO<sub>2</sub>/methane. The hardware was coated with carbon but the deposits did not build up on the tubes.

ORIGINAL PAGE IS  
OF POOR QUALITY



Figure 56. Carbon Buildup with LO<sub>2</sub>/RP-1



Figure 57. Carbon Buildup with LO<sub>2</sub>/Propane



ORIGINAL PAGE IS  
OF POOR QUALITY

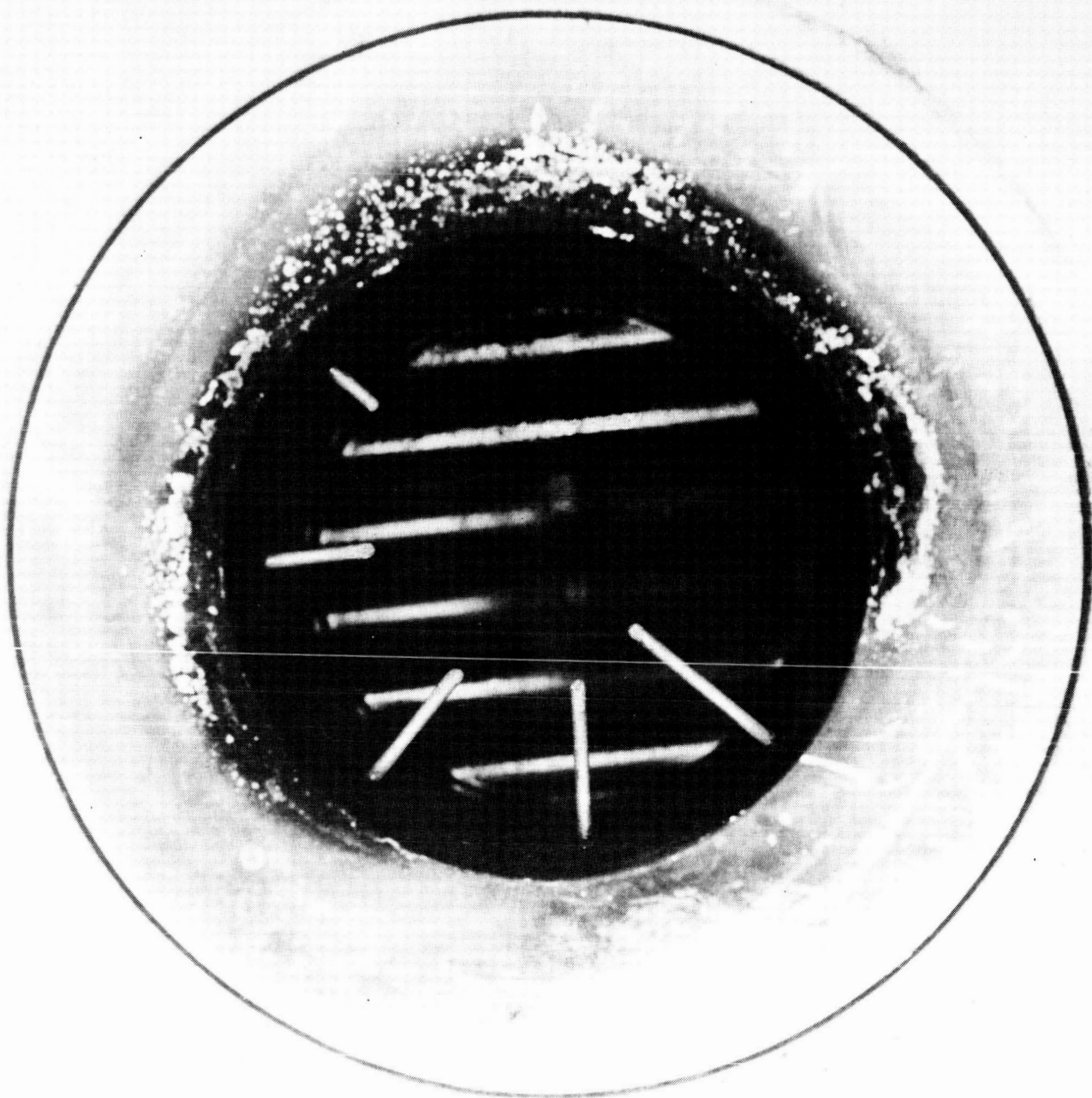


Figure 58. Condition of the Turbine Simulator after Testing with LO<sub>2</sub>/Methane



#### 4.4, Gas Generator Test Results (cont.)

##### 4.4.4.1 Turbine Simulator Flow Blockage Analysis

The downstream to upstream turbine simulator pressure ratio measurement is used to indicate whether or not carbon buildup occurs. The pressure upstream of the turbine simulator, PCTSU, should increase with time as buildup occurs due to the decreasing available flow area. Accordingly, the pressure downstream of the turbine simulator should decrease due to restricted gas generator flowrate. This means the ratio PCTSD/PCTSU should decrease as carbon builds up on the turbine simulator.

Mathematically, the flow area through the turbine simulator can be calculated using the subsonic, compressible isentropic flow equation expressed in terms of the ratio of the upstream and downstream pressure measurements:

$$\dot{w}_x = A_x P_t \sqrt{\frac{2 g_c \gamma MW}{(\gamma-1) R T_t} \left[ \left( \frac{P_x}{P_t} \right)^{2/\gamma} - \left( \frac{P_x}{P_t} \right)^{\frac{\gamma+1}{\gamma}} \right]}$$

Letting  $C_D A = A_x$  be the area available for flow, and solving for  $C_D A$  gives

$$C_D A = \frac{WTOT}{PCTSU} \sqrt{\frac{RT_t (\gamma-1)}{2g_c \gamma MW \left[ PRTSC^{2/\gamma} - PRTSC^{\frac{\gamma+1}{\gamma}} \right]}}$$

WTOT = total flowrate

PCTSU = pressure upstream of turbine simulator

MW = molecular weight

$g_c$  = gravitational constant

R = Universal gas constant

T = gas temperature

PRTSC = PRTS - CORR for '85 RP-1 tests (corrected PCTSD/PCTSU)  
PRTS for '84 RP-1 tests (PCTSD/PCTSU)

$\gamma$  = gas specific heat ratio

#### 4.4, Gas Generator Test Results (cont.)

From the detailed data obtained from Reference 2, correlating equations were obtained for the gas molecular weight, gas temperature, and gas specific heat ratio in terms of mixture ratio for the RP-1/L<sub>O</sub><sub>2</sub> propellant combinations, only. They are:

$$\begin{aligned} MW &= -112.5 MR + 67.5 \\ T &= 3350 MR + 660 \text{ (R)} \\ \gamma &= 0.325 MR + 1.010 \end{aligned}$$

These equations are valid only for the RP-1/L<sub>O</sub><sub>2</sub> propellant combination in the 750-1500 psia (5.17 to 10.34 MPa) chamber pressure range and 0.2-0.4 mixture ratio range.

No correlating equations were obtained for propane or methane, so the  $C_D A$  equation was modified to eliminate the dependence on the gas temperature and gas mixture ratio. Using the two equations for  $C^*$ :

$$C^* = \frac{P_c g_c A_t}{\dot{w}_t}$$

and

$$C^* = \left[ \frac{g_c R T_{\text{gas}}}{\gamma MW} \left( \frac{\gamma+1}{2} \right)^{\frac{\gamma+1}{\gamma-1}} \right]^{1/2},$$

solving them simultaneously for MW and replacing them in the above equations, the  $C_D A$  equation becomes:

$$C_D A = A_t \sqrt{\frac{\gamma-1}{2 \left( \frac{\gamma+1}{2} \right)^{\frac{\gamma+1}{\gamma-1}} \left[ PRTSC^{2/\gamma} - PRTSC^{\frac{\gamma+1}{\gamma}} \right]}}$$

#### 4.4, Gas Generator Test Results (cont.)

where  $A_t$  is the measured throat area of the exit nozzle. A value of  $\gamma = 1.2$  was chosen for use in this equation because calculations using specific heat ratios from 1.1 to 1.3 showed that with all other variables fixed, no significant differences in  $C_D A$  was shown.

##### 4.4.4.2 Effect of Fuel Selection and Mixture Ratio Upon Exhaust Plume Appearance

The observed exhaust plumes were also used to characterize carbon deposition since the amount of carbon buildup on the tubes is a function of the amount of carbon generated. The amount of carbon in the exhaust plume is directly proportional to the darkness of the plume. Exhaust plumes were photographed for each of the fuels tested. Figures 59, 60, and 61 show the exhaust plumes. Figure 59 shows the exhaust plumes for selected  $LO_2/RP-1$  tests. Each exhaust plume shows some carbon in the plume which is then subsequently verified by both pressure drop increases during the test and carbon buildup on the turbine simulator tubes during hardware disassembly. The exhaust plumes for  $LO_2$ /propane, Figure 60, are clear or very light for mixture ratios below 0.35. At higher mixture ratios corresponding to the high  $C^*$  step, the exhaust plume is dark indicating the presence of carbon. Above the C-H thermal decomposition threshold temperature, the various gaseous hydrocarbon species and miscellaneous olefins decompose into  $gH_2 + C_{(s)}$  which is reflected in an abrupt reduction in gaseous combustion product molecular weight, even if not reflected in a gas temperature step, thus resulting in a step  $C^*$  performance increase.

##### 4.4.4.3 Effect of Mixture Ratio Upon Deposition Rate

Typical deposition data were plotted versus mixture ratio for each propellant combination in Figures 62, 63, and 64. Deposition for  $LO_2/RP-1$ , Figure 62, is a minimum at a mixture ratio of 0.30. Data scatter or impurities in the fuel may account for the increase in deposition at

1000 P<sub>c</sub> LO<sub>2</sub>/RP-1

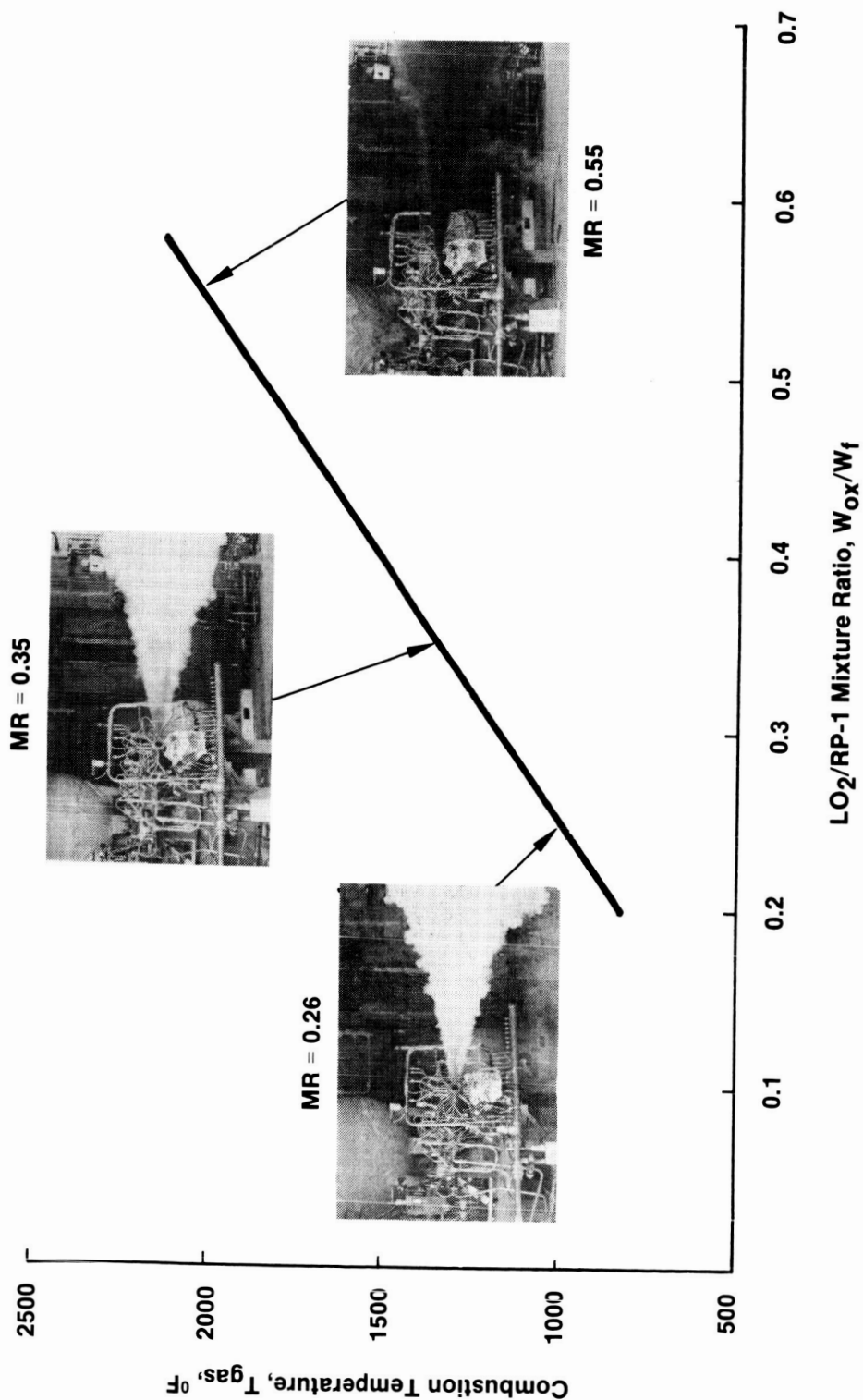


Figure 59. Exhaust Plumes for LO<sub>2</sub>/RP-1

1000 P<sub>c</sub> LO<sub>2</sub>/C<sub>3</sub>H<sub>8</sub>

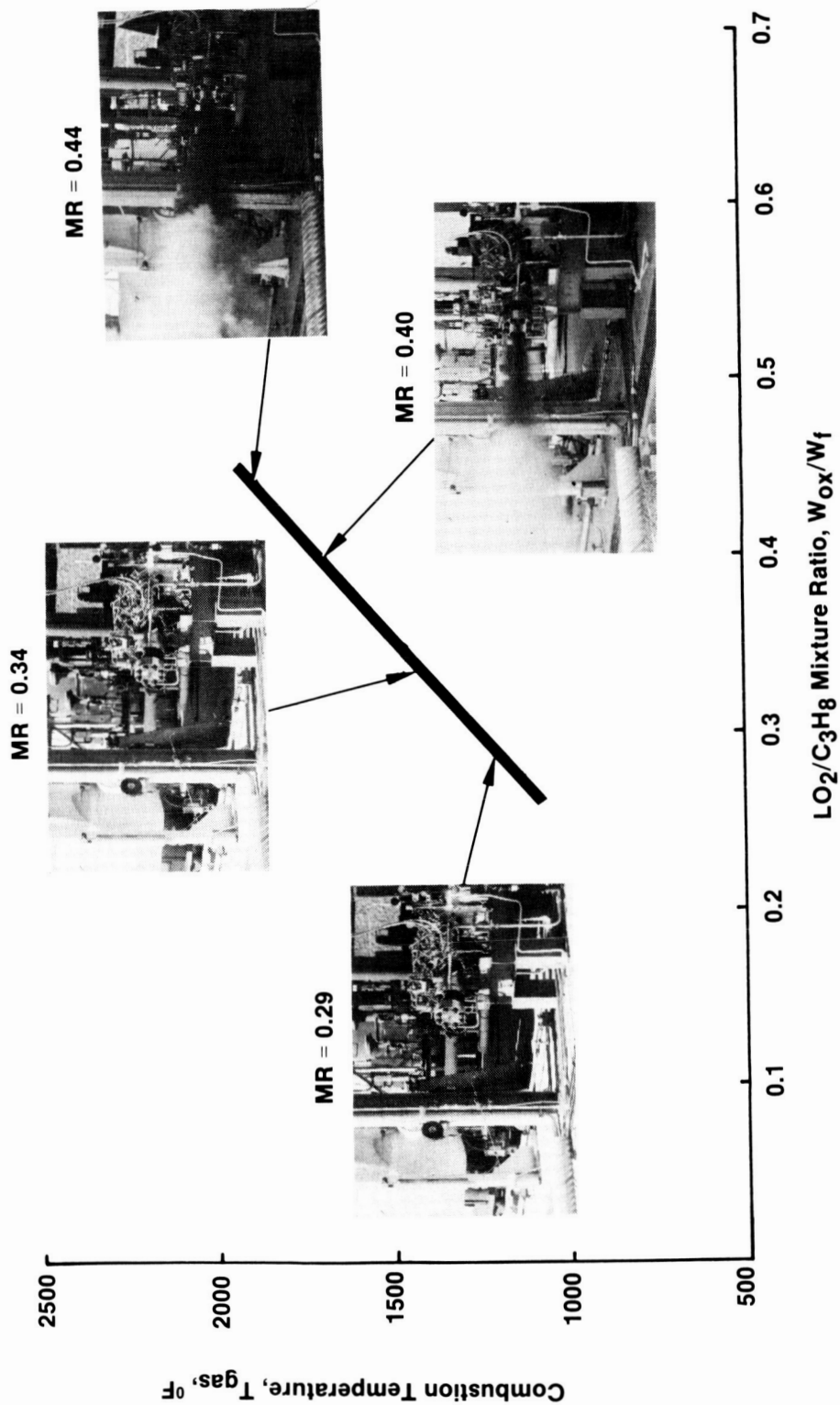


Figure 60. Exhaust Plumes for LO<sub>2</sub>/Propane

ORIGINAL PAGE IS  
OF POOR QUALITY

ORIGINAL PAGE IS  
OF POOR QUALITY.

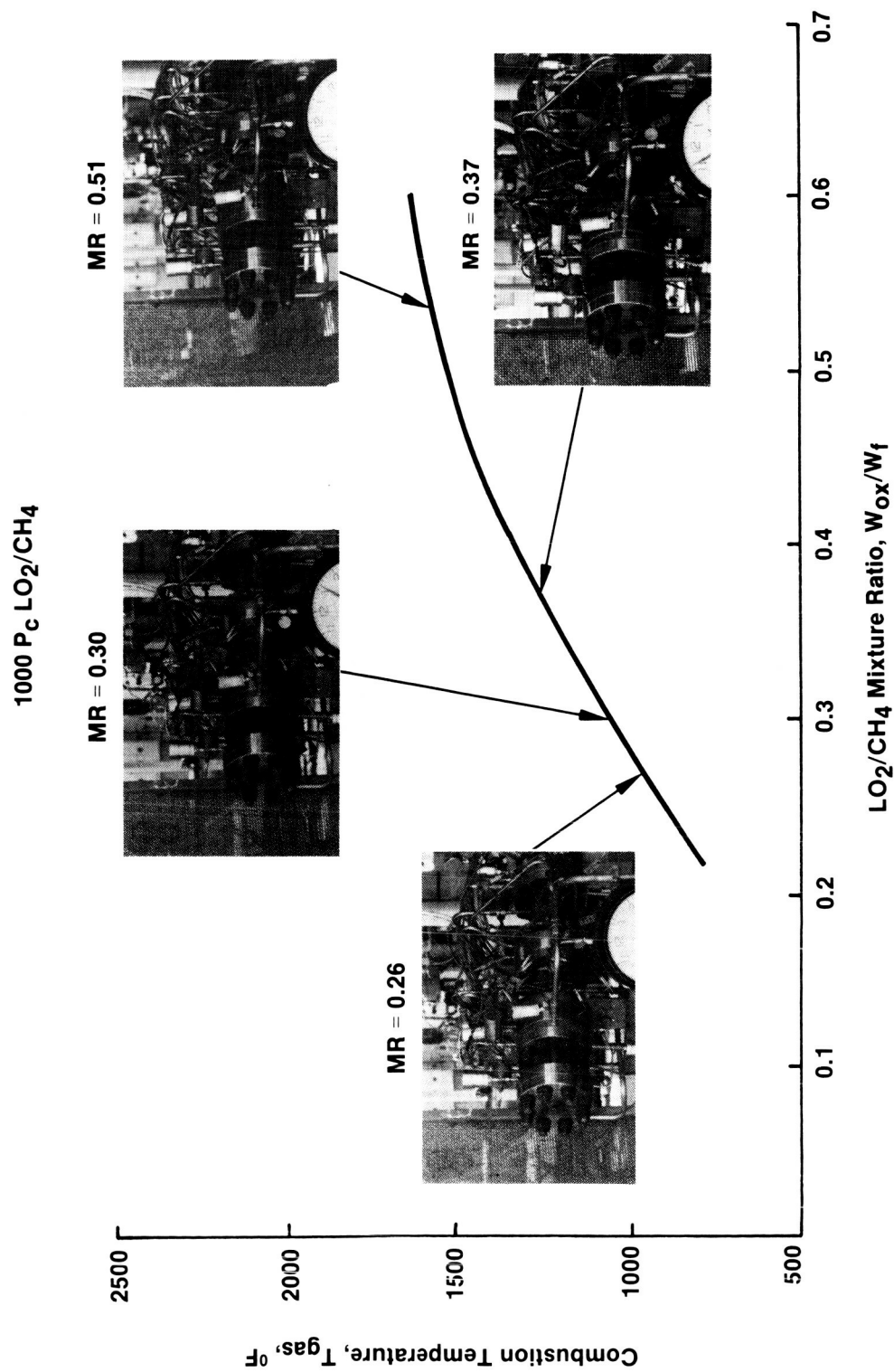


Figure 61. Exhaust Plumes for LO<sub>2</sub>/Methane

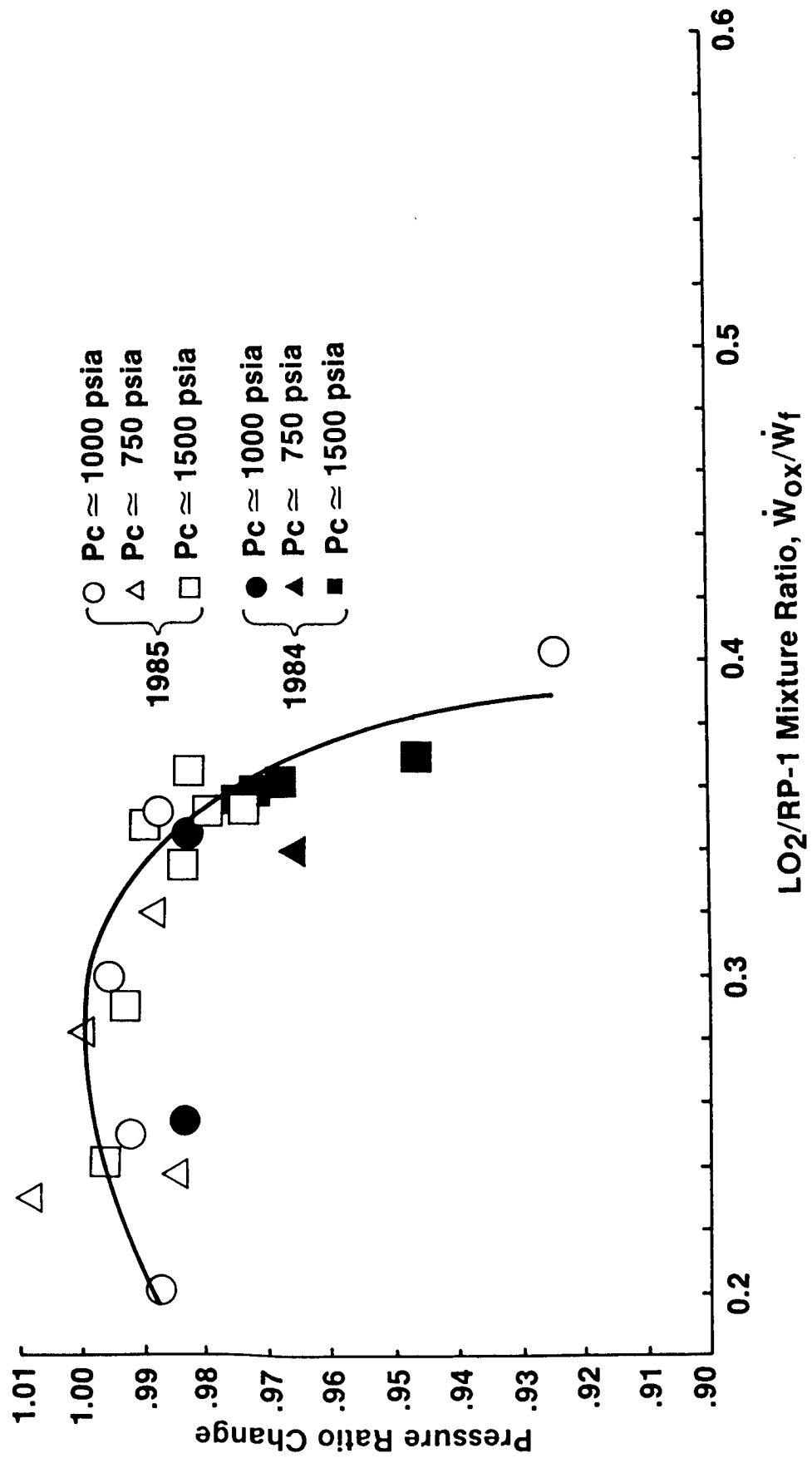


Figure 62. Carbon Deposition for LO<sub>2</sub>/RP-1

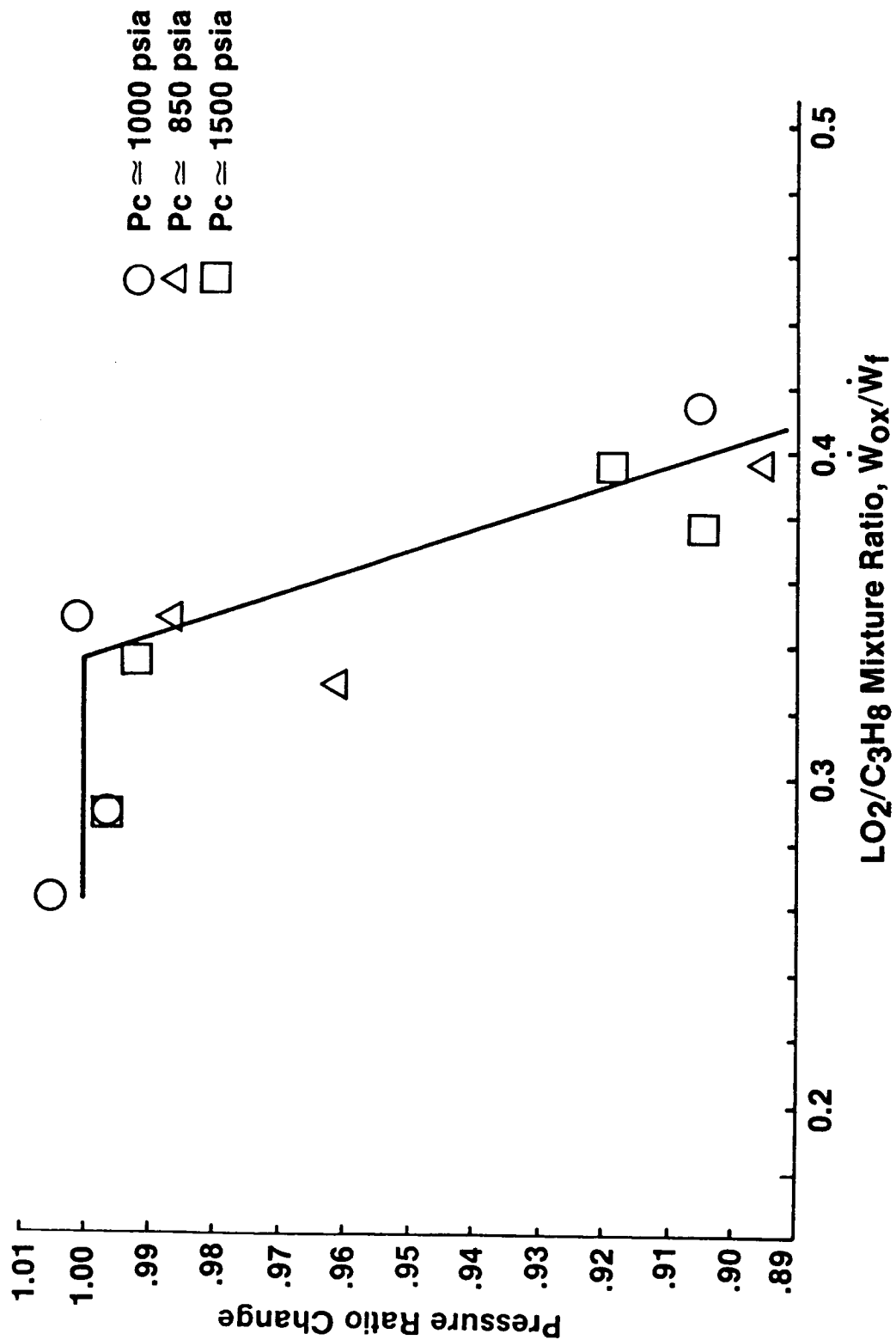


Figure 63. Carbon Deposition for  $\text{LO}_2/\text{Propane}$



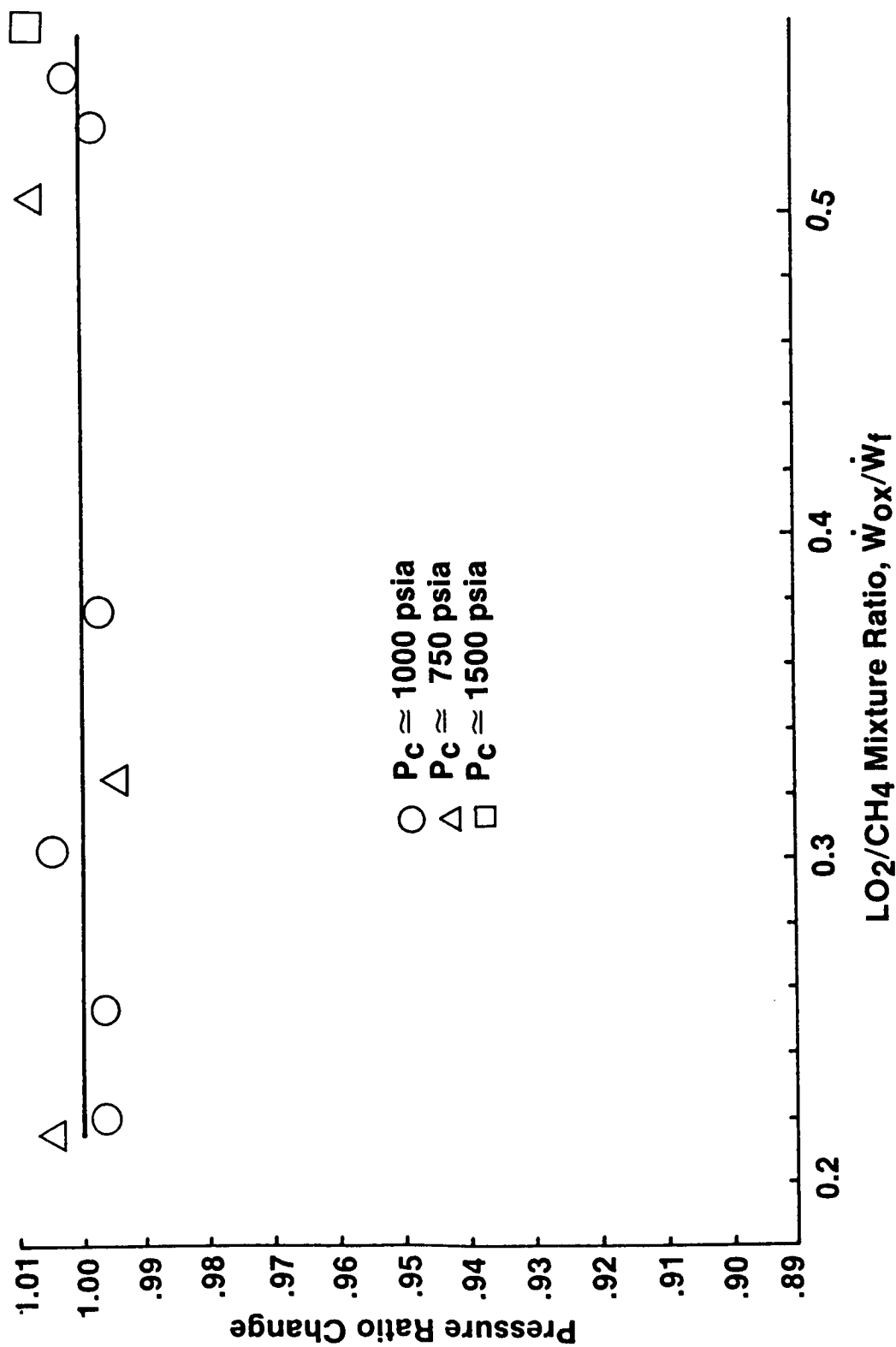


Figure 64. Carbon Deposition for LO<sub>2</sub>/Methane

#### 4.4, Gas Generator Test Results (cont.)

mixture ratios less than 0.30 (References 6, 7 and 8). Deposition for  $\text{LO}_2/\text{propane}$ , Figure 63, did not occur prior to a mixture ratio of 0.35. At a mixture ratio of 0.40, the pressure ratio across the turbine simulator tubes decreased by ten percent. Deposition occurred at higher mixture ratios and higher gas temperatures probably because the solid carbon formation mechanism requires a high activation energy. Deposition was not observed for  $\text{LO}_2/\text{methane}$ , Figure 64, for any test condition ( $\text{MR} = 0.21$  to  $0.6$  and  $P_c = 750$  to  $1650$  (5.17 to 11.38 MPa)).

##### 4.4.4.4 Effect of Chamber Pressure on Deposition Rate

Upon close scrutiny of Figures 62, 63, and 64, one can see that the carbon deposition rate is not significantly affected by chamber pressure within the range from 750 to 1500 psia (5.17 to 10.34 MPa).

##### 4.4.4.5 Effect of Mass Flux on Deposition Rate (1985 RP-1 Tests, Only)

Two RP-1 tests were examined to see whether the deposition rate is influenced by the mass flux, which was varied by using different size exit nozzles. Test 139 uses the -3 exit nozzle which had an exit area of  $0.1001 \text{ in.}^2$  ( $0.646 \text{ cm}^2$ ) and Test 144 used the -1 exit nozzle, which had an exit area of  $0.1944 \text{ in.}^2$  ( $1.25 \text{ cm}^2$ ). The mass flux was calculated using the equation:

$$\text{mass flux} = \frac{\dot{w}_t}{A_{\text{exit}}}$$

Figure 65 shows that the deposition rate, which is the slope of the curves in the figure, is not affected by the change in mass flux.

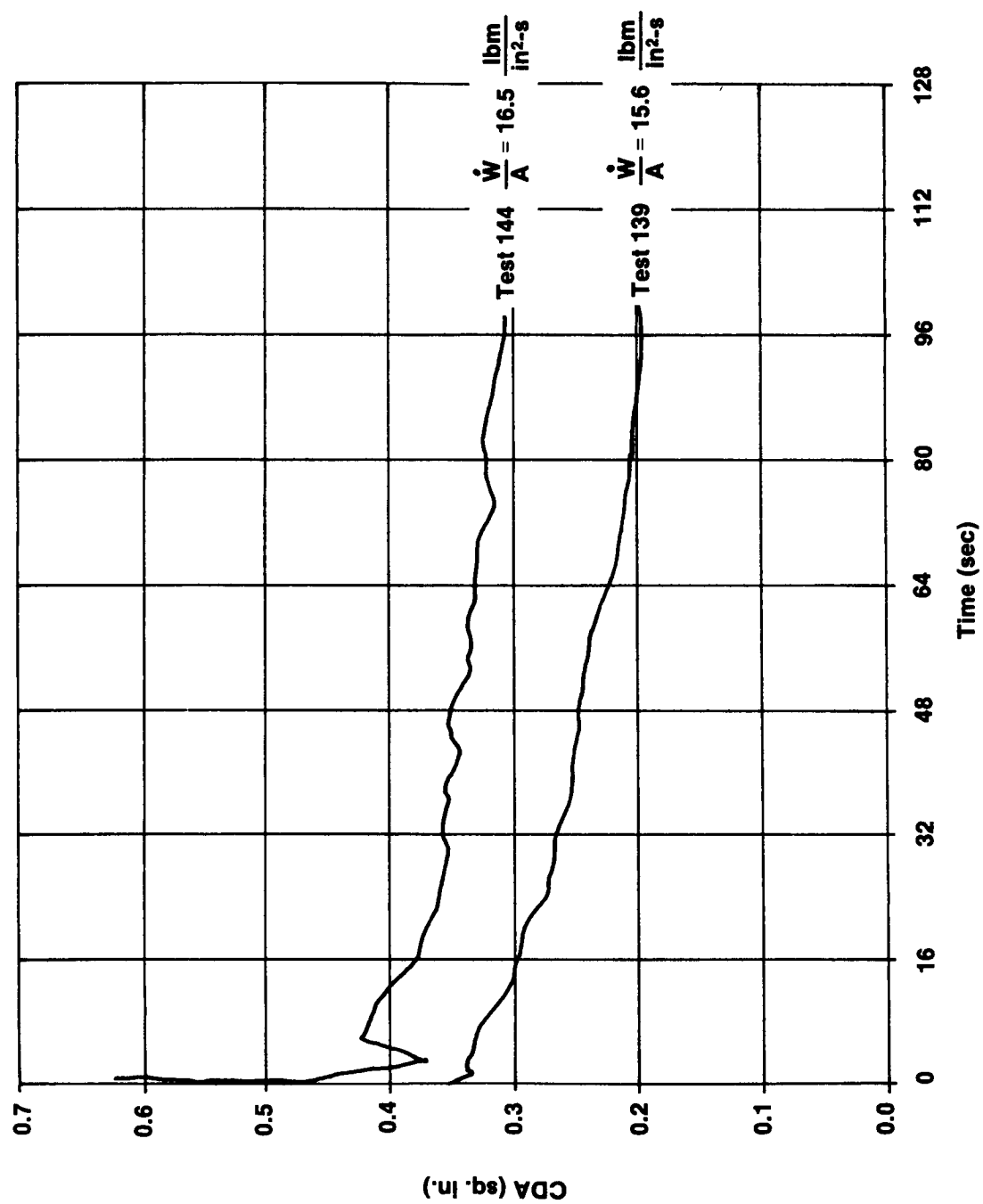


Figure 65. Effect of Mass Flux on Deposition Rate

#### 4.4, Gas Generator Test Results (cont.)

##### 4.4.4.6 Effect of Velocity on Deposition Rate (1985 RP-1 Tests Only)

The effect of velocity variation on deposition rates due to turbine simulator area change was examined for Tests 144 and 156. Test 144 used the cooled turbine simulator which has a flow area of 0.239 in.<sup>2</sup> (1.54 cm<sup>2</sup>). Test 156 used the uncooled turbine simulator, which had a flow area of 0.196 in.<sup>2</sup> (1.26 cm<sup>2</sup>). The velocity was calculated using:

$$\dot{W} = \rho v A$$

The density,  $\rho$ , was estimated using the ideal gas law. Figure 66 shows the deposition rate,  $d(C_D A)/dt$ , is not affected by the change in gas velocity.

##### 4.4.4.7 Effect of Turbine Simulator Geometry on Deposition Rate

In RP-1 Tests 2427-936-A6-156 through 160, a conventional, uncooled, 3-D converging throat was installed, replacing the cooled turbine simulator, to see if any carbon deposition would occur (see Figure 23). Unfortunately, since the new piece was uncooled, it thermally expanded radially inward under transient thermal strain reducing the throat area. The pressure differential measurement correspondingly increased, which gave an initially erroneous conclusion that carbon had deposited in the throat. Upon inspection, no carbon was present. In Test 160, the exit nozzle was removed as shown in Figure 24 to produce sonic conditions at the throat, but still no carbon deposition occurred.

##### 4.4.4.8 Effect of Shutdown Transients on Residual Carbon Deposits

In several early RP-1 tests, it was noted that pressure drop measurements indicated carbon buildup on the turbine simulator, but on disassembly, no carbon buildup was found. Review of the shutdown transient

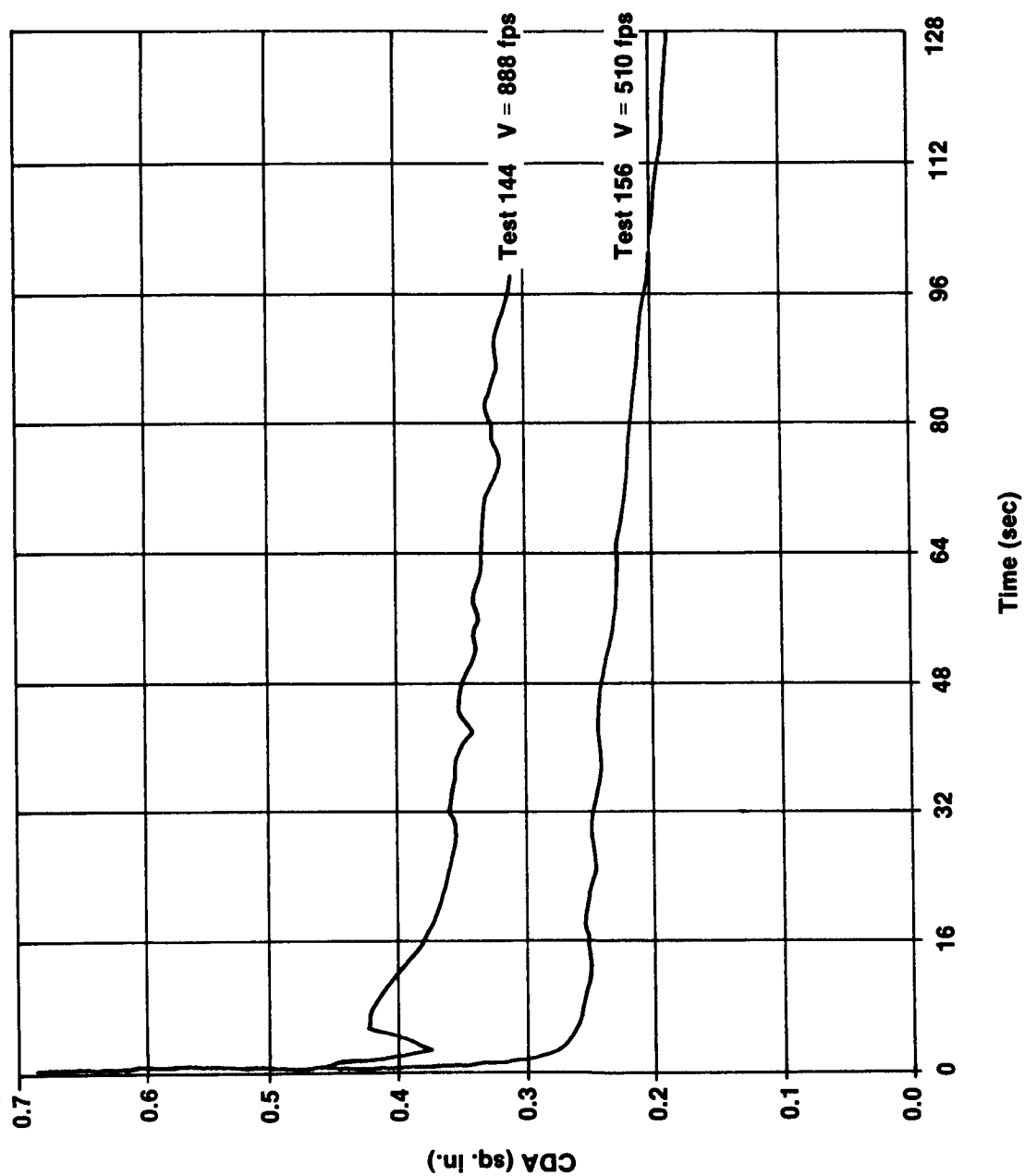


Figure 66. Effect of Gas Velocity on Deposition Rate

#### 4.4, Gas Generator Test Results (cont.)

data analysis showed that the shutdown environment was oxidizer-rich. The oxidizer rich shutdown was being caused by the different manifold expulsion rates caused by the high cryogenic  $\text{LO}_2$  vapor pressure relative to the low RP-1 vapor pressure. It is theorized that this oxygen-rich environment at high chamber pressures virtually consumed all the deposited carbon upon shutdown.

To ensure a fuel-rich environment, the fuel valve closure was delayed on shutdown and the upstream thermocouples were monitored for gas temperature increases. A comparison of the thermocouple response of the original shutdown sequence against the modified sequence is shown in Figure 67. Resultant back-to-back tests ( $P_c = 1500$  psia (10.34 MPa) and  $MR = 0.35$ ) for this test series are compared to the original test program in Figure 68. The results are fairly consistent with the original test data. In the original test program, the carbon buildup was presumed to have been consumed during the high pressure, oxygen-rich shutdown. The carbon generated with the fuel-rich shutdown was soft and could be easily removed; therefore, it is presumed that the carbon was either washed away by the liquid fuel deluge on shutdown or dislodged from the tubes during the purge process at shutdown.

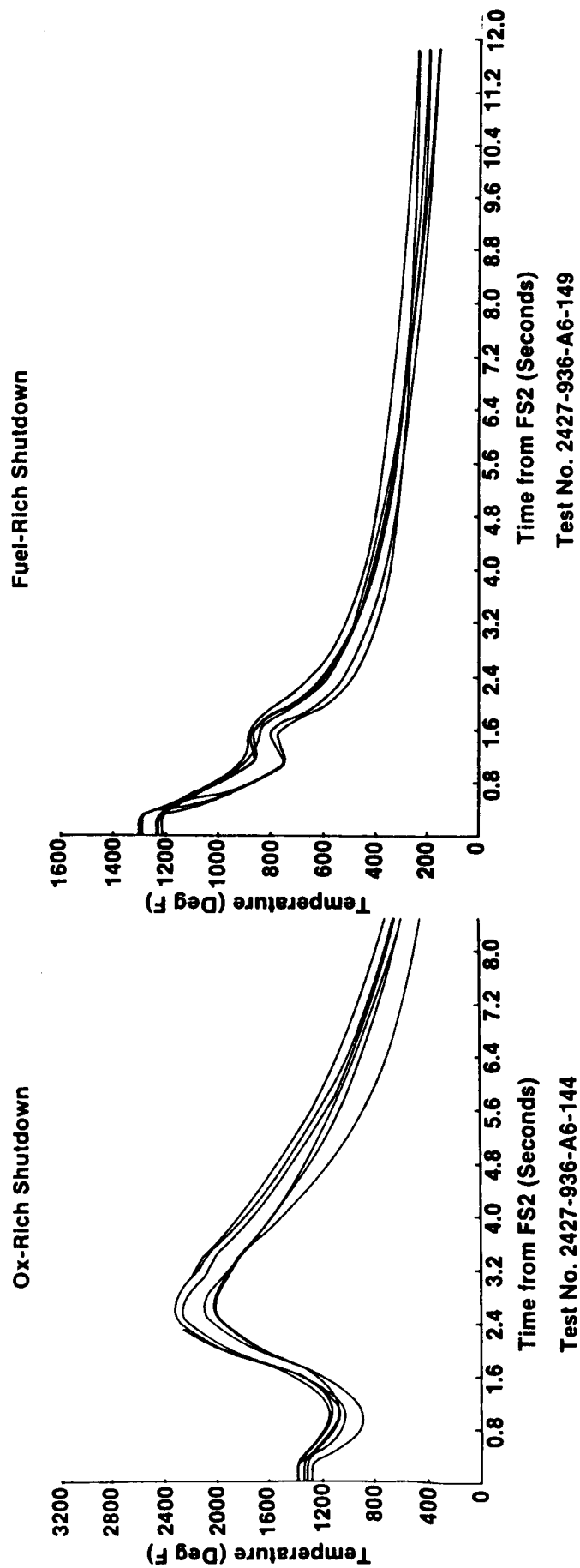


Figure 67. Comparison of Thermocouple Response

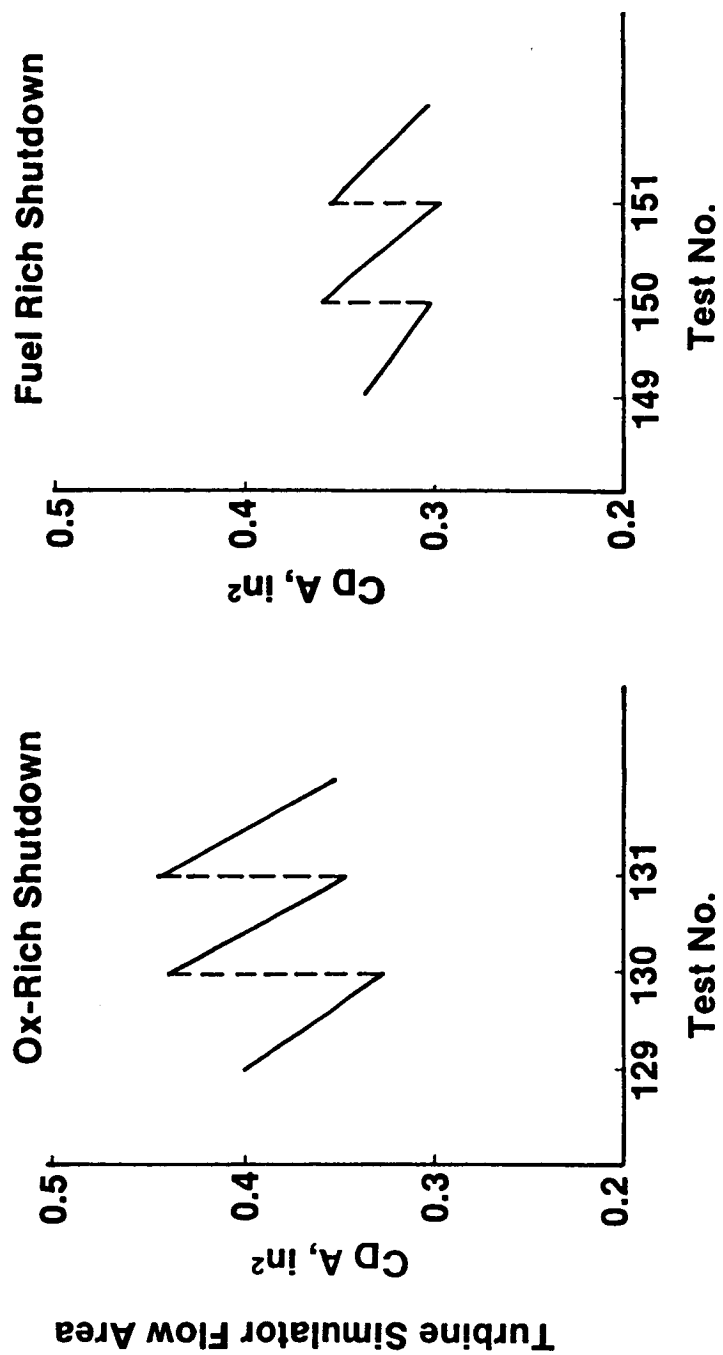


Figure 68. Comparison of Back-to-Back Tests



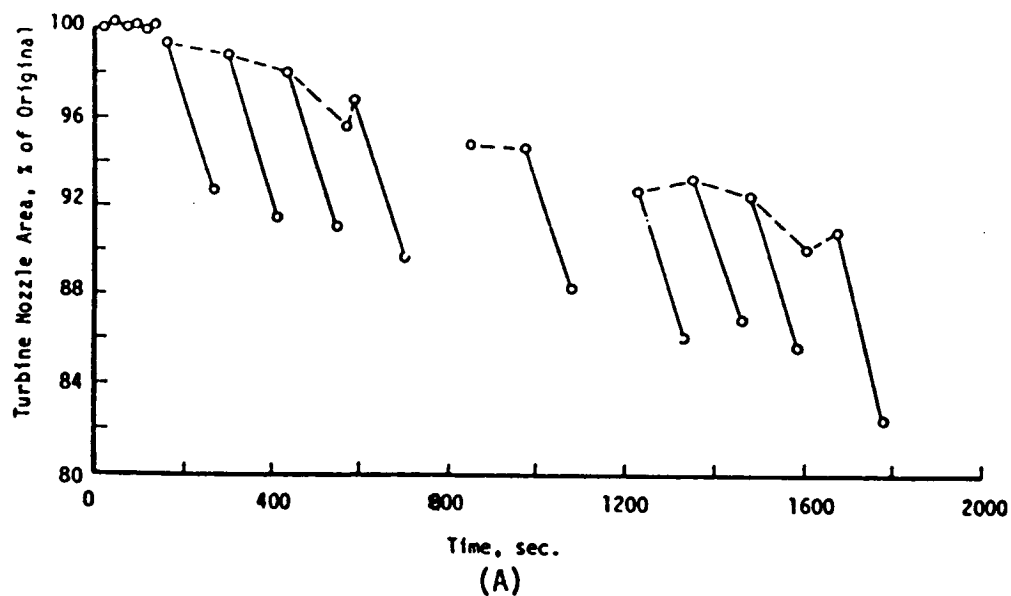
## 4.0, Technical Discussion (cont.)

### 4.5 FUEL-RICH HYDROCARBON COMBUSTION DATA ANALYSIS

#### 4.5.1 Related Experience

Little quantitative data exists in the open literature on carbon deposition in and downstream of gas generators and preburners. Our database in this area is derived from Aerojet's experience in the development of Titan I gas generators and in ATC's NASA contracts (References 1 and 2), and from Rocketdyne's experience (Reference 9) with  $\text{LO}_2$ /hydrocarbon preburner technology. Titan I is a particularly good source in that both the first and second stages employed fuel-rich gas generator cycle  $\text{LO}_2$ /RP-1 engines. During Titan I engine development, carbon deposition in the turbine nozzles was a primary concern, and a considerable amount of testing was devoted to obtaining deposition data. The NASA contracts with ATC and Rocketdyne focused on extending the  $\text{LO}_2$ /hydrocarbon gas generator/preburner technology to higher pressures. These contracts had the acquisition of carbon deposition data as a contract goal.

During development of the Titan I gas generator, deposition was monitored in terms of turbine nozzle flow area reduction. A typical history spanning nearly 1800 seconds of firing duration and numerous restarts is presented in Figure 69A. This plot of effective turbine inlet nozzle flow area versus time provides valuable insight into the deposition process. The most apparent feature is that during each 120 to 160 second full mission duration firing, the turbine nozzle flow area was reduced by approximately 8% due to carbon deposition. At the beginning of the subsequent firing, 80% to 90% of this obstructed area was recovered. It was hypothesized that either the carbon deposited during the firing spalled off on shutdown resulting from thermal cycling or was burned off during the oxidizer rich shutdown transient due to the higher  $\text{LO}_2$  vapor expulsion pressure.



MIXTURE RATIO INFLUENCE ON TURBINE NOZZLE AREA REDUCTION  
TITAN I FIRST STAGE GAS GENERATION  
FS<sub>1</sub> + 20 SEC. TO FS<sub>1</sub> + 110 SEC.

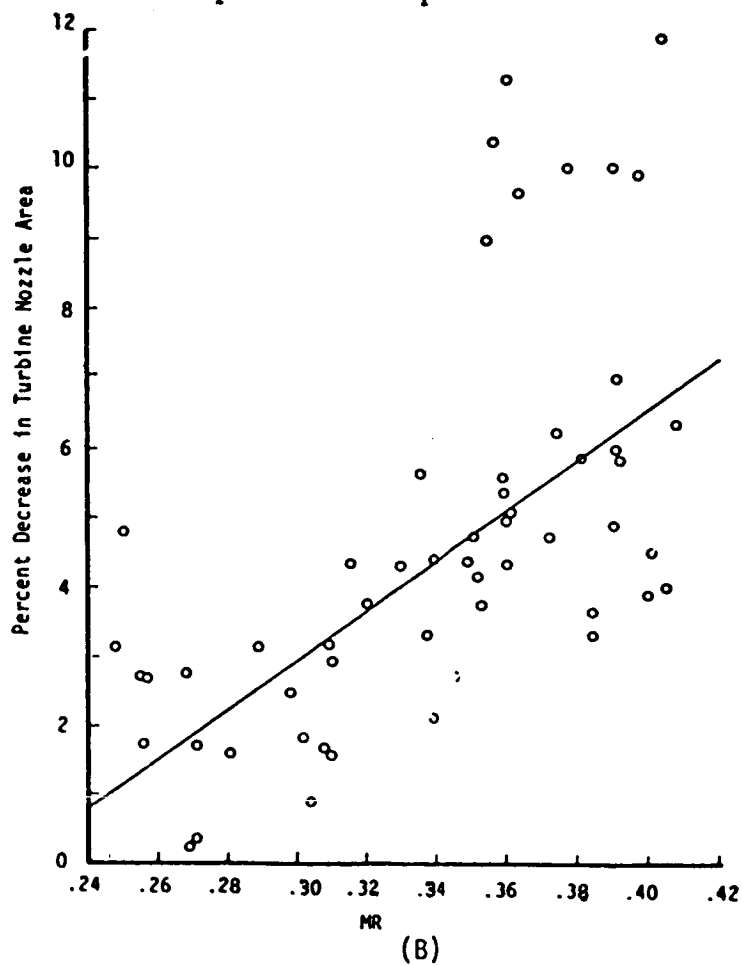


Figure 69. Long Duration Carbon Deposition Effects in Titan I Gas Generators

#### 4.5, Fuel-Rich Hydrocarbon Combustion Data Analysis (cont.)

The effect of gas generator mixture ratio on carbon deposition was also established on Titan I. A plot of the data is given in Figure 69B. This plot shows the decrease in turbine nozzle flow area during a 90 second period starting 20 seconds into a firing. The results indicate the deposition process to be very mixture ratio sensitive with increasing mixture ratios producing higher deposition rates. The general observation of those working the Titan I gas generator development program was that relatively light and easily removed deposits were formed at gas temperatures below about 1200 to 1300°F (922 to 977K). In the temperature range from about 1300 to 1700°F (977 to 1200K) the deposits became thicker and were very hard and tenacious while at temperatures above about 1700°F (1200K) the deposits become thinner. This temperature sensitivity is considered to be indicative of the decomposition products of RP-1 since the majority of the fuel present at these low mixture ratios is unreacted RP-1. This is supported by the results of tests on the thermal stability of RP-1 conducted by the Jet Propulsion Laboratory in the late 1950's. Flow tests with heated RP-1 in the absence of oxygen showed a dramatic increase in carbon deposition once the RP-1 temperature reached 1330°F (994K), confirming the gas generator results. Apparently, when RP-1 is heated above 1300°F (977K) its decomposition products include a very sticky tar-like substance which adheres to almost any surface and hardens when it cools. If the RP-1 is heated above about 1700°F (1200K) this tar-like substance no longer is encountered.

The Titan I results also correlate well with the observation by Glassman, Reference 10, that in very fuel-rich combustion there is a range over which the addition of more oxidizer catalyzes soot formation. The Titan I data would indicate this range spans about 1300°F to 1700°F (977 to 1200K).

Another significant phenomenon was encountered in the early 1960's during the LO<sub>2</sub>/RP-1 F-1 fuel rich gas generator development program (Ref. 11). All F-1 GG's encountered high amplitude (up to 800 psi (5.52 MPa)

#### 4.5, Fuel-Rich Hydrocarbon Combustion Data Analysis (cont.)

Pk-Pk) combustion oscillations above 1550 to 1600°F (1088 to 1144K) gas temperature. It was later ascertained that the onset of these combustion oscillations could be attributed to the C\* step which results from the kinetically limited decomposition of the C-H bond. This decomposition causes a reduction in gas molecular weight and an increase in C\* performance. This resulted in an increase in PcGG which, in turn, reduced oxidizer injection flowrate causing a reduced MRGG causing C\* to transition back to the low step performance. It is interesting to note that this is very near the C\* step transition temperature which was also observed in recent LO<sub>2</sub>/propane testing (see Figures 51 and 54). The high amplitude F-1 GG combustion oscillations prevented operating above 1600°F (1144K) for any significant test duration, so no comment was made regarding an abrupt increase in observed carbon deposition rate. Based on recent knowledge shed upon this phenomenon, however, an increase in carbon deposition rate had to be inevitable.

##### 4.5.2 Fuel Property Comparisons

Table XX compares pertinent fuel properties between RP-1, propane and methane. Based on Aerojet combustion design models the following fuel properties either directly or indirectly affect carbon deposition.

Viscosity	-	high viscosity produces larger fuel drop sizes; low viscosities are preferred.
Surface Tension	-	high surface tension produces larger fuel drop sizes; low surface tensions are preferred.
Critical Temperature	-	high critical fuel temperature reduces differential temperature between combustion gases and fuel droplets which slows fuel vaporization rate; low critical temperatures are preferred.
Latent Heat of Vaporization or Heat Capacity (C <sub>p</sub> )	-	high latent heat of vaporization or high C <sub>p</sub> reduces fuel volatility and reduces fuel droplet vaporization rate; low heat of vaporization and low C <sub>p</sub> are preferred.
C:H Ratio	-	high carbon to hydrogen mole ratio increases probability of carbon deposition; low C/H ratio is preferred.

TABLE XX

## COMPARISON OF HYDROCARBON FUEL PROPERTIES

Name	Units	RP-1		Propane	Methane
Chem. Formula	--	C <sub>12</sub> H <sub>26</sub> (avg)	C <sub>3</sub> H <sub>8</sub>	CH <sub>4</sub>	
H/C-Ratio		2.17		2.67	4.00
Molecular Wt.	--	172		44	16
Critical Pres.	psia	315		617	673
Critical Temp.	°F	758		206	-117
Normal Boiling Point	°F	422		-44	-259
Latent Heat of Vap. (@ NBP)	Btu/Uom	125		185	225
Typical Inj. Temp.	°F	70	200	-30	-220
				200	-140
Specific Gravity	--	0.80	0.75	0.57	0.39
Density	lbm/ft <sup>3</sup>	50.	47.	35.8	24.3
Viscosity	lbm/ft-sec	112 x 10 <sup>-5</sup>	41 x 10 <sup>-5</sup>	10 x 10 <sup>-5</sup>	4.8 x 10 <sup>-5</sup>
Surface Tension	lbf/in.	17.5 x 10 <sup>-5</sup>	13.7 x 10 <sup>-5</sup>	8.2 x 10 <sup>-5</sup>	5.4 x 10 <sup>-5</sup>
Vapor Pressure	psia	<.01	2.1	20	60
Heat Capacity	Btu/lbm-°F	0.48	0.54	0.54	0.88
				600	420
				1.2	1.43

NOTE: See Appendix A for SI unit conversions.

#### 4.5, Fuel-Rich Hydrocarbon Combustion Data Analysis (cont.)

- Vapor Pressure - low vapor pressure (at given fuel droplet temperature) reduces fuel volatility; high vapor pressure is preferred.
- Molecular Weight - high molecular weight reduces molecular diffusion and mixing rate; low molecular weight is preferred.
- Critical Pressure - Not a significant carbon deposition parameter.
- Density - Not a significant carbon deposition parameter.

Taken at face value, the above criteria clearly indicate from an analytical consideration that methane is the preferred hydrocarbon fuel for minimizing carbon deposition. The experimental data heretofore has largely substantiated these expectations. There are, however, other mitigating considerations besides carbon deposition which have to be considered in selecting a final optimum fuel.

From a vehicle-mission-performance standpoint, fuel density is a very important parameter. Maximizing the fuel density minimizes the required fuel tankage volume and hence vehicle dry weight. Other things being equal, this results in increased payload capability and reduced launch cost per pound.

The turbomachinery is a very intricate and costly engine component. Maximizing the fuel density results in smaller fuel pumps, slower turbine speeds, and lighter weight pumps, which operate at lower stress levels and increased reliability. Furthermore, the gas generator flowrate is reduced which minimizes the GG engine cycle Isp performance penalty.

Additional design considerations to minimize carbon deposition for whichever fuel is ultimately selected are addressed separately in Section 4.5.3.2.

## 4.5, Fuel-Rich Hydrocarbon Combustion Data Analysis (cont.)

### 4.5.3 Fuel-Rich Combustion Model

Fuel-rich RP-1 combustion at low gas temperatures at low GG mixture ratios has very slow reaction kinetics. The result is that, in conventionally sized hardware, the combustion process does not have sufficient reaction time to achieve chemical equilibrium. This was observed indirectly during Titan I development when measured gas generator  $C^*$  values were consistently lower than the equilibrium values. Rocketdyne and Aerojet each recognized and addressed this problem in their respective NASA preburner contracts. Rocketdyne did this by empirically adjusting their equilibrium model using Atlas gas generator data to correct for kinetics. Aerojet addressed the problem by constructing a kinetically limited fuel-rich combustion model (FRCM). The FRCM was developed on contract NAS 3-21753 (Ref. 1) and is described below.

Combustion in fuel-rich preburners is presumed to occur as illustrated in Figure 70. The cryogenic  $LO_2$  is assumed to vaporize rapidly and react stoichiometrically with a small portion of the fuel. The remainder of the fuel undergoes vaporization and thermal decomposition to arrive at the final combustion products. Equilibrium combustion of the oxidizer is assumed such that the starting gas-phase properties are defined by ODE combustion products. The gas-phase temperature is higher at the injector-end than at the nozzle-end since the starting gas-phase mixture ratio is higher than the overall mixture ratio. The gas temperature diminishes as the excess diluent fuel vaporizes and undergoes kinetically limited thermal decomposition. The net effect is that the gas properties and  $C^*$  performance are slightly dependent on residence time. The rate of temperature decay depends on the fuel vaporization rate which is approximated with an exponential function (see Figure 71). The appropriate exponential vaporization rate constants are determined analytically from the fuel vaporization model which is then calibrated with experimental data.

● FUEL RICH COMBUSTION

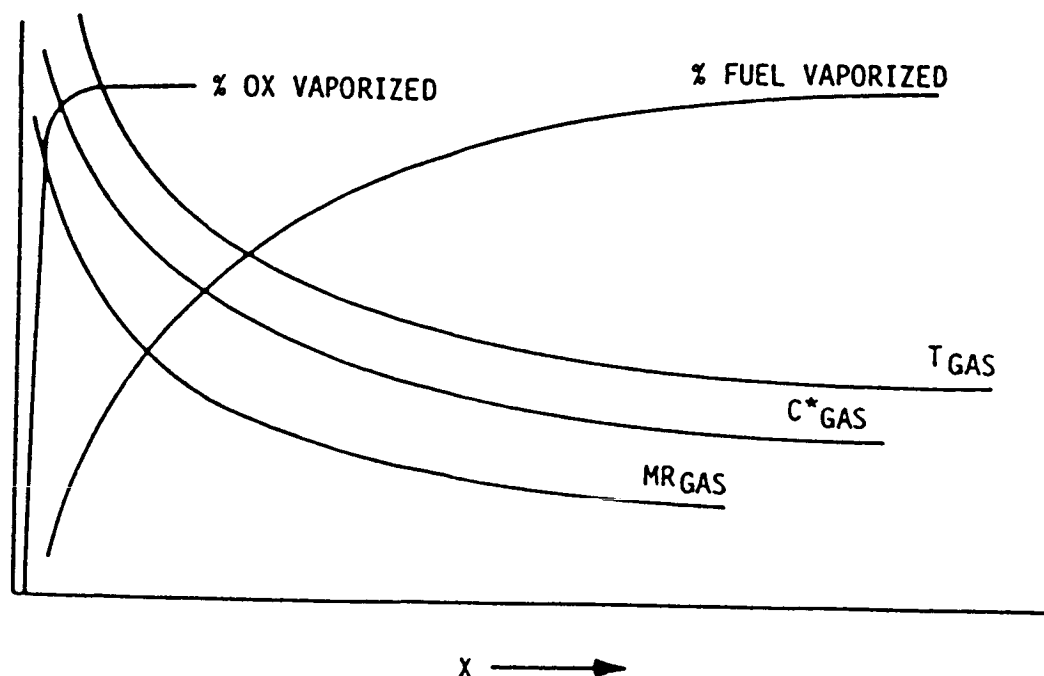
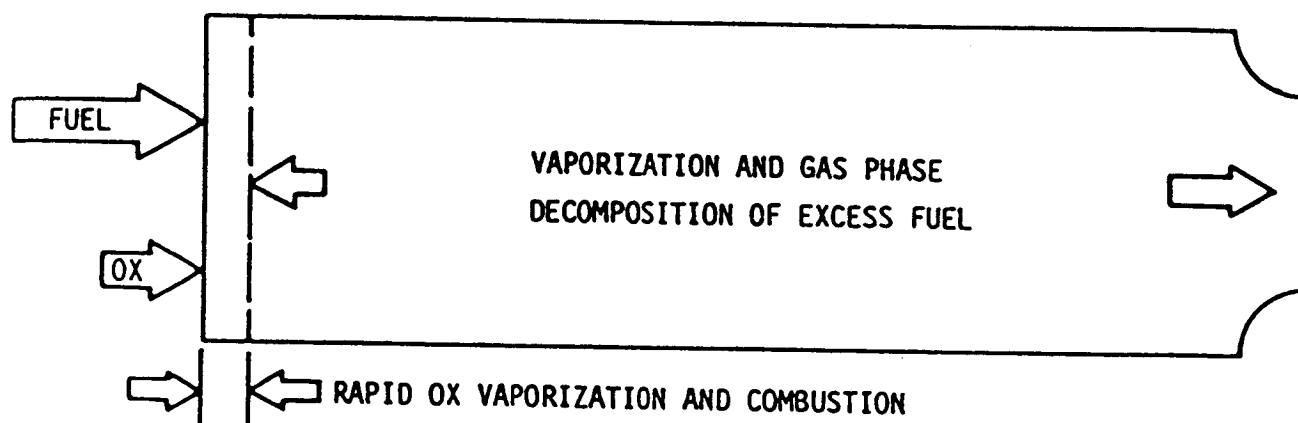
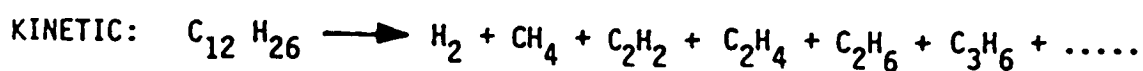
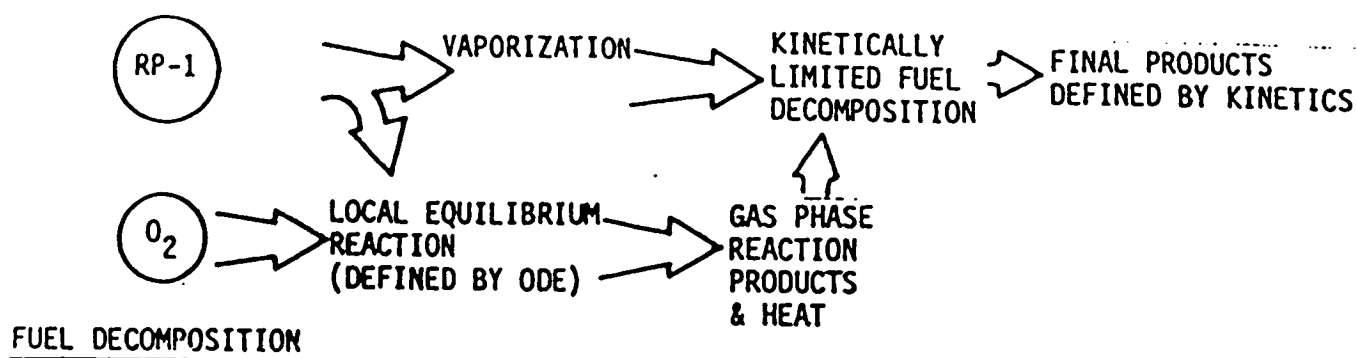


Figure 70. Fuel-rich LOX/RP-1 Combustion Model



$\eta_{vap} = 1 - C_f/C_i$        $A = \text{CONSTANT, } 1 \times 10^4$   
 $C_f/C_i = e^{-X/V} (Ae^{-\Delta H/RT})$        $\Delta H = \text{ACTIVATION ENERGY}$   
 $X = \text{LENGTH, INCHES}$        $R = \text{GAS CONSTANT, } 1.987$   
 $V = \text{CHAMBER VELOCITY, INCHES/SEC}$        $T = \text{TEMPERATURE, } ^\circ K (^\circ R)$

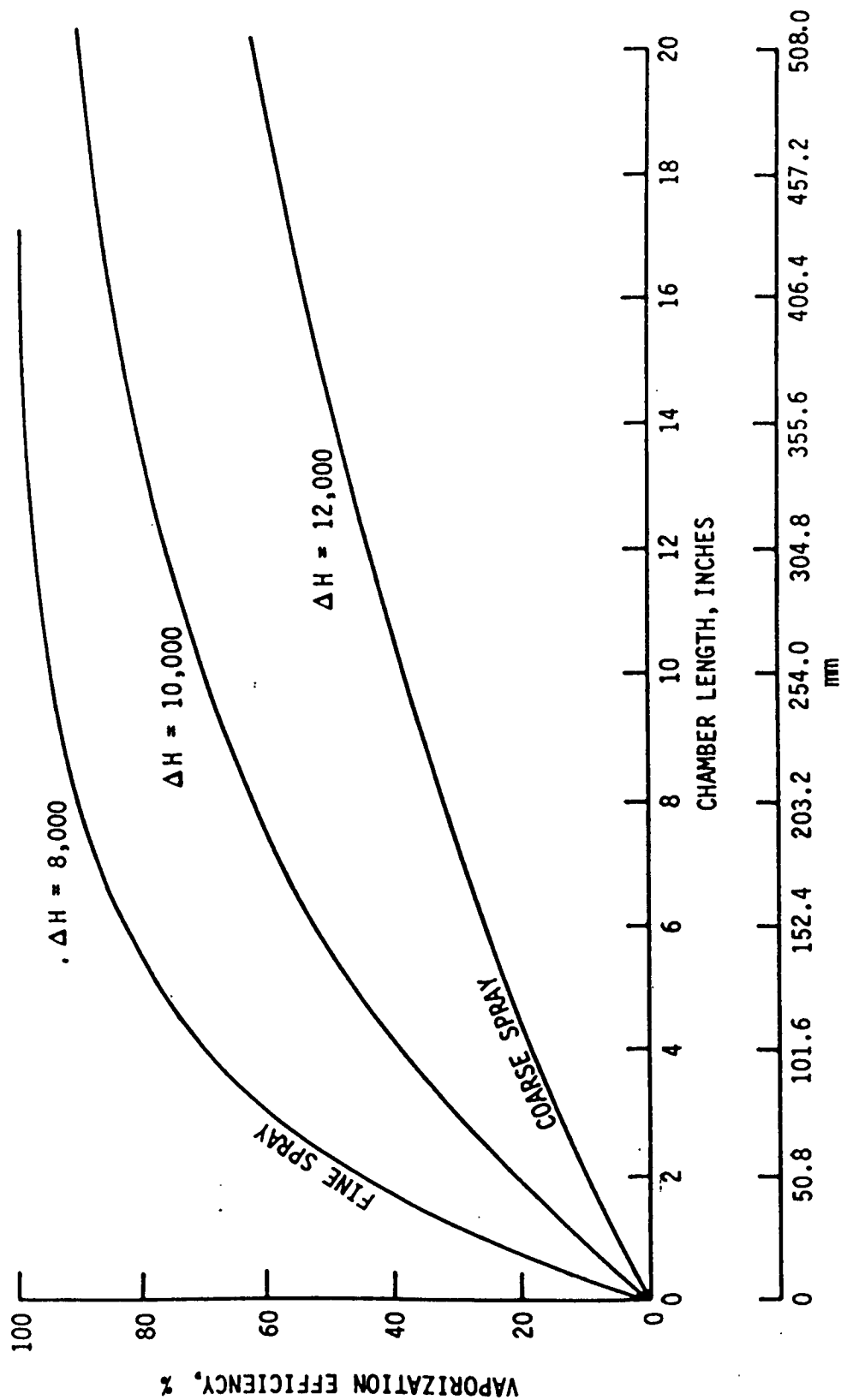


Figure 71. Fuel Vaporization Model

#### 4.5, Fuel-Rich Hydrocarbon Combustion Data Analysis (cont.)

The model assumes the chemical reaction scheme shown in Figure 72. Both the oxygen and RP-1 are injected into the combustion chamber in the liquid phase. The liquid oxygen rapidly vaporizes, leaving a large amount of unvaporized RP-1. The oxygen vapors quickly react with the available fuel vapors at a mixture ratio that is higher than the overall MR. The oxidation of the RP-1 vapor is assumed to result in equilibrium products due to the higher mixture ratio. With the exception of hydrogen, these products do not undergo further reaction in the chamber. Based on previous calibrations, the appropriate value for the assumed starting mixture ratio has been determined to be on the order of 1.2. The oxidation process provides the needed for the vaporization and thermal decomposition processes.

The unreacted liquid RP-1 vaporizes and undergoes a two-step gas-phase thermal decomposition. The two steps consist of (1) RP-1 fragmentation (primary reactions) and (2) gas-phase reaction (secondary reactions). The primary reactions fragment the RP-1 into lighter hydrocarbons, such as  $H_2$ ,  $CH_4$ ,  $C_2H_4$ ,  $C_3H_6$ , etc. These fragments then undergo secondary reactions with the hydrogen molecules that are produced by the starting RP-1 oxidation reactions. The net effects of the fuel-rich RP-1 vaporization and RP-1 decomposition are a reduction in gas temperature. As a result, the RP-1 decomposition takes place in an ever decreasing low-temperature environment and thus the decomposition reactions proceed progressively slower and are limited by the kinetic reaction rate.

In its currently existing form, the model does not predict solid carbon formation since an appropriate reaction mechanisms has not been identified. It predicts only the precursors, such as  $C_2H_2$ . Table XXI is a listing of the chemical reactions considered by the model.

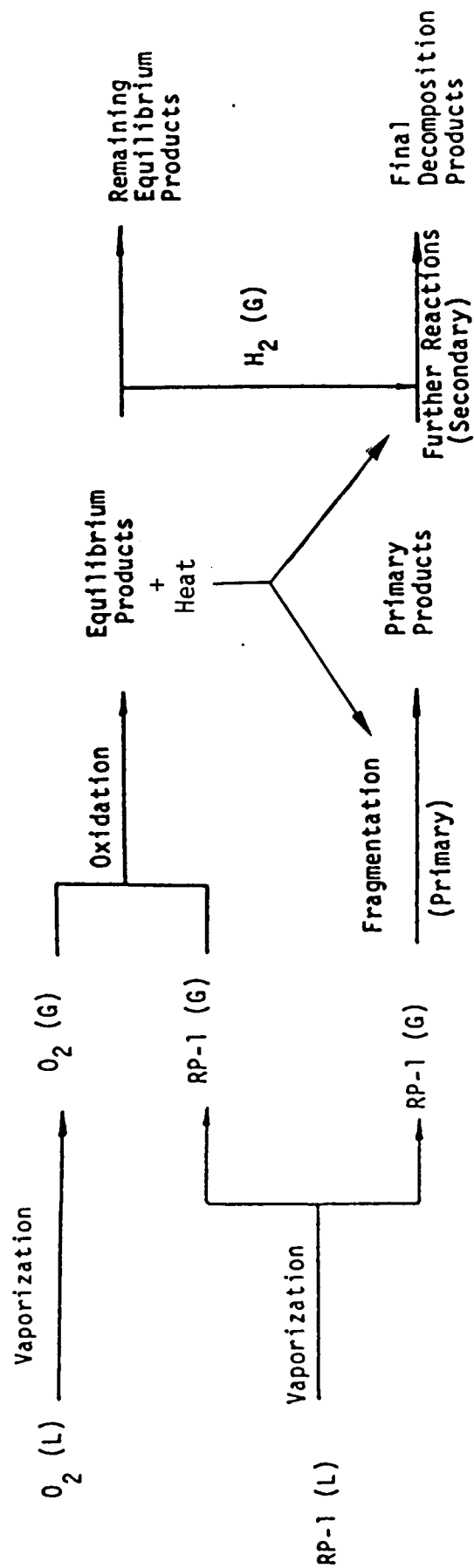


Figure 72. Fuel-rich Combustion Model Reaction Schematic

FUEL-RICH COMBUSTION MODEL CHEMICAL REACTIONS

145

## 4.5, Fuel-Rich Hydrocarbon Combustion Data Analysis (cont.)

### 4.5.3.1 Hydrocarbon Decomposition Kinetics

#### 4.5.3.1.1 Gas Temperature (MRGG) Effects

The higher the mixture ratio, the higher the gas temperature. This is due to the exothermic nature of the bipropellant oxidation reaction. In the fuel-rich regime, as more oxidizer is added (higher mixture ratio), the decomposition kinetic reaction rates speed up and proceed more nearly toward chemical equilibrium which manifests itself in higher carbon deposition rates. Best examples of this are Figures 51, 54, and Figure 63.

#### 4.5.3.1.2 Pressure Effects

Higher chamber pressure increases gas density and hence increases the intermolecular collision frequency. Thus, the effect is a logarithmic influence which is small in comparison to the gas temperature effect, which is exponential. Hence the experimental data has shown that the chamber pressure, when only varied over a factor of 2:1, has a weak effect on the rate of carbon deposition. Some weak pressure influence was observed in the  $\text{LO}_2/\text{RP-1}$  gas temperature data of Figure 50.

#### 4.5.3.1.3 Gas Residence Time Effects

The gas residence time,  $\tau$ , indicates how long it takes an average gas molecule to be exhausted through the nozzle throat measured from the time it is injected and combusted. This parameter is calculated using the following equation:

$$\tau = \rho \frac{V_C}{\dot{W}_t}$$

where:

$V_C$  = volume of the chamber

$\rho$  = gas density

$\dot{W}_t$  = total flowrate

#### 4.5, Fuel-Rich Hydrocarbon Combustion Data Analysis (cont.)

This equation indicates that the gas residence time is a function of the chamber length, contraction ratio, operating chamber pressure, mixture ratio and total flowrate. The gas residence time can be related to the amount of fuel decomposition using the laws of chemical kinetics. The rate of disappearance of fuel A by irreversible reaction:



may be written

$$r_A = - \frac{dC_A}{dt} = k C_A^a C_B^b$$

Then a is the order of the reaction with respect to A, and b is the order with respect to B. The proportionality constant, k, called the reaction rate constant, is independent of concentrations.

The dependency of k on temperature follows the Arrhenius equation

$$k = Ae^{-E/R_gT}$$

where A is the frequency (or preexponential) factor and E is the activation energy. Combining the above two equations yields

$$r = - \frac{dC_A}{dt} = Ae^{-E/R_gT} C_A^a C_B^b$$

This provides a description of the rate in terms of the measurable variables, concentration and temperature.

Assuming a first order reaction with respect to A, the above equation reduces to

$$- \frac{dC_A}{dt} = Ae^{-E/R_gT} C_A$$

#### 4.5, Fuel-Rich Hydrocarbon Combustion Data Analysis (cont.)

solving for  $C_A$  gives

$$\ln \frac{C_A}{C_{A_0}} = - A e^{-E/R_g T} t$$

where  $C_{A_0}$  is the initial concentration of fuel A.

Rearranging and solving for  $t$  gives:

$$t = - \frac{\ln (C_A/C_{A_0})}{A e^{-E/R_g T}}$$

For a given  $C_A/C_{A_0}$ , which is actually one minus the fraction decomposed,  $t$  is the time required to achieve this percent decomposition. This parameter can also represent the chamber residence time required for a certain amount of reactants to achieve a certain percent decomposition. Note that the residence time is also a function of temperature.

Using values of  $A = 10^{12}$  and  $E = 79000$ , which are the Arrhenius constants for methane, a plot of gas residence time vs temperature is shown in Figure 73 for various percent methane decomposition. This figure shows that if a certain percent methane decomposition is to be maintained, the gas residence time must be reduced if the gas temperature increases. Methods of reducing gas residence time include increasing throat area and shortening chamber length, both of which reduce the chamber volume.

##### 4.5.3.2 Injector Design Effects

The foregoing sections of this report and its associated appendices have described in great detail the enormous quantity of experimental carbon deposition test results which have been amassed for three distinctly different hydrocarbon fuels. Carbon deposition has been characterized at both main chamber and gas generator operating mixture ratios, different

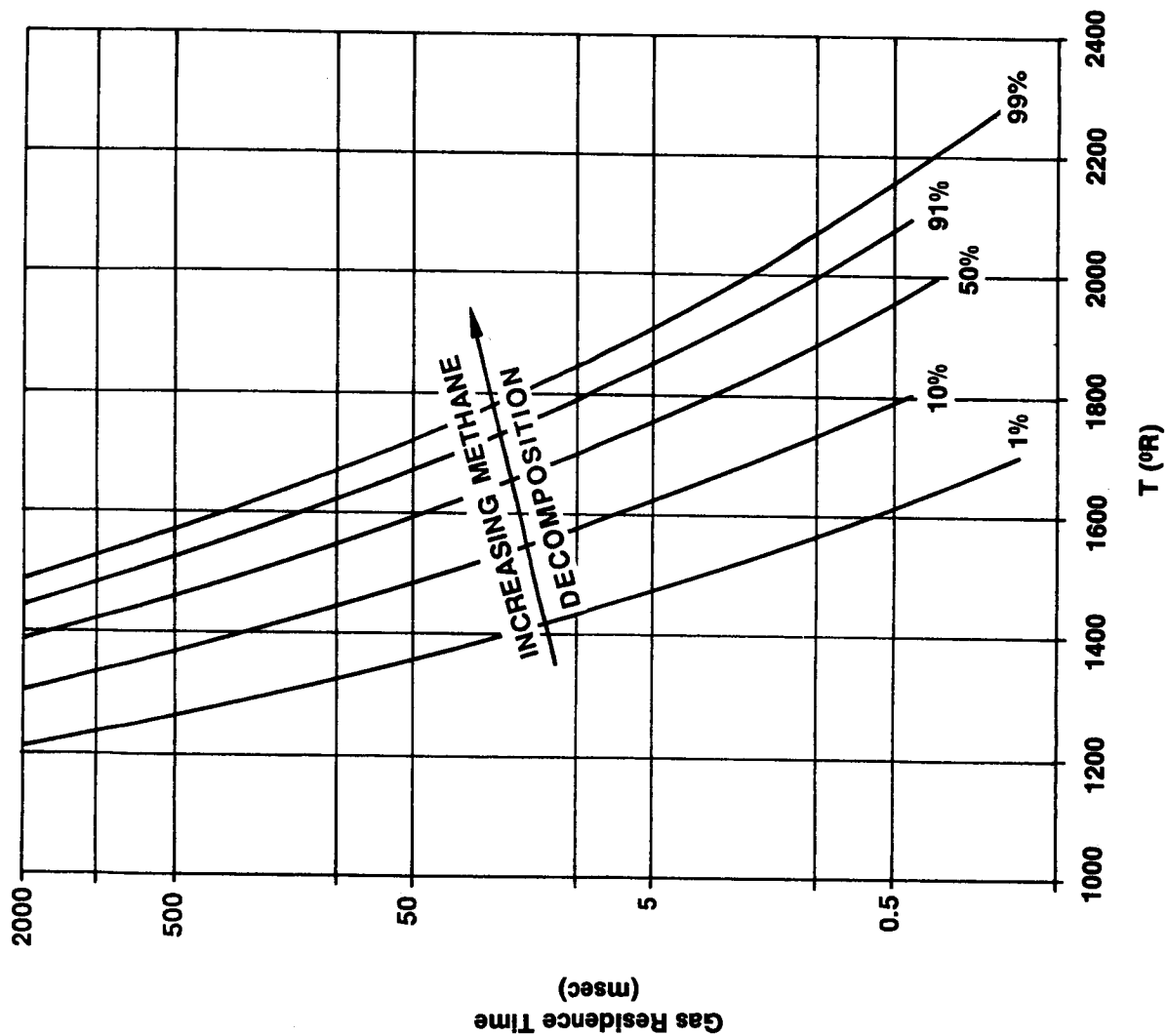


Figure 73. Gas Residence Time vs. Temperature for Methane Decomposition



#### 4.5, Fuel-Rich Hydrocarbon Combustion Data Analysis (cont.)

fuels and different operating conditions. Due to cost considerations, however, only one injector design has been evaluated. The GG evaluated an F-O-F triplet whose circuits were reversed and also tested as an O-F-O triplet at main chamber conditions.

It is of extreme technical importance to Aerojet TechSystems Co. to clearly separate those effects which are either fuel property selection related or chemical kinetics limited to which all future STBE engine contractors are subjected to by nature's laws versus those influences which are injector design related by which a contractor can minimize carbon deposition degradation by utilization of its unique design know how.

This report would be remiss if it did not address the first order injector design sensitivities analytically predicted by existing ATC combustion design models.

##### 4.5.3.2.1 Droplet Atomization Distribution

Gas generators typically operate at low ( $1000^{\circ}\text{F}$  to  $1800^{\circ}\text{F}$ ) ( $811$  to  $1255\text{K}$ ) gas temperatures. Thus the combustion gas to fuel droplet temperature differential limits the droplet vaporization potential. This problem is further aggravated if the selected fuel has a high critical temperature (such as RP-1). The only design variable available to the designer to compensate for this thermodynamic deficiency is to maximize the fuel droplet vaporization surface area; i.e., small fuel drop size.

A desirable feature of any fuel rich  $\text{LO}_2$ /hydrocarbon GG injector is to provide a fine fuel atomizer. On the other hand, the  $\text{LO}_2$  injector requires maximum atomized drop size to minimize carbon deposition. This seemingly incongruous requirement is due to the high volatility of cryogenic  $\text{LO}_2$  coupled with the physical phenomenon of being completely inundated in fuel rich vapors. A stoichiometric flame region surrounds each oxidizer

#### 4.5, Fuel-Rich Hydrocarbon Combustion Data Analysis (cont.)

droplet so that unlike the fuel droplets, the  $LO_2$  droplets vaporize at rates comparable to main chamber conditions. Too rapid  $LO_2$  vaporization rate near the injector face increases local vaporization mixture ratio which accelerates kinetic decomposition rates and increases carbon deposition.

The optimum injector design is one which produces large  $LO_2$  drop sizes such that its vaporization rate at stoichiometric  $\Delta T$  results in equal axial vaporization rate as a fine fuel atomization with a low  $\Delta T$  so that the vaporized mixture ratio is equal to the overall injected mixture ratio so that the high temperature streaks near the injector face are minimized.

The usual design practice of 1960 Technology  $LO_2$ /RP-1 gas generator designs was to utilize nearly equal diameter fuel and oxidizer injection orifices. The fuel rich GG mixture ratio was achieved by providing more fuel elements and fewer oxidizer elements. Thus virtually all GG's encountered oxidizer rich combustion near their injector faces. This can be attributed to two factors. First, the GG injector designers utilized their previous design experience based on main injector development programs. Second, mechanistic analytical combustion models describing the cause and effect relationship between injector design and gas generator operation were unavailable at the time.

##### 4.5.3.2.2 Fuel Volatility Influences

Section 4.5.2 already addressed the first order effect of fuel type selection upon carbon deposition. In addition, there is a second order but still significant influence which the engine system designer or component designer can still exert upon minimizing carbon deposition for any given fuel selection.

#### 4.5, Fuel-Rich Hydrocarbon Combustion Data Analysis (cont.)

Fuel volatility can be controlled somewhat by variation in fuel injection temperature. This can be achieved by selection of fuel storage temperature in the fuel tank, the fuel bulk temperature rise for regenerative cooling, or even by providing a heat exchanger for fuel temperature conditioning. Fuel heating causes reduction in viscosity and surface tension which yields smaller fuel droplet sizes for a given injection element type and orifice diameter. In addition, it decreases its vapor pressure, reduces its heat sink capacity and speeds up fuel vaporization rate. It is advantageous to heat the hydrocarbon fuel as hot as possible (but less than 20°F (266K) below its critical temperature) without incurring liquid coolant side coke deposits. The reason that fuels should not be heated to within closer than 20°F (266K) of the critical temperature is that wide variations in fuel density, viscosity and vapor pressure occur very near the critical temperature which makes analytical predictability less reliable.

The optimum LO<sub>2</sub>/hydrocarbon system is one which utilizes a very dense fuel stored at cold temperature in the fuel tank. This minimizes fuel tankage weight, fuel turbopump size and weight, and GG cycle performance degradation. This cold fuel should then be used to regeneratively cool low to moderate heat flux components such as main engine nozzles, gas generator and turbine manifold, warm gas ducts, etc. If this heating is inadequate, a fuel heat exchanger may also be desirable before injecting the warm lower density fuel into the gas generator and main injector.

##### 4.5.3.2.3 Mixing Uniformity Effect on Carbon Deposition

An injector pattern which provides uniform fuel/oxidizer mixing will maximize fuel droplet vaporization rate in the shortest possible chamber. A uniform mixer offers the following design benefits:

#### 4.5, Fuel-Rich Hydrocarbon Combustion Data Analysis (cont.)

- Maximum  $[T_{\text{gas}} - T_{\text{fuel droplet}}]_{\text{local}}$  maximizes fuel vaporization efficiency for given fuel drop size.
- Uniform mixing minimizes the hottest gas streak temperature which slows carbon deposition producing kinetic rates.
- Coolest streak temperature reduces GG/TPA development risk and maximizes engine cycle life.
- Minimizes required GG chamber length and hence gas residence time available for carbon deposition reaction kinetics.

##### 4.5.3.2.4 Mixer Design Benefits

Molecular diffusivity is reduced by high molecular weight gases, low gas temperatures and high combustion gas pressures. All of these conditions can occur in fuel-rich  $\text{LO}_2$ /hydrocarbon gas generators. Mechanical mixers can be used to augment the injector designed liquid phase  $\text{LO}_2$ /hydrocarbon mixing distribution.

The requirement for mechanical mixing aids is due to gas generator combustors being relatively low energy systems. Analysis has shown that the bulk of the bipropellant combustion enthalpy released by the lean propellant occurs within the first 1-in. (2.54 cm) or 2-in. (5.08 cm) from the injector face. This zone is characterized by intense combustion turbulence coupled with injector pattern induced fluid dynamic effects. Downstream of this zone, however, the combustion process is primarily reduced to one of diluent vaporization of the rich propellant. From a differential enthalpy standpoint it is practically inert. Thus if the injector spray pattern is not uniform, the diluent vaporization results in progressive self-insulation

#### 4.5, Fuel-Rich Hydrocarbon Combustion Data Analysis (cont.)

between relatively hot and cold gas zones. These striated temperature regions effectively form stream tubes which are essentially axial with little radial mixing.

Lateral mixing between these cool fuel rich zones and hotter oxidizer rich zones can be enhanced by utilizing turbulence rings, splash plates, lateral mixing baffles, reverse flow gas ducts or packed columns. The basic design principle which makes these devices effective depends upon forcing lateral movement of the hotter combustion products relative to the unvaporized diluent "droplets" which are not deflected laterally as much as the combustion gases due to their higher density and initial momentum. Differences in gas temperature, molecular weight and  $\gamma$  between hot and cold stream tubes accentuate differences in gas velocity through or around these restrictions and increase shear mixing efficiency. the abrupt chamber expansion or turn downstream of the restriction will induce gas recirculation and further mixing.

Two primary considerations should be given to the mixing aid design. First, if placed too close to the injector face, lean droplet impingement can cause mixer overheating and erosion. Mixing effectiveness is maximized if it is located where the stream tube thermal striations are greatest. The vaporization analysis can determine the optimum axial location for each gas generator. Second, a tradeoff must be made between combustion gas  $\Delta P$  across the mixing aid vs desired mixing efficiency.

The packed column technology is based upon a different set of design principles. Packed columns have long been utilized in the chemical process industries wherein gas/liquid reactions are limited by contact surface area, low temperature differentials, small chemical species differentials in absorption/desorption devices, or otherwise inhibited by mixing limitations.

#### 4.5, Fuel-Rich Hydrocarbon Combustion Data Analysis (cont.)

Developers of the Ariane launch vehicle for the European Space Agency have designed and demonstrated a stoichiometric  $\text{LO}_2/\text{LH}_2$  preburner design which incorporates a Rashig ring to promote diluent vaporization and mixing. The purpose of the Rashig ring is to increase diluent droplet residence time in short chamber lengths having short gas residence times, increase available diluent surface contact area with the gas, increase liquid film/gas velocity differential to increase evaporation efficiency, provide thermal conduction from hot to cold zones while accelerating vaporization rates in cooler zones, and promote turbulent mixing via the tortuous flow path. The feasibility of using this mixing concept might provide benefits for minimizing carbon deposition.

The packed column design concept utilizing packings such as the Raschig ring is illustrated in Figure 74. Because most packed column chemical processes take place at near atmospheric pressure levels, the applicability of this data to fuel-rich  $\text{LO}_2$ /hydrocarbon gas generator design, particularly in regard to acceptable packing  $\Delta P$ , needs to be evaluated.

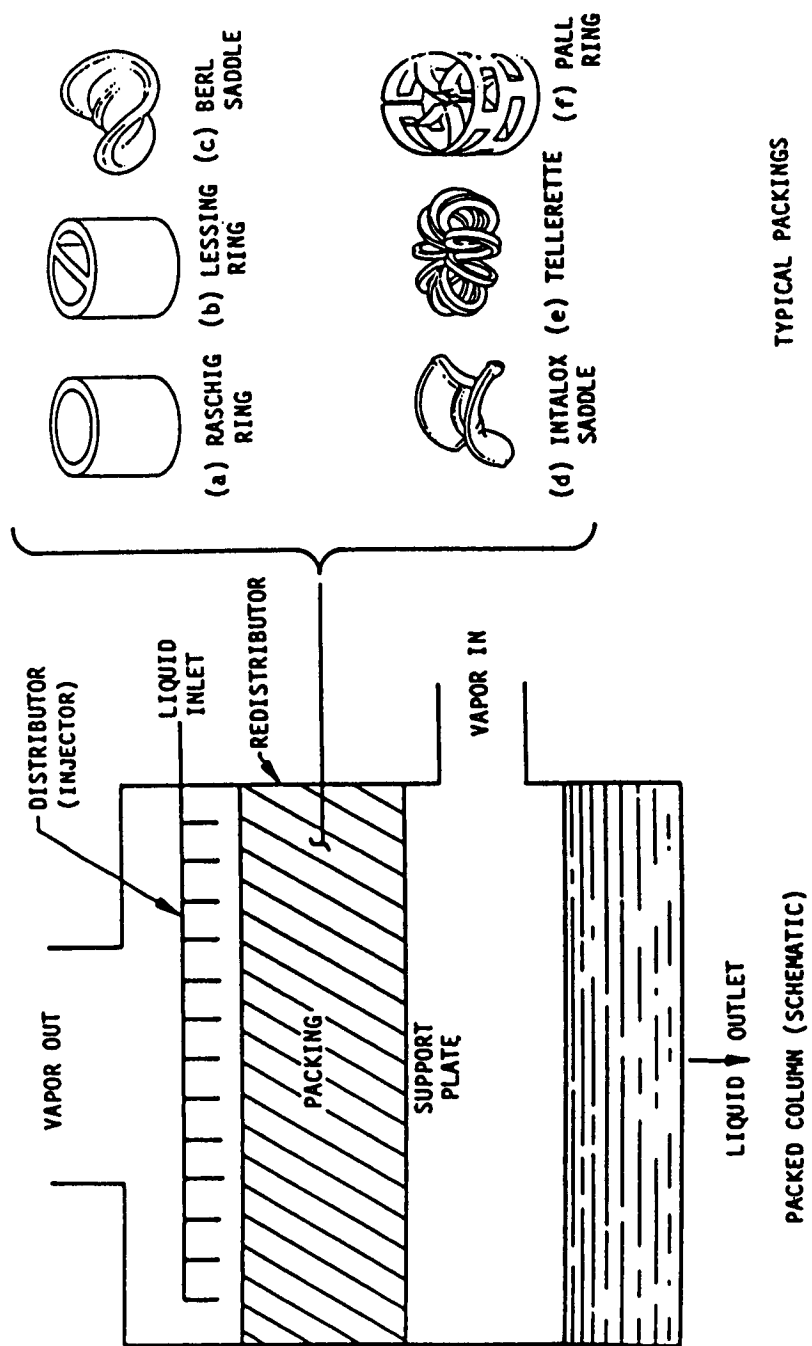


Figure 74. Packed Column Technology is Mature in Chemical Process Industry

## REFERENCES

1. Fuel/Oxidizer-Rich, High Pressure Preburners, Contract NAS 3-21753.
2. Testing of Fuel/Oxidizer-Rich, High Pressure Preburners, Contract NAS 3-22647.
3. Combustion Performance and Heat Transfer Characterization of LOX/Hydrocarbon Type Propellants, Contract NAS 9-15958.
4. Dual-Fuel and Dual-Throat Engine Preliminary Analysis, Contract NAS 8-32967.
5. High-Density Fuel Combustion and Cooling Investigation, Contract NAS 3-21030.
6. Taylor, W.F., "Deposit Formation from Deoxygenated Hydrocarbons," Industrial and Engineering Chemistry, 13, [2], 133-138 (1974).
7. Taylor, W.F., "Kinetics of Deposit Formation from Hydrocarbons," Industrial and Engineering Chemistry, 8 [375] (1969).
8. Taylor, W.F. and Wallace, T.J., "Kinetics of Deposit Formation in Hydrocarbons - Effect of Trace Sulfur Compounds," Industrial and Engineering Chemistry, 7 [198] (1968).
9. High-Pressure LOX/Hydrocarbon Preburners and Gas Generators, Contract NAS 8-33243.
10. Glassman, I., "Phenomenological Models of Soot Processes in Combustion Studies," Princeton University Engineering Report No. 1450, July 1979.
11. F-1 Quarterly Progress Report, Period October 1, 1963 to December 31, 1963.



INTERIM FINAL REPORT DISTRIBUTION LIST  
CARBON DEPOSITION MODEL  
NAS 8-34715

<u>Name</u>	<u>No. of Copies</u>
National Aeronautics & Space Administration Washington, D.C. 20546	
Attn: RP/F.W. Stephenson	1
George C. Marshall Space Flight Center National Aeronautics & Space Administration Marshall Space Flight Center, Alabama 35812	
Attn: CN24D	3
AT01	1
CC01	1
EM13B	1
EP53/C.R. Bailey	1
EP52/F.W. Braam	2 + repro
Lewis Research Center National Aeronautics & Space Administration 21000 Brookpark Road Cleveland, Ohio 44135	
Attn: MS 60-3/Library	1
MS 500-219/S. Gorland	1
AMES Research Center National Aeronautics & Space Administration Moffett Field, CA 94035	
Attn: Library	1
Goddard Space Flight Center National Aeronautics & Space Administration Greenbelt, MD 20771	
Attn: Library	1
John F. Kennedy Space Center National Aeronautics & Space Administration Kennedy Space Center, FL 92899	
Attn: Library	1

<u>Name</u>	<u>No. of Copies</u>
Lyndon B. Johnson Space Center National Aeronautics & Space Administration Houston, TX 77058	
Attn: Library	1
Langley Research Center National Aeronautics & Space Administration Langley Station Hampton, VA 23665	
Attn: Library	1
Jet Propulsion Laboratory National Aeronautics & Space Administration 4800 Oak Grove Drive Pasadena, CA 91109	
Attn: Library	1
NASA-Scientific & Technical Information Facility P.O. Box 8757 Baltimore-Washington International Airport Baltimore, MD 21240	
Attn: Accessioning Department	3 + repro
Defense Documentation Center Cameron Station, Building #5 5010 Duke Street Alexandria, VA 22314	
Attn: TISIA	3
Air Force Astronautics Laboratory Edwards, CA 93523	
Attn: Library	1
AFAL/LKDA, M. Walker	1
U.S. Army Missile Command Redstone Scientific Information Center Redstone Arsenal, AL 35808	
Attn: Documents Section	2

NameNo. of Copies

Boeing Company  
Space Division  
P.O. Box 868  
Seattle, WA 98124

Attn: Library

1

General Dynamics/Convair  
P.O. Box 1128  
San Diego, CA 92112

Attn: Library

1

Grumman Aerospace Corporation  
Bethpage, L.I., N.Y. 11714

Attn: Library

1

Lockheed Missile & Space Company  
P.O. Box 504  
Sunnyvale, CA 94088

Attn: Library

1

Marquardt Corporation  
16555 Saticoy Street  
Box 2013 South Annex  
Van Nuys, CA 91409

Attn: Library

1

Martin-Marietta Corporation  
P.O. Box 179  
Denver, CO 80201

Attn: Library

1

McDonnell Douglas Astronautics  
5301 Bolsa Avenue  
Huntington Beach, CA 92547

Attn: Library

1

Rockwell International Corporation  
12214 Lakewood Blvd  
Downey, CA 90241

Attn: Library

1

Name

No. of Copies

United Technologies Pratt & Whitney  
Government Products Division  
P.O. Box 109600  
West Palm Beach, FL 33410-9600

Attn: Library  
MS 731-26/W. Visek

1  
1

Rockwell International Corporation  
Rocketdyne Division  
6633 Canoga Avenue  
Canoga Park, CA 91303

Attn: Library  
FA14/F. Kirby

1  
1

APPENDIX A  
NOMENCLATURE  
AND  
UNIT CONVERSION FACTORS

## NOMENCLATURE

AN	Air Force/Navy Standard fitting
$A_t$	throat area
ATC	Aerojet TechSystems Company
BOSF	Burn Out Safety Factor
$C_{DA}$	effective area for fluid flow
$C_g$	$h_g(\text{experimental})/h_g(\text{theoretical})$
$C_{g,in}$	$h_g(\text{experimental})/h_g(\text{theoretical})$
$c_p$	specific heat at constant pressure
$C^*$	characteristic velocity
$C^*_{\text{gas}}$	gas characteristic velocity
$C^*_{\text{test}}$	characteristic velocity from test data
$C^*_{\text{ODE}}$	characteristic velocity from ODE
C/H	carbon to hydrogen mole ratio
$\text{CH}_4$	chemical formula for methane
$\text{C}_2\text{H}_2$	chemical formula for acetylene
$\text{C}_2\text{H}_4$	chemical formula for ethylene
$\text{C}_2\text{H}_6$	chemical formula for ethane
$\text{C}_3\text{H}_6$	chemical formula for propylene
$\text{C}_3\text{H}_8$	chemical formula for propane
$\text{C}_{12}\text{H}_{26}$	chemical formula for RP-1
$D_c$	chamber diameter
Dia	diameter
$D_o$	oxidizer injector orifice diameter
$D_f$	fuel injector orifice diameter
$D_t$	throat diameter
EB	Electron Beam Welding
EDM	Electro Discharge Machining
FFC	fuel-film cooling
FOF	fuel-oxidizer-fuel injector pattern
FRCM	Fuel Rich Combustion Model
FTY	yield strength
$g_c$	gravitational constant
GG, gg	gas generator
$\text{GH}_2$ , $g\text{H}_2$	gaseous hydrogen
$\text{GN}_2$	gaseous nitrogen

GOX	gaseous oxygen
H <sub>2</sub>	hydrogen
H <sub>2</sub> O	water
HC	hydrocarbon
h <sub>g</sub>	heat transfer coefficient
I <sub>sp</sub>	specific impulse
JANNAF	Joint Army, Navy, NASA, Air Force
KOJ	Kistler high-frequency pressure transducer-oxidizer
KFJ	Kistler high-frequency pressure transducer-fuel
K <sub>w</sub>	hydraulic admittance
L/D	length-to-diameter ratio
LH <sub>2</sub>	liquid hydrogen
LNG	liquified natural gas
L'	chamber length
LOX, LO <sub>2</sub>	liquid oxygen
1L	first longitudinal mode instability
M <sub>inner</sub>	momentum through inner circle of injection elements
M <sub>outer</sub>	momentum through outer circle of injection elements
MR	mixture ratio
MR <sub>gas</sub>	gas mixture ratio
MRGG	gas generator mixture ratio
MW	molecular weight
NASA/LeRC	NASA Lewis Research Center
NBP	normal boiling point
Ni	chemical symbol for nickel
nom	nominal
O <sub>2</sub>	chemical formula for oxygen
O/F, w <sub>ox</sub> /w <sub>f</sub>	mixture ratio
ODE	One Dimensional Equilibrium
OFHC	oxygen-free high-conductivity copper
OFO, O-F-O	oxidizer-fuel-oxidizer injector pattern
OMS	Orbital Maneuvering System
ox, OXID	oxidizer
P <sub>c</sub> or PC	chamber pressure
P <sub>c cav</sub>	pressure in acoustic cavity (Taber transducer)
P <sub>cav HF</sub>	pressure in acoustic cavity (Kistler transducer)
P <sub>coolant in</sub>	coolant inlet pressure
P <sub>coolant out</sub>	coolant outlet pressure
PCTSD	chamber pressure downstream of turbine simulator
PCTSU	chamber pressure upstream of turbine simulator

Pk-to-Pk	peak-to-peak
PFJ	fuel injection pressure
$P_{\text{gas}}$	gas pressure
$P_{\text{in}}$	inlet pressure
$P_{\text{manifold out}}$	manifold outlet pressure
POJ	oxidizer injection pressure
PRTSC	PCTSD/PCTSU
PWC	pressure of water coolant
PWI	inlet pressure of water coolant
R	gas constant
RAD	radius
RCS	
RP-1	hydrocarbon fuel similar to kerosene
SCALED	
SINDA	Systems Improved Numerical Differencing Analyzer
$T_{\text{gas}}$	gas temperature
TC or T/C	thermocouple
TCA	thrust chamber assembly
$T_{\text{coolant in}}$	coolant inlet temperature
$T_{\text{coolant out}}$	coolant outlet temperature
TCR	thermocouple reading
TIG	Tungsten Inert Gas Welding
$T_{\text{manifold out}}$	manifold outlet temperature
TRAN72	computer program to calculate thermodynamic and transport properties of complex mixtures
TWC	temperature of water coolant
$V_c$	chamber volume
$w_f$	fuel flow rate
$w_{\text{ox}}$ or $w_o$	oxidizer flow rate
$w_t$ , WTOT	total flow rate
Zr-Cu, ZrCu	zirconium-copper alloy
$\Delta H$	enthalpy
$\Delta P$	pressure drop
$\eta_{c^*}$	$c^*_{\text{test}} / c^*_{\text{ode}}$
$\epsilon_c$	area ratio in convergent section
$\epsilon_e$	area ratio in divergent section
$\gamma$	gas specific heat ratio, $c_p / c_v$
$\phi_g$	gas side heat flux
$\rho$	fluid density
$\tau$	gas residence time



## UNIT CONVERSION FACTORS

(ENGLISH TO SI)

$$1 \text{ Btu/in.}^2\text{-s} = 0.163 \text{ kW/cm}^2$$

$$1^\circ\text{F} = 32 + 1.8 (^\circ\text{K} - 273)$$

$$1 \text{ ft/s} = 30.48 \text{ cm/s}$$

$$1 \text{ in.} = 2.54 \text{ cm}$$

$$1 \text{ kcal/mol} = 4.184 \text{ kJ/mol}$$

$$1 \text{ lbm/s} = 0.45359 \text{ kg/s}$$

$$1 \text{ psi} = 0.006895 \text{ MPa}$$

APPENDIX B  
LITERATURE REVIEW OF CARBON DEPOSITION MODEL

RPT/AA0631-B

## TABLE OF CONTENTS

	<u>Page</u>
1. Carbon Deposition Fundamentals	B-5
a. Nucleation	B-8
b. Growth and Agglomeration	B-9
c. General Comments	B-10
2. Thrust Chambers	B-12
3. Gas Generators and Preburners	B-38
4. Gas Turbines	B-46
5. Summary of Results	B-50
References	B-61

## LIST OF FIGURES

<u>Figure No.</u>		<u>Page</u>
B-1	The Structure of the Carbon Deposit Reveals the Deposition Mechanism	B-11
B-2	Sellers Data Show Carbon Deposits Build Up or Spall Off	B-13
B-3	Effect of Mixture Ratio on Carbon Deposits	B-14
B-4	Seader and Wagner's Carbon Deposit Correlation	B-16
B-5	P&W Related Carbon Deposits to Fuel Chemistry	B-17
B-6	P&W Data on Carbon Deposit Mixture Ratio Dependence	B-18
B-7	P&W Data Relating Carbon Deposit and Chamber Location	B-19
B-8	P&W Data Show Carbon Buildup Transient	B-21
B-9	Rocketdyne Correlation of P&W Butene-1 Data	B-22
B-10	Rocketdyne Correlation of P&W 100 psia (.689 MPa) Methane Data	B-24
B-11	Rocketdyne Correlation of P&W 250 psia (1.72 MPa) Methane Data	B-25
B-12	Aerojet Flox-Methane Data Show Spalling	B-26
B-13	Rocketdyne Related P&W Data to Combustion Gas Chemistry	B-27
B-14	Rocketdyne Correlations for Deposit Resistance with Different Fuels	B-29
B-15	Carbon Formation Trends Observed on Aerojet Photographic Combustion Program	B-31
B-16	Photo-Combustion Program Data Show High Pressure Reduces Soot Formation	B-32
B-17	Aerojet LOX/RP-1 Calorimetric Heat Transfer Data	B-34
B-18	Rocketdyne Correlation Doesn't Predict Calorimeter Chamber Results	B-36
B-19	Effect of Carbon Deposit Roughness Depends on Chamber Size	B-37
B-20	Long Duration Carbon Deposition Effects in Titan I Gas Generators	B-39
B-21	The Kinetically Limited Combustion Model Matches Preburner Test Data	B-42
B-22	The Turbulence Ring Provided a Very Uniform Gas Cloud	B-44

## LIST OF FIGURES (cont.)

<u>Figure No.</u>		<u>Page</u>
B-23	Carbon Particle Size Determines How It Reaches the Wall	B-49
B-24	Carbon Deposition Trends	B-51
B-25	Hydrogen/Carbon Atomic Ratio Correlation Model	B-52
B-26	Combustion Gas Mass Velocity Correlated Model	B-53
B-27	Combustion Gas Carbon Atomic Fraction Correlation Model	B-54
B-28	Static Pressure Correlation Model	B-55
B-29	Adsorption Correlation Model	B-56
B-30	Reynolds Number Correlation Model	B-57
B-31	Length Based Reynolds Number Correlation Model	B-59
B-32	ALRC Carbon Deposition Correction Model	B-60

This section describes the carbon deposition state-of-the-art particularly as it relates to liquid rocket engine applications. This section is divided into five subsections. The first subsection provides an overview of the fundamentals of the deposition process. The next three subsections address the history and status of carbon deposition in thrust chambers, gas generators (and preburners) and gas turbines. Gas turbines are included because of the nonrocket devices, gas turbines most closely approximate the carbon deposition phenomenon that occurs in rocket engines. The last subsection summarizes the results of the state-of-the-art review, the existing data trends and a review of the potential empirical models.

#### 1. Carbon Deposition Fundamentals

The deposition of carbon from reacting hydrocarbon-oxygen mixtures is the result of two processes. The first is the generation of free carbon (soot) in the reaction zone and the second is the series of events (nucleation or condensation, agglomeration, impingement, and adhesion) which result in the transfer of some of this carbon from the reaction zone to a layer on the container surface. These two processes will be discussed in this subsection.

The formation of soot during the combustion process has been studied extensively by many researchers. An excellent review of the field is that of Glassman (Ref. B-1). Due to the nature of the soot-forming process the majority of the soot formation studies have focused on the chemistry of hydrocarbon pyrolysis and oxidation. Many different series of reactions have been hypothesized as ultimately leading to the formation of soot. This information is too voluminous to be included here. However, there are several important observations from this large body of data which appear particularly relevant to this program. These are:

- (a) In general, the properties (not quantity) of the carbons formed in flames are not particularly sensitive to the type of flame, the fuel used, or the conditions under which it was formed.

- (b) Acetylene is generally considered to be the chemical precursor to soot.
- (c) Soot formation occurs very rapidly in spite of the complexity of the chemical processes leading to it. Soot formation times are typically 1 msec or less at atmospheric pressure.  
(Note: Under high pressure rocket conditions soot formation will likely be even faster.)
- (d) The tendency of a fuel to form soot is not determined solely by its C/H ratio. In an interesting experiment by Glassman et al. (Ref. B-2), the sooting behavior of ethane was compared with that of ethylene-hydrogen, and acetylene-hydrogen mixtures having the same C/H ratio. The acetylene mixture showed a far greater propensity to soot than the ethylene mixture, which soots more extensively than ethane. Although the different combustion temperatures for each fuel contributed somewhat to the difference in sooting, the trends are believed valid.
- (e) The addition of a small amount of oxidizer to a fuel-rich diffusion (i.e., mixing limited) flame strongly increases the sooting tendency. This is the result of the homogeneous catalytic effect of small amounts of oxidizer on pyrolysis reactions. There is a point beyond which the addition of more oxidizer causes a decrease in sooting.

One of the more significant conclusions from the work on soot formation is the dependence of the soot formation process on the flame type. Two categories of flames have been identified: diffusion flames (i.e., mixing limited), and premixed flames (i.e., kinetically limited). The effect of temperature on sooting in these two types of flames is directly opposite. In premixed flames as the temperature rises the rate of oxidative attack on the soot precursors increases faster than the rate of precursor formation through pyrolysis. Thus, the higher the temperature the less is the tendency to soot.

In diffusion flames precisely the opposite occurs. The dominant factors in diffusion flames are the temperature and fuel structure. However, here the rate of pyrolysis of the fuel has no competitive oxidative attack. Thus the higher the temperature, the greater is the rate of fuel pyrolysis and the greater the propensity to soot.

This conclusion has a bearing on the interpretation of test results from this program.  $\text{LO}_2/\text{RP-1}$  main chamber combustion, with the burning of fuel droplets in a cloud of oxygen-rich gas, is generally considered to be a diffusion-type flame. However, there are conditions which could drive the combustion towards a premixed condition. The use of more volatile fuels (methane, propane, heated RP-1) or operating at supercritical pressures could both be expected to encourage premixed flame combustion and modify the carbon formation process.

Once carbon has been formed in the hot gas stream it still must be deposited on the solid surface. Published literature indicate there are two different mechanisms by which this can occur (Ref. B-3). The first is deposition by direct condensation in which individual (gaseous) carbon molecules condense on the surface much the same as steam will condense on a cold metal plate. The second mechanism is by formation of gas-borne aggregates which are then incorporated into a surface deposit. This is analogous to steam condensing as ice particles (as happens with clouds at high altitudes) and the particles subsequently striking and adhering to the surface. In a real system both mechanisms can occur simultaneously.

On the basis of thermodynamics (i.e., minimization of free energy), deposition by direct condensation is favored. It would be the dominant mechanism if there were sufficient surface area conveniently available to prevent the level of supersaturation required to nucleate gas-borne particles. However, this is generally not the case in rocket engines. In rocket components, most of the combustion occurs many mean-free-paths removed from any surface. As a result, direct condensation is minimized and gas-phase nucleation with subsequent wall impingement becomes the most likely source of carbon deposits. The remainder of this subsection discusses this process of gas



phase carbon nucleation, carbon particle growth, and briefly comments on several other aspects of carbon deposition. The development follows that of Jensen (Ref. B-3). The fundamentals of carbon particle impingement and adhesion to the walls will not be included here as they are addressed in connection with gas turbines in Subsection 4.

#### a. Nucleation

A vapor phase will condense only when its vapor pressure exceeds the saturation vapor pressure. In combustion systems, the vapor pressure of  $C_2$  often exceeds the saturation vapor pressure. Homogeneous nucleation (i.e., condensation inside the gas cloud as opposed to condensation on a solid surface) requires the formation of sufficiently large nuclei for subsequent growth from molecules of the vapor. Such formation normally requires a high degree of supersaturation.

The degree of supersaturation required to begin forming solid particles of carbon in the combustion gas cloud depends on the size of the particle nuclei available in the gas cloud. This can be expressed mathematically as follows. The equilibrium vapor pressure ( $P$ ) above a surface (with radius of curvature  $r$ ) exceeds that above a flat surface ( $P_0$ ) as predicted by the Kelvin equation (Equation 1).

$$\ln (P/P_0) = 2\gamma v/kT \ln S \quad (1)$$

In this equation,  $\gamma$  is the surface free energy,  $v$  is the molecular volume in the condensed phase,  $k$  is the Boltzman constant, and  $T$  is the temperature. Therefore, for a supersaturation ratios (i.e.,  $P/P_0$ ) condensation may occur on a spherical droplet of radius  $r$  when Equation 1 is satisfied.

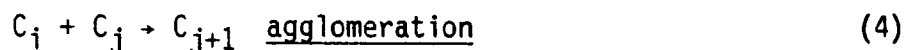
$$r \geq r_c = 2\gamma v/kT \ln S \quad (2)$$

This equation predicts that smaller droplets will evaporate and do not contribute to homogeneous nucleation. Droplets with  $r > r_c$  will tend to grow indefinitely.

It is difficult to calculate  $r_c$  for carbon because of the large uncertainties concerning  $n$  and  $S$  in combustion and pyrolysis systems. It is not likely that  $n$  is as high as  $2 \times 10^{-4}$  J/cm<sup>2</sup> or  $S$  as low as 100 under conditions of incipient soot formation. Therefore, it is unlikely that  $r_c$  will be as large as 0.3 nm ( $V \sim 10^{-23}$  ml). A carbon fragment of this size contains only a few atoms, and as such there is nothing in this classical calculation to suggest that species as small as  $C_2$  and  $C_3$  are not capable of inducing homogeneous nucleation. Thus the formation of solid carbon particles in the combustion gas cloud.

#### b. Growth and Agglomeration

Once carbon particles have formed in the gas cloud they begin to grow and agglomerate. Based on the preceding discussion, it is reasonable to assume that the particles with which nucleation occurs are  $C_2$ ,  $C_3$  and  $C_2H$ . It is also reasonable to suggest  $C_2$ ,  $C_3$ ,  $C_2H_2$  as growth species. The formation of small soot particles may be treated to a first approximation as irreversible. The growth and agglomeration reactions take the following similar forms.



The rate equations will therefore take the following form.

$$-d[C_i]/dk = d[C_{j+1}]/dt = k_{\alpha ij} [C_i][C_j] \quad (5)$$

$$-d[C_j]/dt = d[C_{j+1}]/dt = k_{\beta ij} [C_i][C_j] \quad (6)$$

$$(n_{j+1} - n_j)k_{\beta ij} = n_i k_{\alpha ij} \quad (7)$$

The rate constants ( $k$ 's) for the growth and agglomeration reactions are published in Reference B-3.

The agglomeration and growth rate equations, which must be solved simultaneously with the pyrolysis decomposition equations, are most practically solved by computer analysis. Such a program has been developed by Jensen. When applied to the non-equilibrium decomposition of methane, the concentrations predicted for the various species with time agree fairly well with experimental results if  $C_2H$  is chosen as the initial nucleus with  $C_2H_2$  as the growth species. The accuracy of the rate data used impose the accuracy limits on this analysis.

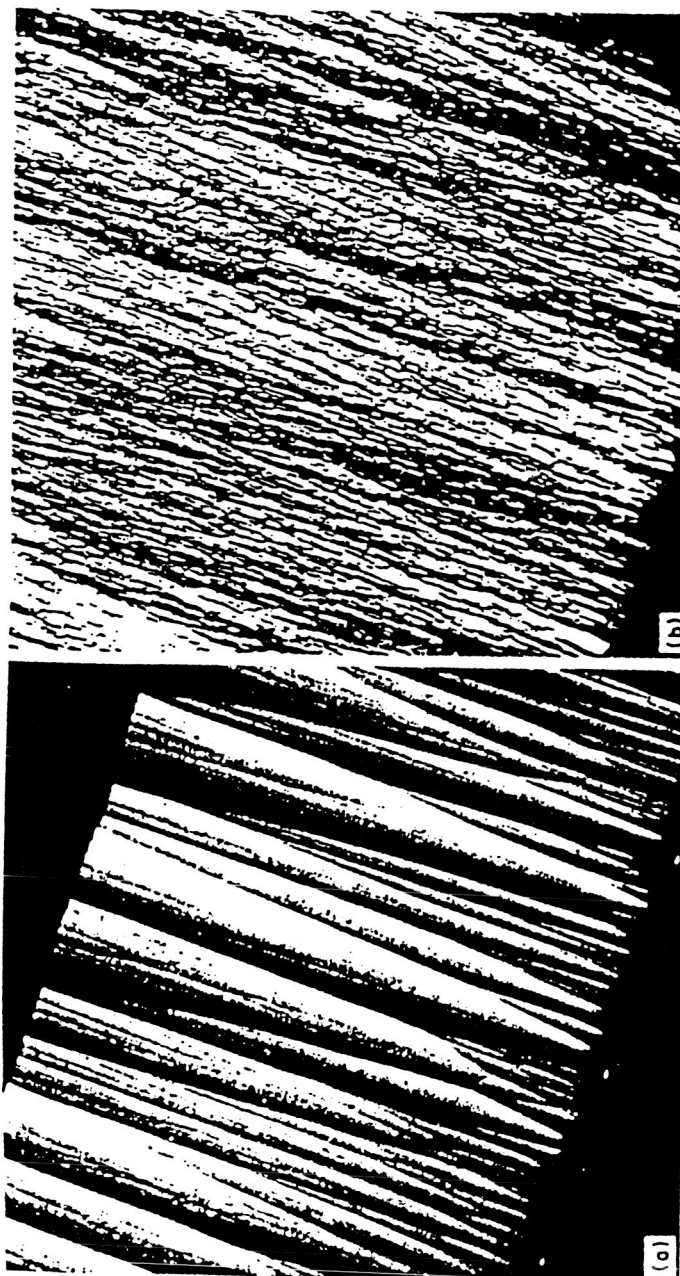
### c. General Comments

In the preceding subsection, it was noted that carbon deposition can occur by two mechanisms: direct condensation from the vapor phase, or by impingement by particles which are formed in the gas cloud. Which of these two mechanisms was involved in creating a particular deposit can be inferred from the structure of the deposit. When viewed metallographically with polarized light, the deposits which are primarily surface nucleated will consist of well-developed growth cones. The presence of gas-borne particles results in what has been described as a continuously nucleated deposit. These two types of deposits are illustrated in Figure B-1 from Bokros (Ref. B-4).

This program addressed both the thermal resistance of carbon deposits (main chambers) and the physical thickness of the deposits (gas generators). If the thermal conductivity of the deposit were known accurately, it would be possible to relate thickness to resistance and possibly simplify the program. With this in mind, it is appropriate that a few comments be made on the thermal conductivity of deposited carbon.

The thermal conductivity of deposited carbon is highly dependent on the crystallite size and the degree of anisotropy. Carbon crystallites conduct primarily along layer planes, and therefore the conductivity of an aggregate of crystallites depends on the crystallite size and the preferred orientation.

ORIGINAL PAGE IS  
OF POOR QUALITY



(a) Singularly or substrate nucleated pyrolytic carbon; (b) regenerative or continuously nucleated pyrolytic carbon. Polarized light.

**Figure B-1. The Structure of the Carbon Deposit Reveals the Deposition Mechanism**

At very high temperatures ( $>2,000^{\circ}\text{C}$ ), the thermal conductivity of polycrystalline carbons has been shown to be much less dependent on crystallite size than at low temperature. The effect of anisotropy (i.e., directional properties) is then the dominant factor at very high temperatures, with isotropic (non-directional) carbons being much more conductive than laminar carbons. High deposition temperatures favor formation of the isotropic deposits. The thermal conductivity of carbon deposits vary considerably due to the high variability in crystallite size and anisotropy inherent in the deposits. For this reason direct measurement of the thermal resistance of a deposit is much more accurate than calculating it based on a measured thickness and published conductivity values.

## 2. Thrust Chambers

In 1961 Sellers (Ref. B-5) presented a paper on carbon deposition in  $\text{LO}_2/\text{RP-1}$  engines. He noted that during engine firings there was a buildup of a gas side carbon layer which acted as a very effective thermal barrier, greatly increasing the wall thermal resistance and dropping the wall heat flux. He also reported that locally the surface temperatures had a sawtooth character which he attributed to a periodic buildup and spalling off of the carbon layer. This behavior is illustrated in Figure B-2 which is a reproduction of his data. Sellers stated that the thermal resistance of the carbon layer was essentially independent of mixture ratio over the range tested as shown in Figure B-3. His data base covered a chamber pressure range of roughly 800 to 1150 psia (5.52 to 7.93 MPa) and mixture ratio range of 1.6 to 2.8. He presented no relationship correlating carbon deposition with engine operating conditions.

In 1964 Seader and Wagner (Ref. B-6) discussed carbon deposition in a paper on regenerative cooling. They presented the following equation relating the steady-state thermal resistance of the deposit to the engine operating conditions.

$$\ln_e\left(\frac{X}{K}\right) = 10 - 0.51 G$$

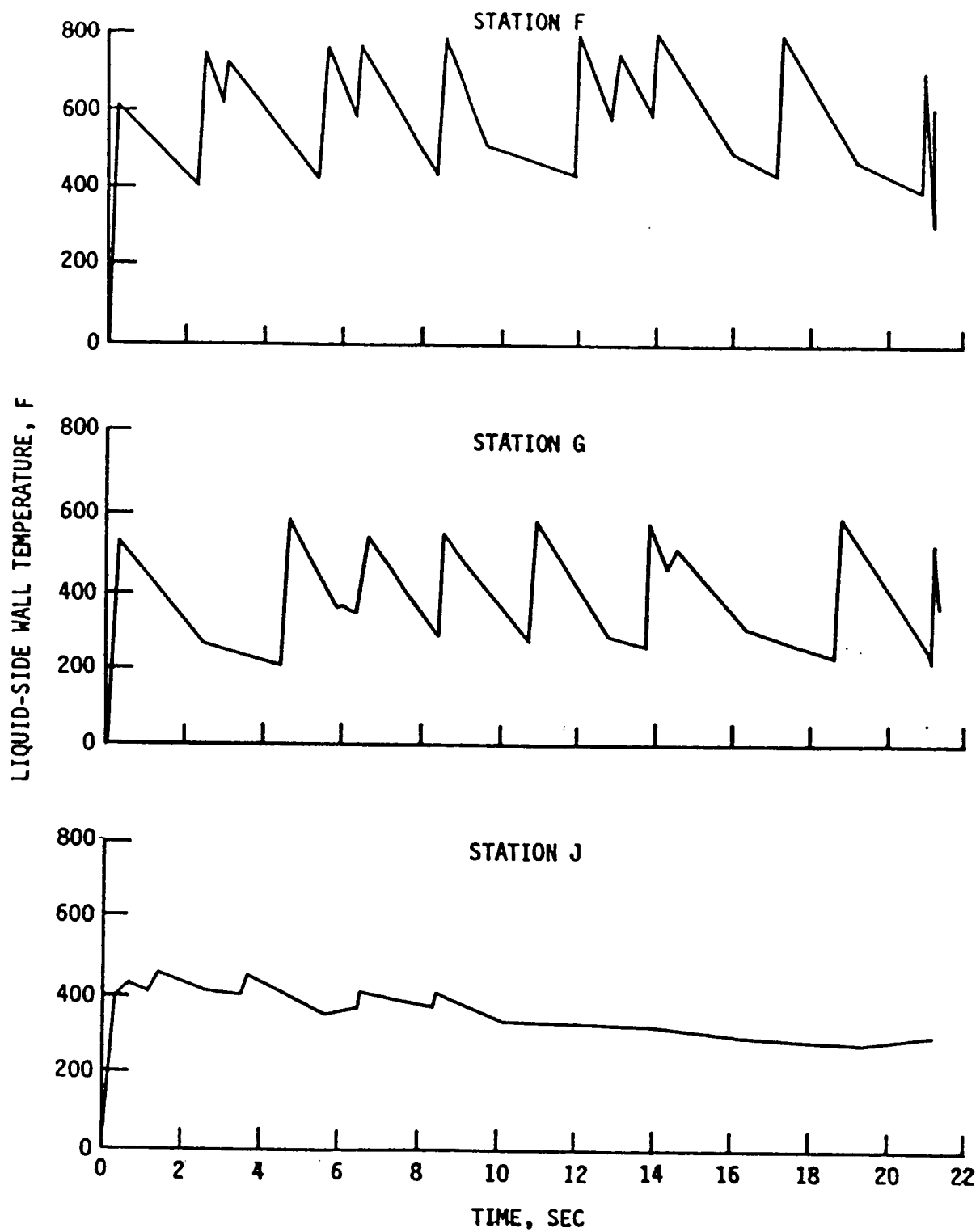
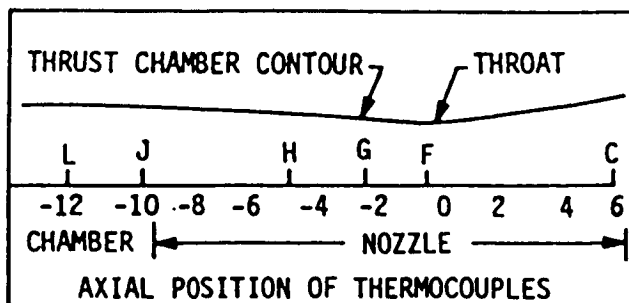


Figure B-2. Sellers Data Show Carbon Deposits Buildup and Spall Off



RUN SERIES	P <sub>c</sub> , PSIA	MR
A	824-878	209-283
B	1109-1144	164-223

EXAMPLE OF CURVE DESIGNATION:

F-B = STATION F, 5 IN UPSTREAM OF THROAT, RUN SERIES 8 B  
THROAT DIA = 3.0 IN.

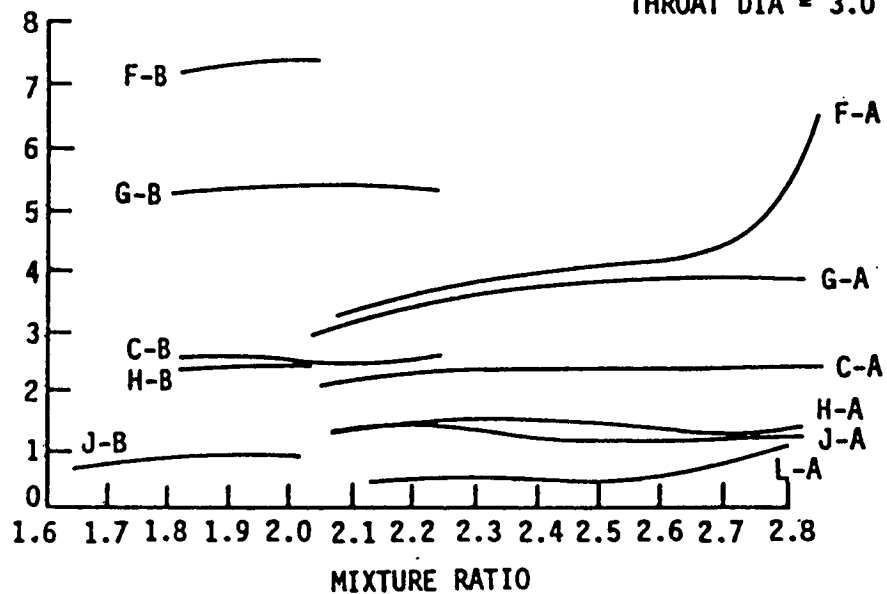


Figure B-3. Effect of Mixture Ratio on Carbon Deposits

where

$$\begin{aligned}\frac{X}{K} &= \text{carbon layer thermal resistance, in.}^2\text{-sec}^\circ\text{F/Btu} \\ G &= \text{mass velocity, lbm/sec-in.}^2\end{aligned}$$

This equation was for LO<sub>2</sub>/RP-1 and was obtained by a curve-fit of data obtained over a pressure range of 830 to 2000 psia (5.72 to 13.78 MPa) as shown in Figure B-4.

During the 60's and early 70's a large amount of heat transfer data with carbon deposition was generated by Pratt and Whitney as part of the space storable propulsion system contracts conducted for NASA. Their data were obtained with fluorine-oxygen mixtures (flox) as the oxidizer and with a variety of hydrocarbon fuels (methane, propane, a pentane blend, and butene-1). Most of the data were obtained at relatively low chamber pressures (ca 100 psia (.69 MPa) although late in this activity some testing and limited data were obtained at 500 psia (3.45 MPa). The following are the significant findings relative to carbon deposition which came out of this work.

(a) The reduction in total heat input to the combustion chamber due to the carbon layer was found to be dependent upon the chemistry of the fuel, with the higher carbon bearing fuels resulting in heavier carbon layers. This result is displayed in the plot shown in Figure B-5.

(b) The heat flux reduction due to carbon layer resistance appeared to indicate a mixture ratio dependence based on steady-state cooled chamber data. This trend is shown in Figure B-6. Not too surprisingly, the carbon deposit appears to decrease at mixture ratios above 4.0. This trend was not apparent in tests with uncooled hardware.

(c) The carbon deposition effect appeared most pronounced in the combustion chamber and throat sections and decreased very rapidly downstream of the throat. This is illustrated in Figure B-7.



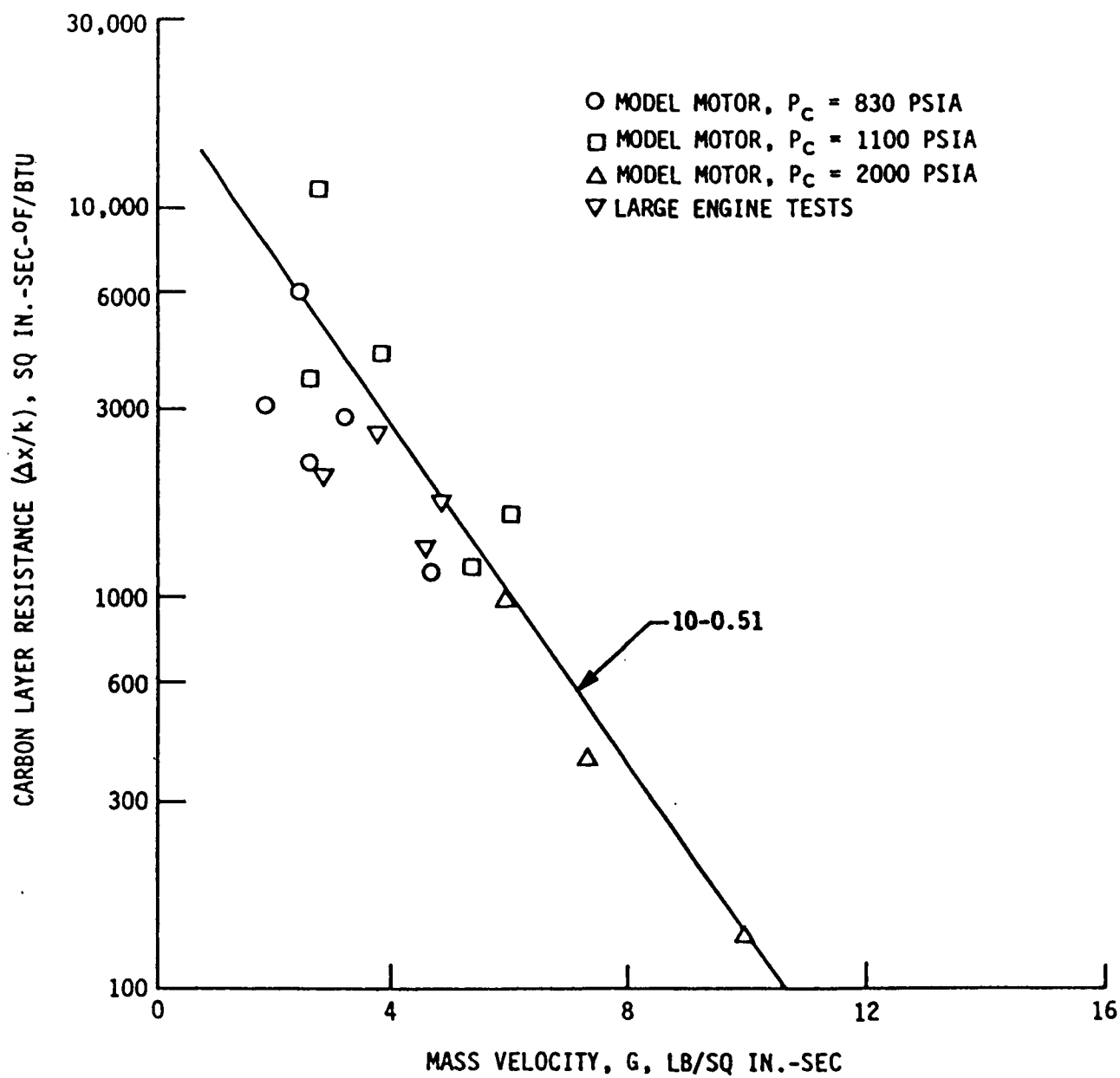


**Figure B-4. Seader and Wagner's Carbon Deposit Correlation**

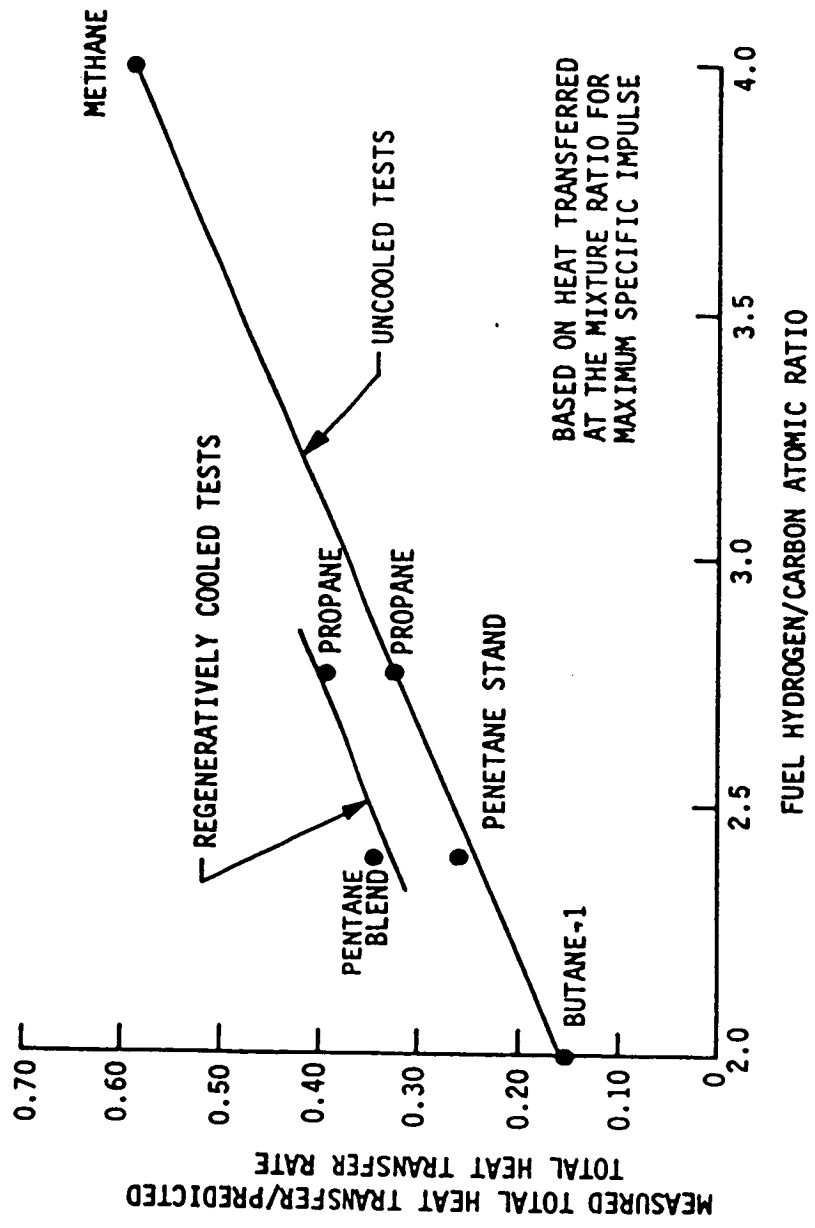


Figure B-5. P&W Related Carbon Deposits to Fuel Chemistry

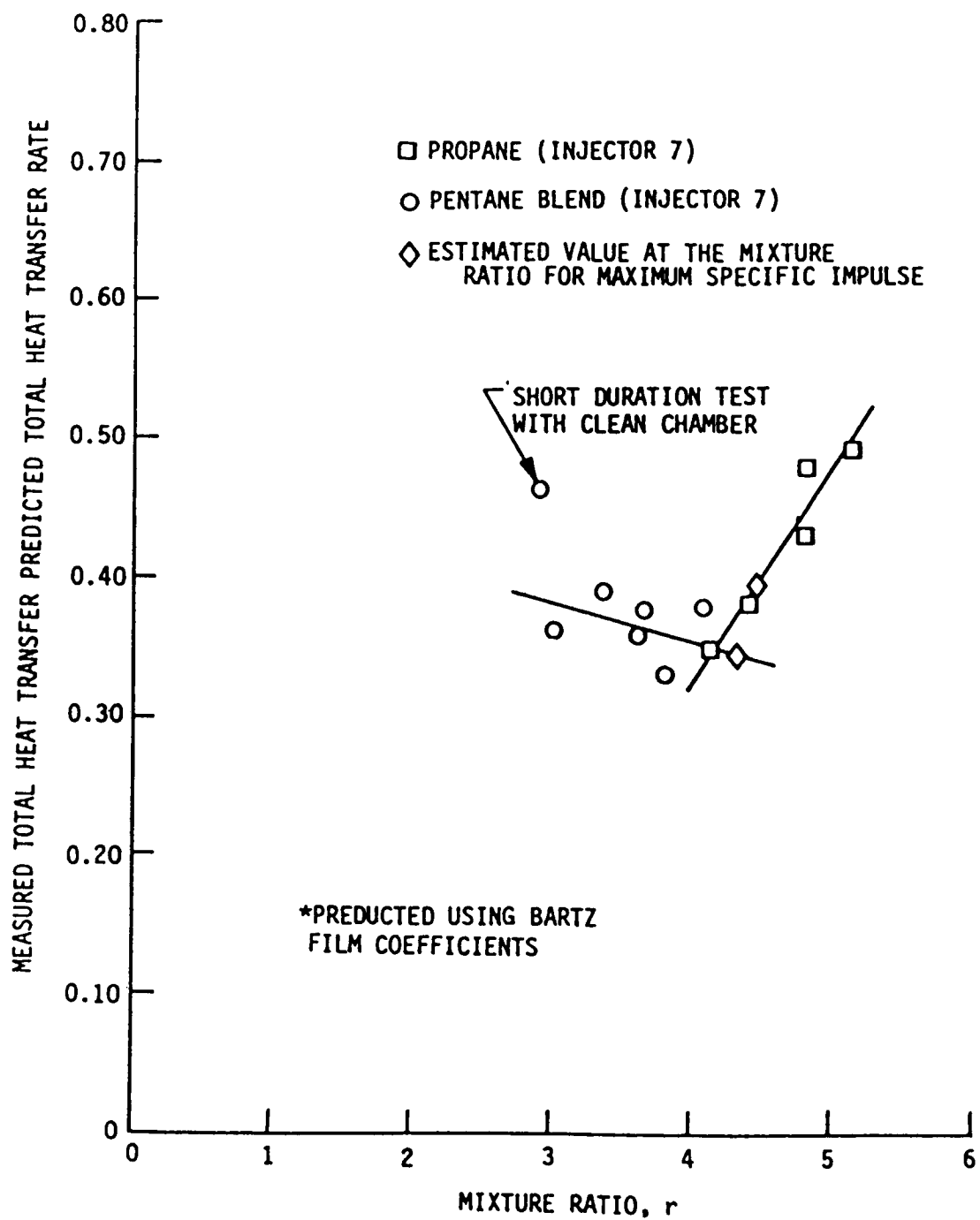


Figure B-6. P&W Data on Carbon Deposit Mixture Ratio Dependence

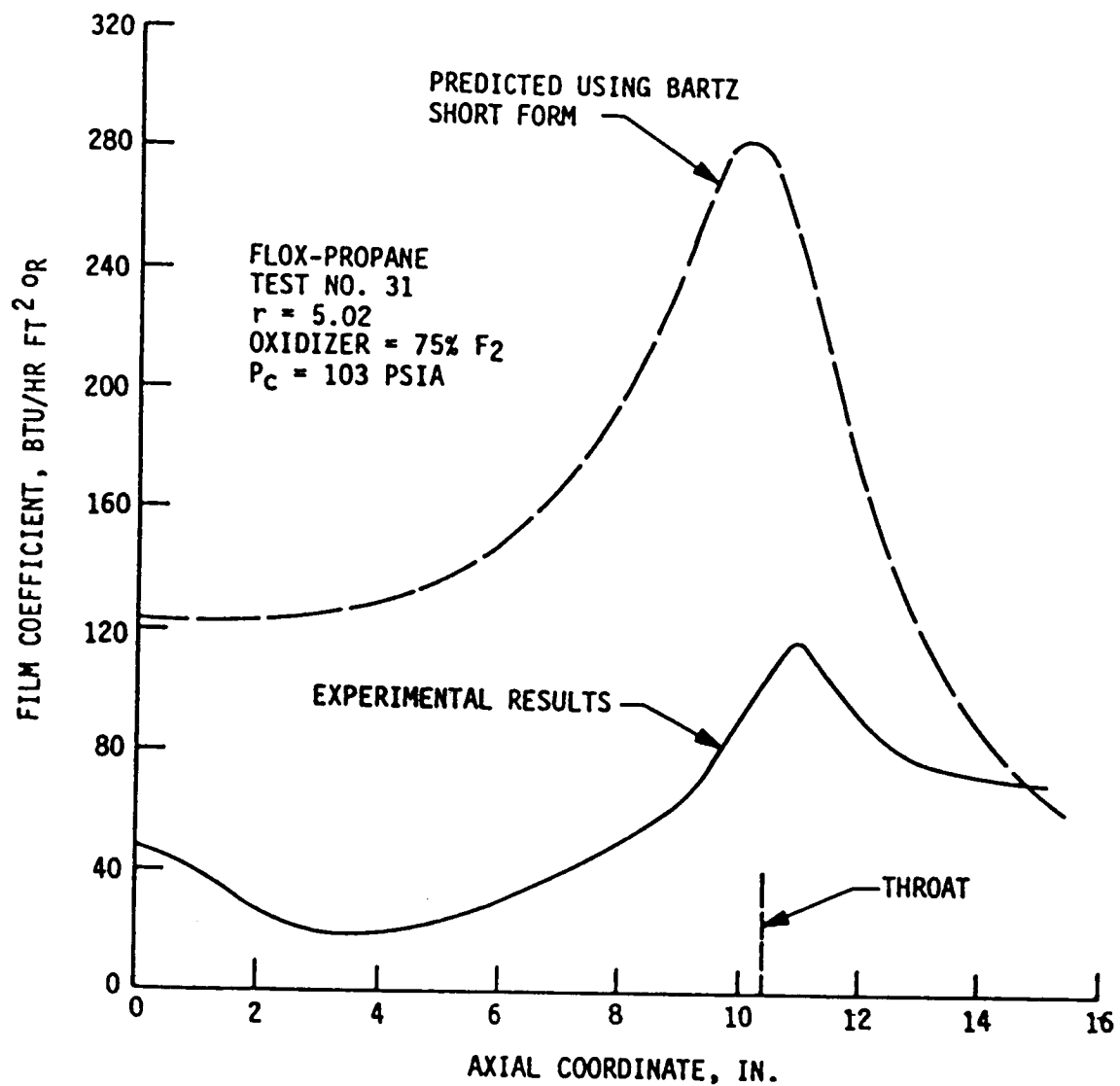


Figure B-7. P&W Data Relating Carbon Deposit and Chamber Location

(d) The time to achieve steady state (i.e., reach maximum buildup) was on the order of one to two seconds with uncooled chambers as shown in Figure B-8. Although no specific response data were given for regeneratively cooled chambers, a comment made in discussing a chamber failure gives it as four to six seconds. (For comparison purposes, note that a two second cycle time for buildup and flake-off characterized the data of Sellers as shown in Figure B-2.)

There was no apparent attempt by Pratt and Whitney to use their data to create a carbon deposition correlation for general design use.

Although P&W did not use their experimental carbon deposition data to generate a design model, some of the data were used by Rocketdyne in Reference B-7 to generate steady-state design correlations. Rocketdyne took the P&W heat sink chamber data and attempted to correlate them using an equation of the form employed earlier by Seader and Wagner. The propane, pentane blend, and butene-1 data were correlated with a single function for the entire nozzle. The correlations were:

$$\ln (x/k) = 10.52 - 6.00G \text{ (FLOX-Propane)}$$

$$\ln (x/k) = 10.06 - 3.26G \text{ (FLOX-Pentane blend)}$$

$$\ln (x/k) = 10.87 - 4.63G \text{ (FLOX-Butene-1)}$$

The ability of this type of correlation to describe the data is worth noting. A plot of the butene-1 data and the correlating equation is given in Figure B-9. These results were characteristic of the propane and pentane data also.

The 100 psia (.689 MPa) flox-methane data did not correlate as well. Two equations were required, one for the converging section and one for the diverging section.

$$\ln (x/k) = 6.33 + 1.83G \text{ (converging)}$$

$$\ln (x/k) = 12.37 - 12.7G \text{ (diverging)}$$

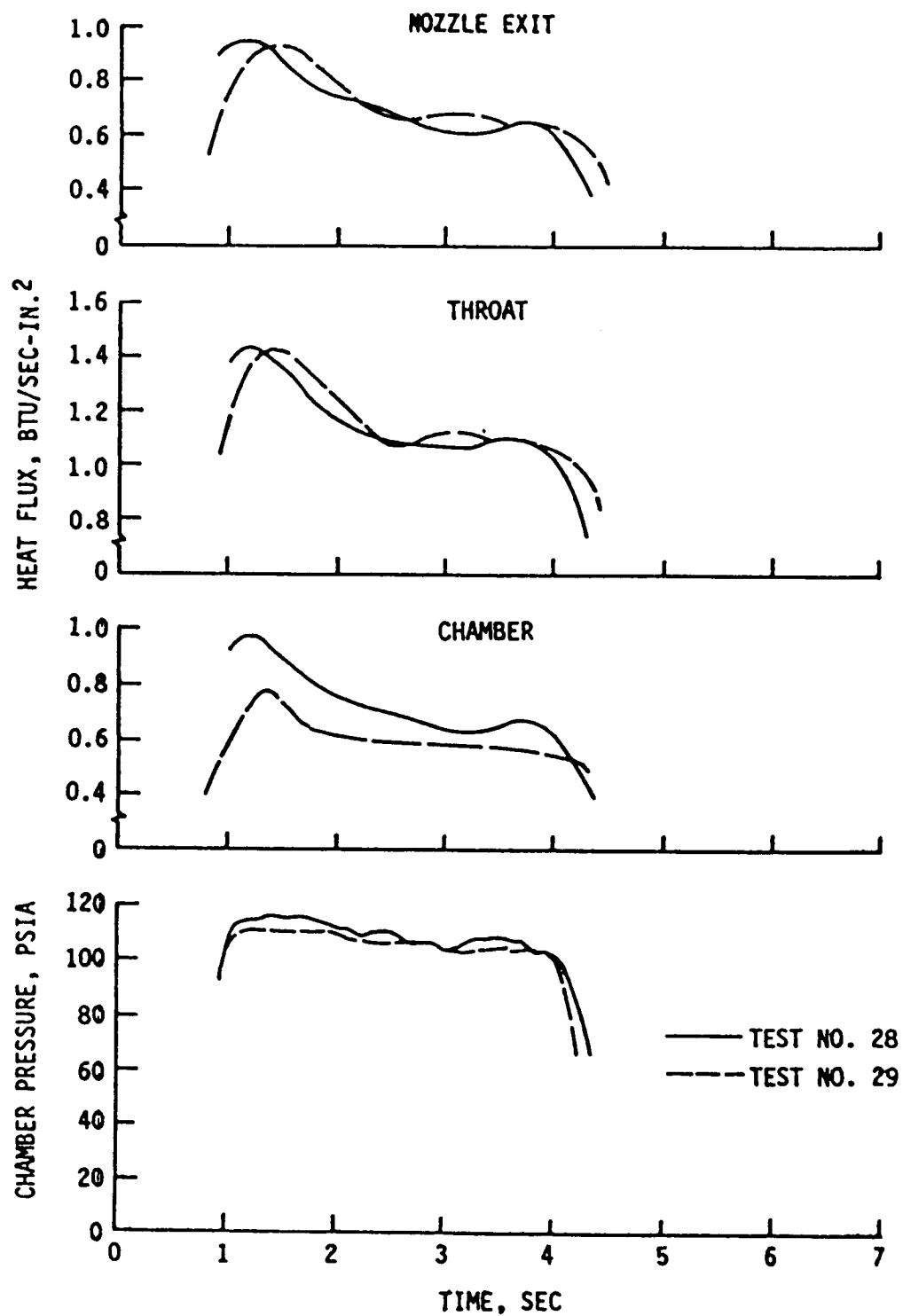
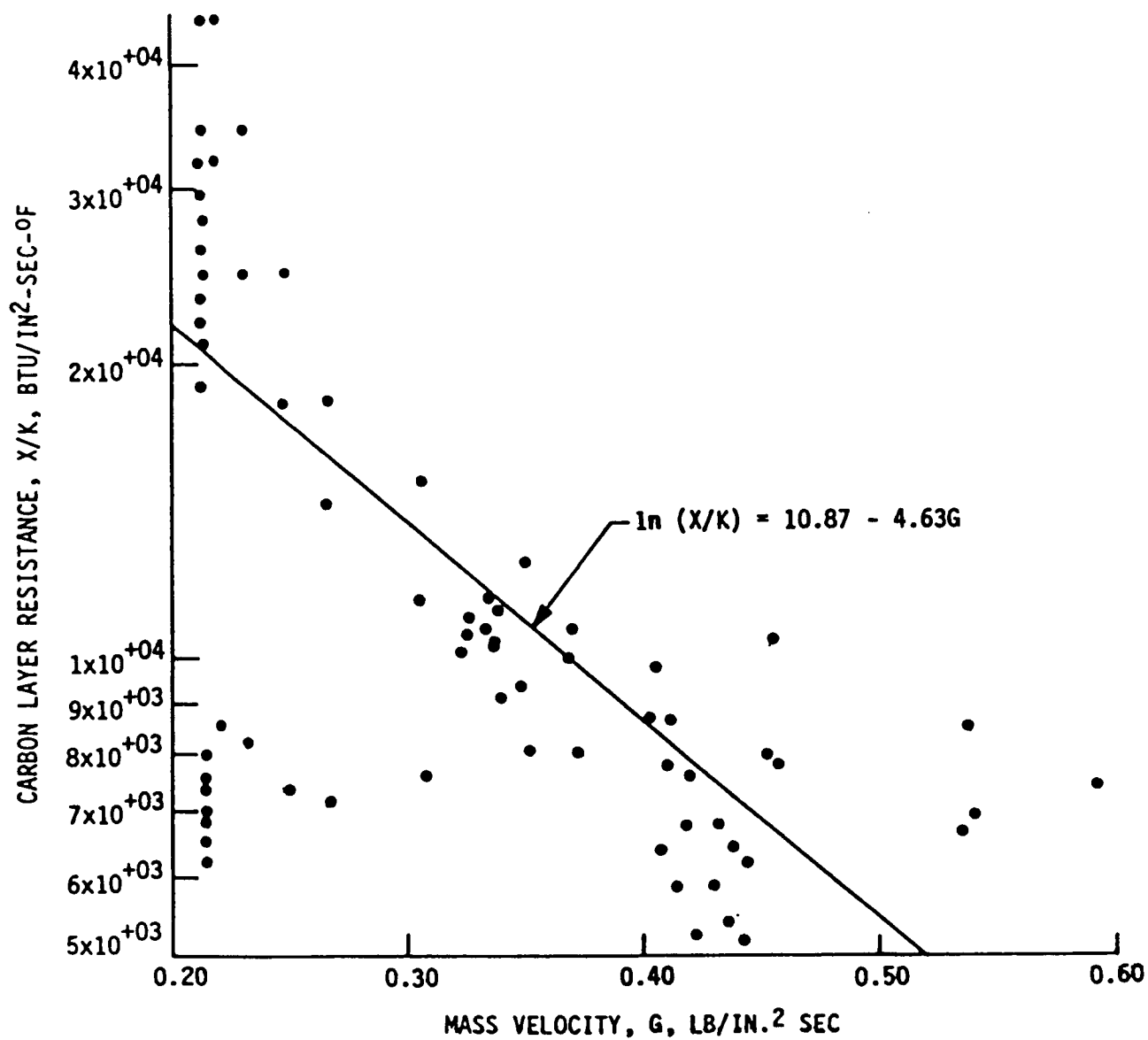


Figure B-8. P&W Data Show Carbon Buildup Transient



These equations and the data are shown in Figure B-10. When the 250 psia (1.72 MPa) flox/methane data were plotted, another set of equations were required for correlation. Substantial data scatter existed. These results are given in Figure B-11. Based on all of this data one would conclude that although these equations have identified key factors influencing the deposition process, they either have ignored some controlling factors, there is substantial scatter in the data, or both.

In the late 60's and 1970 Aerojet conducted a flox-methane program for NASA using a graphite lined regeneratively cooled chamber operating at 500 psia (3.45 MPa) chamber pressure (Ref. B-8). This program was significant in that it employed a fibrous graphite flame liner designed to operate at surface temperatures up to 4000°F (2477K) rather than the relatively cool (approximately 1000°F (811K) metal walls used in the earlier programs. A temperature history measured in the graphite is given in Figure B-12. The same saw-tooth behavior noted by Sellers was observed on this program. However, the carbon buildup cycle times were on the order of 50 seconds as opposed to the two to three second buildups of Sellers.

The renewed interest in  $\text{LO}_2/\text{RP-1}$  in the late 70's resulted in a significant additional data being generated on carbon deposition. As part of a study contract on hydrocarbon cooling (Ref. B-9) Rocketdyne developed carbon deposition correlations for oxygen/RP-1,  $\text{C}_3\text{H}_8$ , and  $\text{CH}_4$ . The experimental data base employed in these correlations was that of P&W described previously. In working with the P&W data, Rocketdyne had two problems to overcome; namely, the P&W data were obtained with flox instead of oxygen, and the data were at relatively low chamber pressures (100 psia (.689 MPa). To extend the data to oxygen and high pressure they took the P&W steady-state data and used it to back out an average carbon layer resistance for the entire thruster. This resistance was then plotted as a function of the combustion gas carbon atom fraction as shown in Figure B-13. By assuming this plot to be independent of oxidizer it was then possible to determine the average carbon deposit resistance for the various  $\text{O}_2$  - hydrocarbon combinations as noted on Figure B-13. These results were then generalized to cover a broad range of mass flux values by assuming the mass flux in the combustion chamber was representative of the engine and using that to construct plots similar to that of Seader and



$P_C = 103 \text{ PSIA} - 120 \text{ PSIA}$

$F = 2.8K - 2.9K$

$\epsilon_0 = 2.78$

MIXTURE RATIO

$= 4.97 - 5.73$

$\epsilon = 3.5$

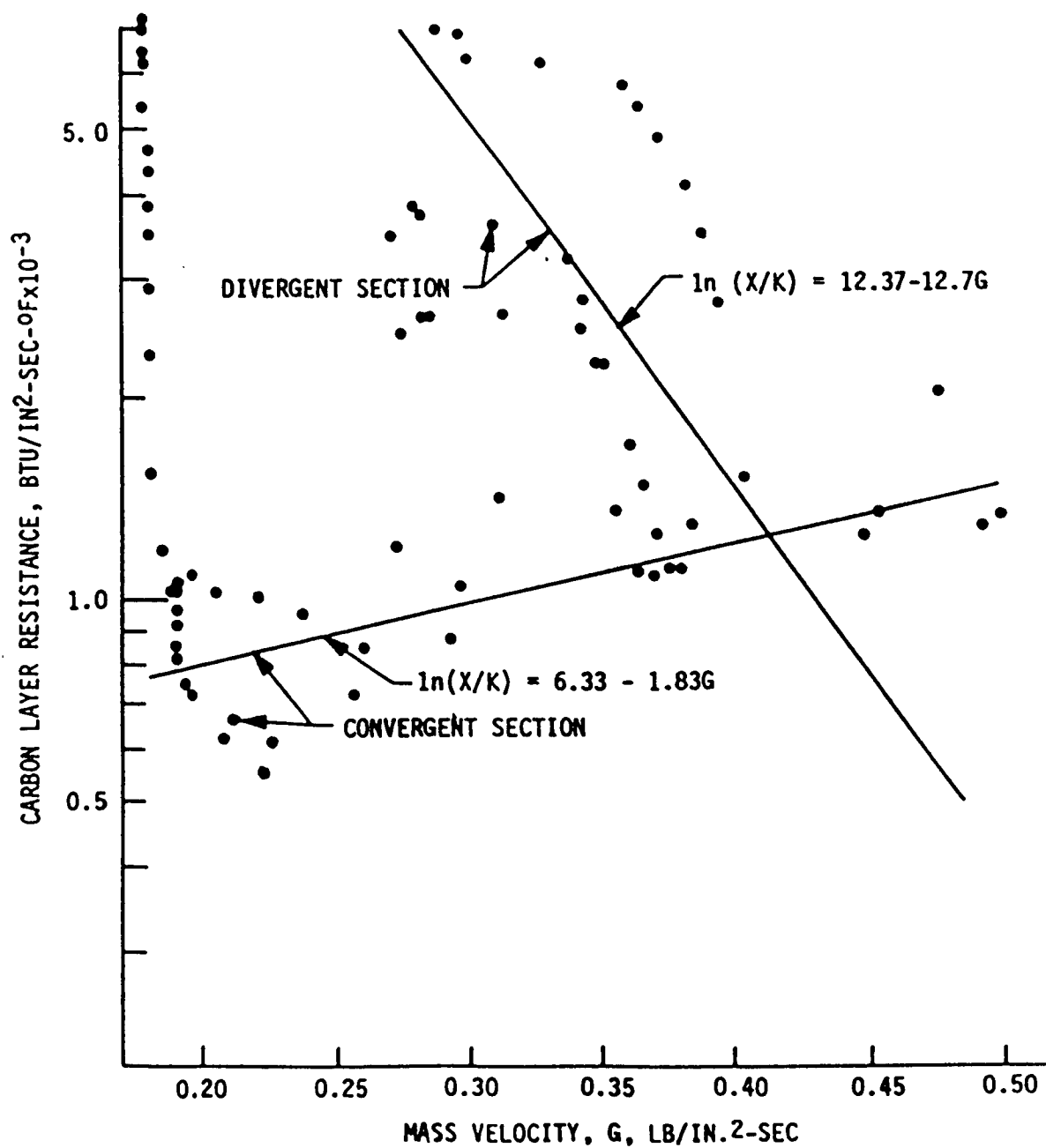


Figure B-10. Rocketdyne Correlation of P&W 100 psia Methane Data

$P_c$  PSIA = 225 - 272

F, LBS = 9300 - 11,300

$\epsilon_c = 2.78$

MR = 3.73 - 6.08

$\epsilon = 3.54$

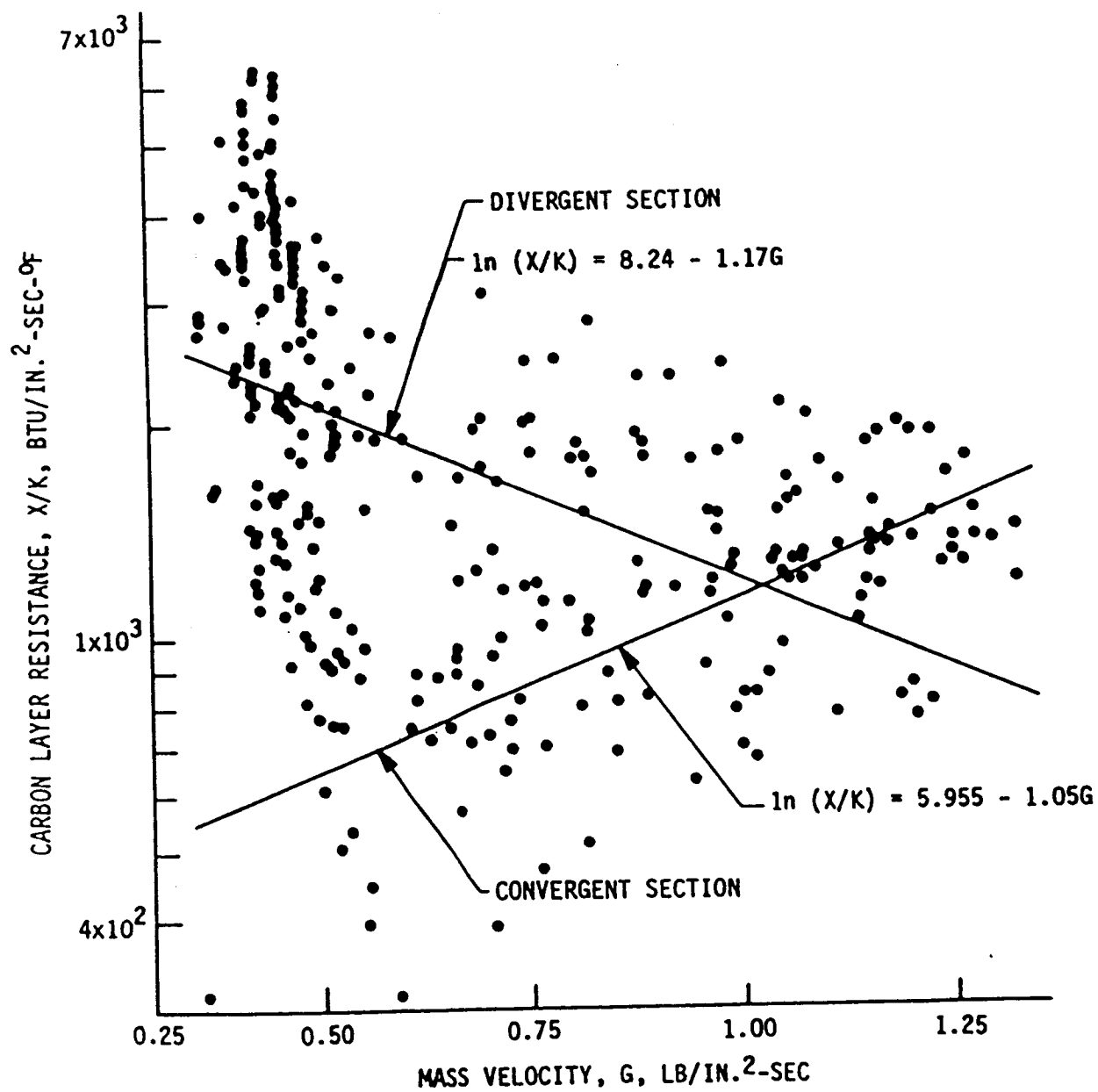


Figure B-11. Rocketdyne Correlation of P&W 250 psia Methane Data

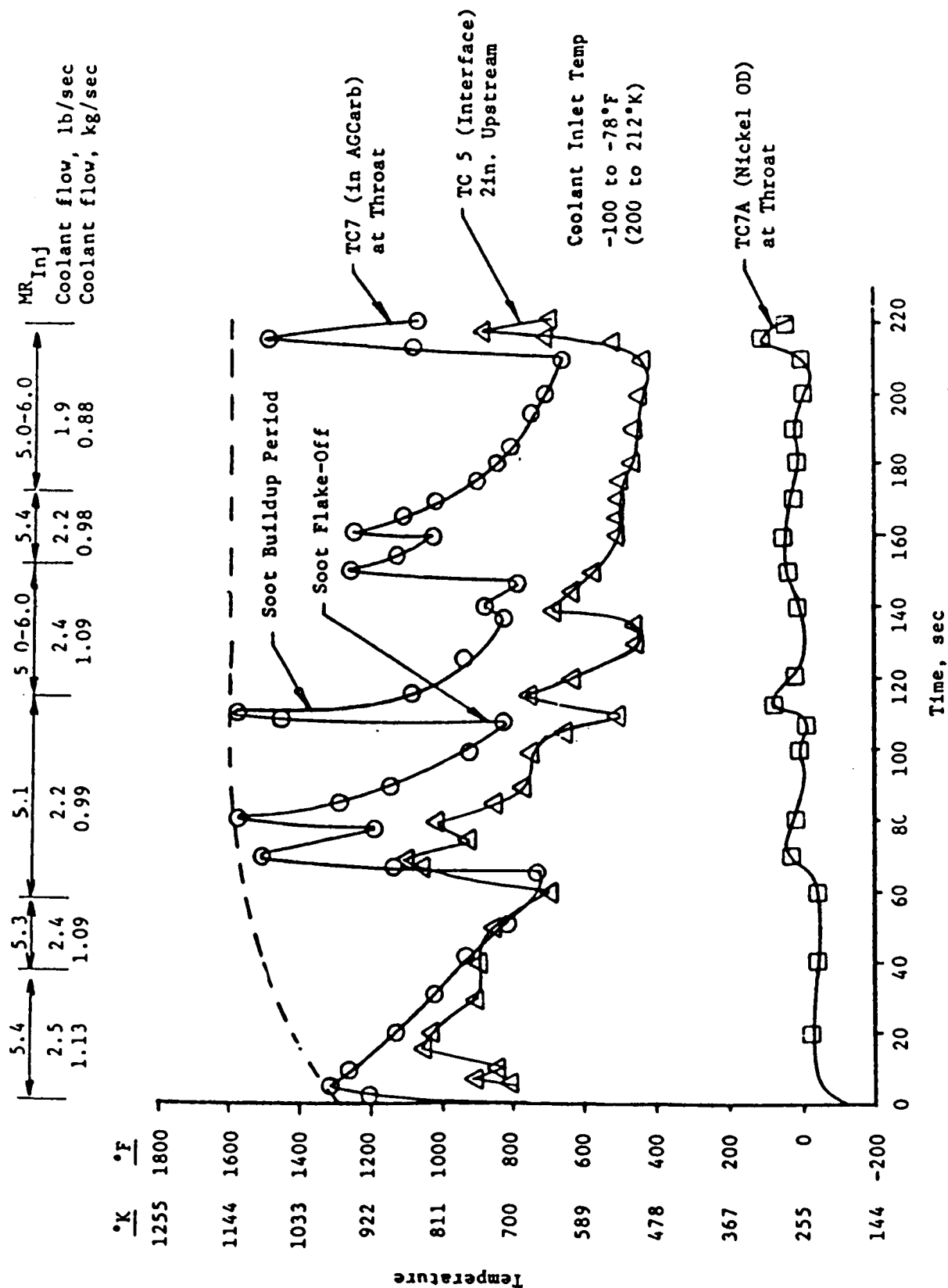


Figure B-12. Aerojet Flox-Methane Data Show Spalling

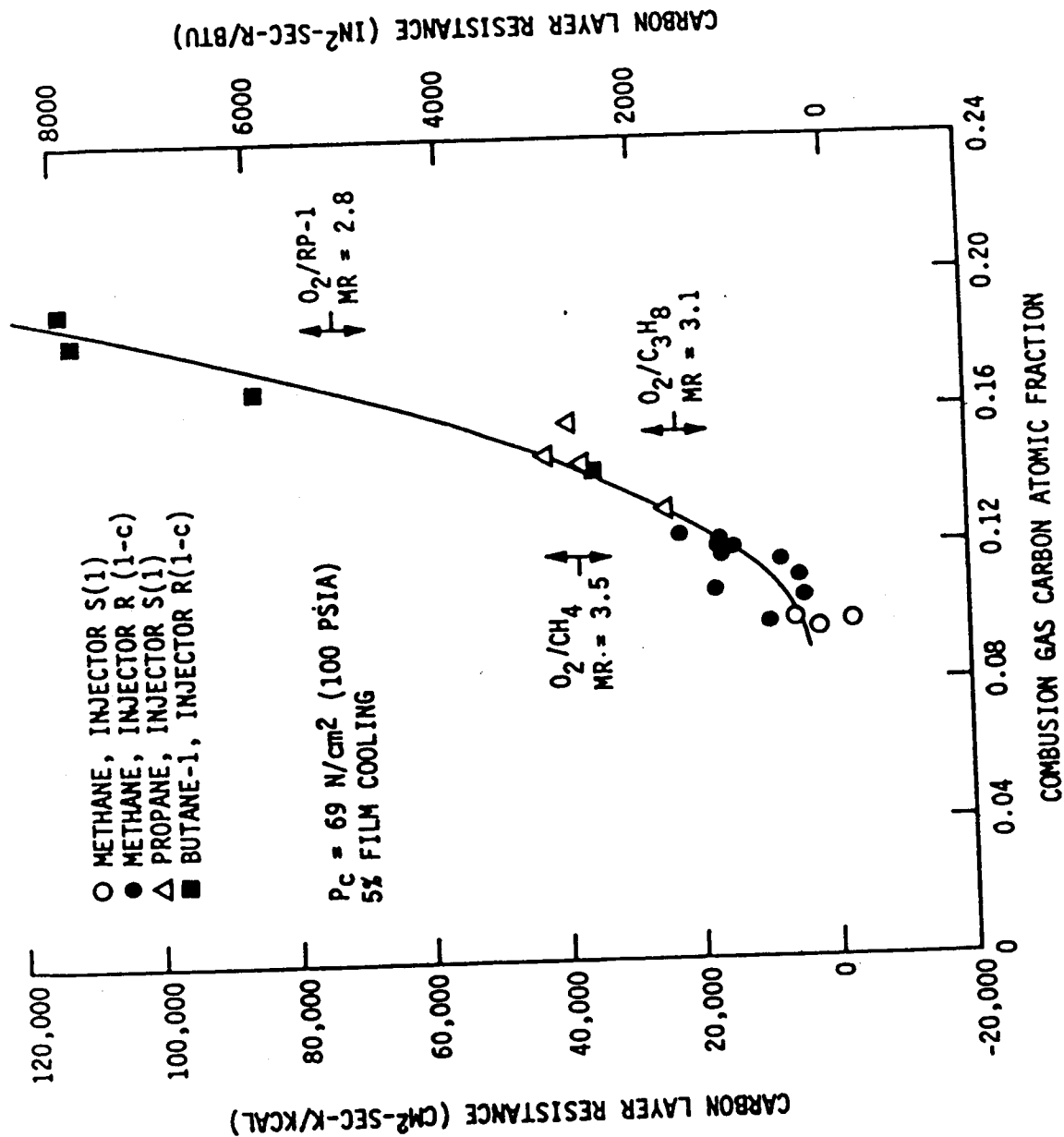


Figure B-13. Rocketdyne Related P&W Data to Combustion Gas Chemistry

Wagner. The results are given in Figure B-14. Two curves for RP-1 are shown in the figure, the original one of Seader and Wagner, and the new one. The original curve used by Seader and Wagner was for film cooling of 10% or more while the more recent curve was for about 5% film cooling. The correlating equations corresponding to these lines are:

- $O_2/RP-1$ ,  $MR = 2.8 \ x/k = e^{9.0 - 0.51G}$
- $O_2/C_3H_8$ ,  $MR = 3.1 \ x/k = e^{8.2 - 0.51G}$
- $O_2/CH_4$ ,  $MR = 3.5 \ x/k = e^{6.9 - 0.51G}$

where  $G$  is in  $lbm/in.^2\text{-sec}$  and  $x/k$  is in  $in.^2\text{-sec-R/Btu}$ . These are the most recent published carbon deposition correlations.

A photographic study of the combustion of  $LO_2$  with  $CH_4$ ,  $C_3H_8$ , and RP-1 was completed by Aerojet under a NASA contract (Ref. B-10). The objective of this program was to gain better insight into the hydrocarbon combustion process through actual observation of combustion under rocket conditions. This was accomplished by high speed color photography (up to 600 frames/sec) of single element injectors in a combustion chamber with quartz windows. A total of 127 tests were conducted over a chamber pressure range of 125 - 1500 psia (.862-10.34 MPa), a fuel temperature range of  $-245^\circ F$  to  $158^\circ F$  (.119 to 343K), and a fuel velocity range of 48 to 707 ft/sec (1463 to 21550 cm/s). Mixture ratios tested were representative of both gas generator and main chamber conditions. The following injector elements were tested:

#### Conventional Machined Elements

OFO Triplet (OFO)  
Rectangular Orifice Unlike Doublet (RUD)  
Unlike Doublet (UD)  
Like-on-Like Doublet (LOL-EDM)  
Slit Triplet (ST)

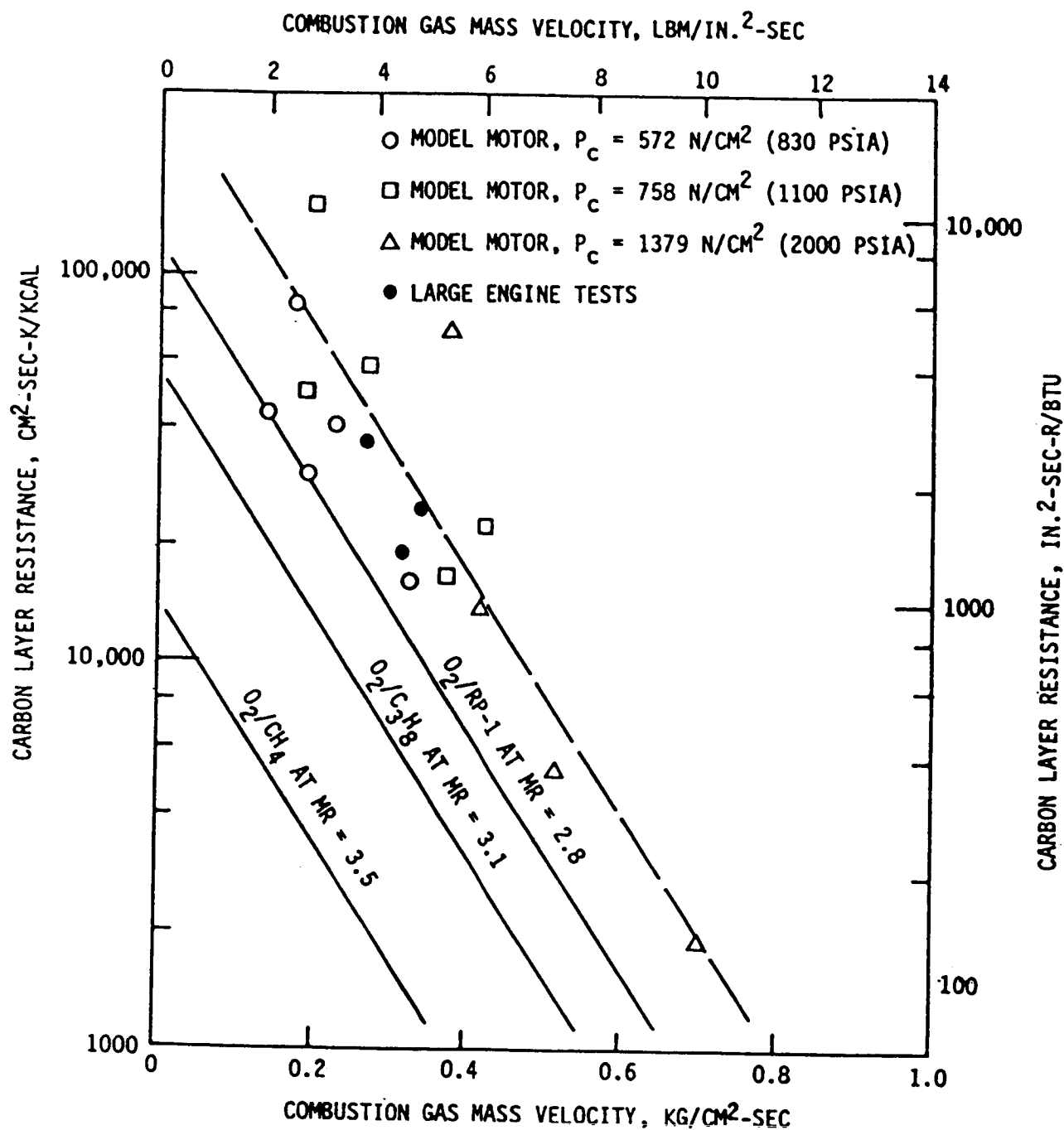


Figure B-14. Rocketdyne Correlations for Deposit Resistance with Different Fuels

## Platelet Elements

Transverse Like-on-Like (TLOL)

Pre-Atomized Triplet (PAT)

One of the goals of the Photographic Combustion Program was to determine the factors influencing the formation (not deposition) of soot or carbonaceous solids during hydrocarbon combustion. Since the data was primarily visual, it was also largely qualitative. To allow data trends to be portrayed, three sooting categories were established: clear (no apparent soot), partially obscured (light to moderate sooting), and obscured (heavy sooting). The results of the program in terms of carbon formation are summarized in Figure B-15. The sensitivity of carbon formation to fuel type and mixture ratio shown in the first two plots agreed with the Pratt and Whitney deposition data noted previously. This is not surprising in that high carbon formation is an expected prerequisite for high carbon deposition. Figure B-15 also shows increasing fuel temperature and increasing chamber pressure both act to decrease carbon formation. The effect of chamber pressure on carbon formation is clearly illustrated in the data of Figure B-16. This figure gives the results of RP-1 combustion tests over an order of magnitude change in chamber pressure. It is very apparent that low pressure favors soot formation. Much the same result was obtained with propane. These results are very significant in that they are addressing the formation of carbon, not the deposition. Obviously before carbon can be deposited, it must be formed, and if less carbon is being formed at high pressure, less will be deposited. The only published carbon deposition model attributes the decrease in carbon deposition at higher pressures solely to the influence of mass flux. These photographic data imply that at least part of the effect is due to decreased carbon formation.

The photographic combustion data can be summarized by noting that in general those factors which accelerate the combustion process were also observed to result in decreased carbon formation. If the acceleration of combustion is assumed to reflect a shift from a diffusion controlled to a premixed flame, then these results would agree with the observations of Glassman (Ref. B-1). As stated previously, Glassman noted that in hydrocarbon combustion the fuel has two paths it can follow. It can either be completely

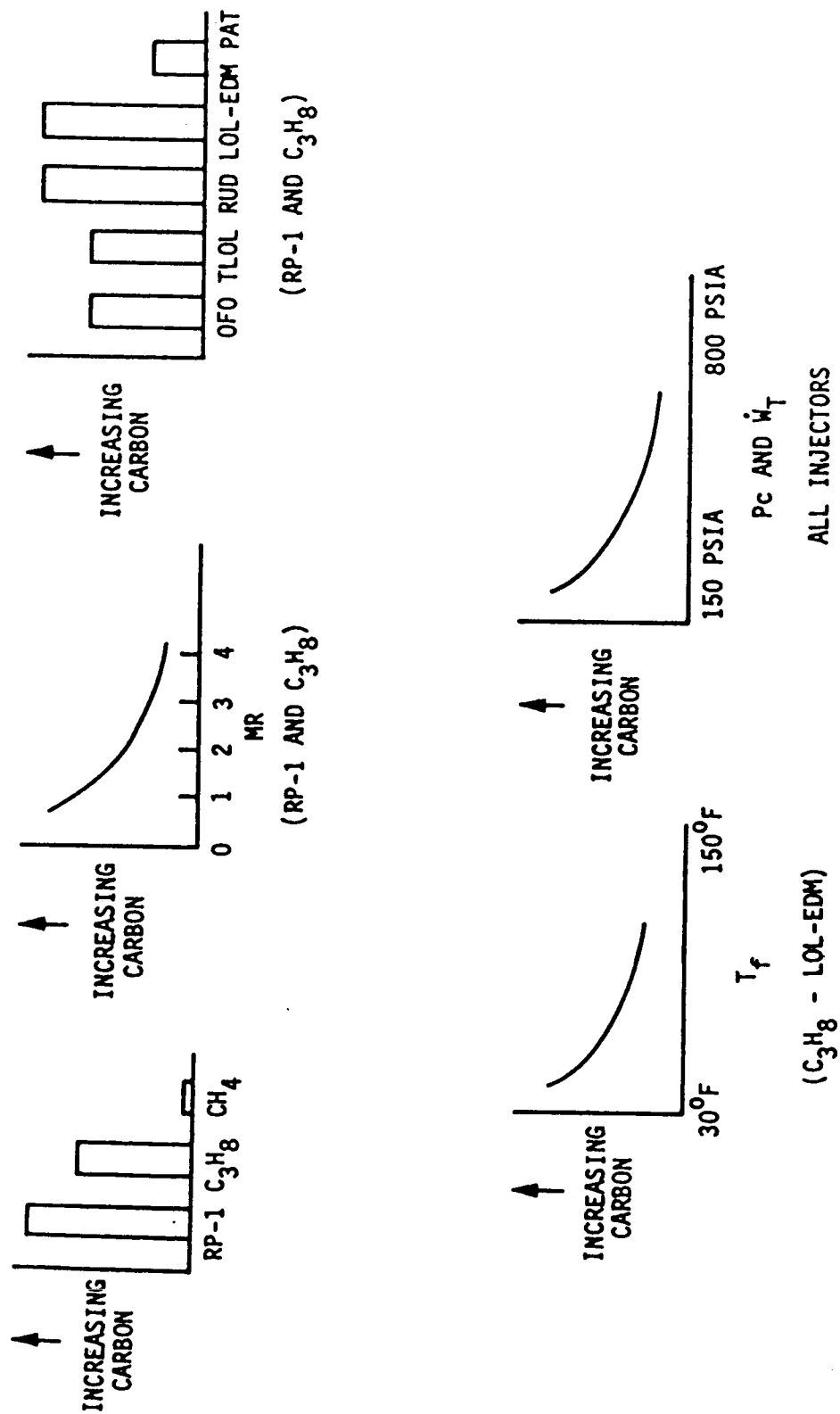


Figure B-15. Carbon Formation Trends Observed on Aerojet Photographic Combustion Program



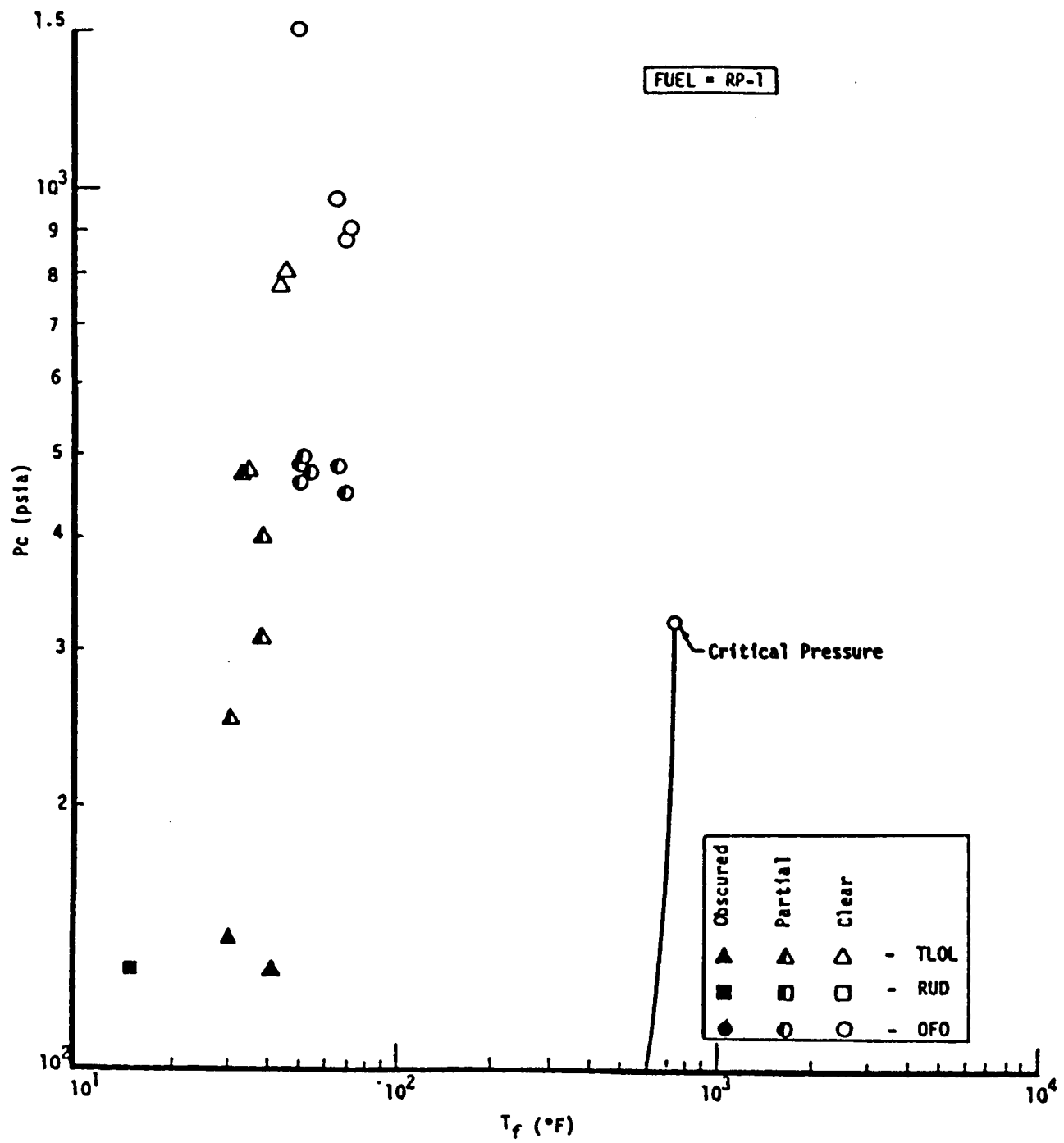


Figure B-16. Photo-combustion Program Data Show High Pressure Reduces Soot Formation

pyrolyzed to form soot or it can react with the oxidizer before pyrolysis is completed. Diffusion flames are characterized by fuel being heated in the absence of oxidizer with resulting soot formation. In premixed flames, the soot precursors are subject to oxidizer attack and soot formation is minimized. This distinction could be an important factor in understanding and explaining test data.

Aerofjet completed an experimental program for NASA (Ref. B-11) in which transient and steady state  $\text{LO}_2/\text{RP-1}$  heat transfer data were obtained at pressures from 1000 to 2000 psia (6.89 to 13.78 MPa) and over a mixture ratio range of 1.9 to 4.1. What made these results particularly significant was that on some of the 2000 psia (13.78 MPa) tests a water-cooled calorimeter chamber was employed which provided separately measured and controlled calorimeter circuits at 34 axial stations. This test apparatus provided very high quality high pressure  $\text{LO}_2/\text{RP-1}$  heat transfer data. A typical plot of the experimental data obtained on this program is given in Figure B-17.

One of the goals of this program was to investigate the effect of carbon deposits on heat transfer. With this goal in mind the calorimeter data were carefully reviewed to obtain quantitative data on carbon deposition. Quite surprisingly the data indicated no carbon thermal barrier developed, even in tests up to 32 seconds duration. Following firing, the chamber interior had a very thin black coating and looked as though it had been freshly painted with tire paint. The first 4 to 6 inches (10.16 to 15.24 cm) of the chamber had noticeably less coating or deposits with the copper wall material showing through in some locations. When the wet coating was wiped off, the copper had a black color on the surface but there was no measurable thickness or roughness associated with it. The measured heat fluxes were higher than predicted everywhere except near the injector, which was the area showing the least carbon deposition.

The test data were also reviewed to determine if they contained any time dependence which might suggest either a buildup or buildup and loss (spalling) of a carbon layer. No such time dependence was found. Both the chamber as a whole and the individual circuits quickly established a steady-state condition which changed only when the operating mixture ratio changed.

TEST 085

15 → 20 SEC

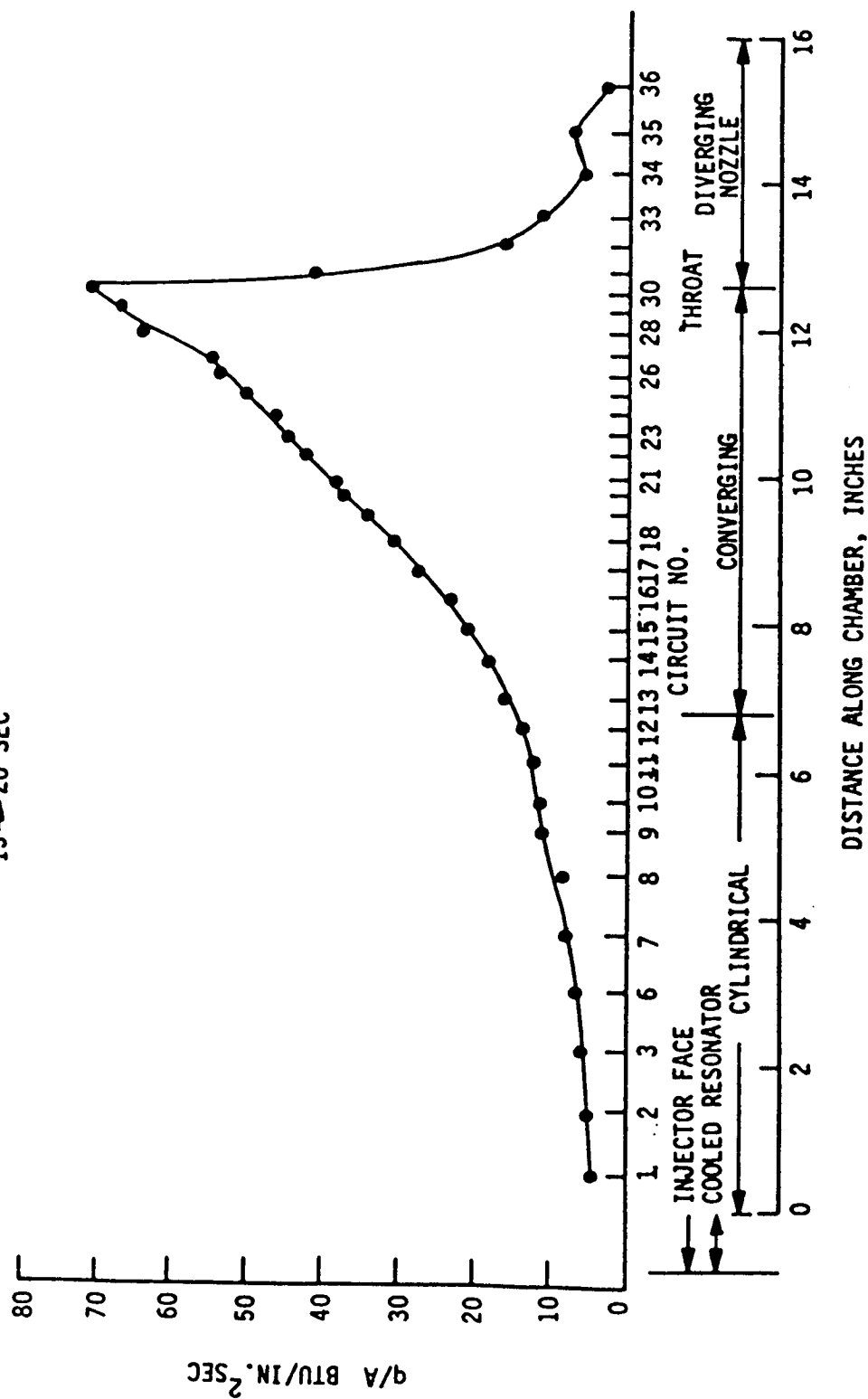
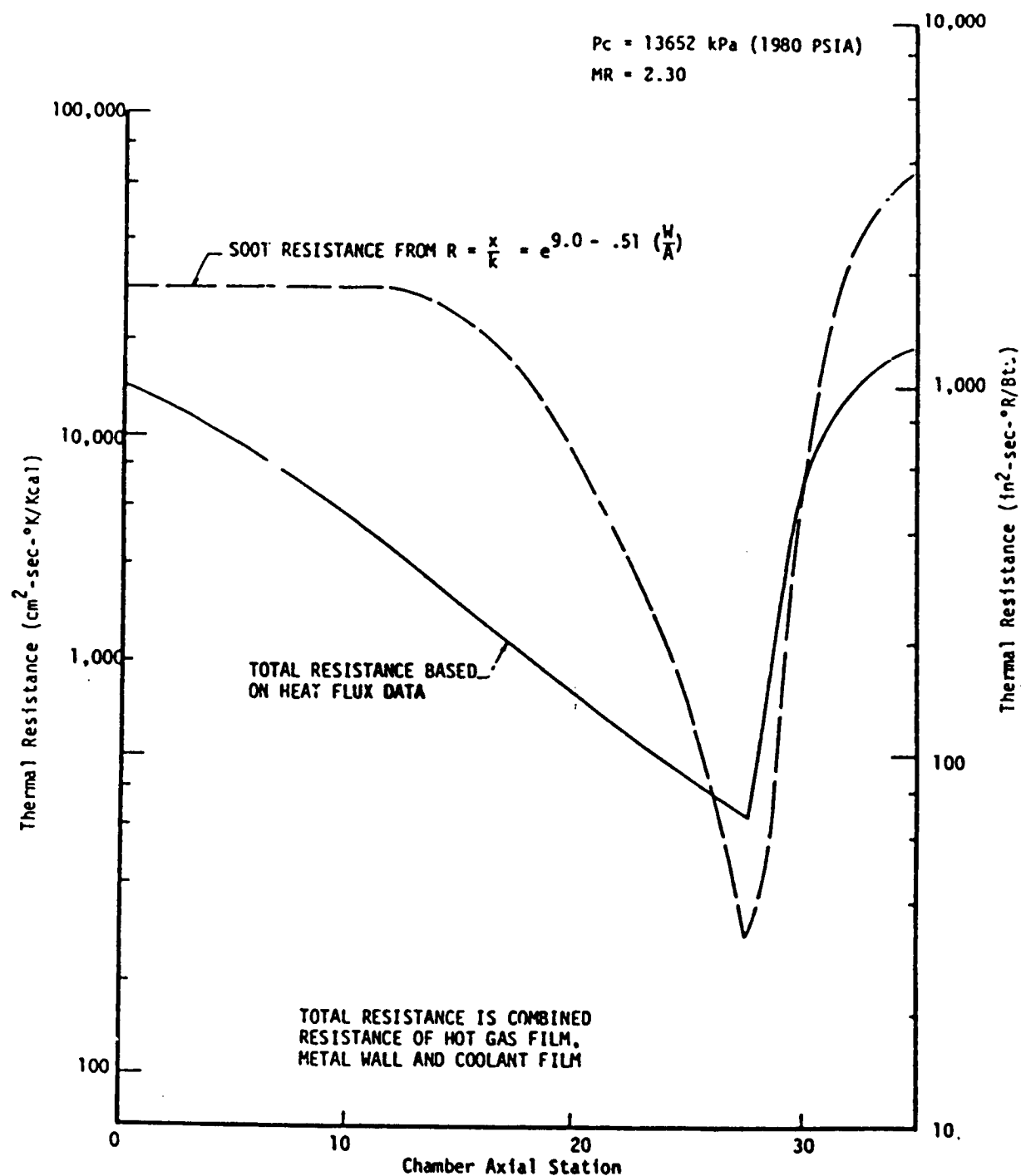


Figure B-17. Aerojet LOX/RPL-1 Calorimeter Heat Transfer Data

As a further check, the carbon layer resistance relationship developed by Rocketdyne (i.e.,  $x/K = e^{9.0 - 0.51G}$ ) was used to calculate a carbon layer resistance profile for the calorimeter chamber. This was compared with the total thermal resistance (defined as the combined resistance of the hot-gas film, the wall, and the coolant film) calculated from the test data for a number of locations on the chamber. The results are given in Figure B-18. They show that, with the exception of a very small region by the throat, the predicted resistance for the deposit was significantly greater than the experimentally determined total wall resistance. Based on this, it is apparent that if there were any soot thermal barrier present, its resistance was very small and substantially less than predicted.

There are several possible explanations for the lack of a carbon thermal barrier developing on the Aerojet test hardware. Possibly the high pressure resulted in suppression of carbon formation as observed in Reference 10. The problem with this explanation is that the Aerojet data showed no carbon barrier even in the 1000 psia (6.89 MPa) tests while Seader and Wagner (Ref. B-6) encountered deposits at pressures up to 2000 psia (13.78 MPa). Another explanation is much (if not all) of the early data and the Rocketdyne correlation is based on results obtained from engines with fuel-film cooling. The Aerojet data were obtained without any film cooling although the injector patterns were designed to provide a fuel-rich orientation at the wall. Consequently, the environment at the wall in the Aerojet testing was likely to be less fuel-rich than that of the early programs, and less soot should be anticipated.

It is also possible that there was a thin carbon layer in the throat which acted to increase rather than decrease the heat flux. This would happen when the wall roughness caused by carbon deposition reduces the resistance of the hot-gas boundary layer more than the presence of the carbon increases the wall resistance. This particular mechanism would be peculiar to high-pressure, low-thrust engines where the boundary layer laminar sublayer is very thin. Carbon deposits which appear hydraulically smooth in engines such as F-1 and Titan I could be rough in engines of the configuration tested in this program. This is illustrated in Figure B-19. This explanation has its greatest validity at the throat plane.



**Figure B-18. Rocketdyne Correlation Doesn't Predict Calorimeter Chamber Results**

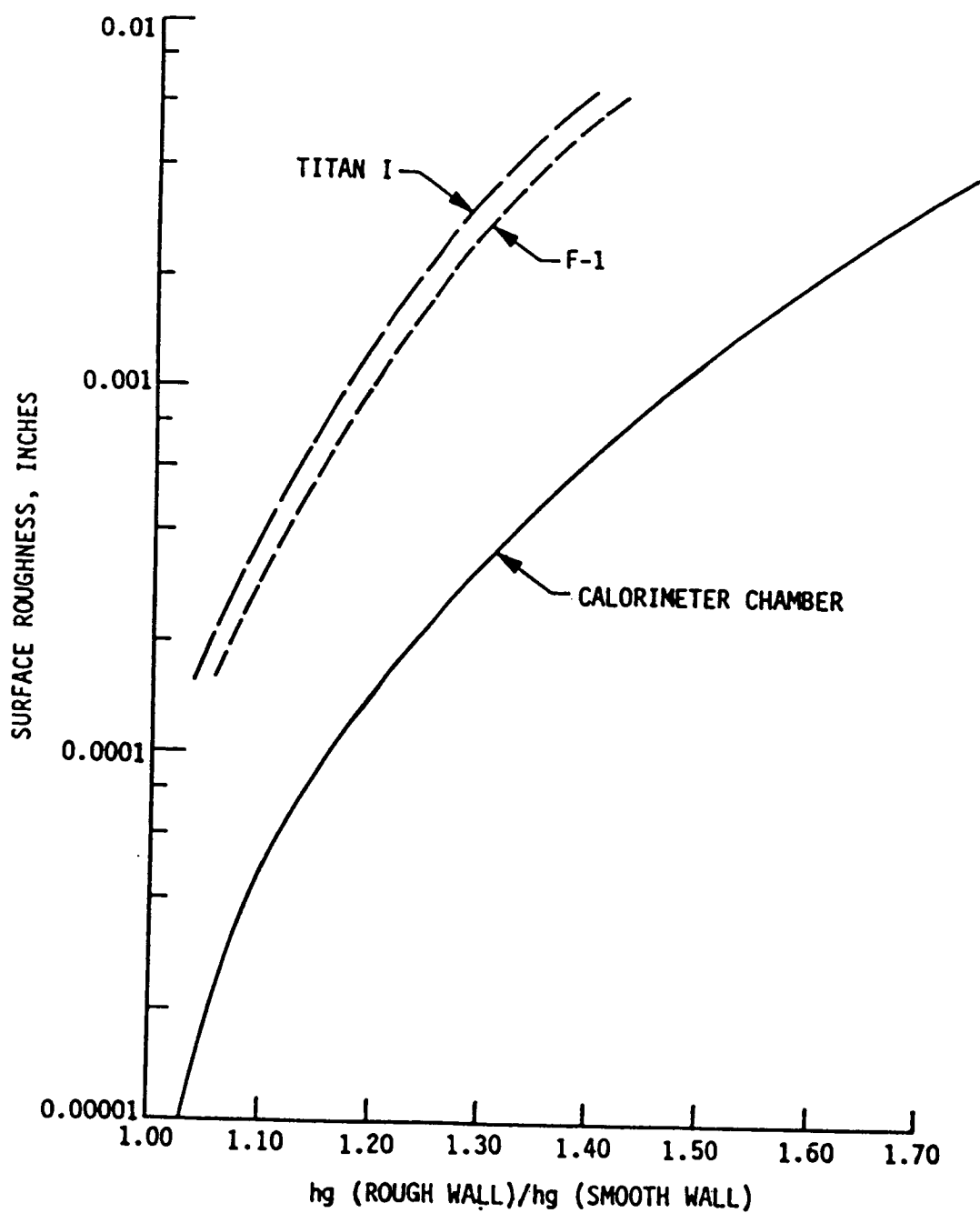


Figure B-19. Effect of Carbon Deposit Roughness Depends on Chamber Size

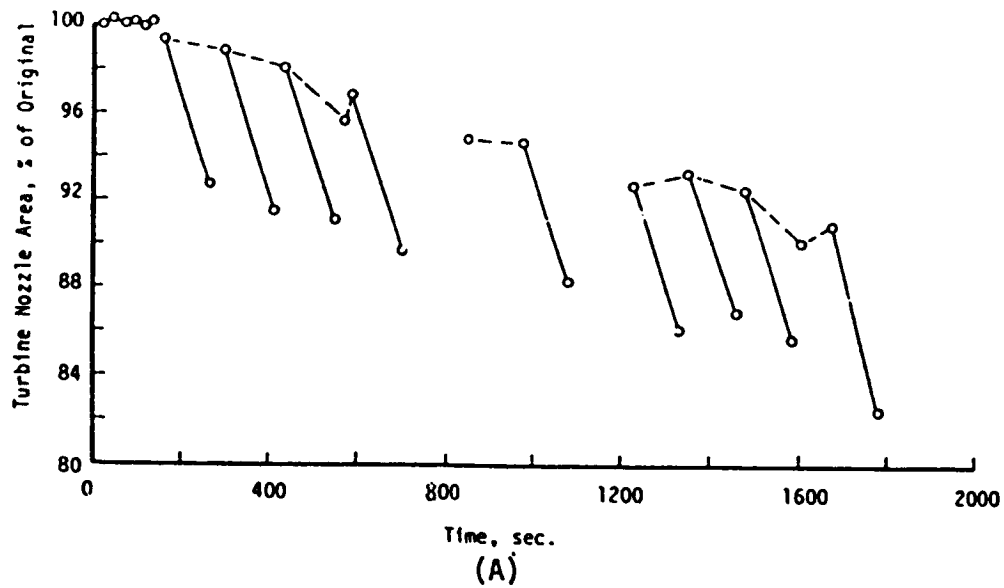
There are two significant conclusions which can be drawn from the preceding review of the thrust chamber carbon deposition state-of-the-art.

- (a) The data base is very spotty at best. (As an example, the only methane and propane data published were obtained with flox, not oxygen, and that was at low pressure.) No comprehensive set of test data has been generated under controlled test conditions.
- (b) Only one carbon deposition correlation has been developed and it was obtained by performing a curve fit to the inadequate database. Although the correlation matches some of the data reasonably well, it misses very badly on other data.

### 3. Gas Generators and Preburners

Little data exists in the open literature on carbon deposition in and downstream of gas generators and preburners. Our database in this area is derived from our experience in the development of Titan I and the NASA contracts with ATC (Refs. B-12 and B-13), and Rocketdyne (Ref. B-14) on  $\text{LO}_2$ /Hydrocarbon preburner technology. Titan I is a particularly good source in that both the first and second stages employed fuel-rich gas generator cycle  $\text{LO}_2$ /RP-1 engines. During Titan I engine development, carbon deposition in the turbine nozzles was a primary concern and a considerable amount of testing was devoted to obtaining deposition data. The NASA contracts with ATC and Rocketdyne focused on extending the  $\text{LO}_2$ /Hydrocarbon gas generator/preburner technology to higher pressures. These contracts had the acquisition of carbon deposition data as a contract goal.

During development of the Titan I gas generator, deposition was monitored in terms of turbine nozzle flow area reduction. A typical history spanning nearly 1800 seconds of firing duration and numerous restarts is presented in Figure B-20A. This plot of nozzle flow area versus time provides valuable insight into the deposition process. The most apparent feature is repetitive spalling. During each 120 to 160 second firing, approximately 8%



MIXTURE RATIO INFLUENCE ON TURBINE NOZZLE AREA REDUCTION  
TITAN I FIRST STAGE GAS GENERATION  
FS<sub>1</sub> + 20 SEC. TO FS<sub>1</sub> + 110 SEC.

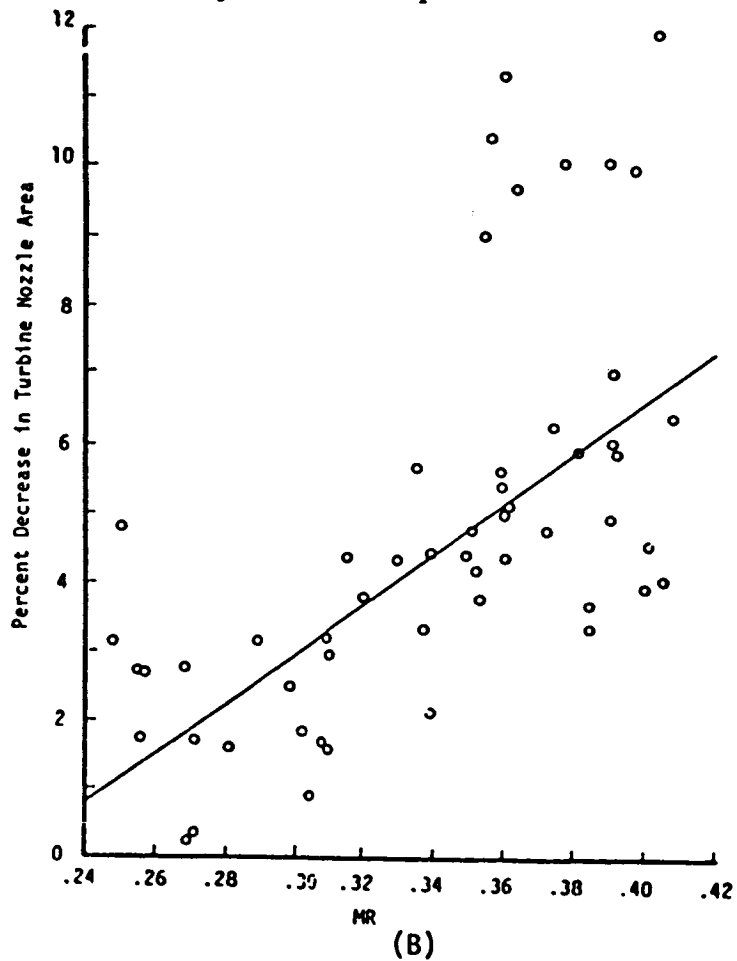


Figure B-20. Long Duration Carbon Deposition Effects in Titan I Gas Generators



of the turbine nozzle flow area was lost to carbon deposition. At the beginning of the subsequent firing, most of this obstructed area opened up, indicating 80 to 90% of the carbon deposited during the firing came off on shut-down and restart. This carbon removal was attributed to spalling resulting from differential expansion (contraction) between the deposit and the metallic substrate as the part was thermally cycled.

The test data of Figure B-20 also showed that in spite of the spalling there was a cumulative deposit buildup which is not lost in cycling. Although the buildup rate is low (about 1% area loss per 200 seconds of firing time) it is high enough to be significant in an engine designed for multiple reuse. It is apparent from this Titan I data that extended firing duration tests without intermediate cleaning should be included in the test program in order to fully evaluate the deposition process. Similar type testing under main chamber conditions might also reveal a cumulative effect.

The effect of gas generator mixture ratio on carbon deposition was also established on Titan I. A plot of the data is given in Figure B-20B. This plot shows the decrease in turbine nozzle flow area during a 90-second period starting 20 seconds into a firing. The results indicate the deposition process to be very mixture ratio sensitive with increasing mixture ratios producing higher deposition rates. These results seemingly run counter to what would initially be expected in that decreasing the amount of fuel present produced increasing deposits. The general observation of those working the Titan I gas generator development was that relatively light and easily removed deposits are formed at gas temperatures below about 1200 to 1300°F (922 to 977K). In the temperature range from about 1300°F to 1700°F (922 to 1200K) the deposits became thicker and were very hard and tenacious while at temperatures above about 1700°F (1200K) the deposits became thinner. This temperature sensitivity is considered to be indicative of the decomposition products of RP-1 since the majority of the fuel present at these low mixture ratios is unreacted RP-1. This is supported by the results of tests on the thermal stability of RP-1 conducted by J.P.L. in the late 1950's. Flow tests with heated RP-1 in the absence of oxygen showed a dramatic increase in carbon deposition once the RP-1 temperature reached 1330°F (994K), confirming the gas generator results. Apparently, when RP-1 is heated above about 1300°F (977K)

its decomposition products include a very sticky tar-like substance which adheres to almost any surface and hardens when it cools. If the RP-1 is heated above about 1700°F (1200K) this tar-like substance no longer is encountered.

The Titan I results also correlate well with the observation by Glassman, noted previously, that in very fuel-rich combustion there is a range over which the addition of more oxidizer catalyzes soot formation. The Titan I data would indicate this range spans about 1300°F to 1700°F (977 to 1200K).

While discussing fuel-rich RP-1 combustion, it should be noted that at low mixture ratios the reaction kinetics are very slow. The result is that in conventional sized hardware the combustion process does not achieve equilibrium. This was observed indirectly during Titan I development when measured gas generator  $C^*$  values were consistently lower than the equilibrium values. Rocketdyne and Aerojet each recognized and addressed this problem in their NASA preburner contracts. Rocketdyne did this by empirically adjusting their equilibrium model using Atlas gas generator data to correct for kinetics. Aerojet addressed the problem by constructing a kinetically limited fuel-rich combustion model (FRCM). Figure B-21 shows the kinetic model (FRCM) predictions from Aerojet compared with equilibrium values and with test data obtained under the Aerojet preburner contract (Ref. B-12). It is obvious that the test results support a kinetically limited model. This is significant in that the difference between the equilibrium combustion temperature and the kinetically limited combustion temperature can easily be 500°F (533K) or more. This has a significant bearing on the selection of an operating mixture ratio, design of test hardware, and interpretation of test data.

The Rocketdyne preburner/gas generator contract mentioned above (Ref. B-14) addressed both fuel-rich and oxidizer-rich  $\text{LO}_2/\text{RP-1}$  and  $\text{LO}_2/\text{CH}_4$  combustion at pressures to 3500 psia (24.13 MPa). A two-inch (5.08 cm) diameter chamber was employed. As the result of a combination of very persistent

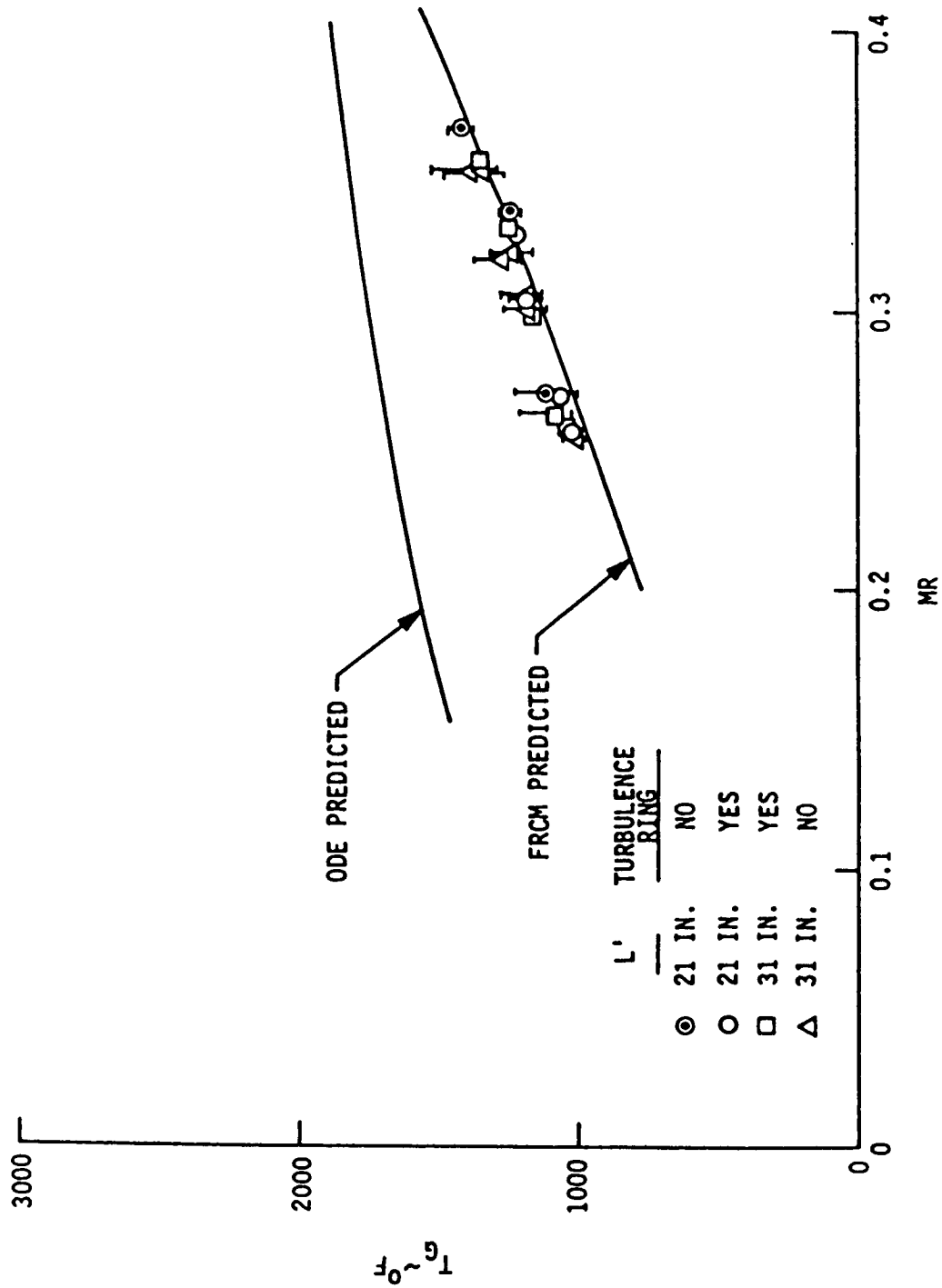


Figure B-21. The Kinetically Limited Combustion Model Matches Preburner Test Data

combustion instability problems and some facility problems, quite a few of the tests were very short. The carbon deposition measuring device was destroyed on its first test and no carbon deposition data were reported.

The ATC preburner work was performed under two NASA contracts; the first one covering design, analysis, and fabrication (Ref. B-12), while the second contract provided for testing with  $\text{LO}_2/\text{RP-1}$  (Ref. B-13). Both fuel-rich and oxidizer-rich preburners were addressed. The fuel-rich preburner had a total propellant flow of nominally 40 lbs/sec (18.14 kg/s) at a chamber pressure of 2500 psia (17.24 MPa). The chamber diameter was slightly larger than four inches (10.16 cm). Two injectors were evaluated; one using platelet technology and the other using an EDM drilled LOL. Tests were run both with and without a turbulence ring. Test equipment used included a temperature and gas sampling rake plus a turbine simulator and main injector simulator for carbon deposition measurement. A total of 17 fuel-rich tests were conducted covering 47 operating points. With the use of propellant flow control valves, as many as five separate operating conditions of two to five seconds each were included in a single firing. The longest firings were 14 seconds duration. A longitudinal mode instability was encountered which was stabilized by the use of the turbulence ring. The entire test program plus an added scope test program were conducted without hardware damage.

The results of this program can be summarized as follows:

- The temperature rake,  $C^*$  data and gas sample measurements all confirmed the kinetic combustion model as just noted.
- The ability of the turbulence ring to provide a very uniform combustion cloud independent of the injector was demonstrated. This is illustrated in Figure B-22 which shows the measured gas temperature spread for the two injectors as a function of mixture ratio. Two sets of data are shown, the one set obtained without the turbulence ring and the other with the turbulence ring. Without the turbulence ring the EDM'd LOL injector shows two to three times the temperature

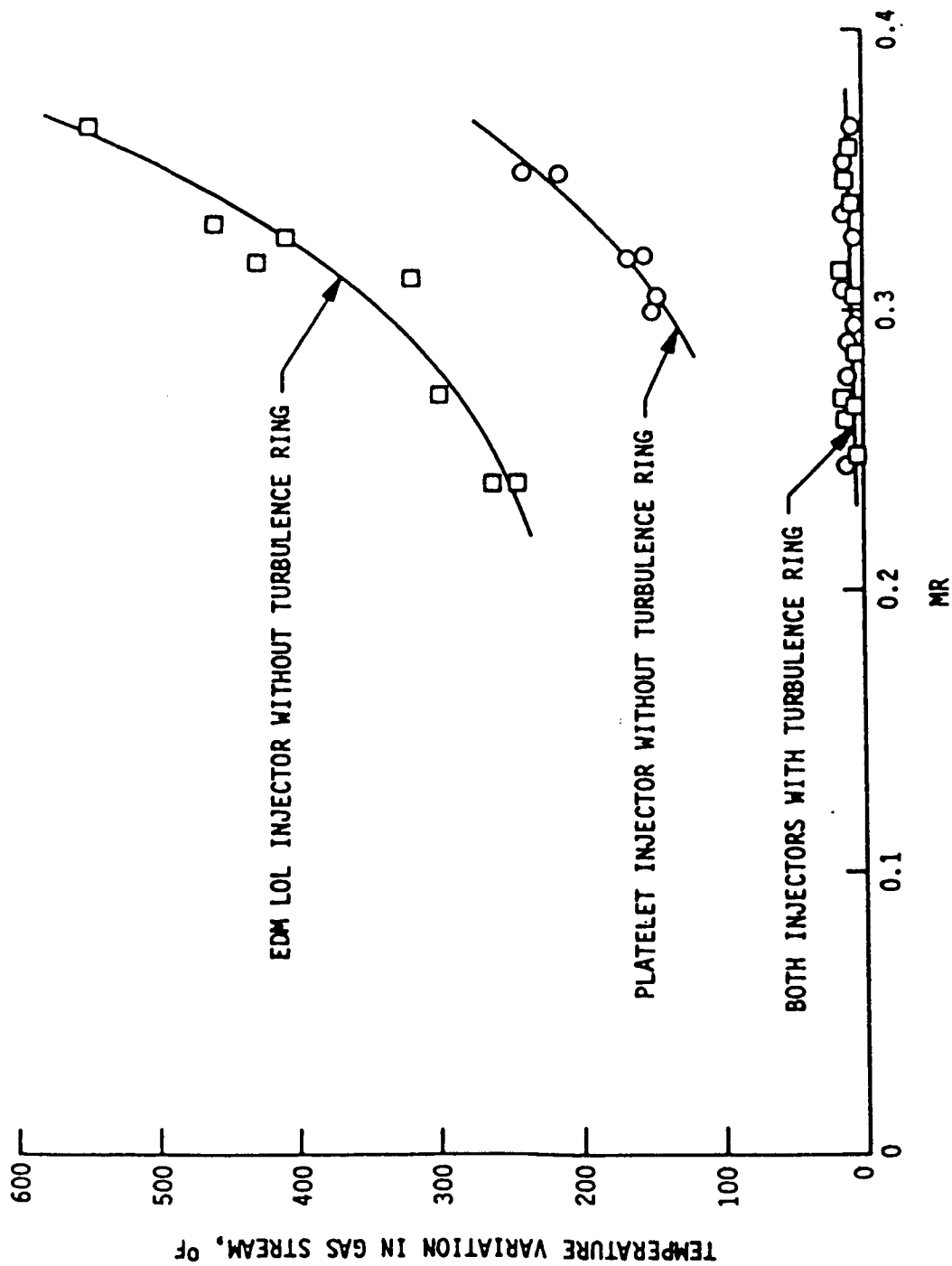


Figure B-22. The Turbulence Ring Provided a Very Uniform Gas Cloud

spread of the platelet injector. With the ring, however, the temperature spread is on the order of 10 degrees for both injectors and they become virtually indistinguishable. Use of a turbulence ring appears to be a valid method for producing a uniform gas stream and eliminating the injector as a key variable.

- Visual observation of the exhaust showed the quantity of soot increased as mixture ratio was increased, confirming the Titan I data and Glassman's observation.
- Essentially no carbon deposition was encountered in the ATC program. Tests were conducted in which pressure drop was monitored across the turbine and main injector simulators. The test results and post-fire inspection of the hardware showed the restricted flow areas were not being obstructed by carbon deposits but rather were being eroded open at a fairly rapid rate. The reason for the erosion instead of deposition remains open to speculation. Droplet or carbon particle impingement and chemical attack have all been hypothesized. The lack of appreciable carbon deposition in the non-eroded areas may be the result of inadequate test durations.

The conclusions which may be drawn from the above are similar to those for main chambers.

- (1) The experimental database of carbon deposition in low mixture ratio devices is minimal and nonquantitative. However, there is some understanding of the mechanisms which contribute to the carbon formation part of the process.
- (2) No modeling of the deposition process for low mixture ratio conditions has been published.

#### 4. Gas Turbines

Carbon deposition in gas turbines occurs under circumstances which in some respects are very similar to those in rocket engine components. However, there are also important differences. In terms of similarities, the jet fuels and natural gas which are widely used as gas turbine fuels are very similar chemically to RP-1 and methane. In addition, both gas turbines and rockets are steady flow devices, and both rely on oxygen as the oxidizer. The most significant difference between rockets and gas turbines is the fact that gas turbines are air breathing devices. The presence of the airborne nitrogen drops the gas turbine combustion temperatures to levels approaching those of rocket gas generators although the mixture ratios are usually more oxidizer-rich than those of a rocket main chamber. Thus, the chemistry of the gases in a gas turbine is considerably different than in a rocket engine. In addition, the pressures and mass flux levels in gas turbines are an order of magnitude or more lower. As noted previously, gas chemistry and mass flux have been identified as first order effects influencing the deposition process. Since gas turbines differ significantly from rocket engines in these two areas, it appears unlikely, based on current knowledge, that any gas turbine carbon deposition data can be used directly in developing a carbon deposition model for rockets. However, the basic modeling work and data trends observed in the gas turbine area may provide valuable insights.

Soot formation and deposition have been of interest to manufacturers of gas turbines concerned with meeting emission control or energy recovery goals. Gas turbine exhaust stream heat exchangers used for energy recovery have encountered serious degradation due to deposition of carbon on the heat exchanger surfaces. When the heat exchanger is designed and located such that convective heat transfer is maximized, convective mass transfer is also maximized. Thus, the heat transfer surface becomes an effective particle collection surface.

Results of an investigation of carbon deposition on gas turbine exhaust gas heat exchanger tubes have been presented by White (Ref. B-15) and typify the status of carbon deposition studies in gas turbines. The data are

for a gas turbine burning JP-5, and air with a downstream heat exchanger simulator and gas sampling ports. Extensive analysis on gaseous and solid products was reported. Soot particle morphological characteristics were examined with a scanning microscope. The experimental data are reported in terms of the equivalence ratio, which is the ratio of the actual fuel/air ratio to the stoichiometric fuel/air ratio. The equivalence ratio and the percent of fuel prevaporized were the primary variables considered.

The water-cooled Hastelloy-X heat exchanger simulator consisted of two tubes mounted one inside the other in an eccentric manner. The outer semiannular region contained the cooling water, and the inner tube transported the gas samples. The gas samples were integrated across the exhaust tube diameter by using several equally spaced sample ports. For example, a soot depositing condition with inlet air temperature and pressure of 32°C and 2.0 atmospheres, for an equivalence ratio of .836, gave an exhaust gas of the following composition: 5.1% CO<sub>2</sub>, 37.7% CO, 2.7% NO<sub>x</sub>, 22.0% unburned hydrocarbons, and 32.5% other combustion and atmospheric gases. This was a fuel-lean mixture.

White reported that the degree of fuel-air premixing completely dominated soot production. At 12% prevaporization or higher, soot formation failed to occur. It was observed that soot particles under fuel-lean to stoichiometric conditions deposited and adhered better than soot particles produced under fuel-rich conditions. Although under fuel-rich conditions smoke was produced, the particles were not as likely to adhere to the surface. The rate of soot deposition was low, ranging from  $2 \times 10^{-5}$  grams/sec for an equivalence ratio of 1.0, to  $3 \times 10^{-5}$  g/s for an equivalence ratio of 0.8. (White did not specify the area over which this deposition was occurring.) Soot formation generally occurred for combustion efficiencies below 97%.

Scanning electron microscope images of gas-borne soot particles captured on filter paper suggested a mechanism for the formation of the particles. The particles with diameters smaller than 0.3 microns were generally spheroidal. These small particles were most likely formed by the process of nucleation and growth from C<sub>2</sub>, C<sub>3</sub>, C<sub>2</sub>H, and C<sub>2</sub>H<sub>2</sub> species in the gas phase.



For particle diameters larger than 0.3 microns, the agglomeration rate appeared to exceed the growth rate. The resulting particles were botryoidal agglomerations of the smaller spheroidal particles. Agglomerated particles with sizes to about 50 microns were observed.

In terms of modeling the process two separate questions were addressed. The first question addressed how the carbon particles were transported to the wall while the second one was whether the carbon particles would adhere once they reached the wall. It was postulated that particle size has a strong effect on the transport of carbon to the deposition surface. Particles smaller than 0.1 microns in diameter were believed to obey Stefan's law of molecular diffusion. Between 0.1 and 1.0 micron, Brownian motion effects were stated to dominate the particle motion and thus the deposition rate. If the particles are larger than 1 micron in diameter, they were thought to be hurled through the boundary layer by their initial velocity in the turbulent flow field. This form of deposition was referred to as turbulent diffusion controlled. If the stopping distances were greater than the boundary thickness, deposition would be turbulent diffusion controlled. In this case, surface roughness would become an important parameter in the deposition process. This occurs because surface roughness produces increased levels of turbulence, giving particles with higher initial velocity vectors toward the wall. (Note that this has interesting implications. If carbon deposition produces surface roughness which in turn accelerates deposition, then an initially smooth surface may experience a slow "priming" followed by more rapid deposition. The Titan I gas generator data of Figure B-20 may be exhibiting this effect during the first 100 seconds of operation.)

Particles larger than 10 microns were stated to undergo inertial impaction. Such particles cannot follow the turns and velocity changes which the gas stream encounters in approaching an obstacle. For the conditions reported, most of the particles were under 10 microns in diameter and turbulent diffusion was probably the primary transport mechanism in the deposition process. The general relationship between deposition rate and particle size as described above is given in Figure B-23 which was taken from Reference B-15.

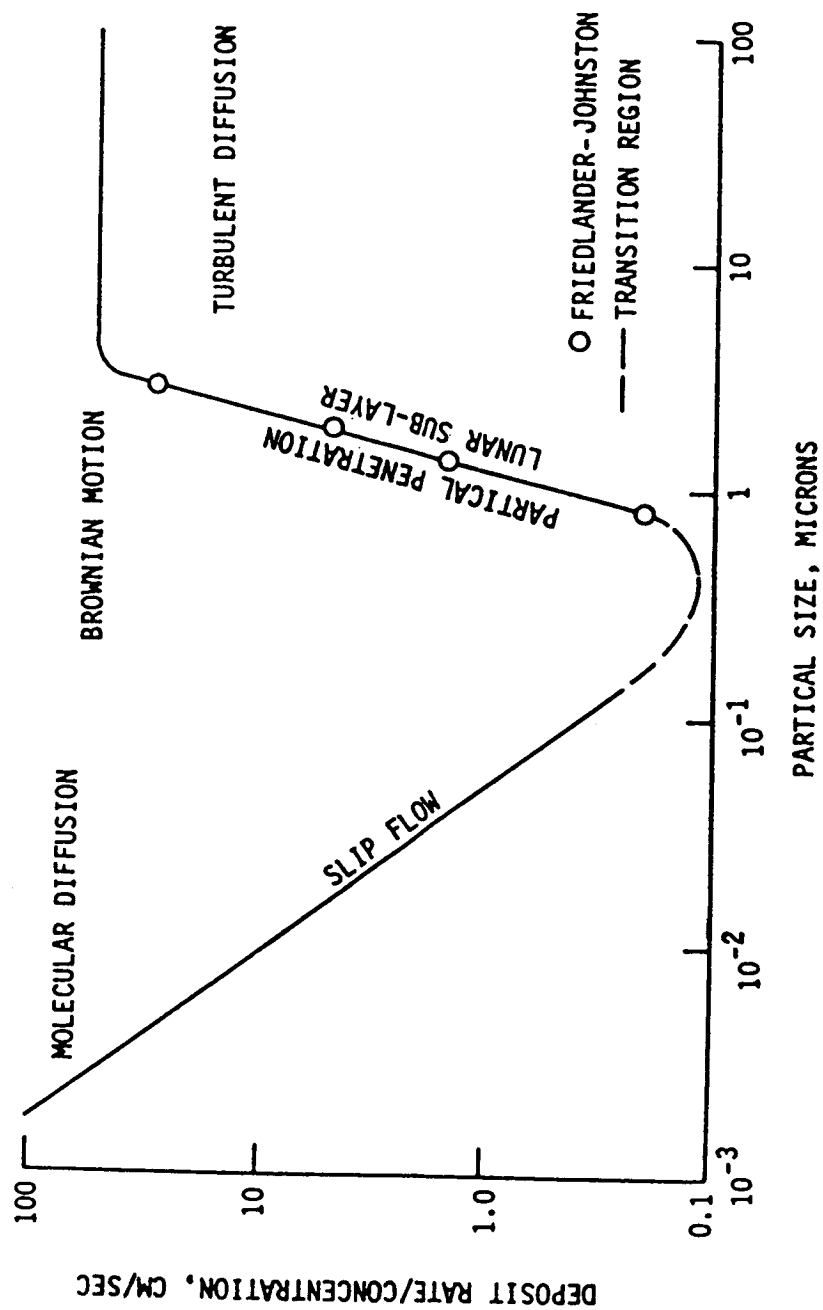


Figure B-23. Carbon Particle Size Determines How It Reaches the Wall

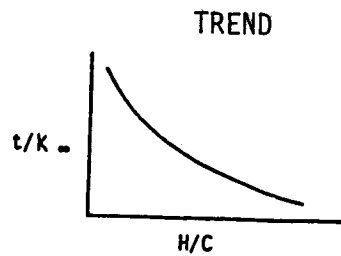
Physical adsorption, rather than chemisorption, is believed to be the main mechanism by which the carbon particles adhere to the surface. The forces causing physical adsorption are similar to those that cause the condensation of a gas to form a liquid. The heat evolved upon physical adsorption is small, and the process is completely reversible.

Soot deposits were analyzed by means of pyrolysis gas chromatography and were found to consist of nearly pure carbon with some adsorbed water. The hypothesis presented by the experimenters is that water molecules adsorbed on the oxide layers of the Hastelloy-X tube were, in turn, adsorbed onto impacted soot particles, providing the means by which the soot adhered. Upon deposition of the first layer of carbon, more water could be adsorbed. Subsequently, if more carbon particles impacted the surface, they could adhere by the same adsorption forces. This hypothesis is supported by the fact that the local conditions of temperature and pressure at the tube surface were well above the dew point of the gas stream. That is, the water present in the soot deposit was not likely to have been the result of condensation. If this hypothesis is correct, rocket chamber soot deposition might be controlled by choosing chamber materials or inserts with the appropriate affinity for water adsorption.

## 5. Summary of Results

The results of the state-of-the-art review are summarized. Only one correlation for carbon deposition for main chamber conditions has been developed (the Rocketdyne "g" model). The model matches some data reasonably well in some cases but misses badly on other data. Generally, the database for main chamber conditions is spotted at best with no comprehensive set of data generated under controlled conditions. For preburner/gas generator conditions, no modeling has been published. The corresponding database is minimal and nonquantitative. The existing data trends are summarized in Figures B-24 through B-26. An attempt to correlate the  $\text{LO}_2$ /propane data with existing empirical models is shown in Figures B-27 through B-29. The results were not conclusive and other potential models were considered. Static pressure did show a very strong influence on carbon deposition rate (see Figure B-30).

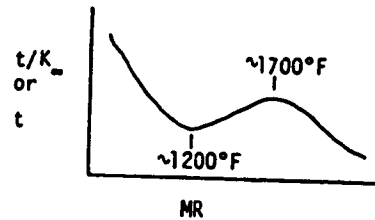
PARAMETER  
HYDROGEN/CARBON RATIO (FUEL)



SUPPORTING DATA

- P&W - YES
- R/D CAF MODEL - YES
- LOW/HC PHOTO COMBUSTION - YES

MIXTURE RATIO



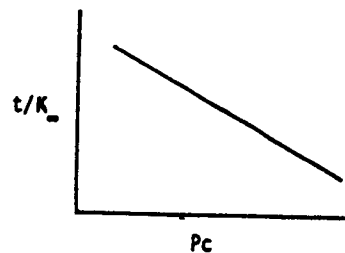
- GLASSMAN/PRINCETON (SOOT MODELS) - YES
- TITAN I G.G. - YES
- P&W - YES
- R/D CAF MODEL - YES
- SELLERS - NO

MIXING

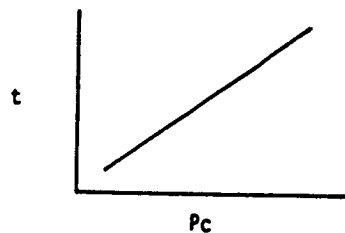


- LOX/HC PHOTO COMBUSTION - YES
- GLASSMAN (DIFFUSION VS PREMIXED) - YES
- WHITE (TURBINE) - YES

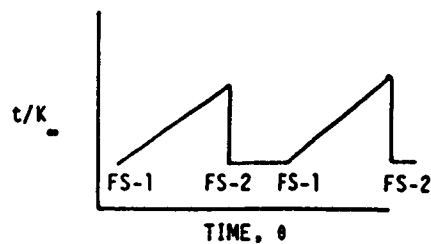
CHAMBER PRESSURE



- SELLERS (LOX/RP-1) - YES
- P&W - YES
- MID PC (LOX/PROPANE) - YES
- LOX/HC PHOTO COMBUSTION - YES
- HDF (LOX-RP-1) - YES
- TITAN I GG - YES
- LOX/RP-1 PREBURNER - YES
- MID PC - YES
- LOX/HC PHOTO COMBUSTION - NO

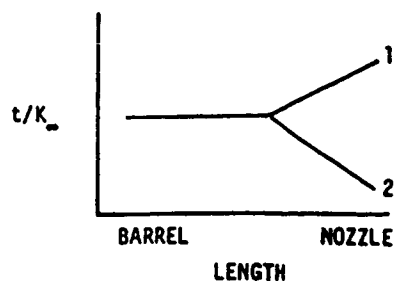


HISTORY



- TITAN I GG (COLD FLOW AFTER SHUTDOWN) YES
- MID PC - YES

CHAMBER PROFILE



- SEADER AND WAGNER (LOX/RP-1) 1
- P&W FLOX/METHANE 1
- P&W FLOX/BUTENE-1/PROPANE 2
- MID PC (LOX/PROPANE) 2

Figure B-24. Carbon Deposition Trends

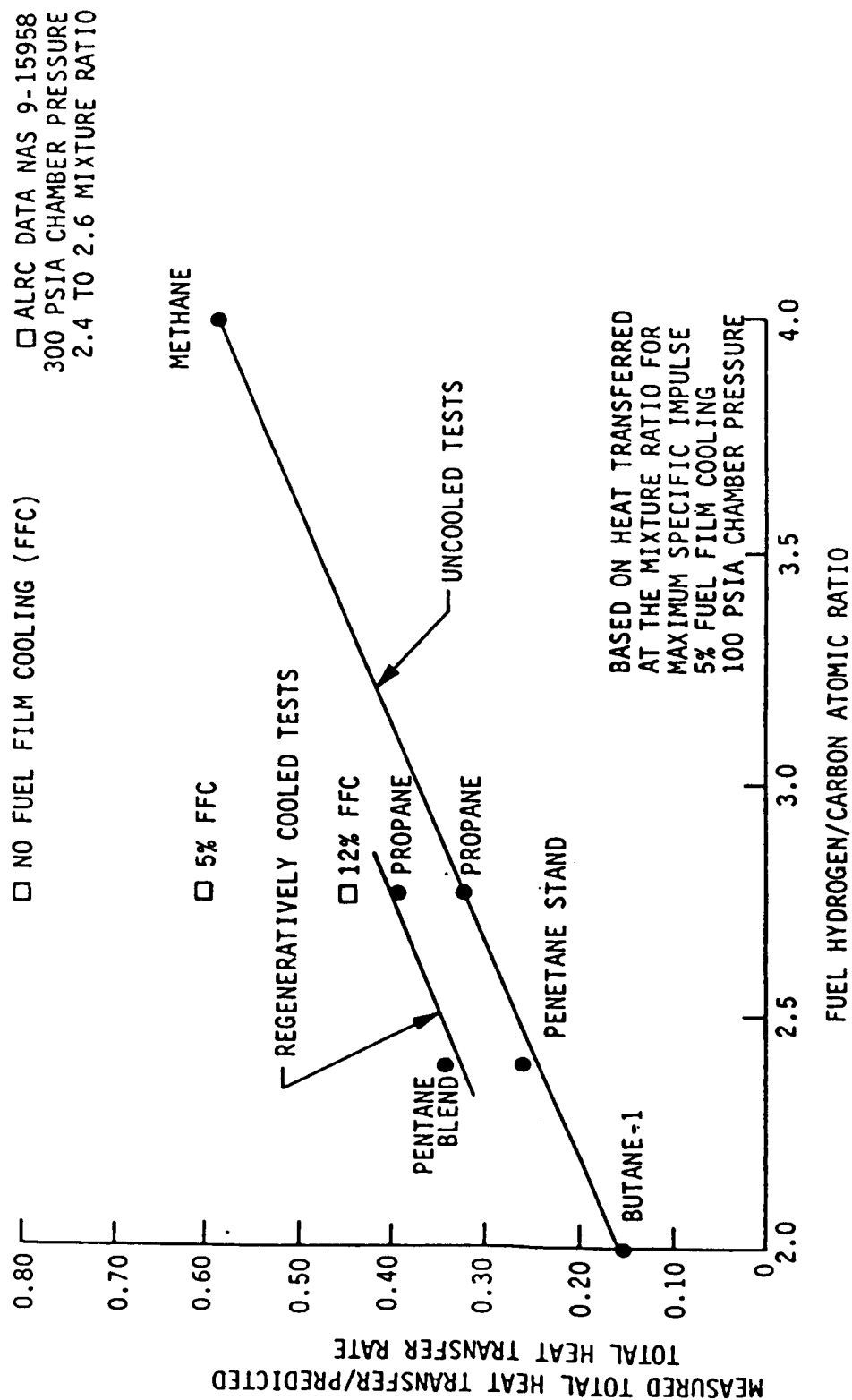


Figure B-25. Hydrogen/Carbon Atomic Ratio Correlation Model

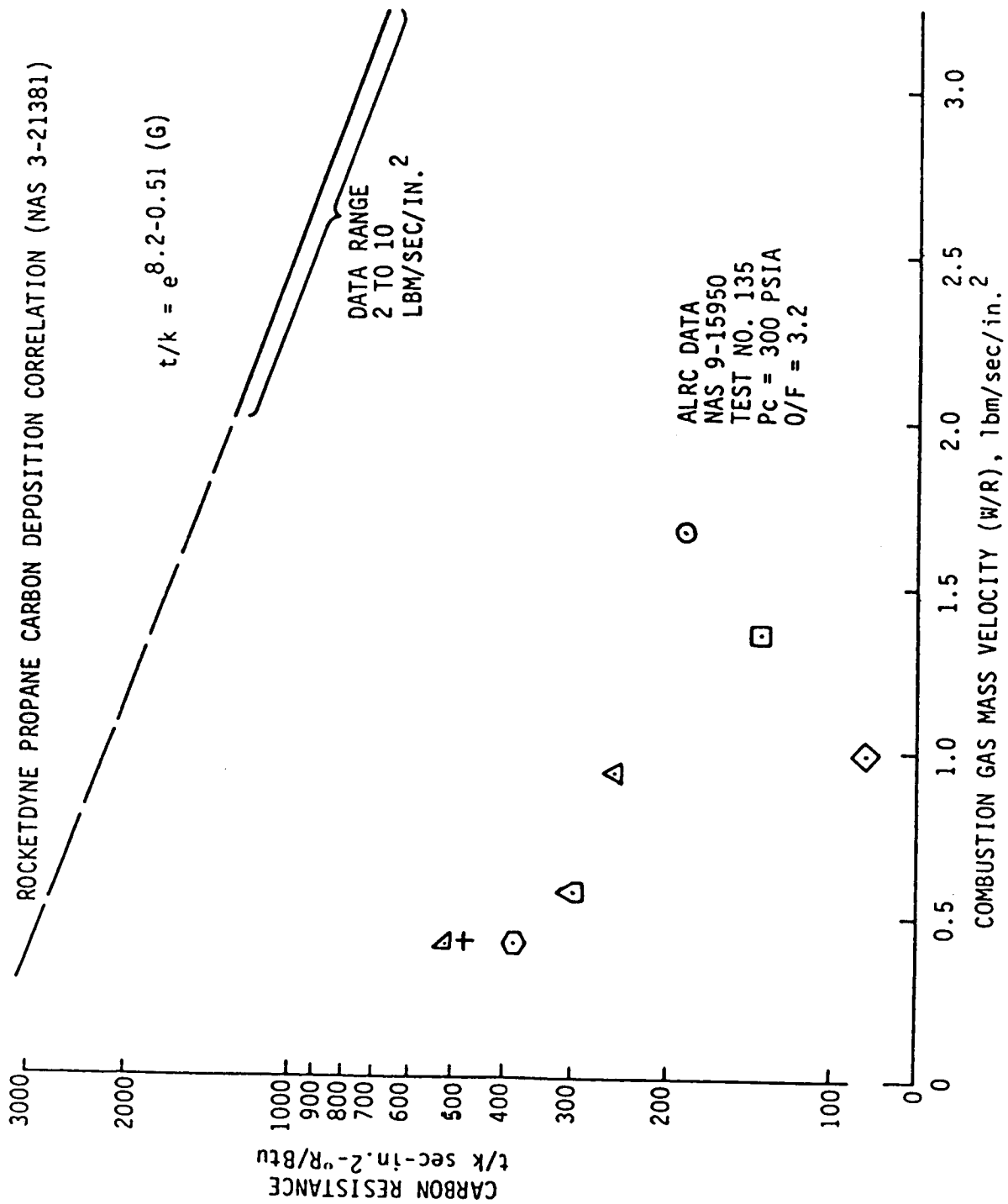


Figure B-26. Combustion Gas Mass Velocity Correlated Model

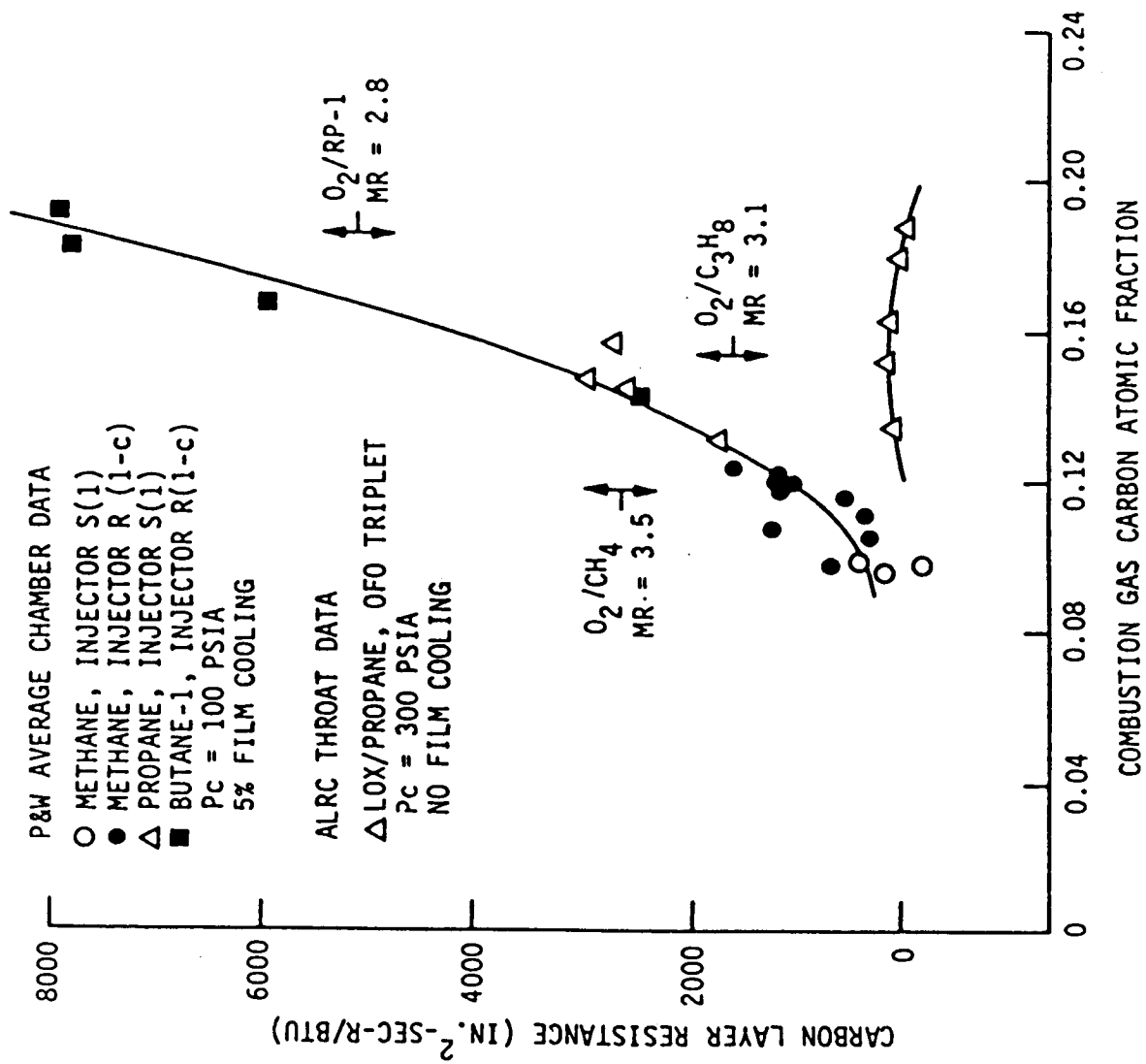


Figure B-27. Combustion Gas Carbon Atomic Fraction Correlation Model

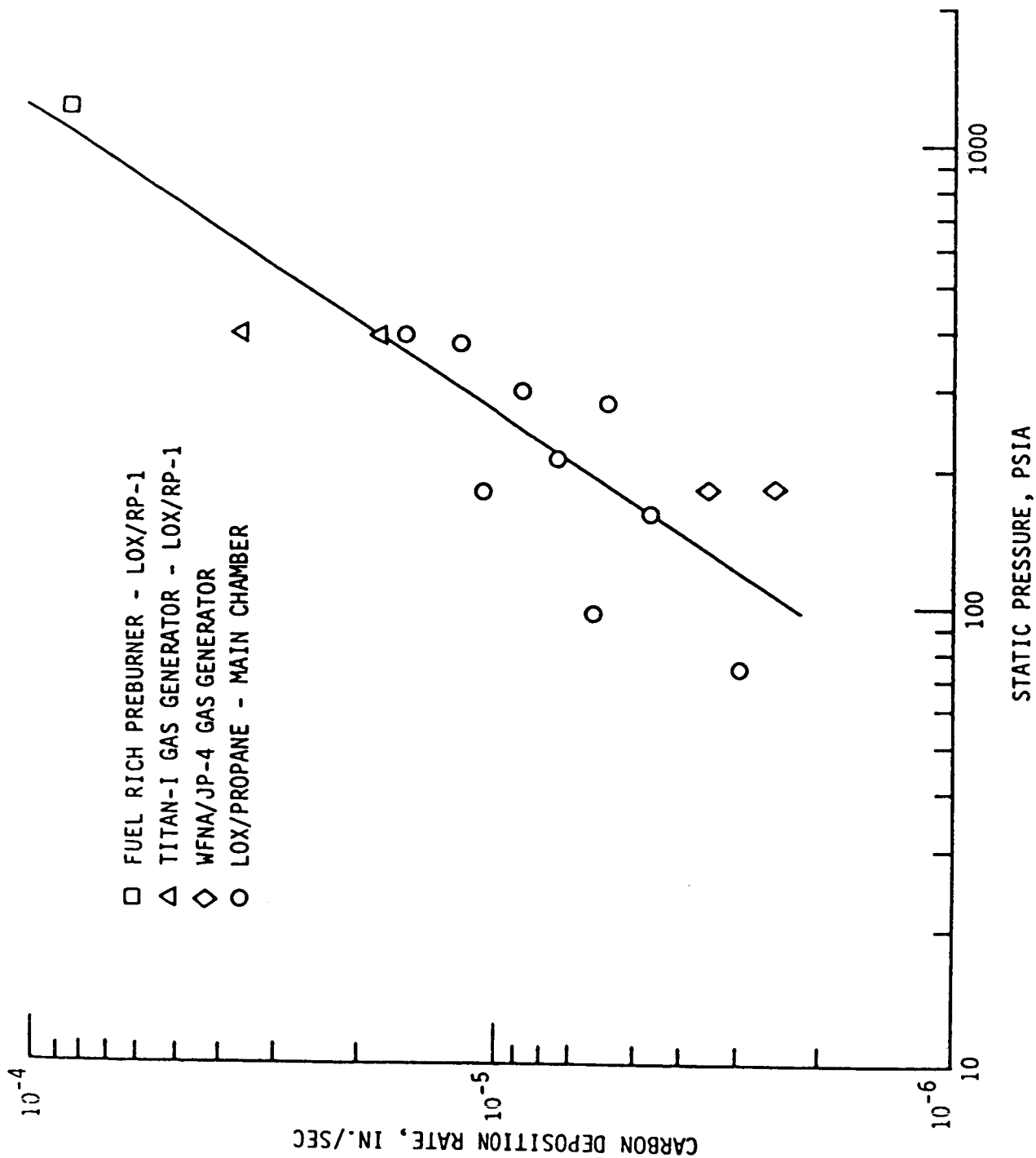


Figure B-28. Static Pressure Correlation Model



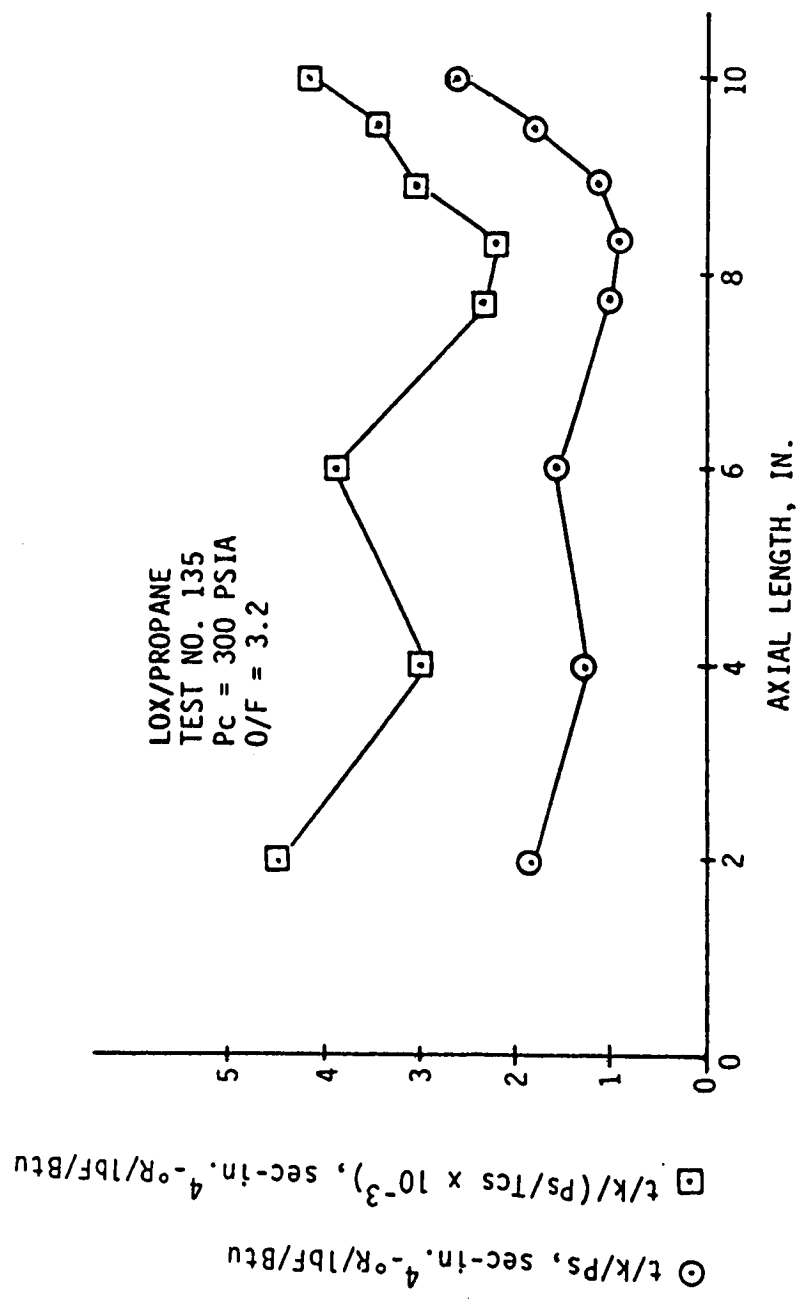


Figure B-29. Adsorption Correlation Model

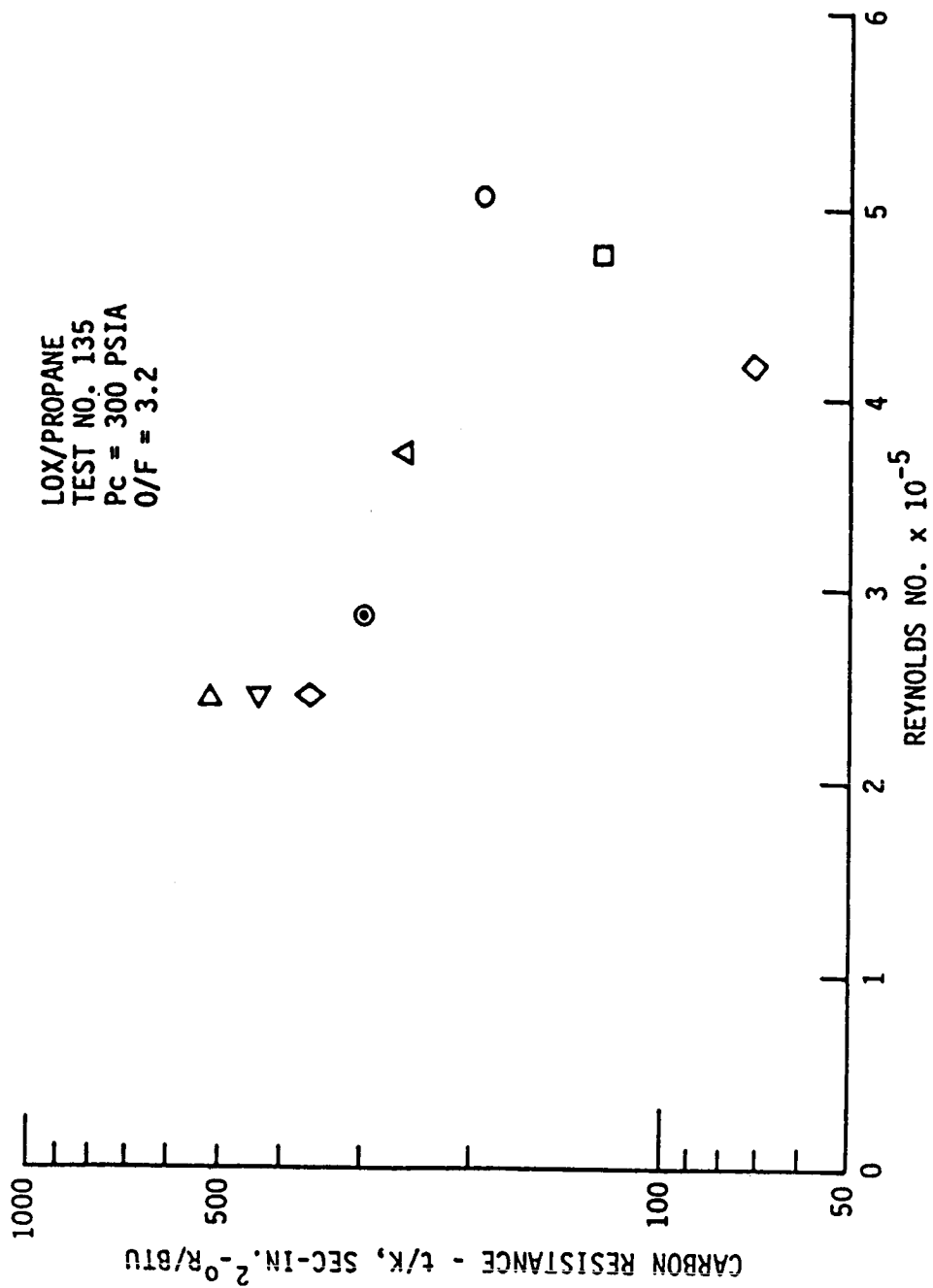


Figure B-30. Reynolds Number Correlation Model

A review of gas turbine related efforts identified adsorption as a possible controlling mechanism for carbon deposition. The term adsorption refers to the existence of a higher concentration of any particular component at the surface of a liquid or solid phase than is present in the bulk. The attraction is caused by the unbalanced molecular forces at the surface of the liquid or solid. For a given substance, the extent of absorption is a function of concentration. Therefore, the amount adsorbed increases with pressure and decreases with temperature. If pressure is the dominant variable, carbon resistance ( $t/k$ ) divided by static pressure through an engine nozzle should be approximately constant. This is not the case for the  $LO_2$ /propane (see Figure B-31). Surface temperature and pressure were both considered to be dominant variables with not much better results (see Figure B-31). But it must be remembered that there are significant differences between gas turbines and rockets. First, the chemistry of gas turbines is nitrogen dilution and oxidizer rich. Second, the pressures and mass fluxes of gas turbines are an order of magnitude lower. Nevertheless, gas turbine data can provide some insight into rocket modeling.

Reynolds number was noted by Rocketdyne as a possible carbon deposition correlation parameter so both diameter and length based values were computed for the  $LO_2$ /propane data. While major trends were correlated (see Figures B-32), the data scatter is very large.

The results of the above noted approach to modeling carbon deposition imply that no one variable can be used to adequately correlate the data and that a general model framework that includes several variables has the greatest potential of meeting the objectives of this program.

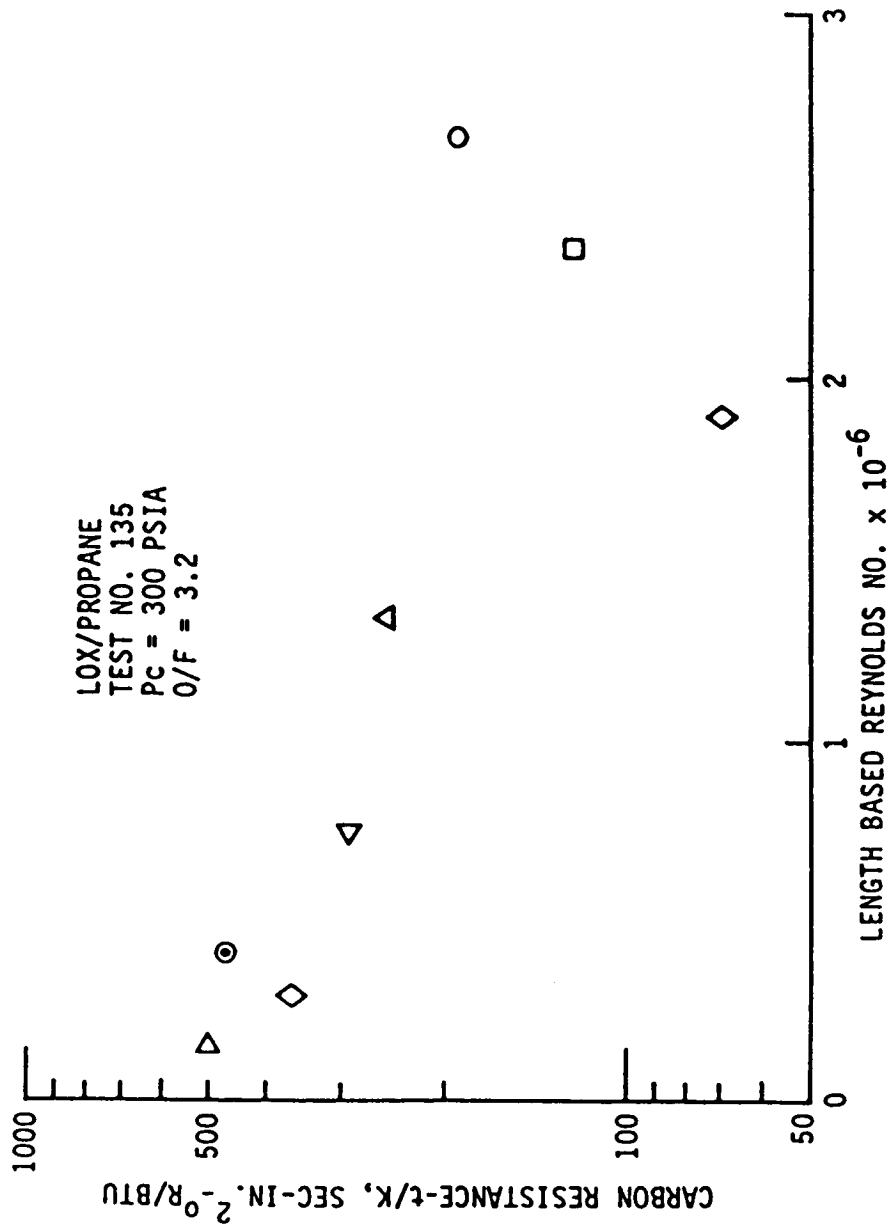


Figure B-31. Length Based Reynolds Number Correlation Model

$$t/K_{\theta} = D/R (1 - e^{-R\theta})$$

$t/K_{\theta}$  - CARBON RESISTANCE @ TIME  $\theta$

D - DEPOSITION TERM

R - REMOVAL TERM

$$t/K_{\infty} = D/R$$

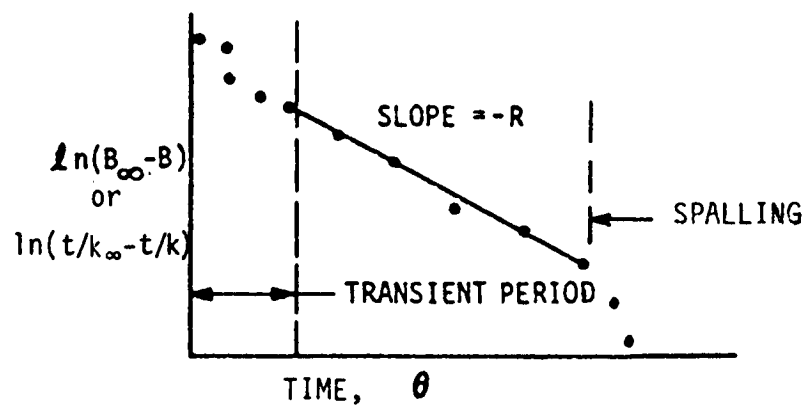


Figure B-32. ALRC Carbon Deposition Correlation Model

## REFERENCES

- B-1. Glassman, I., "Phenomenological Models of Soot Processes in Combustion Studies," Princeton University Engineering Report No. 1450, July 1979.
- B-2. Glassman, I., Yaccarino, P., Manheimer-Timnat, Y. and Schug, P., "Sooting Behavior of Gaseous Hydrocarbon Diffusion Flames and the Influence of Additives," 7th Int'l. Collog. on Gasdynamics of Explosions and Reactive Systems, Gottingen, Germany, August 1979.
- B-3. Jensen, D.E., "Prediction of Soot Formation Rates: A New Approach," Proc.R. Soc. Lond. A.338, 375-396 (1974).
- B-4. Bokros, J.C., in Chemistry and Physics of Carbon, V5, Marcel Dekker, Inc., New York, 1969.
- B-5. Sellers, J.P., "Effect of Carbon Deposition on Heat Transfer in a LOX/RP-1 Thrust Chamber," ARS Journal, May, 1981.
- B-6. Seader, J.D. and Wagner, W.R., "Regenerative Cooling of Rocket Engines," Chemical Engineering Techniques in Aerospace, Chemical Engineering Symposium Series, Vol. 60, No. 52, 1964.
- B-7. Space Storable Regenerative Cooling Investigation, Contract NAS 3-11191.
- B-8. A Graphite Lined Regeneratively Cooled Thrust Chamber, NASA CR-120853, 1971.
- B-9. Investigation of Advanced Cooling Techniques for High Pressure Hydrocarbon-Fueled Engines, Contract NAS 3-21381.
- B-10. "Photographic Combustion Characterization of LOX/Hydrocarbon Type Propellants," Contract NAS 9-15724.
- B-11. High Density Fuel Combustion and Cooling, Contract NAS 3-21030.
- B-12. Fuel/Oxidizer-Rich, High Pressure Preburners, Contract NAS 3-21753.
- B-13. Testing of Fuel/Oxidizer-Rich, High Pressure Preburners, Contract NAS 3-22647.
- B-14. High-Pressure LOX/Hydrocarbon Preburners and Gas Generators, Contract NAS 3-833243.
- B-15. White, D.J., "Effects of Gas Turbine Combustion on Soot Deposition," Solar Turbines International Report SR79-R-4643-oe, March 1979.

APPENDIX C  
HARDWARE DRAWINGS

## HARDWARE DRAWINGS

<u>Drawing No.</u>	<u>Title</u>
1195815	Thrust Chamber Assembly
1195813	Chamber-Barrel Section
1195777	Injector Assembly
1195812	Resonator Ring Fuel-Film Cooling Assembly
1195814	Chamber-Nozzle Section, $P_c = 2000$ psi
1195849	Turbine Simulator
1195850	Kistler Ring
1195851	Turbulence Ring Fuel-Film Cooling Assembly
1195852	Resonator Tuning Ring
1198636	Turbulence Ring
1198637	Upstream L' with Temperature Rake and Pressure Taps
1198638	Downstream L' with Pressure Tap
1198639	Exit Nozzles
1198640	Turbine Simulators



APPENDIX D-1

LO<sub>2</sub>/RP-1 MAIN CHAMBER AND WATER-COOLED  
GAS GENERATOR DATA REDUCTION EQUATIONS

## MAIN CHAMBER CARBON BUILD-UP AND INJECTOR CALCULATION REQUIREMENTS

### Carbon Build-Up

1. Carbon to clean wall heat flux ratio

$$Q/AREd = Q/A_{t=i} / Q/A_{max} \text{ (or } t = \text{TBD sec)}$$

2. Carbon Resistance,  $(t/u)_{t=i}$

$$(t/k)_{t=i} = (T_r - T_w) \left( \frac{1}{Q/A_{t=i}} - \frac{1}{Q/A_{max}} \right) \quad \begin{matrix} T_w = T + R * Q/A_{t=i} \\ T_r = T_{STAT} + R_f (T_c - T_{STAT}) \end{matrix}$$

3. Carbon Build-Up Rate,  $(t/K)_{\Delta t} = [(t/k)_{t=i+1} - (t/k)_{t=i}] / (t_{i+1} - t_i)$

4. Turbine Simulator Pressure Ratio

$$PR_{TS} = PCTSD/PCTSU$$

5. Turbine Simulator Pressure Drop

$$DP_{TS} = PCTSU - PCTSD$$

6. Turbulence Ring Pressure Ratio

$$PR_{TR} = (PCTSU/PC-1)$$

7. Turbulence Ring Pressure Drop

$$DP_{TR} = (PC-1) - PCTSU$$

8. Nozzle Area

$$NA1 = WTOT * C/(PC-1)/gc; \quad C = 5950 \text{ MR} + 720$$

$$NA2 = WTOT * C/PCTSD/gc$$

### Injector

1.  $C^*_{M.C.} = (PC-1) \times A_t \times gc/WTOT$
2.  $WTOT = WOX + WF$
3.  $MR = WOX/WF$
4.  $DPOJ = POJ - (PC-1)$
5.  $DPFJ = PFJ - (PC-1)$
6.  $MMC = MR \times DPOJ/DPFJ \times S.G._F/S.G._{OX}$
7.  $KWOJ = WOX / DPOJ \times S.G._{OX}$
8.  $KWFJ = WF / DPFJ \times S.G._F$

APPENDIX D-2

LO<sub>2</sub>/RP-1 GAS GENERATOR DATA  
REDUCTION EQUATIONS

# RP-1 PREBURNER/GAS GENERATOR TEST SERIES

## CARBON BUILD-UP AND INJECTOR CALCULATION REQUIREMENTS

### Carbon Build-up

1. Turbine Simulator Pressure Ratio

$$PR_{TS} = PCTSD/PCTSU$$

DPTS-C = DPTS measured or (PCTSU-PCTSD) if DPTS measure invalid.

$$DP \text{ CORR} = [(DPTS-C) - (PCTSU - PCTSD)] / 2$$

$$PR_{TS} \text{ CORR} = (PCTSD - DP \text{ CORR}) / (PCTSU + DP \text{ CORR})$$

2. Turbine Simulator Pressure Drop

$$DP_{TS} = PCTSU - PCTSD$$

3. Turbulence Ring Pressure Ratio

$$PR_{TR} = (PCTSU/PC-1)$$

4. Turbulence Ring Pressure Drop

$$DP_{TR} = (PC-1) - PCTSU$$

5. Nozzle Area

$$NA1 = WTOT * C / (PC-1) / gc \quad C = 5950 \text{ MR} + 720$$

$$NA2 = WTOT * C / PCTSD / gc$$

6. Turbine Simulator Area

$$COA = \frac{WTOT}{PCTSU} \sqrt{1544 * T / MW} \sqrt{\frac{2gc k}{k-1} (PR_{TSC})^{2/k} - (PR_{TSC})^{\frac{(k+1)}{k}}}$$

$$T = 3350 \text{ MR} + 660$$

$$MW = -112.5 \text{ MR} + 67.5$$

$$K = 0.325 \text{ MR} + 1.010$$

7. New Turbine Simulator Pressure Ratio

$$PRTS-2 = (PCTSD-2) / (PCTSU-2)$$

$$DPTS2-C = (PCTSU-2) - (PCTSD-2)$$

$$DP-2 \text{ CORR} = [(DPTS-2) - (DPT2-C)] / 2$$

DPTS-2 is measured D-5

$$PRTS2 \text{ CORR} = [(PCTSD-2) - (DP-2 \text{ CORR})] / [(PCTSU-2) + (DP-2 \text{ CORR})]$$

### Injector

1.  $C_{P.B.}^* = PCTSD \times A_t \times gc/WTOT$
2.  $WTOT = WOX + WF$
3.  $MR = WOX/WF$
4.  $DPOJ = POJ - (PC-1)$
5.  $DPFJ = PFJ - (PC-1)$
6.  $WFC = KWFC \star \sqrt{DPFJ \star S.G._F}$      $KWFC = 0.0655 (P.B.)$
7.  $MRC = WOX/WFC$
8.  $MPB = 1/MRC \star \sqrt{DPFJ/DPOJ} \star \sqrt{S.G._{ox}/S.G._F}$     (Momentum outer/inner)
9.  $MMC = MR \star \sqrt{DPOJ/DPFJ} \star \sqrt{S.G._F/S.G._{ox}}$
10.  $KWOJ = WOX / \sqrt{DPOJ \star S.G._{ox}}$      $S.G._{ox} = f (TOTCV, POJ)$
11.  $KWFJ = WF / \sqrt{DPFJ \star S.G._F}$      $S.G._F = f (TFFM)$

APPENDIX D-3

LO<sub>2</sub>/PROPANE AND LO<sub>2</sub>/METHANE GAS  
GENERATOR DATA REDUCTION EQUATIONS

PROPANE AND METHANE TEST SERIES  
CARBON BUILD-UP AND INJECTOR CALCULATION REQUIREMENTS

Carbon Build-up

1. Turbine Simulator Pressure Rates

$$PR_{TS} = PCTSD/PCTSU$$

$$DPTS-C = DPTS \text{ measured or } (PCTSU - PCTSD) \text{ if DPTS measure invalid.}$$

$$DP \text{ CORR} = [(DPTS-C) - (PCTSU - PCTSD)]/2$$

$$PR_{TS} \text{ CORR} = (PCTSD - DP \text{ CORR}) / (PCTSU + DP \text{ CORR})$$

2. Turbine Simulator Pressure Drop

$$DP_{TS} = PCTSU - PCTSD$$

3. Turbulence Ring Pressure Ratio

$$PR_{TR} = (PCTSU/PC-1)$$

4. Turbulence Ring Pressure Drop

$$DP_{TR} = (PC-1) - PCTSU$$

5. Nozzle Area

$$NA1 = WTOT * C / (PC-1) / gc$$

$$NA2 = WTOT * C / PCTSD / gc$$

6. Turbine Simulator Area

$$C_D A = A_t \left[ \frac{(r-1)}{2 \left( \frac{\gamma-1}{2} \right)^{\frac{\gamma+1}{\gamma-1}} \left[ (PR_{TSC})^{2/\gamma} - (PR_{TSC})^{\frac{\gamma+1}{\gamma}} \right]} \right]^{1/2}$$

Calculate  $C_D A$  for  $\gamma = 1.2$



7. New Turbine Simulator Pressure Ratio

$$\text{PRTS-2} = (\text{PCTSD-2})/(\text{PCTSU-2})$$

$$\text{DPTS2-C} = (\text{PCTSU-2}) - (\text{PCTSD-2})$$

$$\text{DP-2 CORR} = [(\text{DPTS-2}) - (\text{DPT2-C})]/2$$

DPTS-2 is measured

$$\text{PRTS2 CORR} = [\text{PCTSD-2}) - (\text{DP-2 CORR})] / [\text{PCTSU-2}) + (\text{DP-2 CORR})]$$

## Injector

1.  $C_{P.B.}^* = PCTSD \times A_t \times g_c / WTOT$
2.  $WTOT = WOX + WF$
3.  $MR = WOX / WF$
4.  $DPOJ = POJ - (PC-1)$
5.  $DPFJ = PFJ - (PC-1)$
6.  $WFC = KWFC \times \sqrt{DPFJ \times S.G._F}$      $KWFC = 0.0655 (P.B.)$
7.  $MRC = WOX / WFC$
8.  $MPB = 1 / MRC \times \sqrt{DPFJ / DPOJ} \times \sqrt{S.G._{ox} / S.G._F}$     (Momentum outer/inner)
9.  $MMC = MR \times \sqrt{DPOJ / DPFJ} \times \sqrt{S.G._F / S.G._{ox}}$
10.  $KWOJ = WOX / \sqrt{DPOJ \times S.G._{ox}}$      $S.G._{ox} = f (TOTCV, POJ)$
11.  $KWFJ = WF / \sqrt{DPFJ \times S.G._F}$      $S.G._F = f (TFFM)$